

# **Deformation of the Human Brain Under Rotational Loading**

---

A Dissertation

Presented to

the faculty of the School of Engineering and Applied Science

University of Virginia

---

in partial fulfillment  
of the requirements for the degree

Doctor of Philosophy

by

Ahmed A. Alshareef

May 2019

# APPROVAL SHEET

This Dissertation  
is submitted in partial fulfillment of the requirements  
for the degree of  
Doctor of Philosophy

Author Signature: 

This Dissertation has been read and approved by the examining committee:

Advisor: Matthew B. Panzer

Committee Member: Jeffrey W. Holmes

Committee Member: Jeff R. Crandall

Committee Member: Silvia S. Blemker

Committee Member: Jason P. Sheehan

Committee Member: \_\_\_\_\_

Accepted for the School of Engineering and Applied Science:



Craig H. Benson, School of Engineering and Applied Science

May 2019

## ABSTRACT

Traumatic brain injuries (TBI) are one of the least understood injuries to the body. Finite element (FE) models of the brain are crucial for understanding brain injury and developing injury mitigation countermeasures, and these models have predicted that the magnitude of human brain deformation (and the resulting brain strain and injury risk) is dependent on magnitude, duration, and direction of the angular velocity of the human head. However, this hypothesis has never been demonstrated experimentally. Furthermore, the computational models lack the experimental data necessary to validate the brain's response to a controlled dynamic rotation that is consistent with exposures in sports and automotive crashes. Therefore, the goal of this dissertation was to improve the experimental understanding of brain deformation under rotational loading and to improve the biofidelity of FE brain modeling capabilities. The goal was achieved using both experimental and computational aims. The experimental aims focused on developing a methodology to measure *in-situ* human brain motion under rotational loading, and on using the methodology to build a dataset of brain deformation. The computational aims focused on developing a methodology to evaluate FE brain models in comparison to experimental data, and a framework to optimize the material properties of the models to improve their biofidelity.

A new method was developed to collect dynamic brain motion data using sonomicrometry. Small, neutrally-dense ultrasound crystals were embedded into human cadaveric brain tissue, and point-to-point distance measurements between crystal pairs were recorded during head impact. This method provided highly accurate and repeatable data that allowed for the measurement of brain deformation at various locations within the brain and for multiple severities for each specimen. A total of six cadaveric human specimens were tested and combined into a brain deformation dataset, containing approximately 5,000 displacement

curves. The dataset was aggregated into average response corridors that represent the variance in brain deformation response among the tested specimens.

To encourage a consistent method of validating FE brain models, two widely used models were evaluated using various techniques of comparing the FE nodal motion to the experimental brain deformation data. A sensitivity analysis of the effect of the models' material properties on brain motion was conducted to identify parameters that could be calibrated to improve the biofidelity of the model. The sensitivity analysis results were then used to predict improved material properties for the FE brain models. Overall, the computational aims provide an overarching framework for FE model developers to evaluate and optimize models based on the experimental dataset.

This dissertation advances the understanding of human brain deformation through the development of a methodology and dataset quantifying *in situ* human brain deformation. The contribution of a dataset of brain deformation, including average data corridors, will have a broad impact on the TBI biomechanics field, allowing researchers to develop and evaluate the next generation of FE brain models. An improved experimental understanding and modeling of brain mechanics will be an important step towards mitigating the incidences and consequences of TBI, thereby helping to reduce the societal burden of brain injuries.

## **DEDICATION**

*To my mother and father, Mohammed, Sameha, and Amro: your love and encouragement have been invaluable.*

*To my wife Aisha and daughter Asiya: thank you for the care and love in this journey.*

*To Amu Louai and my IAC family: thank you for the inspiration and endless support.*

# CONTENTS

|   |             |
|---|-------------|
| <b>ABSTRACT</b> .....                                   | <b>III</b>  |
| <b>CONTENTS</b> .....                                   | <b>VI</b>   |
| <b>LIST OF TABLES</b> .....                             | <b>VIII</b> |
| <b>LIST OF FIGURES</b> .....                            | <b>IX</b>   |
| <b>ACKNOWLEDGMENTS</b> .....                            | <b>XVI</b>  |
| <b>CHAPTER 1: INTRODUCTION</b> .....                    | <b>1</b>    |
| Statement of Problem.....                               | 1           |
| Motivation.....   | 2           |
| Scope.....  | 4           |
| Expected Contributions.....                             | 7           |
| <b>CHAPTER 2: BACKGROUND</b> .....                      | <b>9</b>    |
| <b>CHAPTER 3: METHODOLOGY DEVELOPMENT</b> .....         | <b>29</b>   |
| Introduction.....                                       | 29          |
| Methods.....  | 32          |
| Results.....  | 68          |
| Discussion.....   | 75          |
| Conclusion.....   | 81          |
| <b>CHAPTER 4: TRILATERATION METHODOLOGY</b> .....       | <b>83</b>   |
| Introduction.....                                       | 83          |
| Methods.....  | 85          |
| Results.....  | 99          |
| Discussion.....   | 104         |
| Conclusion.....   | 107         |
| <b>CHAPTER 5: HUMAN BRAIN DEFORMATION DATASET</b> ..... | <b>109</b>  |
| Introduction.....                                       | 110         |
| Methods.....  | 112         |
| Results.....  | 121         |
| Discussion.....   | 129         |
| Conclusion.....   | 134         |
| <b>CHAPTER 6: AVERAGE DATA CORRIDORS</b> .....          | <b>135</b>  |
| Introduction.....                                       | 135         |
| Methods.....  | 138         |
| Results.....  | 148         |
| Discussion.....   | 155         |
| Conclusion.....   | 159         |
| <b>CHAPTER 7: FINITE ELEMENT MODEL EVALUATION</b> ..... | <b>160</b>  |
| Introduction.....                                       | 160         |
| Methods.....  | 163         |
| Results.....  | 171         |
| Discussion.....   | 179         |
| Conclusion.....   | 184         |
| <b>CHAPTER 8: FE MODEL MATERIAL SENSITIVITY</b> .....   | <b>186</b>  |
| Introduction.....                                       | 186         |
| Methods.....  | 189         |
| Results.....  | 196         |

|   |            |
|---|------------|
| Discussion .....                                    | 203        |
| Conclusion .....                                    | 209        |
| <b>CHAPTER 9: CONCLUSIONS .....</b>                 | <b>210</b> |
| Summary and Major Contributions.....                | 210        |
| Lessons Learned.....                                | 214        |
| Future Work .....                                   | 217        |
| <b>PUBLISHED WORK AND CONTRIBUTIONS .....</b>       | <b>221</b> |
| Peer-Reviewed Publications.....                     | 221        |
| Patents .....                                       | 222        |
| Conference Presentations.....                       | 222        |
| Affiliated Publications and Contributions.....      | 223        |
| <b>APPENDIX A: Post-Test Autopsy Notes .....</b>    | <b>225</b> |
| <b>APPENDIX B: Morphing.....</b>                    | <b>228</b> |
| <b>APPENDIX C: Dataset Summary .....</b>            | <b>232</b> |
| <b>APPENDIX D: Brain Deformation Plots.....</b>     | <b>240</b> |
| <b>APPENDIX E: Corridor Scaled Kinematics .....</b> | <b>247</b> |
| <b>APPENDIX F: FE Evaluation Scores .....</b>       | <b>253</b> |
| <b>APPENDIX G: FE Sensitivity Results .....</b>     | <b>260</b> |
| <b>REFERENCES .....</b>                             | <b>267</b> |

## LIST OF TABLES

|   |     |
|---|-----|
| Table 3-1: Perfusion port configurations. aCSF was introduced to the cranial cavity via inlets and drained via outlets. ....  | 51  |
| Table 3-2: Head kinematic sensor list.....  | 61  |
| Table 3-3: Pressure sensor list .....   | 62  |
| Table 3-4: Target Test Condition Matrix* .....  | 68  |
| Table 4-1: Positions for all transmitters (Tx) used in the trilateration simulation. The initial position of the receiver is listed in the last row. ....   | 96  |
| Table 5-1: Specimen information and identification number (ID) for all tested PMHS. ....  | 113 |
| Table 5-2: PMHS anthropometry and mass measurements.....  | 113 |
| Table 5-3: Overview of existing head kinematics-based brain injury criteria.....  | 121 |
| Table 5-4: Summary of peak linear and angular head kinematic for all specimens. Means and standard deviations are shown. ....   | 123 |
| Table 5-5: Regression coefficients, standard, and p-value for the regression of maximum peak-to-peak deformation to the varying head kinematic severities. ....   | 126 |
| Table 5-6: Regression coefficients, standard, and p-value for the regression of mean peak-to-peak deformation to the varying head kinematic severities. ....  | 127 |
| Table 5-7: Correlation of kinematics-based injury criteria to maximum and mean peak-to-peak deformation. For criteria that include an associated risk of mTBI (AIS2+), a regression analysis is also conducted for the injury risk and deformation metrics. ....                                  | 129 |
| Table 7-1: Specimen anthropometry relative to the GHBMC and SIMon FE models... ..   | 165 |
| Table 8-1: Material sensitivity matrix for each the FE model materials. The elastic materials have one parameter, the Young’s modulus or stiffness of the material. The viscoelastic materials have two parameters, the complex modulus ( $G^*$ ) and damping coefficient ( $\tan \delta$ ). .... | 191 |
| Table 8-2: Original material properties for the GHBMC and SIMon models. The range of material properties used in the sensitivity analysis are given in parentheses.....   | 193 |
| Table 8-3: Simulation matrix for each of the GHBMC and SIMon FE brain models. GHBMC included fourteen parts, and SIMon included six parts for the sensitivity analysis for a total of 342 simulations. ....   | 193 |
| Table C-1: Summary of peak head kinematics and brain deformation for specimen 846. ....   | 236 |
| Table C-2: Summary of peak head kinematics and brain deformation for specimen 896. ....   | 237 |
| Table C-3: Summary of peak head kinematics and brain deformation for specimen 900. ....   | 237 |
| Table C-4: Summary of peak head kinematics and brain deformation for specimen 902. ....   | 238 |
| Table C-5: Summary of peak head kinematics and brain deformation for specimen 903. ....   | 238 |
| Table C-6: Summary of peak head kinematics and brain deformation for specimen 904. ....   | 239 |
| Table F-1: Average weighted CORA values for the GHBMC and SIMon models.....   | 253 |

## LIST OF FIGURES

|   |    |
|---|----|
| Figure 1-1: The availability of brain deformation experiments and the development of FE brain models (Alshareef, 2019). .....   | 3  |
| Figure 1-2: Specific aims for the experimental and computational phase of this dissertation. ....   | 6  |
| Figure 2-1: Anatomy of the human head and brain (Source: NIH National Cancer Institute Dictionary (2011)).....  | 10 |
| Figure 2-2: Macroscopic anatomy of the human brain with the three major regions: the cerebrum, cerebellum, and brainstem (Source: Idaho Public Television (“The Brain: Facts (Science Trek: Idaho Public Television),”). .....  | 11 |
| Figure 2-3: Anatomy of the neuron (VectorStock).....  | 12 |
| Figure 2-4: Depiction of focal injuries in the brain (Crandall, 2015). .....  | 13 |
| Figure 2-5: Magnitude of the effect of TBI from diffuse injuries (adapted from Gennarelli 2015). .....  | 15 |
| Figure 2-6: Sagittal view of the Simulated Injury Monitor (SIMon) FE brain model. Different regions are shown, along with the finite element mesh (Takhounts et al., 2008a). .....  | 25 |
| Figure 2-7: Bi-planar X-ray and sonomicrometry in cardiac biomechanics (Alshareef, 2019). .....   | 27 |
| Figure 3-1: CAD assembly of the dynamic rotation test device (RTD). The RTD uses a linear, pneumatic actuator and converts its linear motion into pure rotation through a cable-drum-gearbox assembly. The gearbox allows for efficient mounting of the specimen in all three anatomical directions. .... | 33 |
| Figure 3-2: Head specimen preparation jig. This jig was designed to ensure consistent placement of the mounting hardware and instrumentation relative to the anatomically-defined head CG. ....   | 34 |
| Figure 3-3: Rotation coupling hardware. Collar position A was for axial rotation, B for coronal rotation, and C for sagittal rotation. Note: Only one collar was attached at a time. ....   | 35 |
| Figure 3-4: (Left) In situ sonomicrometry signal transmission test. Four crystals were inserted into a porcine brain in situ via craniotomy. (Right) The craniotomy field was flooded with saline, and then a crystal was placed in the saline outside of the dura. ....                                  | 37 |
| Figure 3-5: An in situ porcine experiment was conducted compare distances between sonomicrometry and planar X-ray. The distance measurements were all within 0.6 mm of the sonomicrometry measurements. ....  | 38 |
| Figure 3-6: Illustration of the use of sonomicrometry to track the 3D position of locations within the brain relative to the skull. ....  | 39 |
| Figure 3-7: Retraction test results using a sampling rate of 1000 Hz. The trials showed a mean signal dropout distance of approximately 117 mm. ....  | 40 |
| Figure 3-8: Transmission overlap in the brain. Fringe levels correspond to the number of transmission signals received at each node in the brain for the finalized transmission crystal array. ....   | 41 |
| Figure 3-9: Hole selection in the instrument insertion plate, shown relative to the skull. Blue and black circles indicate whether one or three crystals were inserted through each hole, respectively. ....  | 43 |

|  |    |
|--|----|
| Figure 3-10: Monofilament barbs installed on a 2-mm receiver crystal. Barbs were constructed of 10-mm length monofilament fishing line, glued to the crystal head using epoxy.....   | 44 |
| Figure 3-11: Insertion mechanism parts. A) Full length of all three parts. B) Close-up of all three parts. C) Needle inserted through a slotted cannula. ....  | 45 |
| Figure 3-12: Summary of the crystal insertion procedure. A) The cannula was inserted to the required depth, and the crystal was pushed down the length using a rod. B) The cannula was retracted, and the next crystal was placed. The ports were sealed using cord grips. C) During the test, the transmitters sequentially sent ultrasound pulses, while the receivers recorded the signals. D) A minimum of three crystal pairs was necessary to find 3D coordinates using trilateration..... | 46 |
| Figure 3-13: StatScan images of the head-neck specimen upon reception from the supplier. No skull abnormalities were revealed, and the brain was in excellent condition.....   | 49 |
| Figure 3-14: Anthropometric measurements of the skull. A) circumference, B) length (anterior-posterior), C) breadth (lateral-medial), D) height (vertex-mentum), E) height (vertex-occiput), F) brow-to-occiput arc length. Note: the measurements depicted in this figure were taken for both the head (before specimen preparation) and skull (after denuding). ....   | 49 |
| Figure 3-15: Cranial cavity without (left) and with (right) aCSF perfusion. Red arrows show air pockets. ....  | 51 |
| Figure 3-16: Identification of lateral anatomical center of gravity markers. ....  | 52 |
| Figure 3-17: Mounting pins were used to align the skull CG within the head preparation jig. ....   | 53 |
| Figure 3-18: Skull fixation plates. Left-to-right: superior, anterior, lateral (left and right), and posterior instrumentation plate. ....   | 54 |
| Figure 3-19: Posterior instrumentation plate post-sonometric crystal insertion. The posterior transmitter was passed through the hole highlighted in red. ....   | 55 |
| Figure 3-20: Four skull mounted transmitting crystals. Shown are the left anterior (LA), anterior (A), right anterior (RA), right posterior (RP), left posterior (LP), and left anterior (LA) transmitters. ....   | 55 |
| Figure 3-21: Receiver crystal projections in the three anatomical planes (left-to-right): axial, sagittal, coronal. Red dots indicate receivers that were unused due to damage to the crystal.....   | 56 |
| Figure 3-22: Transmitter crystal projections in the three anatomical planes (left-to-right): axial, sagittal, coronal. ....  | 56 |
| Figure 3-23: Receivers projected to the sagittal (top), coronal (mid), and axial (bottom) planes. All coordinates are in the head coordinate system. ....  | 58 |
| Figure 3-24: Endevco, surface mounted, pressure transducers (green arrows) were attached directly to the skull. The MSI, suspended, pressure transducer (red arrow) was passed through an M8 cord grip on the posterior fixation plate.....  | 59 |
| Figure 3-25: Sagittal, coronal, and axial mounting configurations. ....  | 59 |
| Figure 3-26: The sensors affixed to the head fixture and RTD include: DTS ARS-8k (left), Endevco 7264B-500 (right). ....   | 61 |
| Figure 3-27: The pressure transducers used in the head included: Endevco 8530B (left) and MSI EBP-100 (right). ....  | 62 |

|   |     |
|---|-----|
| Figure 3-28: Outliers (top) and level shifts (bottom) in raw (left) and corrected (right) distance traces. Outliers were removed, and level shifts were corrected by manually shifting the data.....  | 63  |
| Figure 3-29: “Good” (top, green) and “bad” (bottom, red) traces. Bad traces were omitted when performing trilateration.....   | 64  |
| Figure 3-30: Angular velocity for the four cases of the test matrix for the axial head rotations.....   | 69  |
| Figure 3-31: Six degree of freedom linear acceleration (left), angular velocity (middle), and angular acceleration (right) transformed to the local head coordinate system for specimen 846 for the sagittal 20 rad/s, 30 ms case.....  | 69  |
| Figure 3-32: Intra-cranial pressure measurements for all sagittal cases for specimen 846.....   | 70  |
| Figure 3-33: Select distance traces for the repeated axial 40 rad/s, 30 m/s pulses.....   | 72  |
| Figure 3-34: Trilaterated receiver trajectories in the coronal plane for the coronal tests. Dots indicate the initial receiver and transmitter positions. A detailed view of receivers 9 and 31 are shown on the top.....   | 73  |
| Figure 3-35: Trilaterated displacement results for receivers 9, 16, and 31 for the coronal tests. The applied angular velocity pulses (dashed line) are overlaid.....   | 74  |
| Figure 4-1: The trilateration algorithm depicted using three transmitting points and one receiver point in the same plane. Three transmitters are shown ( $T1, T2, T3$ ) with their associated positions and distances away from the receiver.....  | 87  |
| Figure 4-2: Simulated 3D displacement of an arbitrary receiver.....   | 96  |
| Figure 4-3: Example distance traces from select transmitters (Tx) to the receiver (Rx) with the true distance (black), and distance with the error introduced (red) for noisy only (left), bias only (middle), and both types of error (right).....   | 98  |
| Figure 4-4: Parameter optimization for $\sigma^2$ for the MLE (left) and Kalman-MLE algorithm (right).....  | 100 |
| Figure 4-5: The initial positions estimation for the LLS methods, NLLS, and MLE are shown for one iteration (left). The average error (right) is lowest for the MLE and NLLS methods.....   | 101 |
| Figure 4-6: Distance results from one iteration of a simulation with the ‘noise and bias’ error condition. The plots show the distance from each transmitter to the receiver with the true distance (sono), noisy distance (sono-noisy), and the LLS, MLE (after tuning), and Kalman-CT methods.....  | 101 |
| Figure 4-7: Comparison of trilateration and Kalman filtering algorithms for position error (top), displacement error (middle), and distance error (bottom) for the three error metrics.....   | 103 |
| Figure 5-1: Representative CT images following the specimen preparation and crystal insertion procedure. Specimen 903 (left) includes the mounting plates and instrumentation plate. Specimen 904 (right) shows the transmitters affixed to the skull, the receivers in the brain (note that slack is intentionally introduced in the wires during insertion), and the perfusion ports in the carotid arteries and occipital skull..... | 115 |
| Figure 5-2: Angular velocity (a) and angular acceleration (b) plots for the axial – 40 rad/s – 30 ms rotation for all specimens.....  | 122 |
| Figure 5-3: Trajectory plot for the 20 rad/s – 30ms (a-b) and 40 rad/s – 30ms (c-d) sagittal and axial tests for specimen 900. The red dots symbolize the initial position of each  |     |

|  |     |
|--|-----|
| receiver. The black dot represents the CG of the head, about which the rotation was applied. Blue dots represent the transmitter crystals in the skull. ....   | 124 |
| Figure 5-4: Peak-to-peak deformation of all crystals for all specimens for the axial – 40 rad/s – 30 ms tests in the sagittal (A), coronal (B), and axial (C) directions.....  | 125 |
| Figure 5-5: Box plots of peak-to-peak deformation for all specimens for each test. The blue boxes represent the 25 <sup>th</sup> and 75 <sup>th</sup> quartile values, the red line represents the median, and the dashed lines represent the maximum and minimum values.....  | 125 |
| Figure 5-6: Surface plots depicting the results of the multiple linear regression of maximum peak-to-peak deformation using the maximum angular velocity (ARS) and duration for the sagittal (a), coronal (b), and axial (c) tests. The black dots correspond to the data points used in the regression fit. The sagittal regression model had an R <sup>2</sup> of 0.691. The coronal regression model had an R <sup>2</sup> of 0.693. The sagittal regression model had an R <sup>2</sup> of 0.795. ....   | 127 |
| Figure 5-7: Surface plots depicting the results of the multiple linear regression of mean peak-to-peak deformation using the maximum angular velocity (ARS) and duration for the sagittal (a), coronal (b), and axial (c) tests. The black dots correspond to the data points used in the regression fit. The sagittal regression model had an R <sup>2</sup> of 0.692. The coronal regression model had an R <sup>2</sup> of 0.780. The sagittal regression model had an R <sup>2</sup> of 0.675. ....  | 128 |
| Figure 6-1: A morphing registration method was used to account for anthropometric differences among specimens. The cranium shape of each specimen was registered to a common 3D parametric space, chosen to be the GHBMC brain model, using a surface registration methodology. The registration parameters in each direction (A, B, and C) are used to map the position and displacement to the parametric space.....   | 142 |
| Figure 6-2: Normalized crystal position for all specimens. ....  | 143 |
| Figure 6-3: Depiction of the optimization of the cluster positions. For cases where all specimens had a tight clustering of normalized positions (A), no receivers were removed. For cases where there are outliers (B), up to two receivers were removed from the cluster point average position. ....  | 145 |
| Figure 6-4: Methods of generating discrete points for brain deformation corridor development. In the grid method, points were generated using a spatial grid. Normalized receiver locations are indicated in red. Sample points for the corridors are shown in blue. For the cluster-all method, an average of equivalent receivers was taken for all specimens to generate the corridor points. For the cluster-optimized method, outliers from the cluster-all method were removed to generate average positions based on a subset of specimens..... | 146 |
| Figure 6-5: The transfer function prediction for the x-axis deformation two receivers for the sagittal 40 rad/s – 60 ms (left) and the sagittal 40 rad/s – 30 ms (right) tests. ..   | 149 |
| Figure 6-6: The common input of the scaled kinematics for the axial – 40 rad/s – 30 ms test, with the original pulses (left) and the scaled pulses (right). The average common loading kinematics is denoted by the dashed red curve, denoted by “SCALED”. The red dotted lines indicate the target magnitude and duration of the rotation. ....   | 150 |
| Figure 6-7: Average CORA scores for the simulated transfer function brain deformation response using the original kinematics. Data was averaged ( $\pm 1$ SD) across all axes for all crystals for all loading severities. ....  | 150 |

|  |     |
|--|-----|
| Figure 6-8: Original (blue) and registered (red) initial positions of all receivers for all specimens. The cranium outline is the GHBMC inner skull outline, which used the parametric space for the registration.....   | 151 |
| Figure 6-9: The normalized displacement for receiver (Rx) 24 for specimen 900 under the axial – 40 rad/s – 30 ms tests did not change significantly from the original displacements (left). The trajectory of receivers 16 and 24 are shown in the axial plane (right).....  | 152 |
| Figure 6-10: Optimization of the power ( $u$ ) parameter for the Shepard and Lukaszzyk IDW methods using the grid (left) and cluster-optimized (right) methods. ....   | 153 |
| Figure 6-11: Average RMS error between the true FE brain deformation response at the corridor points and the predicted response using the IDW interpolation. The error in each motion axis (x, y, and z) is shown for rotational loading in each direction (sagittal, coronal, and axial) for the 40 rad/s – 60 ms tests. .... | 154 |
| Figure 6-12: The final corridors for selected grid points for the Axial – 40 rad/s – 30 ms case. The final corridors are calculated after scaling the data using the kinematic transfer function, then normalizing to the common anthropometric space. ....  | 155 |
| Figure 7-1: Depiction of the GHBMC and SIMon FE brain models, with geometric and anatomical characteristics as well as computational efficiency for each model. ....   | 164 |
| Figure 7-2: The original (blue) and morphed (red) GHBMC FE model for specimen 846 (top) and the SIMon FE brain model for specimen 904 (bottom).....  | 167 |
| Figure 7-3: Depiction of the CORA cross-correlation metric to evaluate the similarity between two signals. The phase, size, and shape are equally weighted for an overall maximum score of 1. The corridor rating is discarded for the individual specimen evaluations. ....   | 168 |
| Figure 7-4: Distribution of the maximum MPS across elements for a single head rotation. Solid red lines indicate the 95th and 100th percentile MPS. The green highlighted region indicates the elements that have achieved an MPS of at least 25% during the impact, which are included in the CSDM calculation. ....          | 170 |
| Figure 7-5: Response of the GHBMC model for receiver 13 for the sagittal, 40 rad/s, 60 ms case. All four comparison methods are shown with the sonomicrometry experimental data.....   | 171 |
| Figure 7-6: The weighted CORA for all rotational loading conditions in the sagittal (sag), coronal (cor), and axial (axi) directions for specimen 900 for GHBMC.....   | 172 |
| Figure 7-7: The average weighted CORA in the GHBMC simulations for all specimens. ....   | 172 |
| Figure 7-8: Response of the SIMon model for receiver 16 for the sagittal, 40 rad/s, 30 ms case. All four comparison methods are shown with the sonomicrometry experimental data.....   | 173 |
| Figure 7-9: The weighted CORA for all loading conditions for specimen 900 for the SIMon model. ....  | 174 |
| Figure 7-10: The average weighted CORA for all specimens for the GHBMC model..   | 174 |
| Figure 7-11: The average weighted CORA for all specimens for GHBMC and SIMon for the ‘absolute’ and ‘morphed’ comparison methods.....  | 175 |
| Figure 7-12: The weighted CORA, weighted corridor score, and the weighted overall score for the GHBMC (top) and SIMon (bottom) models compared to the brain deformation corridors.....   | 176 |

|  |     |
|--|-----|
| Figure 7-13: The maximum principal strain for the original, scaled, and morphed models for specimen 904 for the axial, 40 rad/s – 30 ms simulation. ....   | 177 |
| Figure 7-14: The difference in strain for the scaled and morphed (relative to the baseline) GHBMC and SIMon FE brain models. The 95 <sup>th</sup> percentile MPS (MPS95), 50 <sup>th</sup> percentile MPS (MPS50), and CSDM are shown for each model. ....   | 178 |
| Figure 7-15: The correlation between tissue-level strain metrics (MPS-95 <sup>th</sup> , MPS-50 <sup>th</sup> , and CSDM) and experimental peak-to-peak brain deformation was investigated using linear regression for the GHBMC and SIMon models. The resulting best fit line (dashed) and correlation coefficient ( $R^2$ ) are plotted along with the data points (red). ....         | 179 |
| Figure 8-1: Reported material properties for brain tissue for the complex modulus and tan-delta (Panzer, 2012). ....   | 188 |
| Figure 8-2: The material sensitivity parameters for the cerebrum white and cerebellum parts of the GHBMC model, with the complex modulus (left) and tan( $\delta$ ) (right). Gray dots indicate literature material properties. ....   | 192 |
| Figure 8-3: The sensitivity of the cerebrum gray and brainstem parts of the GHBMC model for the high damping, high stiffness case under sagittal rotation. The change in peak-to-peak deformation, relative to the baseline model is shown in color for all nodes with a magnitude greater than 0.25 mm. ....  | 196 |
| Figure 8-4: The absolute value of the significant regression coefficients (p-value < 0.05 and $ A_i  > 0.1$ ) of the cerebrum gray of the GHBMC model for the sagittal rotation are shown for all nodes in response changes in the complex modulus (left). A superior-inferior slice view ( $z = -20$ mm) of the distribution of the regression coefficients is shown on the right. .... | 197 |
| Figure 8-5: The maximum of the absolute value of the regression coefficients across all nodes of the GHBMC model are shown for each of the three rotation directions. For viscoelastic material, the damping (D) and complex modulus (E) are separated for each material. ....   | 198 |
| Figure 8-6: The sensitivity of the CSF and cerebellum parts of the SIMon model for the baseline damping, high stiffness case under sagittal rotation. The change in peak-to-peak deformation, relative to the baseline model is shown for all nodes with a magnitude greater than 0.25 mm. ....  | 198 |
| Figure 8-7: The absolute value of the significant regression coefficients (p-value < 0.05 and $ A_i  > 0.1$ ) of the cerebrum of the SIMon model for the sagittal rotation are shown for all nodes in response changes in the complex modulus (left). A superior-inferior slice view ( $z = 30$ mm) of the distribution of the regression coefficients is shown on the right. ....       | 199 |
| Figure 8-8: The maximum of the absolute value of the regression coefficients across all nodes of the SIMon model are shown for each of the three rotation directions. For viscoelastic material, the damping (D), and complex modulus (E) are separated for each material. ....  | 200 |
| Figure 8-9: The effect of the calibrated material properties for specimen 846 for the axial – 40 rad/s – 60ms rotation. ....   | 201 |
| Figure 8-10: The difference in peak-to-peak deformation between the GHBMC model and sonomicrometry data for the three rotation directions. The calibrated model resulted   |     |

|  |     |
|--|-----|
| in lower average differences in peak-to-peak deformation for the sagittal and axial rotations. ....  | 202 |
| Figure 8-11: The weighted CORA score of the original and calibrated SIMon model in comparison to the specimen 900 brain deformation data for all tests. The tests used to calibrate the material properties are shown with red boxes. ....   | 203 |
| Figure A-1: Brain regions and white/gray matter regions can be identified after brain extraction. ....   | 225 |
| Figure A-2: The dura attachment to the skull was very loose (left) or inseparable (right). ....  | 226 |
| Figure A-3: The dura was either very well connected to the Crista Galli (left) or not connected (right). ....  | 226 |
| Figure A-4: There was a loose connection between the dura and brain, except at the midline. ....   | 227 |
| Figure A-5: Differences in bony anatomy. Specimen 902 shows prominent bony spurs/protrusions, some of which were sharp to the touch. Specimen 903 and 896 show bone decay along the sagittal sinus. ....   | 227 |
| Figure B-1: Representation of the morphing process, with GHBMC as an example. The morphing process includes four main steps: 1) Surface preparation and segmentation, 2) rigid body alignment and scaling, 3) surface registration, and 4) volume morphing and evaluation. ....                                    | 228 |
| Figure B-2: Control points for the morphing process can be chosen manually if the shape of the target and template geometry are similar or there are prominent landmarks available (left). Deviations in shape between the two surfaces can result in variability in the choice of surface landmarks (right). .... | 230 |
| Figure C-1: Angular velocity and angular acceleration for each test severity. ....   | 236 |
| Figure D-1: Sonomicrometry trajectory plots for specimen 846. ....   | 241 |
| Figure D-2: Sonomicrometry trajectory plots for specimen 896. ....   | 242 |
| Figure D-3: Sonomicrometry trajectory plots for specimen 900. ....   | 243 |
| Figure D-4: Sonomicrometry trajectory plots for specimen 902. ....   | 244 |
| Figure D-5: Sonomicrometry trajectory plots for specimen 903. ....   | 245 |
| Figure D-6: Sonomicrometry trajectory plots for specimen 904. ....   | 246 |
| Figure E-1: Original and scaled angular velocity traces each test severity. The maroon dashed angular velocity trace indicates the common scaled corridor kinematics. The dotted red lines indicate the target peak angular velocity and pulse duration. ....  | 252 |
| Figure F-1: The weighted CORA for all rotational loading conditions in the sagittal (sag), coronal (cor), and axial (axi) directions for all specimens for GHBMC. ....   | 256 |
| Figure F-2: The weighted CORA for all rotational loading conditions in the sagittal (sag), coronal (cor), and axial (axi) directions for all specimens for SIMon. ....   | 259 |
| Figure G-1: GHBMC material sensitivity regression for the sagittal, coronal, and axial rotations for all materials. ....   | 264 |
| Figure G-2: SIMon material sensitivity regression for the sagittal, coronal, and axial rotations for all materials. ....   | 266 |

## ACKNOWLEDGMENTS

My PhD journey started as one of Dr. Matthew Panzer's first graduate students, and I am grateful for his role in developing my research curiosity and acumen. More importantly, I am thankful for Matt's friendship and investment in my professional growth throughout graduate school. I also express immense gratitude to my committee, Drs. Jeffrey Holmes, Jeff Crandall, Silvia Blemker, and Jason Sheehan. Your guidance and insightful questions have led me to structure my research thoughtfully and meticulously. To Dr. Jason Forman, thank you for investing much time and effort in this project, as well as teaching me valuable experimental testing skills. To Dr. Robert Salzar, thank you for your assistance in the experiments, as well as the advice and guidance along the way.

I am thankful to have been part of the Center for Applied Biomechanics and acknowledge the many, many people it took to enact such a complex and painstaking project. Firstly, I express thanks to Sebastian Giudice for his friendship since day one, his willingness to help and answer questions whenever it is needed, and his shared sense of inquisitiveness. To Daniel Shedd and Kristen Reynier, thank you for your hard work and the late nights required. To Taotao Wu, thank you for your friendship and thorough inspection of my work. To Lee Gabler, Jacek Toczyski, and Carolyn Roberts thank you for extending your technical expertise and for your friendship. To the staff at the CAB, Sara Sochor, Brian Overby, Kevin Kopp, Joey White, Mark McCardell, and Ted Miller, thank you for making many of the technical and management aspects of the project much easier and for your tireless assistance and support.

Lastly, I would like to thank my friends in Charlottesville that made the city feel like home. You were my family away from home, and I appreciate your care and kindness. I also express thanks to my parents, my siblings, my wife, and my IAC family for always standing by me and giving me the motivation needed to enact this work.

# **CHAPTER 1: INTRODUCTION**

## **STATEMENT OF PROBLEM**

Traumatic brain injuries (TBI) are one of the most common yet least understood injuries to the body. According to the World Health Organization, there has been an increase in global TBI incidences, and it is expected to become the third leading cause of death by 2020 (Meaney et al., 2014). In the United States, an estimated 1.7 million TBIs occur annually, and TBI is a contributing factor in one-third of all injury-related deaths (Taylor et al., 2017). Multiple causes have been implicated in TBI, including falls (35%), motor vehicle crashes (17%), and impacts against or from an object (17%), such as in sports and recreational activities (Faul et al., 2010). Motor vehicle accidents are the leading cause of TBI-related fatalities (Coronado et al., 2012). While TBI is a major public health concern for the general population, it is also a prominent factor in the injuries and deaths of soldiers (Tanielian et al., 2008), where over 310,000 TBI cases were reported during Operation Iraqi Freedom and Operation Enduring Freedom (Helmick et al., 2015).

A majority of TBI cases occur from head impacts without skull fracture, and their effects range on the spectrum from mild to severe (Santiago et al., 2012). Seventy-five percent are classified as mild TBI, or concussion (Faul et al., 2010). Brain injuries can also be classified as either diffuse, including concussion and diffuse axonal injury (DAI), or focal injuries, such as contusion or hemorrhage (Gennarelli, 1993). The reported epidemiology, however, is an underestimate of the actual rate of TBI occurrence in the United States (McCrea et al., 2004; Langlois et al., 2006). It is estimated that half of all TBI cases are not reported due to fluctuating criteria for the diagnosis of concussion, lack

of methods to diagnose concussion shortly after impact, and the competitive nature of sports (Coronado et al., 2012; Harmon et al., 2013).

The study of the biomechanics of the brain and associated tools to predict injury is important for understanding and mitigating brain injuries. Various tools for the assessment of brain injury risk and the evaluation of safety gear, such as computational models of the brain, have been developed in the past two decades. Anatomically-detailed finite element (FE) brain models allow for investigations into brain mechanics that are not possible with dummies or physical models when evaluating the risk of injury. There is, however, a need for the improvement of the biofidelity of these models under impact conditions relevant to diffuse TBI. To reduce the societal burden of TBI, it is necessary to develop improved and more accurate tools to understand what happens to the brain during an impact, and to help assess the effectiveness of safety countermeasures.

## **MOTIVATION**

### **Biofidelity of FE Brain Models**

FE models have been vital to investigating TBI mechanisms, assessing injury risk and safety gear, and developing brain injury criteria based on head impact kinematics (Gabler et al., 2016a, 2017; Sanchez et al., 2017; Takhounts et al., 2013a). Improvements in computational capabilities and the generation of datasets of human brain deformation, namely by Hardy et al. (2001, 2007), have allowed for the creation of numerous FE brain models. Since 2001, there have been at least sixteen models developed, twelve within the past five years (Figure 1-1). Given the importance of these models in influencing standards of safety and product development across multiple industries, it is essential to validate the brain deformation predicted by these models using human brain motion under repeatable

loading conditions that are causative of injury. Current brain deformation datasets are limited and cannot be used to validate FE models for TBI-relevant loading conditions.

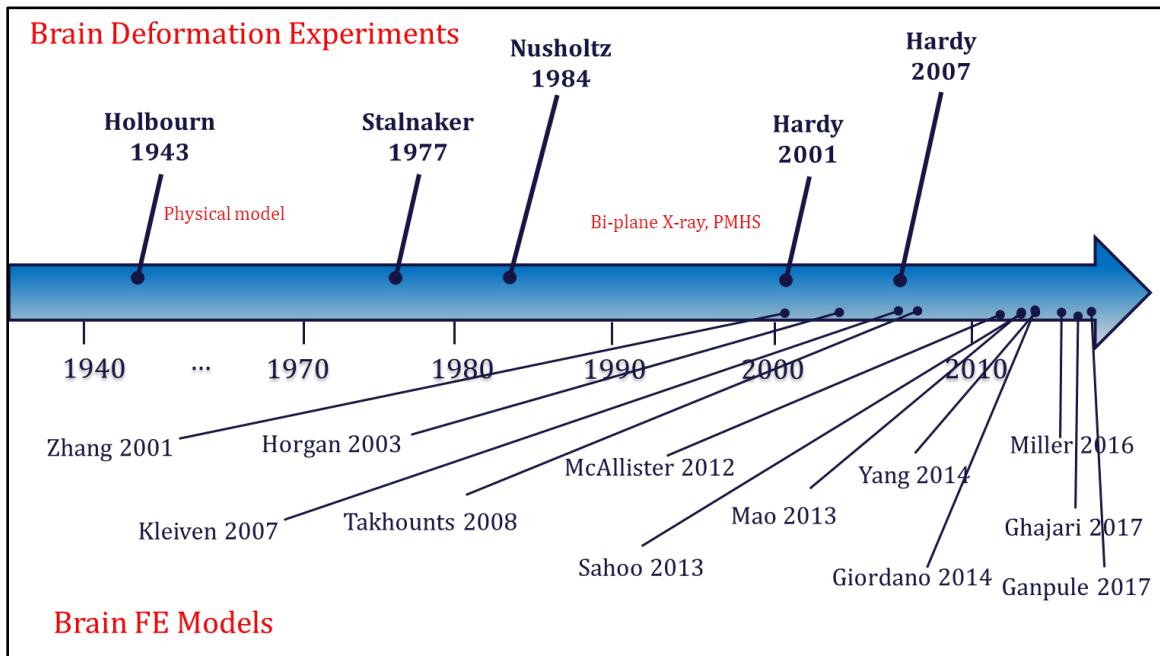


Figure 1-1: The availability of brain deformation experiments and the development of FE brain models (Alshareef, 2019).

Most of the depicted FE models are validated based on two datasets available for brain models consisting of two types: the Hardy brain motion datasets (Hardy et al., 2001, 2007) and preceding brain pressure datasets by Nahum (Nahum et al., 1977) and Trosseille (Trosseille et al., 1992). While the pressure datasets provide a reasonable metric to verify the correct implementation of the brain materials, they are not useful as a validation dataset for brain deformation, nor are they useful from an injury standpoint. The Hardy dataset provides validation data for human brain deformation under impact conditions, but there are many limitations associated with the study, which will be discussed in Chapter 2.

### **Deformation of the Brain under Rotational Loading**

Recently, there has been a breadth of work to identify which head loading conditions and directions cause mild and moderate TBI. Takhounts et al. (2013) found that brain injury

risk depends on angular velocity, with axial rotations of the head being most sensitive to injury. Gabler et al. (2017) examined brain deformations from nearly 1,000 reconstructed sled and crash tests using a human FE brain model. The reconstructed cases, including automotive and sports scenarios, span a range of plausible head kinematics for real-world injury assessment, from non-injury to concussion to moderate and severe TBI, based on brain injury criteria (Rowson and Duma, 2013; Takhounts et al., 2013a; Gabler et al., 2016a; Sanchez et al., 2017). The Gabler study found that in most real-world impact environments, maximum brain deformation depends on the magnitude of angular velocity and duration (or angular acceleration) of the signal. When isolated, the linear acceleration of the head had minimal effects on brain deformation (Gabler et al., 2016a).

The study of human brain deformation predicated the development of biofidelic FE brain models and the assessment of TBI using brain injury criteria. Previous studies of human brain deformation used constant-energy methods to drive impact loading to the head, resulting in primarily linear acceleration, to study brain motion. Additionally, the focus of the tests on linear acceleration limits their use in validating models and tools aimed at predicting diffuse TBI caused by rotation of the head. To correlate the kinematics of the head to brain deformation, the kinematic input conditions imparted to the head need to be as consistent as possible between test subjects and must be representative of the rotational kinematics that cause injury.

## **SCOPE**

### **Hypothesis**

The overarching hypothesis of the research performed in this dissertation is that *the magnitude of brain deformation is dependent on magnitude, duration, and direction of*

*angular velocity applied to the human head.* This hypothesis has been the framework for numerous computational and analytical brain injury metrics. The dependence has been previously tested using computational models (Gabler et al., 2016a), but has never been tested using experimental methods in humans. To test this hypothesis, the overall goal of this dissertation is to improve the field's understanding of brain injury risk by generating an experimental dataset of human brain deformation under rotational loading.

### **Goal and Specific Aims**

The goal will be accomplished through two phases, each with a set of specific aims (Figure 1-2). The experimental phase will focus on the development of a methodology to measure brain deformation using sonomicrometry under pure, repeatable, and controlled rotational loading. After the development of the methodology in Aim 1, the second aim will focus on acquiring a dataset of human brain deformation. The dataset will allow for an in-depth investigation into the factors that affect brain deformation, such as kinematic severity, rotation direction, and region of the brain. The third aim of the experimental phase will focus on combining the data from all specimens into average displacement corridors that can be used to understand population trends and to validate FE models more efficiently.

The computational phase aims to develop a methodology to evaluate and improve human FE brain models. The first aim will investigate different methods of comparing the models to the experiments, based on the geometry of each specimen. The second aim includes a sensitivity analysis of the material properties of FE brain models to identify materials that could improve biofidelity. The last aim of the computational phase will focus

on improving the biofidelity of an FE brain model to the experimental dataset. The specific tasks for each phase are outlined in Figure 1-2.

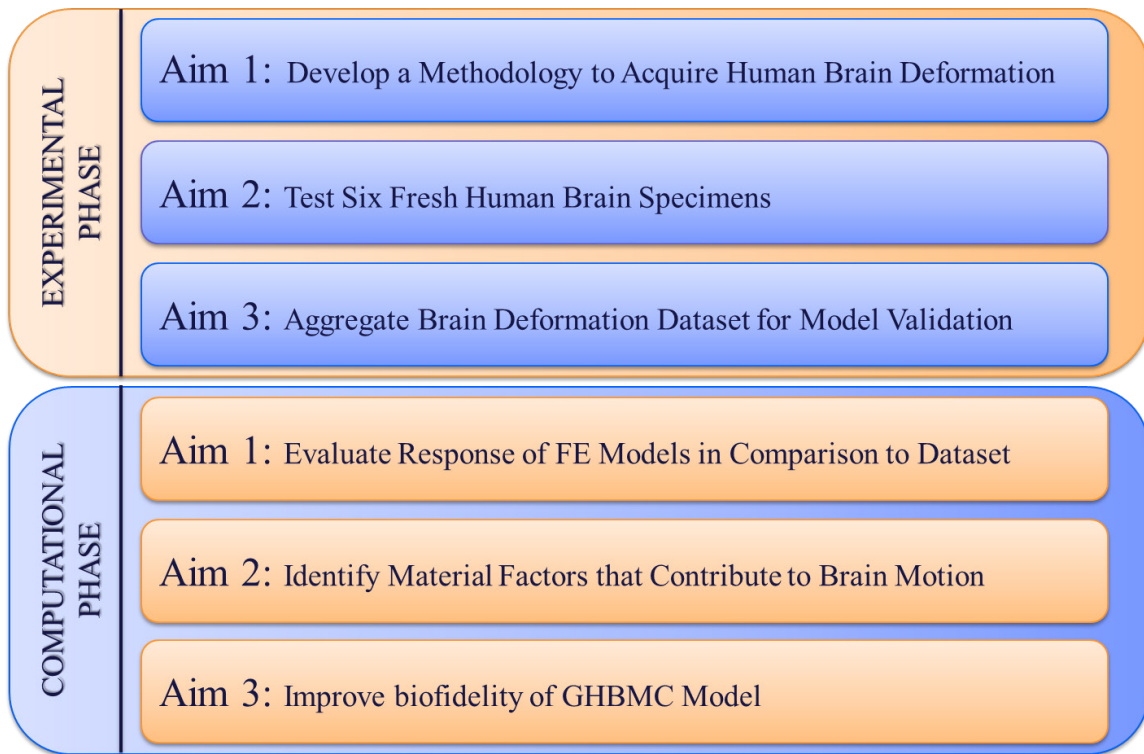


Figure 1-2: Specific aims for the experimental and computational phase of this dissertation.

The focus of the dissertation will be to improve the understanding of brain deformation under rotational loading and the associated FE model implementation - this research does not assess or quantify the extent of brain injury from rotational loading. The bulk of the work will be conducted on human cadaveric specimens, and therefore, the regional and spatial deformation cannot be extrapolated to injury risk. Although diffuse injuries such as concussion and DAI cannot be readily measured in cadaveric specimen, this dissertation will focus on studying the biomechanical response of the brain during rotational loading. The availability of this dataset and methodology will result in future studies that will correlate deformation to risk through methods such as scaling, kinematic injury criteria, and *in vivo* animal experiments.

## **Chapters and Dissertation Content**

The tasks of this dissertation will be completed through several steps, each presented in a separate chapter. A background and literature review will be presented in Chapter 2. The development of the methodology for sonomicrometry and rotational loading will be presented in Chapter 3 (experimental, aim 1), along with pilot data for the first specimen. Chapter 4 will contain an investigation into algorithms of trilateration required to convert sonomicrometry data into dynamic displacements (experimental, aim 1). The full dataset will be presented in Chapter 5, along with an analysis of the factors that affect the severity of brain deformation (experimental, aim 2). Chapter 6 will contain a methodology and results for aggregate data corridors developed from the experimental dataset (experimental, aim 3). The computational aims will be presented in Chapters 7 and 8. Additional data, methods, results, and analyses are presented in the appendices.

## **EXPECTED CONTRIBUTIONS**

This dissertation will address gaps in the understanding of human brain deformation through the development of a methodology and dataset quantifying *in situ* human brain deformation under rotational loading. The methodology provides a unique technique that can be used to further study human brain deformation, as well as directly measure brain deformation in pre-clinical animal injury models. The contribution of a digital dataset of brain deformation, including average data corridors, will have a broader impact on the TBI biomechanics field, allowing researchers to develop and evaluate the next generation of FE brain models using recommended practices identified in the computational phase. It will also provide experimental evidence for theories of brain deformation, such as the

importance of rotational kinematics and the dependence of brain deformation on loading severity and direction.

Ultimately, this work will improve the tools available to investigate brain injury. The experimental and computational framework will assist in the investigation of the mechanics of the brain during injurious conditions and prediction of TBI injury risk. An improved experimental understanding and modeling of brain mechanics will be a necessary step in improving safety standards and the assessment of safety countermeasures, which will mitigate the incidences and consequences of TBI and help reduce the societal burden of brain injuries.

## **CHAPTER 2: BACKGROUND**

### **Human Brain Anatomy**

The brain is the organ responsible for controlling all functions and actions as well as storing memory and influencing emotion and intelligence. It is part of the central nervous system, working in conjunction with the spinal cord. The brain controls autonomous functions, such as the cardiovascular system, as well as voluntary functions, like the movement of limbs or the processing of thoughts (Purves et al., 2011). The brain is approximately  $1227 \pm 135 \text{ cm}^3$  in volume (Matsumae et al., 1996). It is encompassed by the skull, a hard material made of cortical and trabecular bone. The cranium is approximately  $1384 \pm 139 \text{ cm}^3$  in volume (Matsumae et al., 1996). Between the skull and the brain are the meninges: three layers that cover and protect the brain (Purves et al., 2011). All other spaces in the cranial cavity, including hollow channels within the brain called ventricles and areas between the meninges, are filled with cerebrospinal fluid (CSF). CSF is a clear, watery substance that is constantly being absorbed and replenished (Purves et al., 2011) (Figure 2-1).

The meninges serve to protect and nourish the brain. The outermost layer, the dura, is an approximately 0.3-0.8 mm thick, firm membrane made primarily of collagen fibers. It lines the inside of the skull and covers the brain (Bashkatov et al., 2003). The dura folds into the two halves of the cerebrum, where it is referred to as the falx. It also folds into the inferior regions covering the cerebellum and the brainstem, where it is referred to as the tentorium. The middle layer, the arachnoid, is a 0.035-0.04 mm thick membrane that covers most of the brain (Reina et al., 2010). The arachnoid contains blood vessels, some of which span the subdural space between the dura and arachnoid to reach the brain. The layer closest

to the brain, the pia mater, is a 0.015 mm thick membrane that follows the folds of the brain and contains a large number of blood vessels (Reina et al., 2004). The subarachnoid space, between the pia mater and arachnoid, is the main path of CSF flow around the brain.

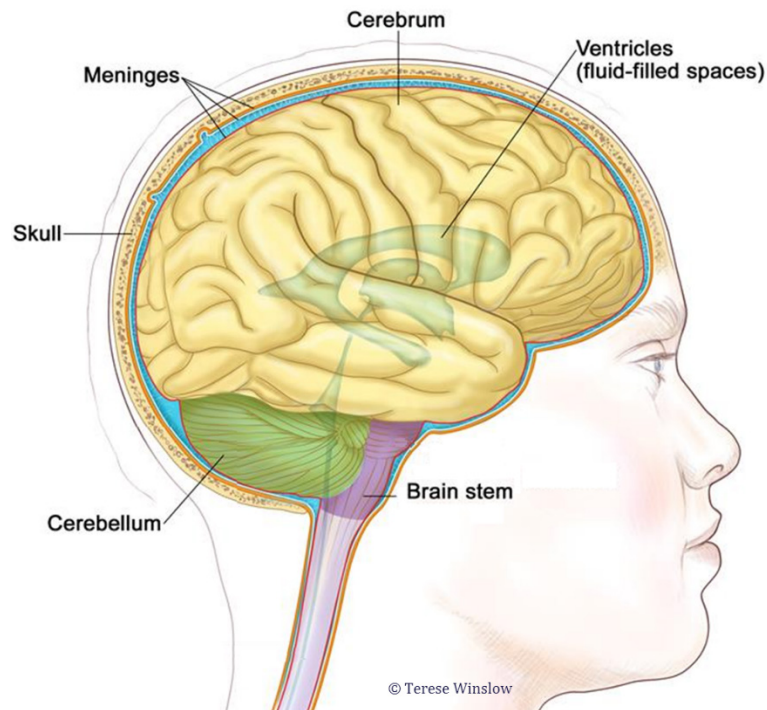


*Figure 2-1: Anatomy of the human head and brain (Source: NIH National Cancer Institute Dictionary (2011)).*

Macroscopically, the brain is composed of three main parts: the cerebrum, cerebellum, and brainstem (Purves et al., 2011) (Figure 2-2). The cerebrum comprises the largest volume of tissue in the brain and is divided into two halves, the left and right. A groove, the longitudinal fissure, separates the two halves until they are joined at the inferior side by the corpus callosum. The outer surface of the cerebrum, the cerebral cortex (or gray matter), is wrinkled in appearance. The presence of sulci and gyri results in folds and grooves in the tissue surface. Beneath the cortex is the white matter, which is composed of connecting fibers between the neurons of the brain. The cerebrum is divided into four lobes: frontal, parietal, temporal, and occipital (Purves et al., 2011). The frontal lobe is the largest

and is responsible for motor skills, including motion, speech, and behavioral function. This lobe also plays a part in memory, intelligence, and personality. The parietal lobe interprets signals from other parts of the brain, including hearing, vision, and memory. The temporal lobe is in charge of visual and verbal memory, allowing humans to recognize objects and understand language. The occipital lobe enables the processing of visual information such as shapes and colors (Purves et al., 2011).

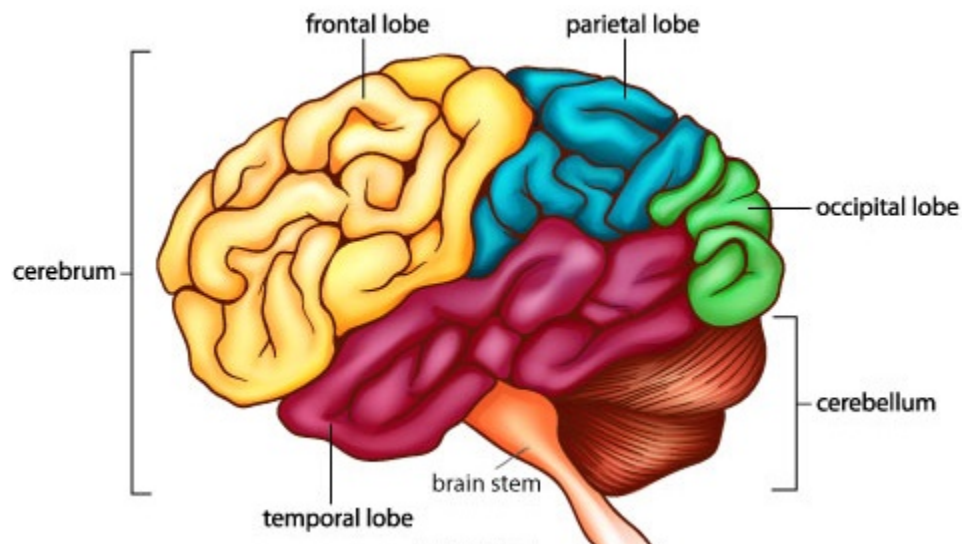


*Figure 2-2: Macroscopic anatomy of the human brain with the three major regions: the cerebrum, cerebellum, and brainstem (Source: Idaho Public Television (“The Brain: Facts (Science Trek: Idaho Public Television),”).*

At the microscopic scale, the brain consists of two cell types: neurons and glia. Neurons serve to process and send information throughout the brain and the rest of the human body. The neuron is divided into three parts: soma or cell body, dendrites, and an axon (Figure 2-3). The soma houses the nucleus of the cell and typically has many dendrites and one axon stemming from either side. The dendrites are filaments that branch out and receive electrical signals from other neurons. The axon, commonly surrounded by a lipid-rich wrapping called the myelin sheath, serves to transmit electrical signals from the soma to other neurons using the terminals. The myelin sheath serves to maintain efficient

conduction of electrical signals (Purves et al., 2001). Axons are typically 0.01 to 0.05 mm in diameter and vary from inches to several feet in length (Purves et al., 2011).

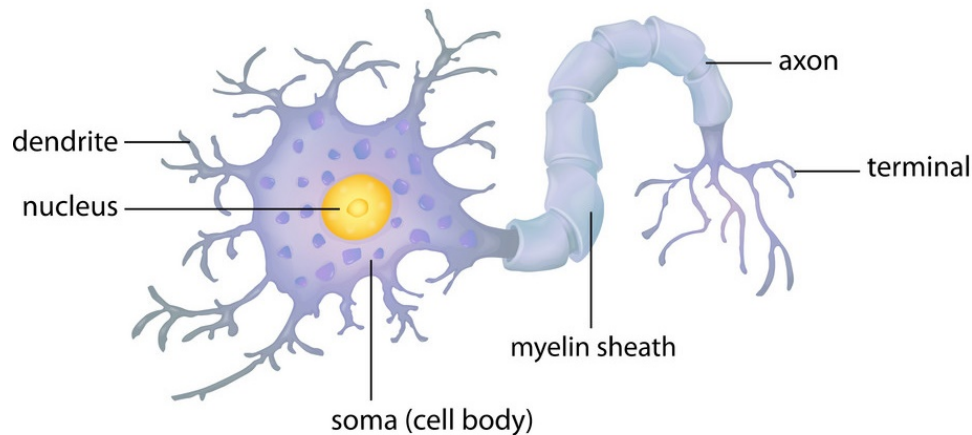


*Figure 2-3: Anatomy of the neuron (VectorStock).*

Glial cells are the most common type of cell in the brain, with an approximate count ratio of 3 to 1 to neurons. Although they do not participate directly in synaptic signaling, glia are essential to brain function. They provide support and nutrition to the brain by maintaining ionic hemostasis, forming myelin, and facilitating signal transmission across the nervous system (Purves et al., 2001). There are three types of glia in the brain: astrocytes, oligodendrocytes, and microglia. Astrocytes are star-shaped cells that help maintain the chemical environment for signaling in neurons and help form the blood-brain barrier. Oligodendrocytes construct the myelin sheath around neuronal cells. Microglia serve as scavenger cells to remove debris during normal function and injury (Purves et al., 2001).

### **Brain Injury**

Brain injuries typically result from trauma to the head. There are various types of brain injuries within TBIs that fall on the spectrum from mild to severe, and are usually classified under one of two categories: closed or penetrating. In a penetrating TBI, a sharp object,

such as a bullet, fractures the skull and punctures through the meninges and brain, lacerating the brain and exposing it to the external environment (Santiago et al., 2012). Penetrating trauma usually results in higher severity focal injuries. Closed head trauma involves blunt or inertial loading of the head that can cause focal injuries (e.g., hematomas, contusions, and lacerations) and diffuse injuries, such as concussion and diffuse axonal injury (DAI) (Gennarelli, 1993). Closed brain injuries from blunt impact can also result in skull fracture under severe loading conditions. This dissertation will focus only on brain deformation caused by closed head injuries from blunt and inertial impact.

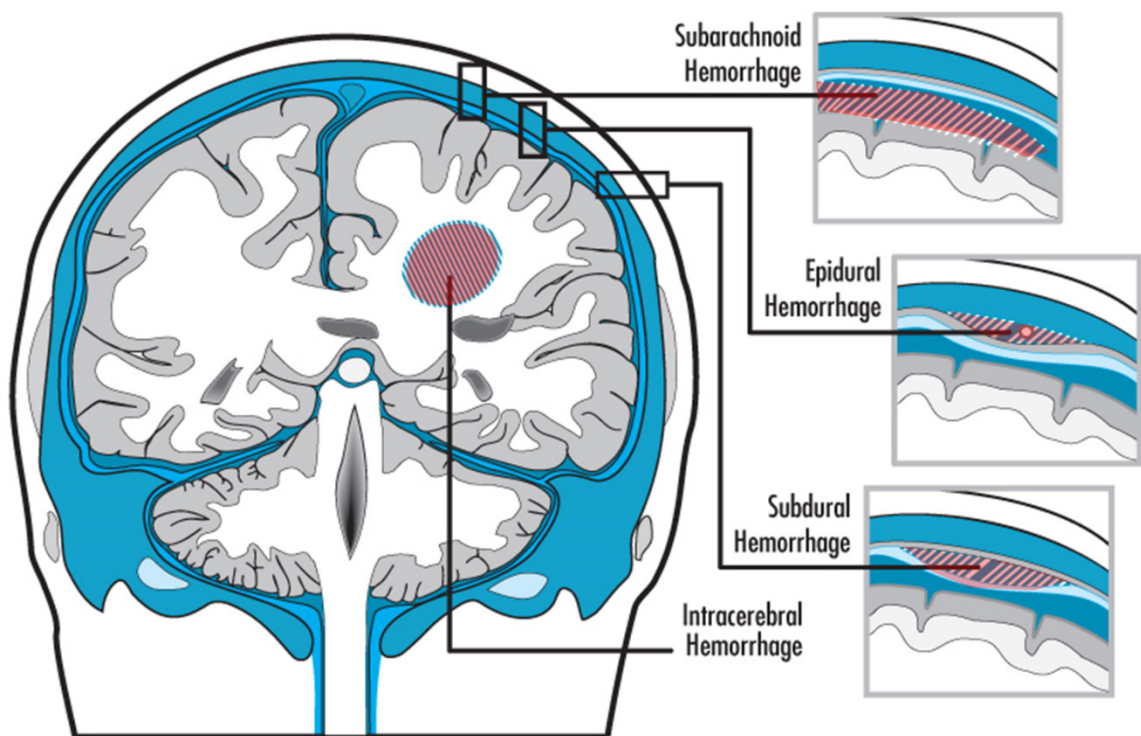


*Figure 2-4: Depiction of focal injuries in the brain (Crandall, 2015).*

Focal and diffuse injuries to the brain can occur as a result of similar loading types. Typically, focal injuries are identified using standard clinical imaging such as Computed Tomography (CT) or Magnetic Resonance Imaging (MRI) because of the locally disruptive nature of the injury. The most common focal injury is bleeding in the brain, such as cerebral

hematomas, cerebral contusions, or tissue lacerations. Focal injuries can also occur on the surface of the brain between the meningeal layers, such as subdural hematomas, subarachnoid hemorrhage, or extradural hematomas. Focal injuries usually result from moderate to severe TBI loading conditions, except for subarachnoid hemorrhage which, in rare cases, can be present in mild TBI (Gennarelli, 1993; Ommaya, 1984).

Diffuse injuries to the brain are characterized by a distributed pattern of microscopic damage to neurons in the brain and are not typically present with visible injury locations. Unlike focal injuries, which are associated with moderate to severe TBI, diffuse injuries can be mild to moderate (concussion) or moderate to severe (DAI). While mild TBI accounts for almost 80% of all TBI cases in the United States, DAI is often more costly due to the chronic and deadly pathological mechanisms of the injury (Meaney et al., 2014). Diffuse brain injuries primarily cause damage to the white matter of the brain, specifically the axonal fibers. DAI symptoms are commonly localized in the subcortical white matter, gray-white matter interface, and corpus callosum (Gennarelli et al., 1982; Ommaya, 1984; Smith and Meaney, 2000), as well as at points of attachment, such as cranial nerves (Viano et al., 1997). During high-severity impacts associated with DAI, stretching of the axons in the white matter can lead to rupture or gradual degeneration of axonal tracts. DAI usually presents with loss of consciousness as well as gross, often irreversible damage to many regions in the brain, most prominently in the brainstem and corpus callosum. The magnitude of symptoms associated with diffuse brain injuries, including physical symptoms, physiological changes, and mechanical injury are associated with the severity of the injury (Gennarelli, 2015) (Figure 2-5).

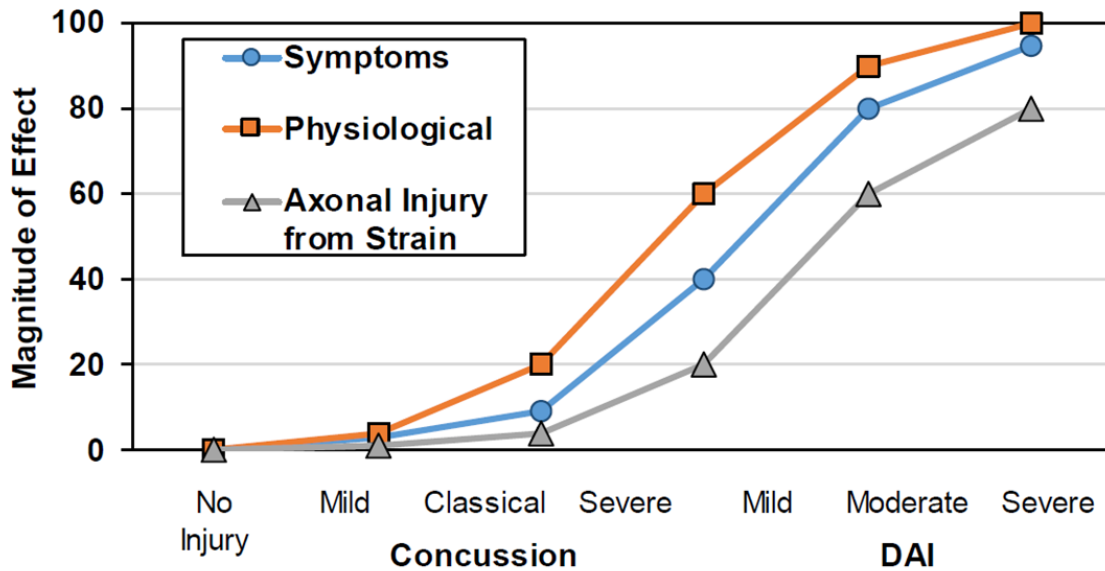


Figure 2-5: Magnitude of the effect of TBI from diffuse injuries (adapted from Gennarelli 2015).

The effects of a concussion are much more variable and complex than severe injuries like DAI. Although cerebral concussion has been mentioned in medical literature as far back as Hippocrates (McCrorry and Berkovic, 2001), the definition and clinical symptoms have changed. The consistent trend in the definition of concussion is that a blow or impact to the head causes damage (typically reversible) that results in an altered mental or behavioral state. Concussions can include a loss of consciousness for a short period of time, but it is not necessary to have any external physical symptoms during or after a head impact. As stated in Ommaya 1974, “cerebral concussion would then be defined as a graded set of clinical syndromes following head injury wherein increasing the severity of disturbance in level and content of consciousness is caused by mechanically induced strains affecting the brain in a centripetal sequence of disruptive effect on function and structure” (Ommaya, 1984). In the field of sports medicine, a concussion is defined as a TBI that is caused by either a direct or indirect impact to the head, and often “results in the rapid onset

of short-lived impairment of neurological function that resolves spontaneously (McCrorry et al., 2017).”

### **Brain Mechanics and Material Properties**

The study of the mechanics of the human brain, including its shape, structures, and material properties, is critical in developing accurate tools to predict and assess injury. Parallel to its complex structure and function, the mechanics of the brain are challenging to assess. The material properties of the brain have mostly been estimated through *ex situ* mechanical experiments, including tensile (Miller and Chinzei, 2002), compressive (Laksari et al., 2012; Prevost et al., 2011), shear (Garo et al., 2007, 2007; Jin et al., 2013; Prange and Margulies, 2002; Thibault and Margulies, 1998), and indentation (Alshareef et al., 2015; Gefen et al., 2003; Shafieian et al., 2009). The brain is non-linearly viscoelastic, incompressible, and anisotropic, with differences across different regions of the brain (Arbogast and Margulies, 1998; Budday et al., 2018; Jin et al., 2013; Prange and Margulies, 2002). The material properties of the brain are also dependent on age (Finan et al., 2012; Gefen et al., 2003; Thibault and Margulies, 1998) and sex (Sack et al., 2009).

There have been many studies on the material properties of the brain, and there is a broad range of reported values: the complex shear modulus spans three orders of magnitude ranging from 0.1-100 kPa, and the damping coefficient ( $\tan\delta$ ) ranges from 0.1-4 (Meaney et al., 2014). The lack of a defined set of material properties stems from many factors, including spatial differences in the tissue, experimental methods, and the constitutive models used to describe the material response. The spatial differences in brain tissue can account for some variation in the material properties. The white matter regions of the brain, such as the corpus callosum or the cerebellum, contain axonal fibers that are

highly organized, forming a preferred fiber direction. This structural anisotropy makes their response stiffer and varies depending on the direction of loading. Conversely, the gray matter regions of the brain are typically softer, mechanically isotropic, and can have region-dependent variation in material properties (Arbogast and Margulies, 1998; Hrapko et al., 2008; Jin et al., 2013).

Differences in experimental testing methods of human brain tissue have also contributed to the variations in reported mechanical properties. The mechanical properties of brain tissue were dependent on temperature during testing (Arbogast and Margulies, 1998; Hrapko et al., 2008), the magnitude and rate of the loading (Hrapko et al., 2008; Jin et al., 2013), the type of loading (e.g., shear or compression) (Hrapko et al., 2008; Jin et al., 2013), tissue perfusion, and storage conditions (Fallenstein et al., 1969). Additionally, there were differences in the post-mortem time the tissues were tested, with a range of 48 hours to 12 days (Garo et al., 2007). Brain tissue mechanical properties were dependent on time post-mortem (Garo et al., 2007), supporting physiological studies that indicate that nerve tissue autolyzes shortly after death (Fountoulakis et al., 2001).

The mechanical characterization of the brain has also led to the derivation of constitutive models that mathematically relate stress (or loading magnitude) and strain (or deformation) across multiple loading severities or regimes. Constitutive models are useful for the creation of analytical or computer models that predict human brain mechanics during injury. The most common constitutive formulation implemented in FE brain models is a linear viscoelastic model. This model demonstrated applicability for small deformations (up to 20% strain); a quasilinear viscoelastic model is required for up to 50% strain, and a nonlinear viscoelastic model is required after that point (Takhounts et al.,

2003). For finite element implementation of brain material properties, most models utilize a linear viscoelastic constitutive model with one time constant (Madhukar and Ostoj-Starzewski, 2019) and these models have reasonable validation with existing brain deformation datasets (Mao et al., 2013; Miller et al., 2016; Takhounts et al., 2008a).

### **Mechanisms of Brain Injury**

Various mechanisms for TBI have been studied for decades in an attempt to link external head kinematics (linear and rotational motion) to the injurious macroscopic and microscopic deformations of brain tissue. The focus on correlating external head kinematics to brain injury risk has been motivated in part by the goal of developing TBI risk functions for assessing the efficacy of helmets and automotive countermeasures (Newman et al., 2000; Rowson and Duma, 2013; Takhounts et al., 2013a; Versace, 1971). Much of the early work in TBI biomechanics focused on the mechanism of injury and understanding what aspects of loading contributed to the disruption of the brain tissue.

Although controversy regarding the mechanism of TBI exists, recent studies have suggested that rotational head motion, not linear, is the primary cause of brain deformation, and this motion leads to diffuse injuries ranging from mild concussion to diffuse axonal injury (DAI). This theory was initially hypothesized by Holbourn (1943) using fundamental mechanics to describe the motion of the brain relative to the skull (Holbourn, 1943). Holbourn used photoelastic materials to highlight areas of high shear strain in a physical brain surrogate during rotational motion. The models predicted that cortical regions were most susceptible to sagittal plane rotations, while deeper brain structures were more susceptible to coronal plane rotations. Holbourn hypothesized that the shear strains were proportional to the rotational acceleration for long duration impacts and the rotational

velocity for short duration impacts. He also noted that the linear acceleration of impacts did not significantly contribute to deformations in the brain.

Experimental work on animal models in the decades after Holbourn's study confirmed his hypothesis. In seminal papers by Gennarelli and Ommaya (Gennarelli et al., 1972, 1987; Ommaya, 1984), primates were subjected to pure linear and rotational loading of the head. While the rotational motion caused diffuse TBI, linear accelerations up to 1400 g failed to produce cerebral concussion or other symptoms of diffuse injury. The TBI biomechanics field, however, gravitated towards experimental work showing a relationship between linear acceleration and cerebral injuries (Nusholtz et al., 1984; Ono et al., 1980; Stalnaker et al., 1977). These experiments were successful in predicting skull fracture and certain focal injuries associated with severe TBI; however, the relevance of the rotational mechanisms of injuries associated with mild and moderate TBI was sidelined. The studies using linear acceleration to cause head injury led to the development of injury criteria for head and brain injury that are still used in government and protective equipment safety standards (e.g., the Head Injury Criterion [HIC]) (Versace, 1971).

Given that water is the major constituent of brain tissue (Carey, 1990), the brain mechanically behaves like an incompressible material. Its bulk modulus (~2.1 GPa) is a million times larger than its shear modulus (~5 kPa) (Shuck and Advani, 1972), making it more susceptible to shearing deformations that change its shape rather than volumetric loads that would change its size. Furthermore, the coupling of the brain to the skull, which is a much stiffer material, and the anatomical structure of the head and cervical spine make rotational deformation dependent on the direction of loading. The significance of axis-dependent rotational motion has been corroborated through numerous experimental

(Gennarelli et al., 1972, 1987; Margulies et al., 1990; Ommaya et al., 1971; Smith et al., 1997) and computational studies (Gabler et al., 2016a; Kleiven, 2007; Rowson and Duma, 2013; Takhounts et al., 2013a) since the original animal studies by Ommaya and Gennarelli. There are no experimental studies that confirm the dependence of human brain deformation on axis-dependent, controlled rotational motion.

### **Human Brain Deformation Experiments**

Various techniques have been utilized to study *in vivo*, *in situ*, and *in vitro* human brain motion in response to motion of the head (Bayly et al., 2005; Hardy et al., 2001; Stalnaker et al., 1977). One approach for investigating *in situ* brain motion has been high-speed X-ray imaging of radio-opaque objects implanted in the brains of post mortem human surrogates (PMHS). Stalnaker (Stalnaker et al., 1977) used lead markers to quantify brain motion during the repressurization of the vasculature and ventricles and showed that the coupling between the brain and skull increased with the increased pressure. Nusholtz (Nusholtz et al., 1984) injected a neutral-density radio-opaque gel into the brain to measure brain motion in PMHS using high-speed cineradiography. Frontal impacts using a padded linear impactor on the specimen resulted in head linear accelerations ranging from 25-450 g, head rotational velocities ranging from 18-52 rad/s, and durations ranging from 8-50 ms. Minimal brain distortion was observed during these tests, except for the displacement of 6 mm in a specimen that also sustained skull fracture.

After these early tests using X-ray, the focus of the biomechanics field shifted towards using kinematic sensors to measure brain motion. Trosseille et al. (1992) used accelerometers implanted in the brains of cadavers to conduct validation tests for an FE model (Trosseille et al., 1992). A subsequent study by Hardy et al. (1997) used similar

triaxial neutral density accelerometers designed to move with the brain tissue and measure tissue motion (Hardy et al., 1997). The measured acceleration was then compared to skull-mounted accelerometers to compare relative motion, with 3-5 mm of peak displacement observed in the brain. Although the method was validated against X-ray measurements of brain motion, the accelerometers do not directly measure brain displacement, and errors were introduced in the displacement calculations.

In the early 2000s, the accelerometer method was abandoned with improvements in digital X-ray imaging technology. A large dataset of *in situ* human brain deformation was generated by Hardy et al. (2001, 2007)(Hardy et al., 2001, 2007). The experimenters used high-speed bi-planar X-ray to track the 3D motion of neutrally-dense targets (NDT) made from tin granules embedded in polystyrene tubing and were implanted in columnar and cluster arrays in the brains of post-mortem human subjects (PMHS) head-neck specimens. The head-neck specimens were inverted and subjected to frontal, occipital, and coronal impacts. The impacts were imparted on the head using a padded linear impactor which caused resultant head linear accelerations ranging from 38-291 g, rotational velocities ranging from 4-30 rad/s, and head rotational accelerations ranging from 2,370 to 24,206 rad/s<sup>2</sup>. The markers in the brain were observed to follow figure-eight patterns with peak-to-peak excursions as high as 13.4 mm. The observed deformation was largest in the inferior regions of the brain.

Other imaging modalities have also been used to characterize brain motion. Mallory et al. (Mallory, 2014) conducted low-severity sagittal head rotations (2 rad/s, 120-140 rad/s<sup>2</sup>) on repressurized cadavers and measured brain deformation using B-mode ultrasound at the surface of the dura. The study was useful in identifying relative localized

motion between the brain and surrounding anatomical structures but was limited by the penetration depth of ultrasound waves and the substantial disruption of the brain-skull boundary condition. Bayley et al. (Bayly et al., 2005), Feng et al. (Feng et al., 2010), Sabet et al. (Sabet et al., 2008), and Knutsen et al. (Knutsen et al., 2014) used tagged MRI to quantify *in vivo* brain deformation in human volunteers during low-severity, repeated sagittal head accelerations (2-3 g, 40 ms) and coronal rotations (300 rad/s<sup>2</sup>, 40 ms). The tagged MRI method has the potential to measure dynamic deformation of the human brain in a living person, but the technology is still in development. Limitations of this technique are also a potential barrier for high-rate, injurious loading conditions: The subjects must be tested multiple times to capture each “frame” of the motion using MRI. Thus, the tests must be very repeatable, and small variation can alter the results. Additionally, the sampling rate is approximately 15-20 Hz, which is not high enough to capture the deformation of the brain relevant to brain injury (500-1000 Hz required). The tests were also conducted on human volunteers, and the loading was not large enough to cause deformations that would be valuable for injury simulation using an FE model.

### **Brain Biomechanics**

Brain biomechanics is a research field that focuses on understanding brain mechanics during inertial loading to the head. Injuries to the brain are elusive and complex because it is difficult to quantify or assess what the brain experiences during an impact. There have been many experimental and computational studies that have attempted to link the external motion of the head to the biomechanical effects on brain tissue. One of the most common and readily available methods to predict injury risk is through injury criteria, which are usually developed based on tolerances derived from a combination of experimental and

computational studies. Brain injury criteria typically consist of a biomechanical metric, such as head angular velocity, and a related injury risk function. The injury risk function relates the biomechanical metric to some probability of TBI such as the risk of concussion. Such injury criteria have been used to evaluate the protective efficacy of automotive countermeasures (National Highway Traffic and Safety Administration, 2015; Takhounts et al., 2013) and to predict the possibility of injury to football players using helmet-mounted kinematic sensors (Duma et al., 2005). Biomechanical injury criteria have been developed either as kinematics criteria, based on the motion of the head or as tissue-level criteria, based on the mechanics of the brain tissue.

Kinematics-based injury criteria have been widely used to assess automotive and helmet safety. It is relatively easy to collect information on the head motion, using anthropomorphic test devices, helmet sensors, or video. The injury criteria are typically analytical equations, which can be solved relatively quickly. Kinematic injury criteria are based on head kinematics: linear, rotational, or both. Tissue-level injury criteria delve deeper into brain mechanics by assessing the relationship between the biomechanics of the brain (with metrics such as strain) to injury. Direct measurement of tissue-level deformation of the brain during head impact, however, remains elusive and challenging. Anatomically-detailed finite element (FE) models provide a valuable alternative and have been vital to investigating TBI mechanisms, assessing injury risk and safety gear, and developing brain injury criteria based on external head kinematics (Gabler et al., 2016a; Sanchez et al., 2017; Takhounts et al., 2013a). FE models are typically used in engineering design and optimization to predict the mechanical response of an object under various loadings. The models implement the finite element method to divide a complex object into

finite elements for which the mechanical response can be individually solved using continuum mechanics (Madhukar and Ostoja-Starzewski, 2019). With sufficiently small finite elements, the response and interaction of the elements can predict the macroscopic mechanical response of the object.

FE models provide an advantage over kinematics-based metrics because of their ability to measure complex patterns in the response of the brain instead of using a relationship between peak kinematics and brain deformation (Figure 2-6). By applying known six degree-of-freedom (DOF) head kinematics to the FE models, the temporal and spatial mechanical behavior of the brain can be approximated. These models allow for the in-depth investigation of brain response under various loading conditions at a level that is not possible using cadaveric or human experiments. They have been created to predict injury using summary strain-based injury metrics such as maximum principal strain (MPS) and the cumulative strain damage measurement (CSDM) (Gabler et al., 2016a; Kleiven, 2007; Sanchez et al., 2017; Takhounts et al., 2013a; Zhang et al., 2004). Although these injury metrics and models are computationally-based, they are considered the state-of-the-art method for evaluating a large number of head impacts and kinematics in an attempt to relate to injury (Deck and Willinger, 2009).

A limitation of FE models is the computational time, with typical simulation times of several hours for a ~100 ms impact. The computational cost and time prevent their use in real-time or field analysis. An additional consideration for the use of FE models is their biofidelity in comparison to experimental human brain deformation. To make significant conclusions about tissue-level deformation, the biomechanical response of the model must match closely to physical human brain deformation. Although many of the models are

validated using the same single dataset of human brain deformation, the results of the models can vary significantly for the same kinematic inputs. An analytical review of FE brain models suggests that the factors affecting the output of these models include material properties, geometric differences, the mesh (size, type, and quality), and FE parameters such as hourglass control (Giudice et al., 2018a). Additionally, the models are often simulated under conditions that vary from the head kinematic impacts they were validated against, raising questions about the applicability of the models and what conclusions can be drawn from the results.

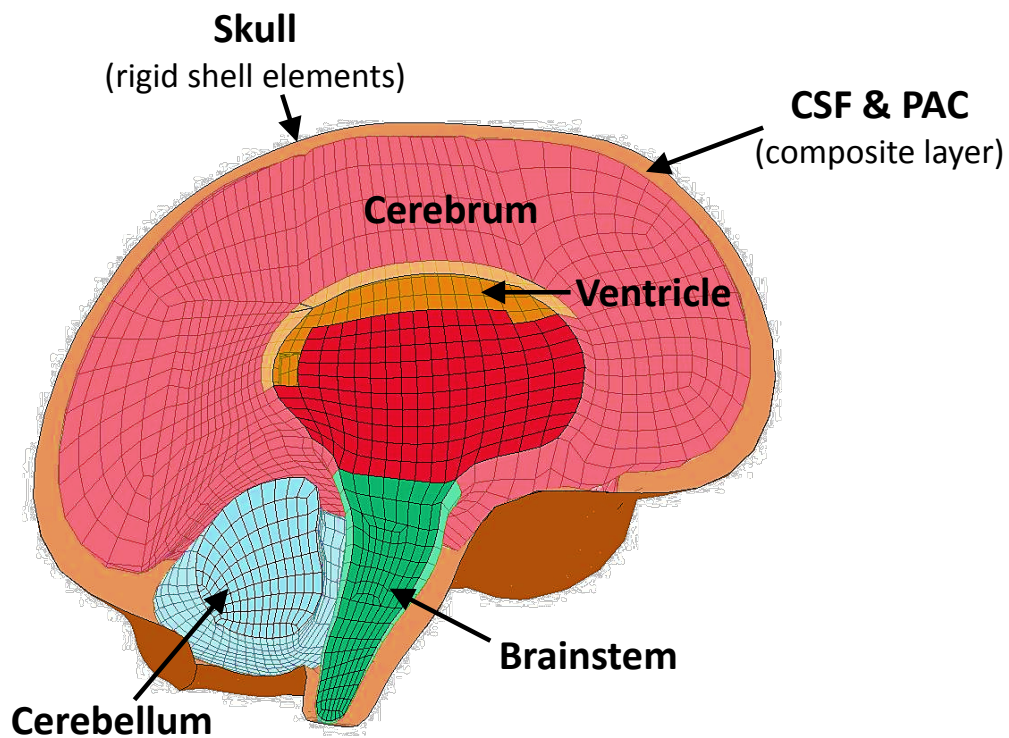


*Figure 2-6: Sagittal view of the Simulated Injury Monitor (SIMon) FE brain model. Different regions are shown, along with the finite element mesh (Takhounts et al., 2008a).*

### **Sonomicrometry**

There are various techniques in the field of biomechanics that have been used to track deformation of soft biological tissue. In the cardiac biomechanics field, bi-planar X-ray

was the method of choice from the 1920s to the 1980s to track heart motion, quantify volume, and measure deformations relevant to cardiac disease. In the 1980s, a new technique called sonomicrometry was introduced. Sonomicrometry utilizes an array of small, implantable piezoelectric crystals to dynamically measure distances between points in the tissue by recording ultrasound time-of-flight between crystal pairs. The technology has been extensively used for the past 30 years for various *in vivo* and *in situ* biomedical research applications, including joint biomechanics and tissue testing. It provided an order of magnitude-improved accuracy and did not need external tracking or radiation (Figure 2-7). 3D digital sonomicrometry had a high degree of agreement with measures derived from a materials testing machine (displacement difference of  $0.037 \pm 0.0137$  mm) (Stonecash, 2005), a Kuka robot (displacement difference of  $0.04 \pm 0.001$  mm) (Sipes et al., 2005), single-plane fluoroscopy (absolute difference of  $1.06 \pm 0.27$  mm) (Meyer and Wolf, 1997), and bi-planar X-ray (absolute difference of  $0.63 \pm 0.46$  mm) (Meoli et al., 1998). The studies comparing sonomicrometry to bi-planar X-ray found an order-of-magnitude improvement in displacement accuracy, with spatial resolutions of 0.024 mm for sonomicrometry versus 0.24 mm for high-speed X-ray (Dione et al., 1997; Hardy et al., 2001).

After two decades of vetting the technology in comparison to fluoroscopy and bi-planar X-ray, sonomicrometry has largely replaced biplanar X-ray as the preferred method for high-rate internal motion tracking in cardiac mechanics experiments (Dione et al., 1997; Van Trigt et al., 1981; Sarazan and Schweitz, 2009; Fomovsky et al., 2012; Holmes, 2004).

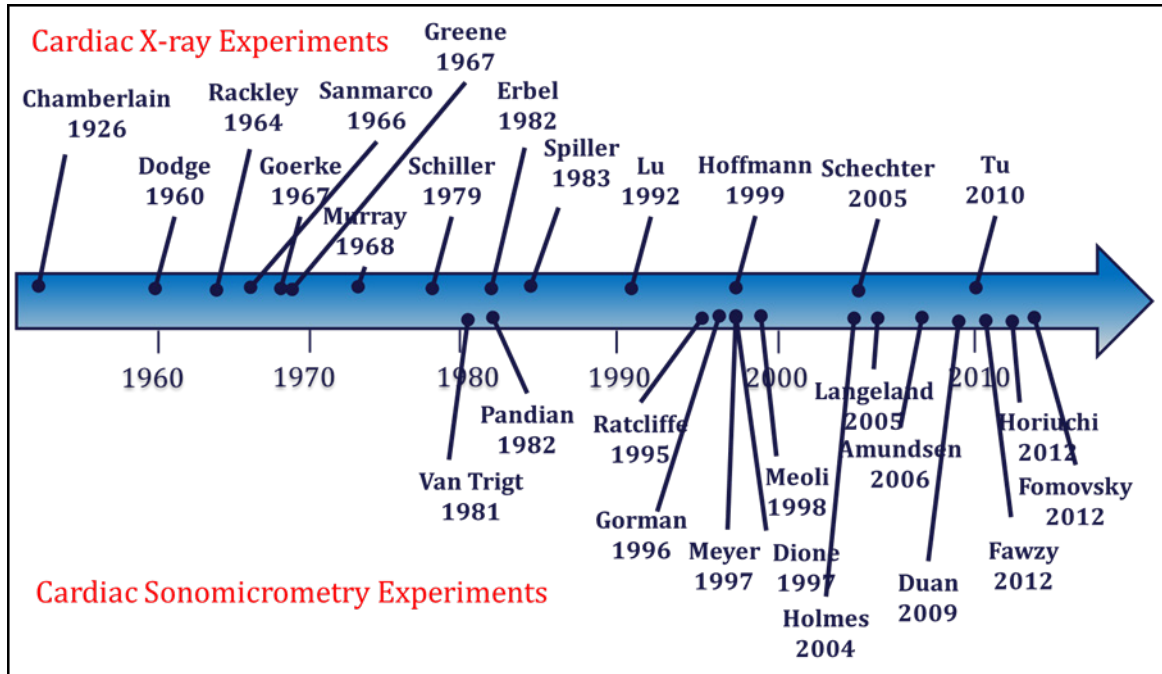


Figure 2-7: Bi-planar X-ray and sonomicrometry in cardiac biomechanics (Alshareef, 2019).

In addition to improved accuracy, sonomicrometry crystals do not have line-of-sight imaging requirements, allowing for a larger array of crystals that can be distributed throughout all regions of the brain, and each specimen can be tested in multiple loading severities and directions. Bi-planar X-ray has been the method of choice in brain deformation experiments, but sonomicrometry has the potential to improve the state of brain deformation research. The use of sonomicrometry to measure brain deformation provides a more accurate and robust technique to generate a dataset of brain deformation.

## **Summary**

The motivation and background of this dissertation can be summarized in the following points:

- TBI is a leading cause of injury, with a substantial societal burden.
- Most brain injuries are closed-head injuries, with focal or diffuse injury patterns.

- In sports and automotive environments, diffuse injuries, including concussion and DAI, are the most common. Biomechanical assessments of TBI contribute to the evaluation of protective equipment and automotive crashworthiness.
- The biomechanics of TBI is typically assessed using kinematic-based metrics, such as brain injury criteria, and tissue-level tools, such as FE brain models, to relate the motion of the head to the deformation and correlated injury risk of the brain.
- The biofidelity of FE brain models is essential to their use in biomechanics. Currently, models have limited brain deformation validation datasets, and there is no consensus on the method of validation.
- Sonomicrometry provides a promising technique to measure brain deformation in comparison to the standard technique of X-ray imaging.
- A dataset of human brain deformation will provide an important validation tool, as well as insight into the biomechanics of the human brain under rotational loading.

## **CHAPTER 3: METHODOLOGY DEVELOPMENT**

The measurement of *in situ* human brain deformation under rotational loading will provide necessary data for understanding the mechanics of TBI and validation of FE brain models. The techniques of applying a pure rotation to the head, as well as accurately measuring brain deformation under multiple loading conditions, however, are complex and require the development of a new test device. The objective of this chapter was to develop a methodology for the investigation of three-dimensional (3D) brain deformation during pure rotational loading of the head. The first goal was to devise a well-defined test method to apply rotational loading to the head. The second aim was to demonstrate sonomicrometry as a tool for quantifying brain deformation. The contributions of this chapter will provide a framework for quantifying *in situ* brain deformation using sonomicrometry under pure rotational loading of the head. Portions of this chapter were published previously (Alshareef et al., (2018). A Novel Method for Quantifying Human In Situ Whole Brain Deformation under Rotational Loading Using Sonomicrometry. *Journal of Neurotrauma*, 35(5), 780-798), and were adapted for this dissertation.

### **INTRODUCTION**

Various mechanisms for TBI have been studied for decades in an attempt to link external head kinematics (linear and rotational motion) to the macroscopic and microscopic deformations of brain tissue that leads to injury. The focus on correlating external head kinematics to brain injury risk has been motivated in part by the goal of developing TBI risk functions for assessing the efficacy of helmets and automotive countermeasures (Newman et al., 2000; Rowson and Duma, 2013; Takhounts et al., 2013a; Versace, 1971). Although controversy regarding the mechanism of TBI still exists, recent studies have

suggested that rotational head motion, not linear, is the primary cause of brain deformation, and leads to diffuse injuries ranging from mild concussion to DAI. The significance of axis-dependent rotational motion has been corroborated through numerous experimental (Gennarelli et al., 1972, 1987; Margulies et al., 1990; Ommaya et al., 1971; Smith et al., 1997) and computational studies (Gabler et al., 2016a; Kleiven, 2007; Rowson and Duma, 2013; Takhounts et al., 2013a).

Various FE models of the head have been created to predict injury using strain-based injury metrics (Kleiven, 2007; Takhounts et al., 2013a; Zhang et al., 2004). These models allow for the in-depth investigation of the brain response under various loading conditions at a level that is not possible using cadaveric or human experiments. Since brain strain is the primary outcome measure typically used to predict brain injury, it is essential to validate the brain deformation predicted by these models using human brain motion observed in laboratory experiments.

Various techniques have been utilized to study human brain deformation (Bayly et al., 2005; Hardy et al., 2001; Stalnaker et al., 1977). One approach for investigating *in situ* brain motion has been high-speed X-ray imaging of radio-opaque objects implanted in the brains of post mortem human surrogates (PMHS). Hardy (Hardy et al., 2001, 2007) used high-speed bi-planar X-ray to track the 3D motion of neutrally-dense targets (NDT), made from tin granules embedded in polystyrene tubing, implanted in columnar and cluster arrays in the brains of PMHS head-neck specimens. The head-neck specimens were inverted and subjected to frontal, occipital, and coronal impacts. Impacts were imparted on the head using a padded linear impactor which resulted in resultant head linear accelerations ranging from 38-291 g, rotational velocities ranging from 4-30 rad/s, and

head rotational accelerations ranging from 2,370 to 24,206 rad/s<sup>2</sup>. The markers in the brain were observed to follow figure-eight patterns with peak to peak excursions as high as of 13.4 mm. The results obtained from this study provided a valuable validation dataset for FE model development but included several limitations. Bi-planar X-ray requires that each implanted NDT be continuously viewable in each frame, and each must be consistently distinguishable and identifiable from the other surrounding NDTs. This constraint limits the number of NDTs that may be used in a given test, as too high of a concentration of markers in any area would confound consistent identification of the NDTs (Hardy et al., 2007). High-speed X-ray also has a discretization limitation in tracking the positions of the NDTs, providing an inherent error of 0.24 mm on all measurements (Dione et al., 1997; Hardy et al., 2001). The method also limits test fixture design to prevent interference with X-ray videos and constrains loading conditions such that the head trajectory is confined within the field of view of the X-ray system.

Many of the limitations of the existing methodologies for measuring brain deformation can be remedied using sonomicrometry. Sonomicrometry utilizes an array of small, implantable piezoelectric crystals to dynamically measure distances between points in the tissue by recording ultrasound time-of-flight between crystal pairs. Sonomicrometry crystals do not have line-of-sight imaging requirements, which allows for a more extensive array of crystals that can be distributed throughout all regions of the brain and allows each specimen to be tested in multiple loading conditions and directions.

The objective of this study was to develop and test a methodology for the investigation of three-dimensional (3D) brain deformation during pure rotational loading of the head. The methodology development includes design and fabrication of the test device and

mounting hardware, the sonomicrometry deformation measurement methodology, the specimen selection criteria, design and assembly of the perfusion system, the specimen preparation procedure, selection and procurement of instrumentation, and the testing procedure. The methodology development is followed by results from a set of pilot tests performed with a single cadaveric human specimen, to validate the reliability and repeatability of the testing methods and the sonomicrometry technique.

## **METHODS**

### **TEST DEVICE AND PREPARATION HARDWARE**

#### **Fixture Design and Fabrication**

The fixture design and fabrication included three mechanical systems: the rotational loading test device (RTD), a jig to facilitate consistent installation of instrumentation and mounting hardware on the test specimen, and a coupling mechanism to attach the head specimen to the RTD and allow testing about the three axes of the head.

#### **Rotation Test Device (RTD)**

The RTD is driven by a DSD Single Intrusion Cylinder (Dr. Steffan Datentechnik GmbH, Linz, Austria). This multi-purpose drive system uses a pneumatically-driven, servo-hydraulically controlled active feedback control system to generate dynamic linear loading with controlled acceleration, velocity, and displacement pulse characteristics. This system was chosen for its ability to deliver user-defined acceleration pulses with high repeatability and accuracy. The RTD uses a cable-drive system to translate the linear output of the DSD into a rotational pulse that can be applied to rotate a specimen rapidly. The device includes two cables - a drive cable and deceleration cable - attached to a drive drum to allow for controlled rotational acceleration and deceleration. The drive drum was

connected to a 1:1, heavy-duty bevel gearbox with two perpendicular output shafts, to allow for rotation in three directions while maintaining a consistent (inverted) initial head position. For sagittal and coronal rotations, the specimen was mounted to the through-shaft of the gearbox. For axial rotation, the specimen was mounted to the perpendicular output shaft. In all cases, the head was initially oriented in an inverted position before the initiation of the test, approximately perpendicular to the ground. An illustration of the CAD assembly for the RTD is shown in Figure 3-1.

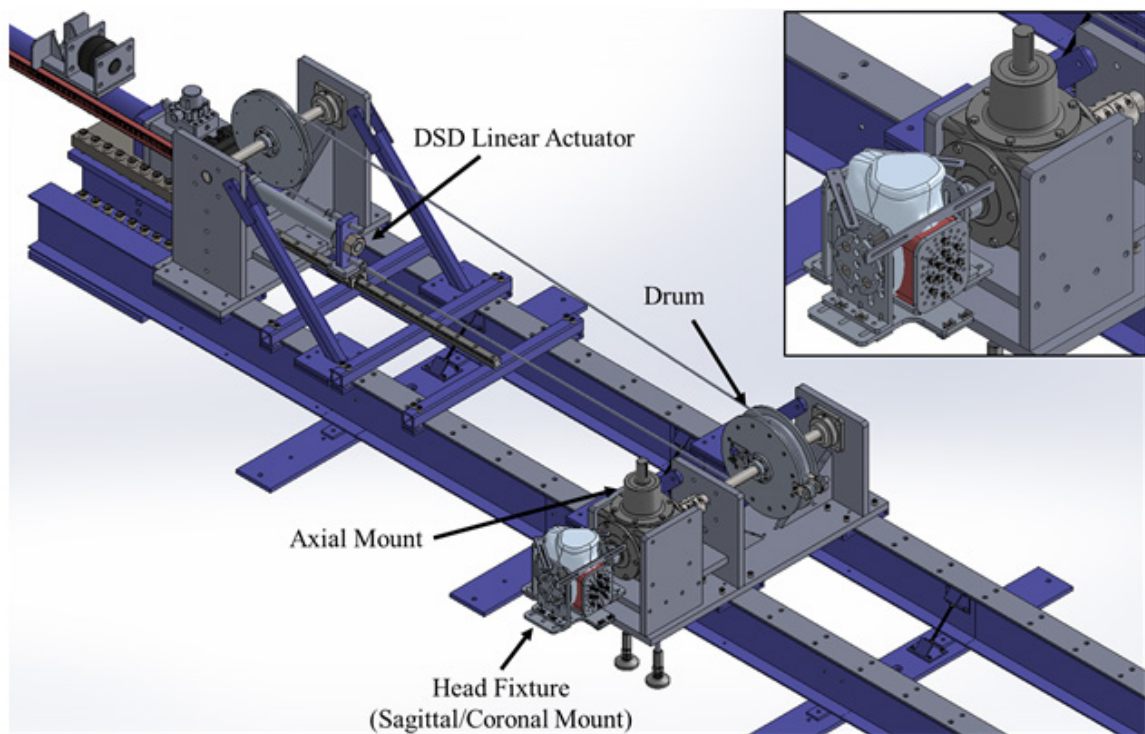


*Figure 3-1: CAD assembly of the dynamic rotation test device (RTD). The RTD uses a linear, pneumatic actuator and converts its linear motion into pure rotation through a cable-drum-gearbox assembly. The gearbox allows for efficient mounting of the specimen in all three anatomical directions.*

### **Specimen Prep Jig**

A specimen prep jig was developed to ensure consistent installation of instrumentation and mounting hardware on each specimen. The specimen was aligned within the jig based on the specimen's anatomically-identified center of gravity (CG) (refer to "Specimen

Preparation” section below for details) and alignment pins were used to guide the fixation of plates to all sides of the head. Illustrations of the CAD assembly for the specimen prep jig are shown in Figure 3-2.

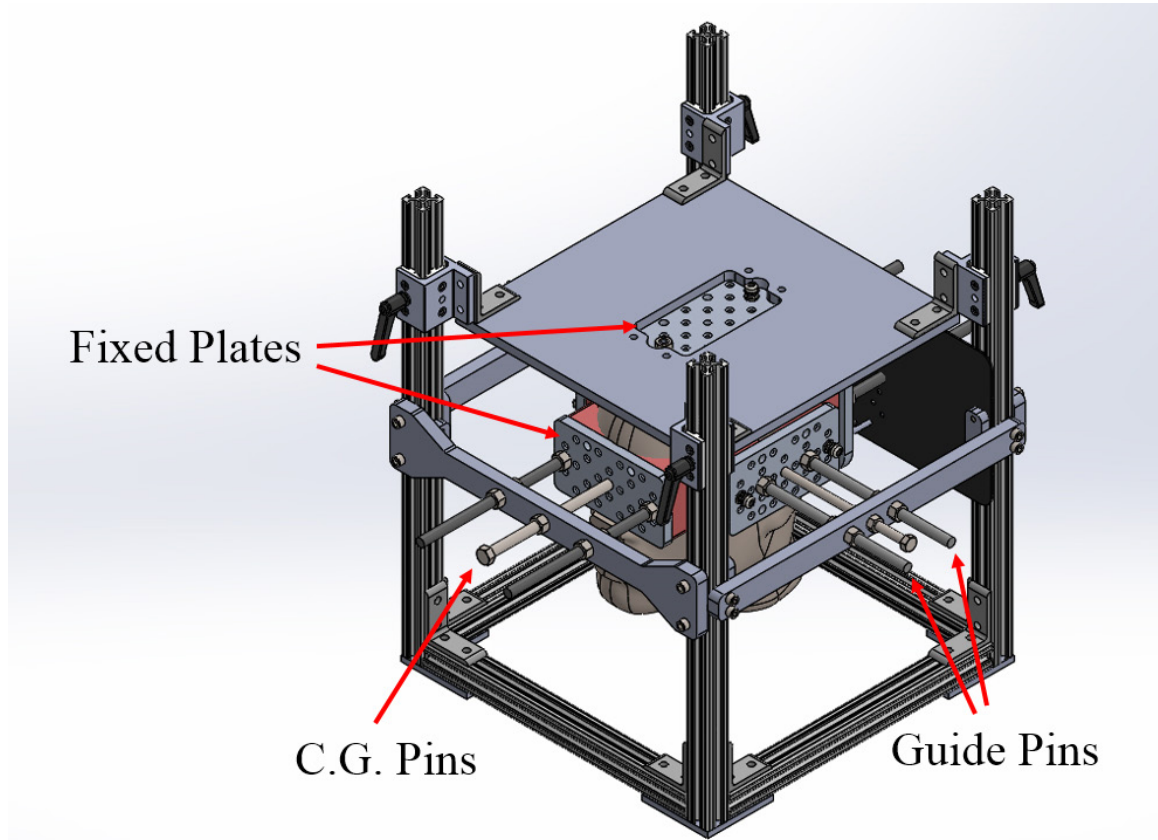


*Figure 3-2: Head specimen preparation jig. This jig was designed to ensure consistent placement of the mounting hardware and instrumentation relative to the anatomically-defined head CG.*

### **Rotation Coupling**

A set of mounting plates were designed to couple the head to the output shafts of the RTD gearbox. They are attached to the mounting plates fixed to the head, with an attached collar to interface with the gearbox. An isometric view of the head specimen mounted to the rotation coupling can be seen in Figure 3-3. The collars have three possible mounting positions, one for each axis of rotation. This assembly also had a mounting location for a

multi-degree of freedom kinematic sensor package to record the head kinematics during testing.

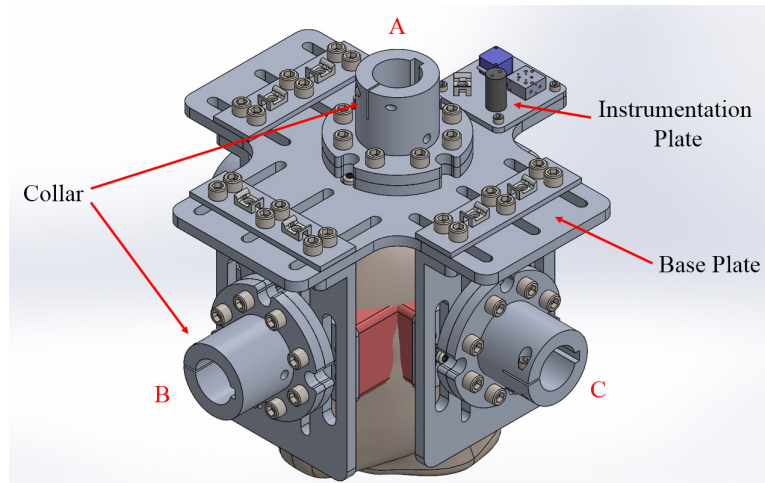


*Figure 3-3: Rotation coupling hardware. Collar position A was for axial rotation, B for coronal rotation, and C for sagittal rotation. Note: Only one collar was attached at a time.*

### **Pulse Tuning**

To obtain the desired pulse magnitude and duration, both the linear acceleration input curve to the DSD and the DSD feedback control were tuned. The tuning process involved optimization of the duration and magnitude of the input curve as well as the PID control. An instrumented plate with a variable moment of inertia (MOI) was fabricated and used to conduct speed runs on the RTD. The blocks were adjusted to yield approximately the same calculated MOI as the head and mounting fixture (derived from the CAD assemblies). For pulse tuning, the MOI plate was mounted in the axial test configuration. The DSD input curve was tuned by calculating the linear input required to produce a specified downstream angular velocity. Iterations to this input curve were made to account for variations in the MOI, the coupling between the linear cylinder and rotational components, and the mechanical resonance frequency of the RTD.

## **SONOMICROMETRY**

Sonomicrometry crystals were employed to quantify brain deformation in response to the dynamic rotation pulses. The 2-3 mm crystals are capable of transmitting and receiving ultrasonic pulses, which have a frequency of 100 MHz. The crystals weigh approximately 0.02 grams and are neutrally dense. The crystal wires are ultra-thin, flexible, and neutrally dense. For each transmitter-receiver crystal pair, the time of flight of the ultrasound pulse is captured by a central data acquisition system. By assuming a speed of sound through the tissue, a segment distance can then be calculated between the two crystals. With the inclusion of at least three crystal pairs, trilateration can be used to determine the 3D coordinates of each receiving crystal in the array. Sonomicrometry offers the advantages of being minimally invasive, neutrally dense relative to brain tissue, and capable of measuring 3D deformation.

Initial testing of the crystals was performed *in situ* using porcine brain tissue to confirm that the crystals could be easily inserted, functioned properly, recorded accurate data, and caused no gross disruption of the brain tissue. The following sections describe the verification of the sonomicrometry technique in brain tissue, the selection of transmitter and receiver crystal positions, crystal modification and insertion procedure, identification of the maximum sampling rate, and the development of the brain crystal insertion procedure.

### **Verification of Sonomicrometry Performance in Brain Tissue**

Trials were performed on two post-mortem porcine head specimens to verify the performance of the sonomicrometry system in an inhomogeneous, *in situ* brain environment and to practice insertion and port-sealing techniques. The specimens were

obtained from the UVA Department of Comparative Medicine. Specimen procurement, handling, and disposal were performed in accordance with the protocols of the UVA Department of Comparative Medicine and the UVA Institutional Animal Care and Use Committee. Tests were performed within 48 hours of death.

Two specimens were procured and tested. The first specimen was used to verify sonomicrometry signal transmission in the inhomogeneous brain tissue environment. First, the dorsal surface of the dura and the brain was exposed via 2” diameter craniotomy (Figure 3-4). Care was taken to minimize disruption to the dura. Once the area was exposed, four sonomicrometry crystals were inserted into the brain (two in each hemisphere) via the cannula insertion technique (see “Specimen Preparation”). Good signal quality was observed between each of the pairs, with no discernable signal transmission or noise issues.

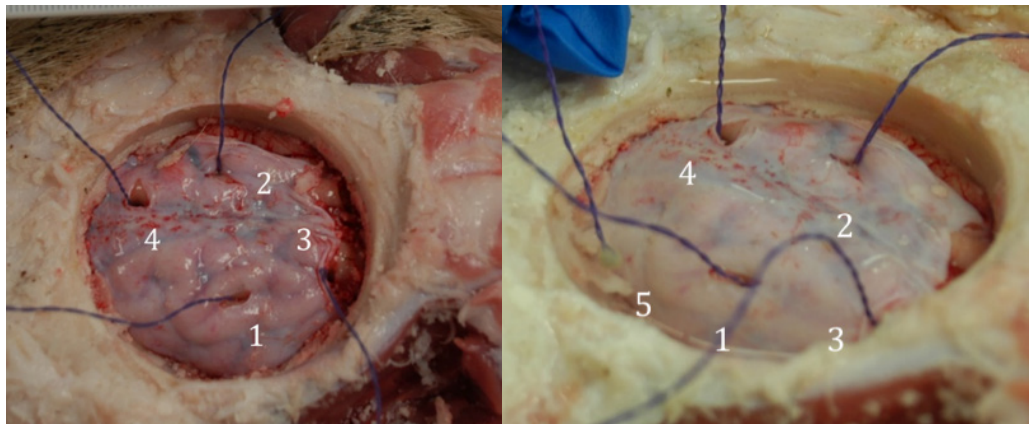
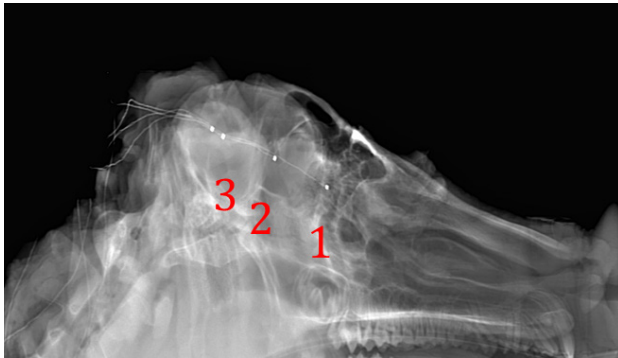


*Figure 3-4: (Left) In situ sonomicrometry signal transmission test. Four crystals were inserted into a porcine brain in situ via craniotomy. (Right) The craniotomy field was flooded with saline, and then a crystal was placed in the saline outside of the dura.*

Signal transmission through the dura was also checked using the same specimen. The brain within the cranial vault was filled with saline solution, and a 5<sup>th</sup> crystal was placed in the fluid outside of the dura (Figure 3-4). The signal quality between this extradural crystal and the implanted brain crystals was then checked as the extradural crystal was moved to

various distances outside of the dura. In all cases, good signals were assessed, without noise or transmission problems.

A second porcine specimen was used to determine crystal distance accuracy via planar X-ray for a quantitative comparison to sonomicrometry. A series of crystals were inserted into the brain in a line coplanar with the planned X-ray image to facilitate distance measurement using planar X-ray. A sagittal plane X-ray was then captured using a StatScan machine (Figure 3-5). The measured X-ray distances were then compared to the crystal pair distances measured via sonomicrometry. This comparison was performed with the speed of sound in the sonomicrometry system set to the default setting (1590m/s). The crystal pairs exhibited good agreement with the measured X-ray distances, consistently within approximately 0.5mm.



| Pair  | Measured Distance | Sonometrics Distance |
|-------|-------------------|----------------------|
| 1 - 2 | 25.2 mm           | 25.75 mm             |
| 1 - 3 | 51.5 mm           | 51.63 mm             |
| 2 - 3 | 24.4 mm           | 24.29 mm             |

*Figure 3-5: An in situ porcine experiment was conducted compare distances between sonomicrometry and planar X-ray. The distance measurements were all within 0.6 mm of the sonomicrometry measurements.*

### **Maximum Transmission Distance**

To track the 3D motion of sonomicrometry crystals within the brain, sonomicrometry uses trilateration based on distance measurements between the brain crystals and transmitting crystals affixed to the inner surface of the skull (which function as a fixed reference frame; Figure 3-6). A set of crystals is fixed to points on the interior surface of

the skull, and a set of crystals is placed within the brain. The skull crystals primarily act as “transmitters,” and the brain crystals act as “receivers.” An ultrasound wave is emitted from a given transmitter and is received by all other crystals, giving the distances from the transmitters to all receivers. The next transmitting crystal emits a pulse that is received by all other crystals to acquire pair-to-pair distances. This process is then repeated for all transmitting crystals. After determining the distance of each receiver from each transmitter, trilateration is used to determine the position of the receiving crystal in the skull reference frame. Redundant distance measurements are available to quality-check the resulting data.

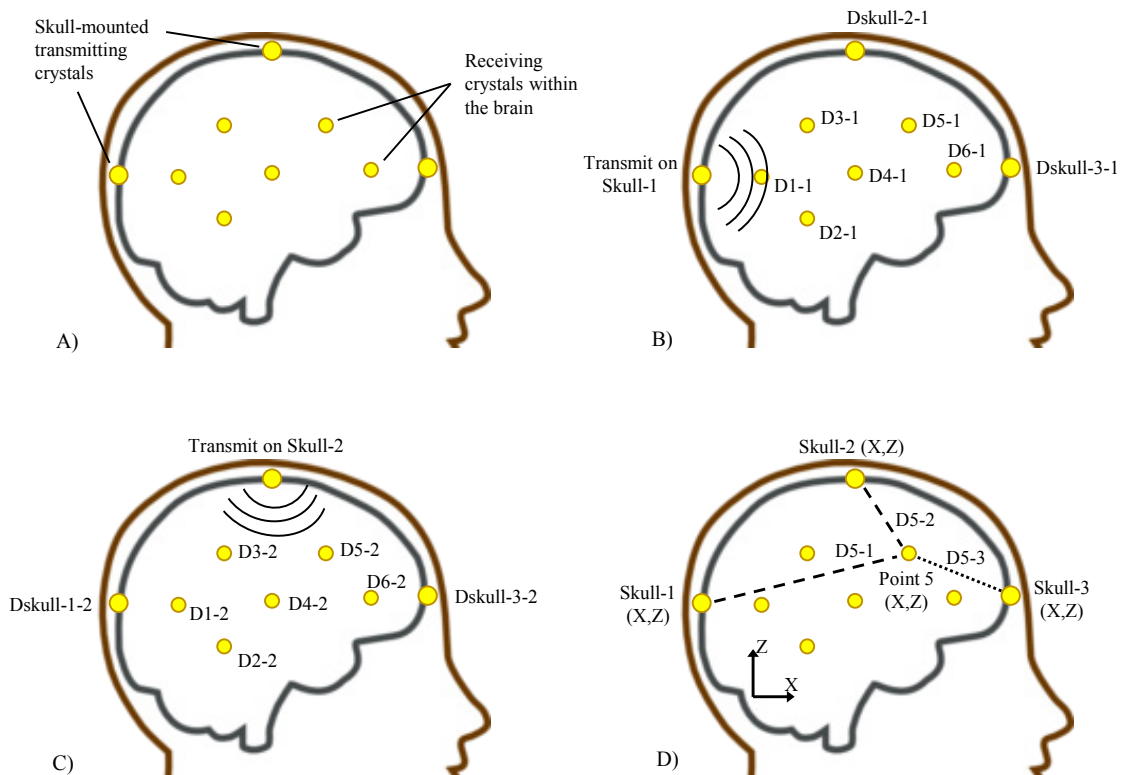


*Figure 3-6: Illustration of the use of sonomicrometry to track the 3D position of locations within the brain relative to the skull.*

Each receiver needs to be able to receive at least three transmitter signals to be able to perform trilateration, with more transmission signals yielding a more accurate trilateration solution. The maximum transmission distance through brain tissue is needed to identify an

ideal transmission crystal array that maximizes transmission overlap. A test with a porcine brain was performed to determine the maximum transmission range of the crystals. Minced porcine brains, purchased frozen, were thawed and placed within a translucent plastic anatomical skull model. A transmitter was affixed to the inner skull, and an insertion cannula was utilized to push a 2-mm receiving crystal very close to the transmitter. Data were collected at a sampling rate of 1000 Hz while the receiving crystal was slowly retracted away from the transmitter. On average, the maximum transmission distance was  $117.6 \pm 8.12$  mm through the porcine brain (Figure 3-7). A maximum transmission distance of 100 mm (mean minus two standard deviations) was used to determine the transmitter crystal array to ensure reliable transmission.

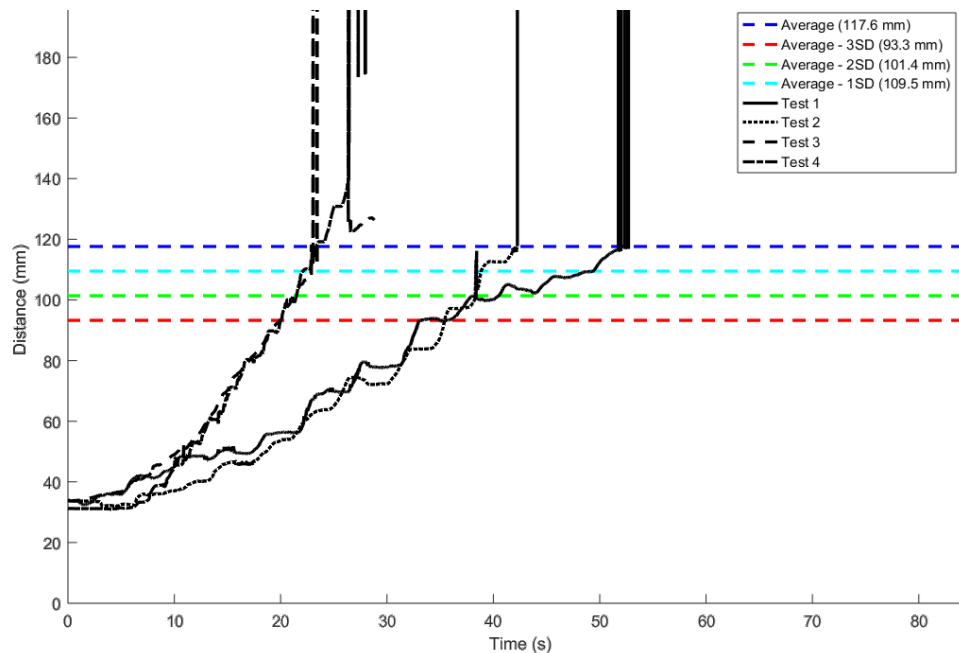
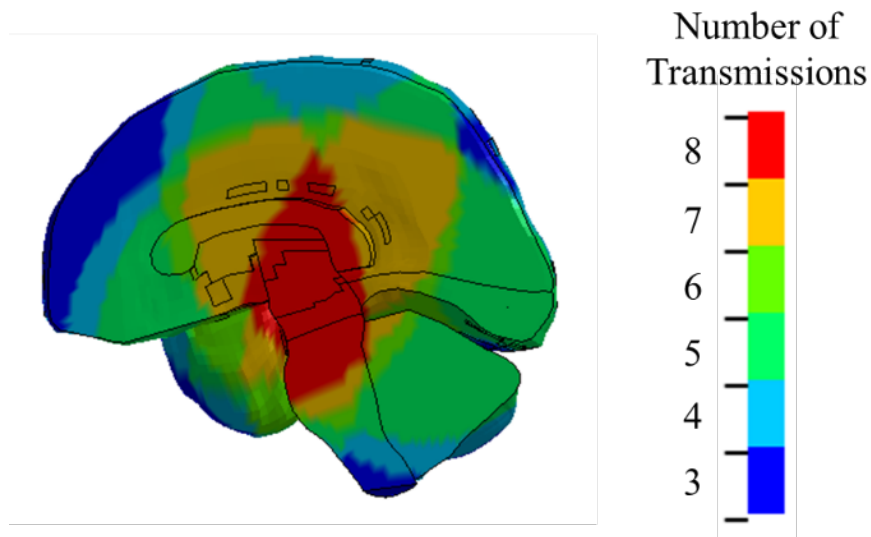


Figure 3-7: Retraction test results using a sampling rate of 1000 Hz. The trials showed a mean signal dropout distance of approximately 117 mm.

### Transmitter Array Geometry

The positions of the fixed transmitting crystals are crucial to obtaining accurate trilateration data. Therefore, it was necessary to optimize the transmitter positions to

maximize regions of transmission overlap with a minimum number of transmitters. The transmission crystal array geometry was designed using the Global Human Body Model Consortium (GHBMC) M50 v4.4 skull and brain finite element model. Eight nodes on the outer surface of the skull part were identified as possible locations for transmitter crystals, and the distances from each of these nodes to every node in the brain were calculated. For each node in the brain, the number of transmitting nodes within the transmission radius (100 mm) was recorded. Ultimately, ten different transmission crystal arrays, with eight transmission crystals each, were investigated. Compared to the other iterations, the finalized array with eight transmission crystals had the greatest amount of brain nodes receiving four or more transmission signals (Figure 3-8). In general, the brain regions receiving the least amount of transmission signals were limited to the outer edges of the brain.



*Figure 3-8: Transmission overlap in the brain. Fringe levels correspond to the number of transmission signals received at each node in the brain for the finalized transmission crystal array.*

The final transmitter array included crystals in the in posterior, anterior, left, and right at or a short distance above the Frankfurt plane. The last four transmitters were placed

symmetrically in the left and right posterior and anterior portions of the top of the skull. The coordinates of each transmitter relative to the anatomically-defined head CG are identified using computed tomography (CT) scans.

### **Receiver Crystal Array**

The primary goal of the receiver crystal array design was to maximize the coverage of recorded brain deformation throughout the volume of the brain. Nonetheless, the brain anatomy imposes several limiting areas where crystal placement was avoided. These areas include included the ventricles within the midbrain, and cortical tissue no closer than 20 mm from the skull surface.

The GHBMC M50 v4.4 finite element model was used to identify the target locations of the receiving crystals relative to the skull geometry. First, the geometry of the instrument guide plate (designed for crystal insertion during specimen preparation) was imported into LS-PrePost along with the GHBMC skull and brain model. The plate was aligned such that its center was located halfway between the occiput and crown of the skull. Next, all parts the brain parts except the ventricles were hidden, and insertion holes on the plate were selected based on whether they avoided the ventricles (Figure 3-9). For the selected holes, nodes (representing receiver locations) were evenly spaced throughout the brain on the projected path of the selected holes. The majority of selected holes in the cerebrum had three crystals inserted through them. The remaining selected holes, in the cerebellum and brainstem, had one crystal inserted. Finally, the position of each of the selected receiver nodes was normalized by the maximal length of the skull (anterior-posterior) to determine their position relative to the size of the skull.

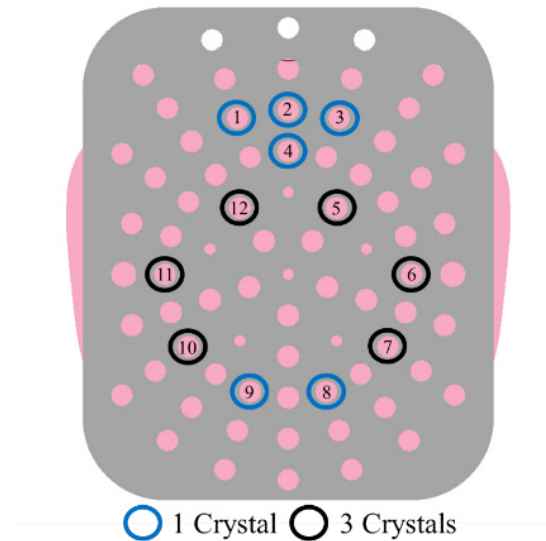


*Figure 3-9: Hole selection in the instrument insertion plate, shown relative to the skull. Blue and black circles indicate whether one or three crystals were inserted through each hole, respectively.*

### **Insertion Procedure and Crystal Modifications**

Monofilament barbs were glued to the 2-mm receiver crystals (which are inserted into the brain) to anchor the crystals within the brain tissue. The 10-mm barbs were attached to the crystals with Loctite 382 epoxy which has a specific gravity of 1.05 (Figure 3-10). Crystal transmission tests were conducted in a water bath to confirm that the process of gluing barbs to the crystals did not damage or interfere with the crystals' ability to receive the transmitted signals. Furthermore, insertion tests using gelatin and porcine brains demonstrated that crystals with barbs maintained their position during the insertion process much more effectively than those without any modifications.

The transmitting crystals were also modified to ensure a rigid connection between the crystal and skull. Two inch long epoxy-lined heat shrink tubing was applied to the wires at the interface with the crystal to increase the effective wire diameter. The heat shrink tubing was cut to different lengths based on the approximate skull thicknesses where the transmitting crystals were to be inserted. This modification allowed the transmitter crystals

to be rigidly positioned at the end of the skull surface, close to the dura, with adjustability in the depth of insertion. M8-sized cord grips (Sealcon, CO, USA) were used to secure the modified transmitters to the skull and seal the drilled ports. The transmitters located on the left, right, and posteriorly passed through fixation plates attached to the skull at those locations. The transmitters located anteriorly and along the crown were secured in threaded holes tapped directly into the skull. All transmitter assemblies were tested after fabrication to ensure full functionality.

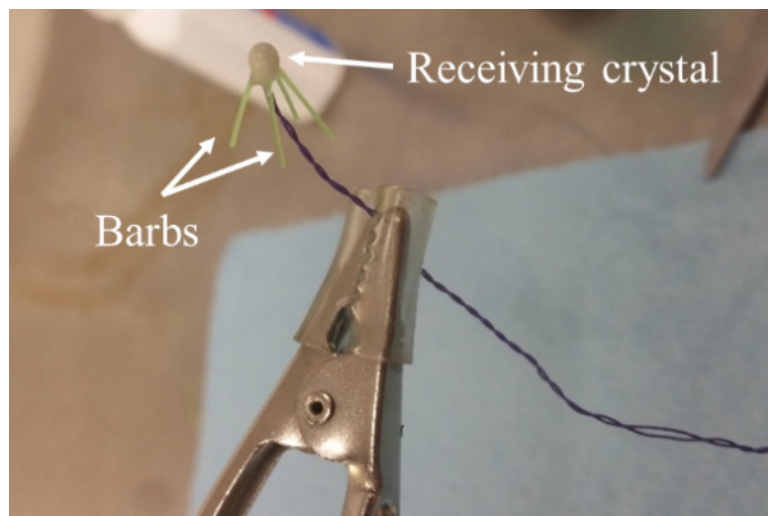


*Figure 3-10: Monofilament barbs installed on a 2-mm receiver crystal. Barbs were constructed of 10-mm length monofilament fishing line, glued to the crystal head using epoxy.*

A custom-built insertion mechanism was designed to insert the receiving crystals into the brain without coring or otherwise grossly disrupting the tissue. This mechanism included three parts: a needle, a 4.6 mm diameter slotted cannula, and a push rod (Figure 3-11).

Ports were drilled into the skull based on the selected insertion plate hole layout (Figure 3-9). To introduce a crystal, the needle was placed within the 4.6 mm diameter slotted cannula and together were inserted into the brain, through the port, to the desired depth. The inclusion of the needle within the cannula prevented coring of the brain tissue.

Next, the needle was removed, and the rod was used to push the crystal down the length of the cannula. The insertion cannula was slotted to facilitate the removal of the crystal wires. Once the cannula was removed, a piece of slotted tubing was placed around the crystal wire, and an M8-sized cord grip (threaded into the selected insertion hole) was used to tighten around the crystal wire, sealing the hole and providing strain relief from external tractions. Before sealing the port, a length of the crystal wire was pushed into the hole to ensure that adequate slack was present inside the hole to avoid constraining the crystal motion.

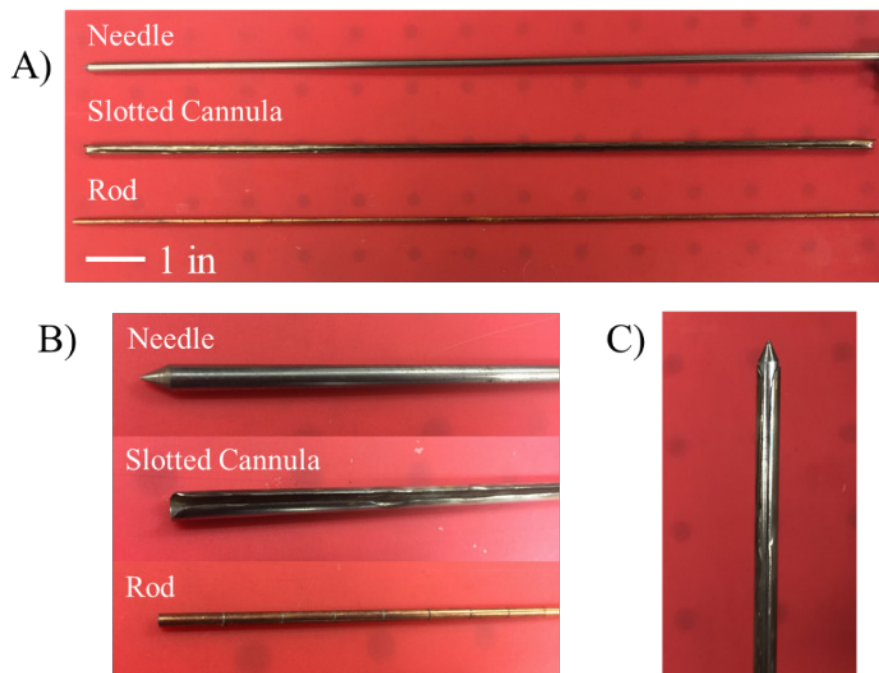


*Figure 3-11: Insertion mechanism parts. A) Full length of all three parts. B) Close-up of all three parts. C) Needle inserted through a slotted cannula.*

In the case where three crystals were inserted through a hole, the needle and cannula were inserted to the maximum desired depth through that hole to insert the farthest crystal first. The cannula was then retracted to the next depth and the second crystal was placed. The third crystal on the string was then placed in the same manner. Figure 3-12 illustrates the receiver crystal insertion procedure for one set of crystals. This insertion procedure was

validated using gelatin, Sylgard 527 gel (Dow Corning, MI, USA), and porcine brains. In all cases, no gross peripheral material disruption or coring were observed.

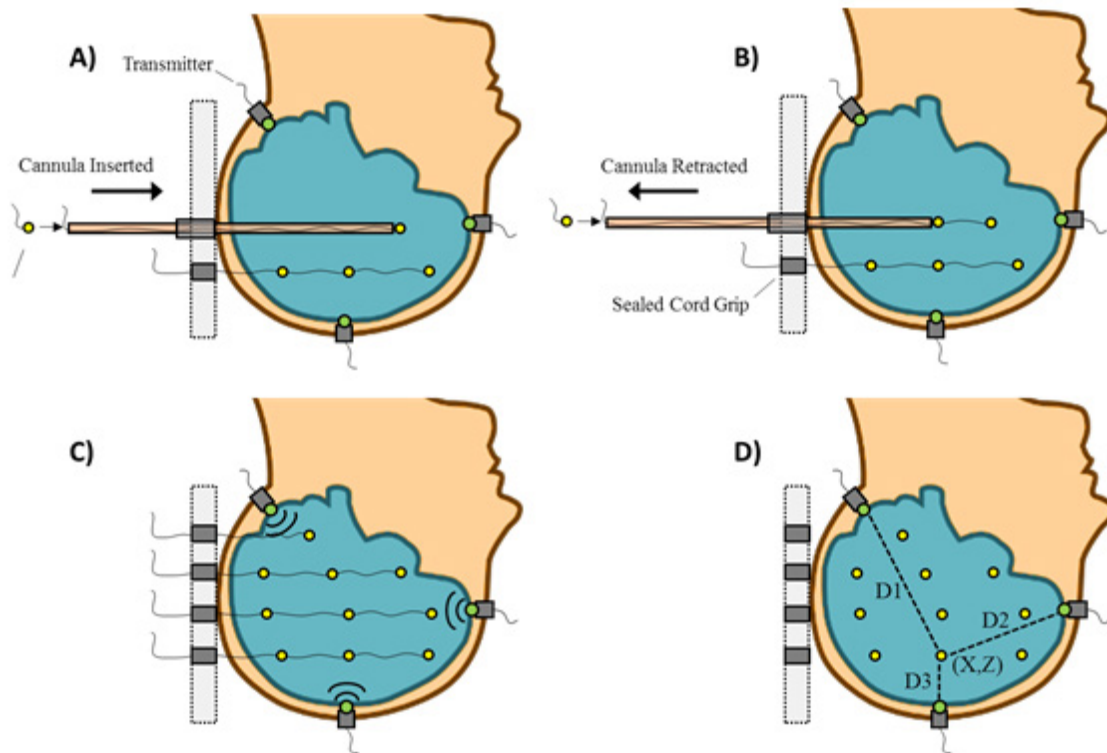


*Figure 3-12: Summary of the crystal insertion procedure. A) The cannula was inserted to the required depth, and the crystal was pushed down the length using a rod. B) The cannula was retracted, and the next crystal was placed. The ports were sealed using cord grips. C) During the test, the transmitters sequentially sent ultrasound pulses, while the receivers recorded the signals. D) A minimum of three crystal pairs was necessary to find 3D coordinates using trilateration.*

## **SPECIMEN ACQUISITION AND INFORMATION**

### **Specimen Acquisition**

All tissue donation, testing, and handling procedures were approved by the University of Virginia Center for Applied Biomechanics (UVA-CAB) Institutional Review Board – Human Surrogate Use (IRB-HSU) Committee. UVA-CAB is a Biosafety Level II (BSL-II) post-mortem human subject (PMHS) test facility regulated by the standards set by the UVA Institutional Biosafety Committee. All test procedures were approved by the UVA

Institutional Review Board prior to any testing. All research personnel involved in the experiments are annually trained in bloodborne pathogen prevention, and all follow guidelines adopted by UVA-CAB for the safe and ethical handling of biological tissue. PMHS specimens were screened for HIV, for Hepatitis B and C, and for pre-existing pathologies that may influence the cranial or intracranial properties.

Since the brain autolyzes more rapidly than other tissues and degenerates under freezing (Fountoulakis et al., 2001), a time limit was set, so all tests were performed within 72 hours after death with the tissue kept in a fresh (unfrozen and unembalmed) state. Pre-test radiographs were taken at the UVA-CAB using an on-site multi-planar StatScan X-ray system to screen the specimen for acute fractures or other pre-existing cephalus trauma that would exclude it from the study. The specimen was then prepared on-site, and the locations of all installed instrumentation and mounting hardware were documented using a CT scan. After the completion of testing, another CT scan was performed. The instrumentation and mounting hardware were then removed, and the head and brain were examined under dissection.

### **Specific PMHS Inclusion and Exclusion Criteria**

Exclusion criteria for the acquisition of the specimens included any factors that may compromise the anatomy or material properties of the skull or brain tissue. These criteria included diagnosed skull lesions or trauma, neurological disease, or neurological lesions. The medical history information provided by the donation source was also reviewed for common known risk factors for any diffuse disease of the brain that could alter brain function/structure such as sudden onset dementia, Alzheimer's disease, ischemic or

hemorrhagic cerebrovascular accidents, encephalopathy, and other degenerative nervous system diseases.

Specimens were selected per the final selection criteria below. In summary, the final priorities for specimen selection were (in this order):

1. Age ( $\leq 70$  years preferred) and any exclusion criteria (cause of death / pre-existing neurodegenerative conditions)
2. Stature - 172-180 cm preferred, though flexible to meet age and c.o.d. targets
3. Sex – male (female permissible if within stature target)

### **Specimen Information and Anthropometry**

Specimen acquisition occurred on an “on-call” basis, with the preparation, testing equipment, and personnel, ready when a specimen was available and passed all of the inclusion criteria and blood work. The specimens were unembalmed and never frozen. Since the goal was to complete all testing within 72 hours post-mortem (p.m.), specimens had to be acquired within 36 hours post-mortem to allow sufficient time for the preparation and experiments. The specimen was disarticulated through the T1 vertebral body before or shortly after delivery.

This chapter will include details from the first specimen (specimen 846) to highlight the acquisition and preparation procedure. Specimen 846 was a male specimen and was received 14 hours p.m. The donor was 53 years old at the time of death. Height and mass were 173 cm and 255 lbs., respectively. Cause of death was congestive heart failure. Preliminary planar X-ray imaging of the head revealed no abnormalities of the skull, and the brain was noted to be intact and in excellent condition (Figure 3-13). All serology tests (including quick-tests and laboratory-based tests) were non-reactive.

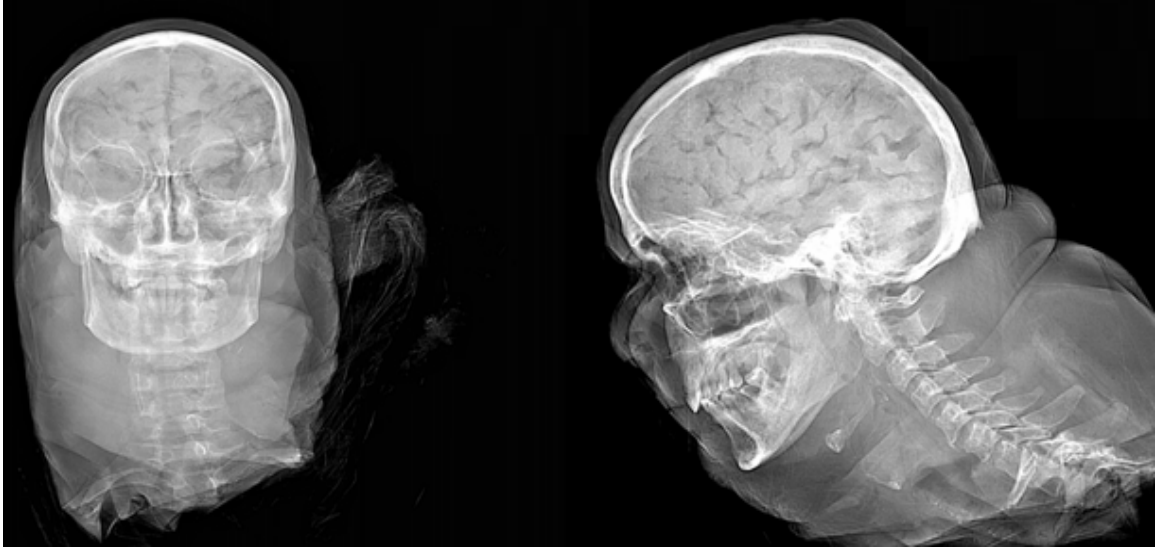


Figure 3-13: StatScan images of the head-neck specimen upon reception from the supplier. No skull abnormalities were revealed, and the brain was in excellent condition.

Relevant anthropometric measurements are included in Figure 3-14, and the measurements for the pilot specimen are provided in Chapter 4.

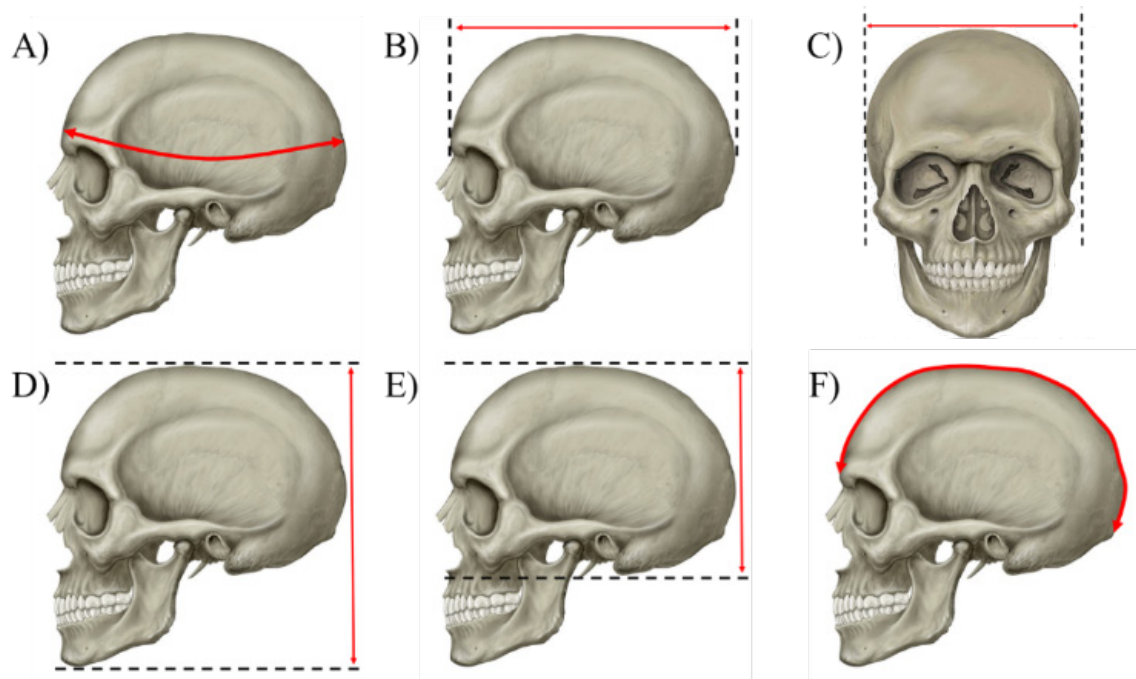


Figure 3-14: Anthropometric measurements of the skull. A) circumference, B) length (anterior-posterior), C) breadth (lateral-medial), D) height (vertex-mentum), E) height (vertex-occiput), F) brow-to-occiput arc length. Note: the measurements depicted in this figure were taken for both the head (before specimen preparation) and skull (after denuding).

## **SPECIMEN PREPARATION**

The overall goal of this study was to measure brain deformation under highly controlled loading conditions that could be readily repeated across specimens. As such, precision was required to ensure that specimen preparation was performed in a controlled manner relative to the center of gravity (CG) of the specimen's head. Specimen prep is summarized as follows:

1. Attachment of perfusion ports
2. Identification of head anatomical CG
3. Attachment of fixation plates
4. Instrumentation (sonomicrometry and pressure transducers)
5. Attachment of rotation coupling hardware

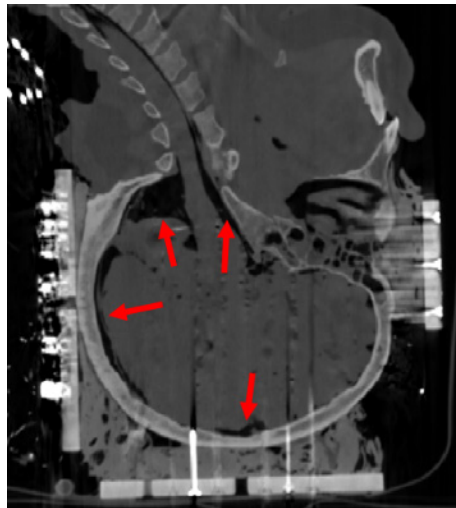
### **Perfusion System**

A perfusion system was designed to apply a static pressure head of artificial cerebrospinal fluid (aCSF) to the brain utilizing ports located at the left and right carotid arteries, left and right jugular veins, dura of the spinal cord, and transcranial ports at the sagittal sinus and occiput. These ports were allocated as either inlets or outlets (Table 3-1). The aCSF recipe was used by Sugawara et al. (1996)(Sugawara et al., 1996). CT imaging demonstrated that the cranial cavity was fully perfused with the proposed configuration (Figure 3-15). During testing, the specimen was continuously perfused with a static pressure head via a fluid reservoir hung approximately 102 cm above the specimen to achieve a target intracranial pressure of approximately 75 mmHg. As fluid drained from the specimen, it was collected in a catch basin underneath the specimen and recirculated to

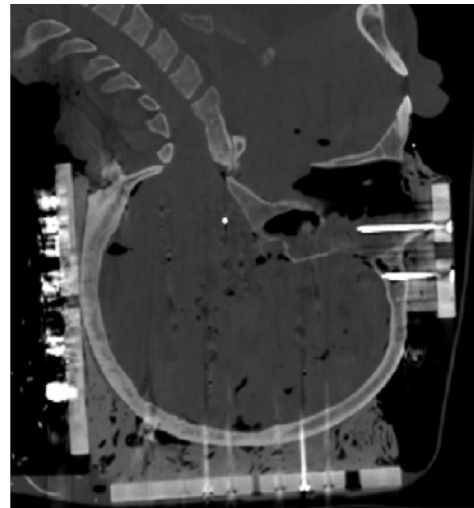
the overhead reservoir via a recirculating pump. Light perfusion was also applied during prep with refrigerated aCSF to maintain a low temperature within the specimen.

*Table 3-1: Perfusion port configurations. aCSF was introduced to the cranial cavity via inlets and drained via outlets.*

| Port Location                 | Inlet or Outlet |
|-------------------------------|-----------------|
| Carotid Arteries              | Inlet           |
| Jugular Veins                 | Outlet          |
| Spinal Cord                   | Outlet          |
| Sagittal Sinus (Transcranial) | Inlet           |
| Occiput (Transcranial)        | Inlet           |



No Perfusion



Perfusion

*Figure 3-15: Cranial cavity without (left) and with (right) aCSF perfusion. Red arrows show air pockets.*

### **Identification of Anatomical Center of Gravity**

The head CG was identified to ensure that rotation was applied through the anatomical CG with the axes of rotation oriented orthogonal to the principal anatomical planes of the head. The anatomical head CG was also used as the basis for the local head coordinate system to which all brain deformation and head kinematic data were transformed. A multi-

step process was utilized to identify the approximate anatomical CG (Figure 3-16), based on (Robbins et al., 1983).

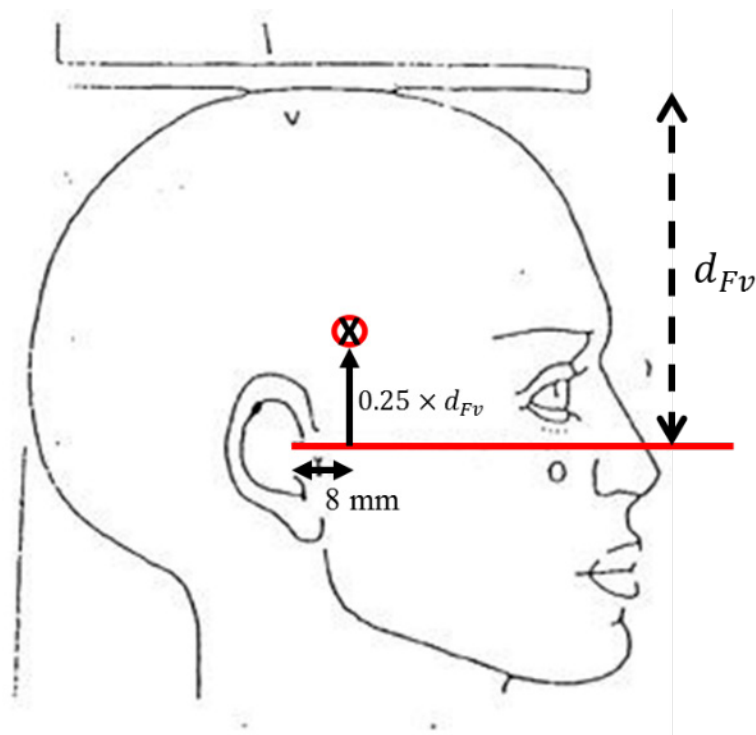


Figure 3-16: Identification of lateral anatomical center of gravity markers.

1. The Frankfort plane was identified by marking a line between the inferior margin of the orbit and the notch above the tragus.
2. The distance between the Frankfort plane and the vertex of the head was calculated.
3. The lateral CG marker was drawn 8 mm anterior to the tragus on the Frankfort plane, and 25% of the distance vertically from the Frankfort plane to the vertex.
4. The z-axis is identified to be perpendicular to the Frankfort plane, with the positive direction pointing from the CG to the neck.
5. The x-axis is identified to be perpendicular to the line connecting the left and right CG reference points, with the positive direction pointing from the CG to the face.

6. The y-axis is the cross product of the z and x axes, with positive direction pointing from the CG to the right ear.
7. Steps 1-3 were repeated on the opposite side of the head.
8. The posterior CG marker was defined at the midpoint of the circumferential line connecting the two lateral markers, parallel to the Frankfort plane.

### **Attachment of Fixation Plates**

After the anatomical CG was identified and marked, the skull was denuded by removing the head soft tissue from the nose to the occiput. Fixation plates were attached to the superior, lateral, and posterior surfaces of the skull. A custom built fixation jig was designed and assembled to ensure that all fixation plates were centered upon the desired axes of rotation (through the CG) and were orthogonal to each other (Figure 3-2). Mounting pins were used to align the skull CG within the jig (Figure 3-17) and a combination of Bondo and #6 size wood screws were used to rigidly couple the fixation plates to the skull. Wood screw lengths were carefully selected for each hole such that they would not penetrate the cranial cavity. Any wood screws that penetrate the cranium (checked during the pre-test CT scan) were removed or replaced with shorter screws.

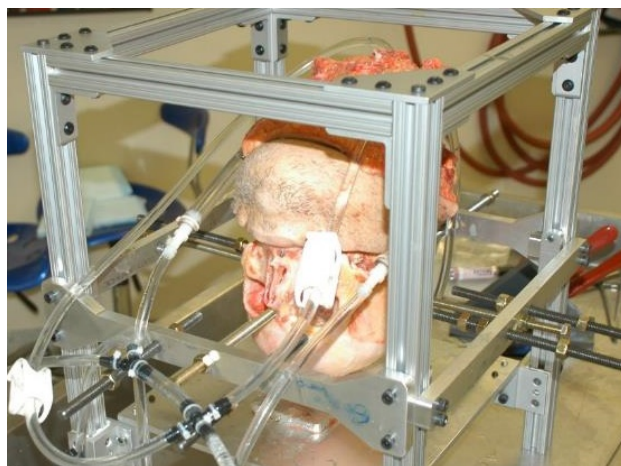


*Figure 3-17: Mounting pins were used to align the skull CG within the head preparation jig.*

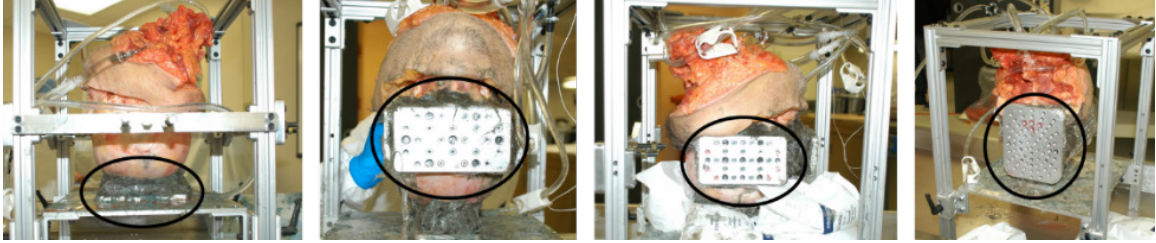


*Figure 3-18: Skull fixation plates. Left-to-right: superior, anterior, lateral (left and right), and posterior instrumentation plate.*

### **Sonomicrometry Crystal Insertion**

Following attachment of the posterior instrumentation insertion plate, sonomicrometry crystals were inserted into the brain using the procedure outlined in Figure 3-12. A total of 32 crystals was utilized in this pilot test, with transmitting crystals affixed to the inner skull and receiving crystals inserted in the brain tissue. Twenty-four receivers were inserted through twelve of the holes on the posterior guide plate (Figure 3-19). To introduce a crystal, the needle was first inserted into the cannula, and both pushed to the desired depth within the brain. Once all crystals were inserted, the ports were sealed using cord grips. Wire slack was intentionally introduced for each receiver to allow the crystals to move with the brain and not introduce any tethering effects.

The crystals inserted into the brain parenchyma were 2 mm in diameter and were barbed with thin pieces of monofilament wire. Eight transmitters were rigidly attached to the skull. M8-sized holes were drilled and tapped at the eight transmitter crystal locations. M8 cord grips were screwed into the holes, and the transmitters were passed through and secured using the cord grips. Care was taken to ensure that the transmitting crystals did not penetrate the dura or brain.

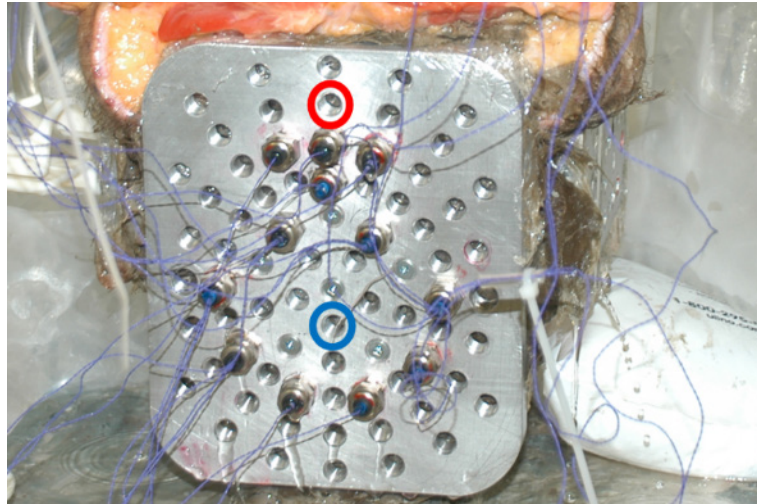


*Figure 3-19: Posterior instrumentation plate post-sonometric crystal insertion. The posterior transmitter was passed through the hole highlighted in red.*

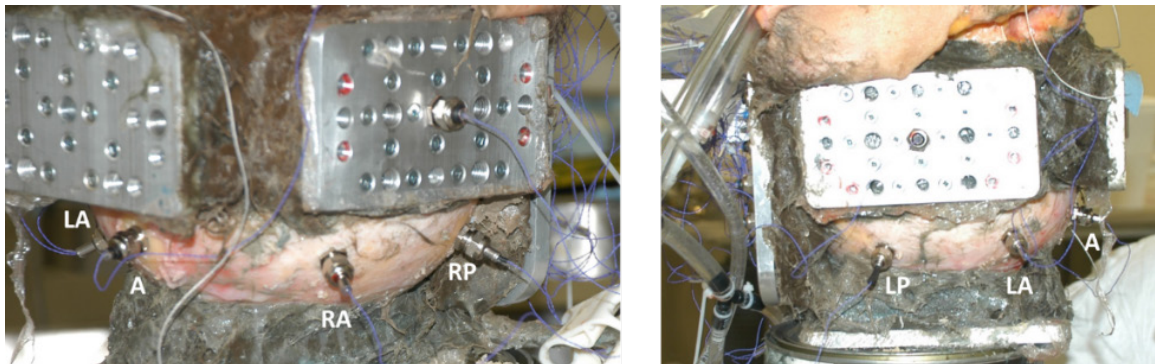


*Figure 3-20: Four skull mounted transmitting crystals. Shown are the left anterior (LA), anterior (A), right anterior (RA), right posterior (RP), left posterior (LP), and left anterior (LA) transmitters.*

The projection of all receiver crystals in the three anatomical planes is shown in Figure 3-21. Before testing, the signals from each receiver were qualitatively assessed to ensure functionality. During this process, it was discovered that the signals from five receivers (marked red, Figure 3-21) were excessively noisy for the pilot specimen. It was speculated that during the insertion process, these crystals or wires were damaged. Throughout data processing, the signals from these crystals were neglected. For future specimens, six extra receivers and two extra transmitters were placed in the brain and skull in the case that they

need to be swapped for non-functioning crystals. The positions of the eight transmitters projected to the three anatomical planes are depicted in Figure 3-22.

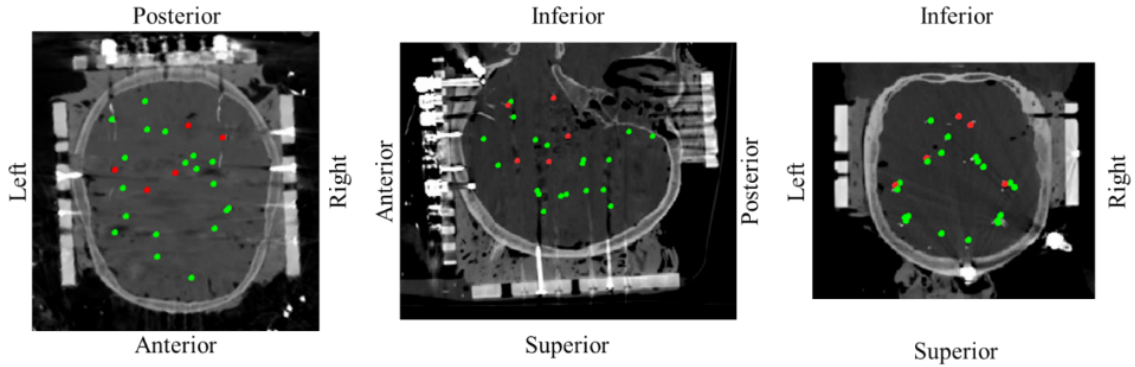


Figure 3-21: Receiver crystal projections in the three anatomical planes (left-to-right): axial, sagittal, coronal. Red dots indicate receivers that were unused due to damage to the crystal.

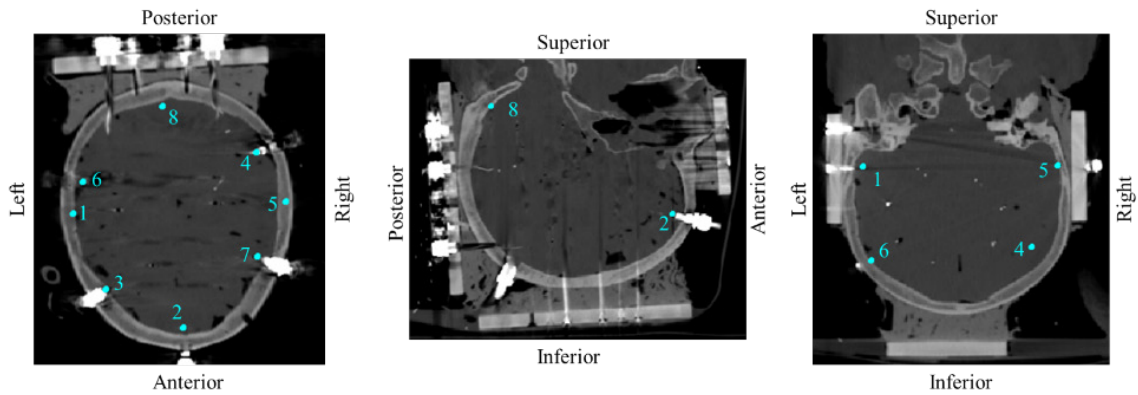
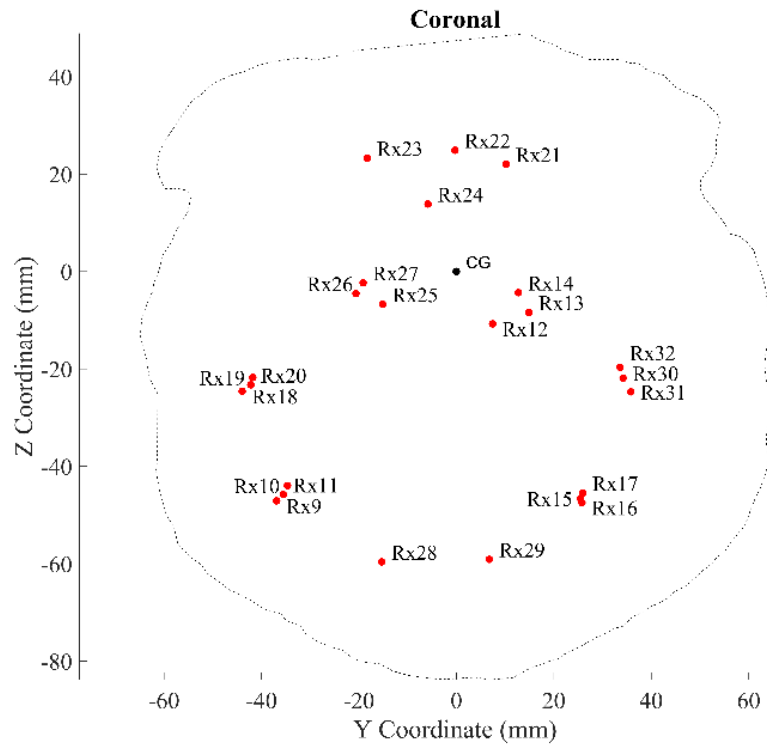
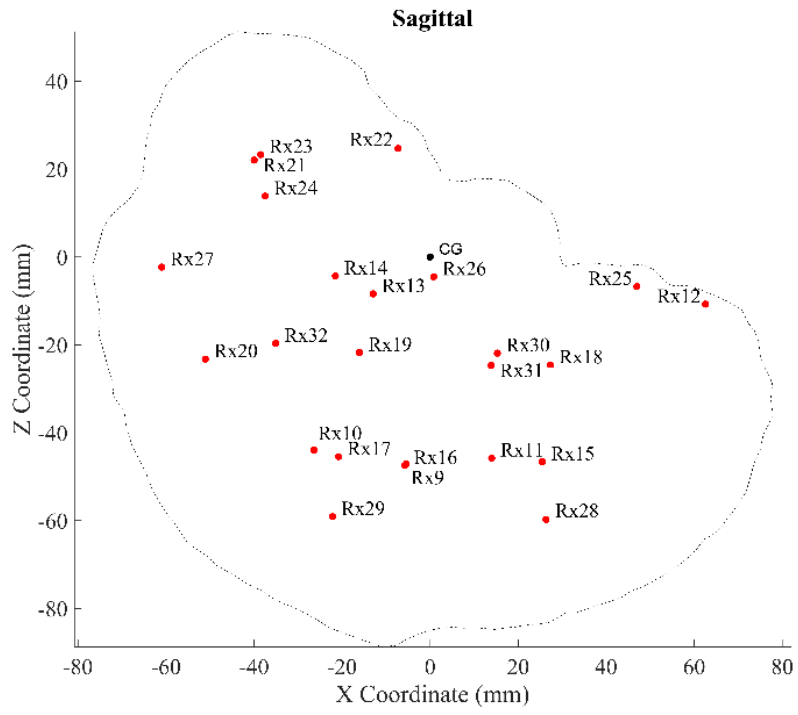


Figure 3-22: Transmitter crystal projections in the three anatomical planes (left-to-right): axial, sagittal, coronal.

The coordinates of each receiver, transformed to the head coordinate system, as determined from the pre-test CT scan, are shown projected to the anatomical planes in Figure 3-23. The head coordinate system for these measurements followed the SAE J211 (SAE, 2007) standard. Note that receivers were numbered from 9 – 32 according to which channel they were plugged into in the sonomicrometry data acquisition box.



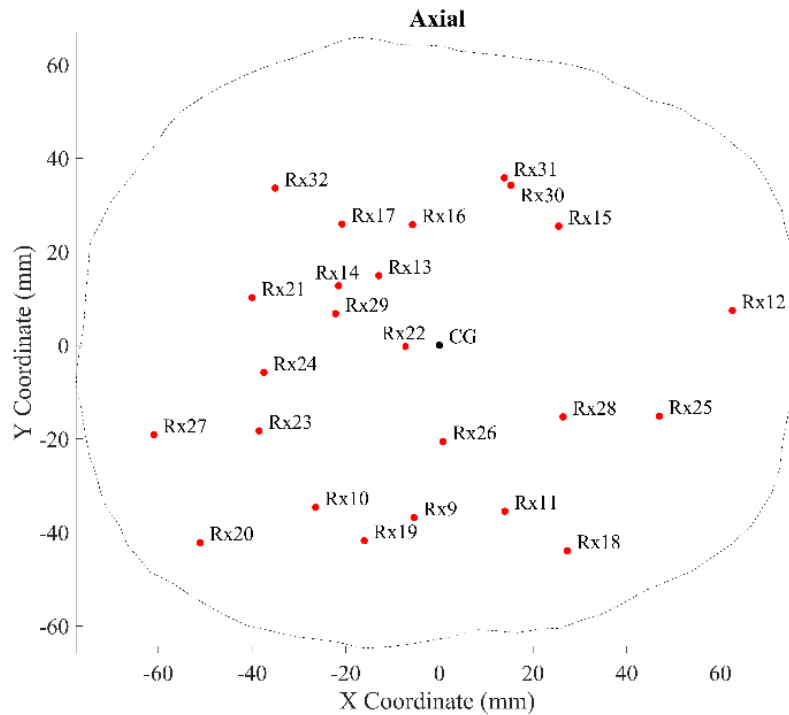
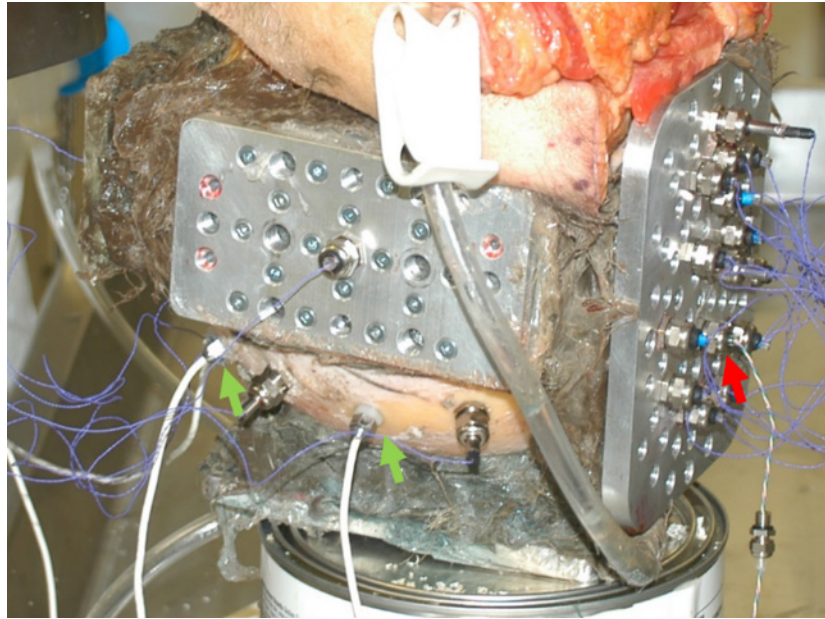


Figure 3-23: Receivers projected to the sagittal (top), coronal (mid), and axial (bottom) planes. All coordinates are in the head coordinate system.

### **Pressure Transducers**

Pressure transducers were used in the pilot specimen to confirm that the rotation of the brain causes significant deformation of the brain without causing a considerable magnitude of intra-cranial pressure. Two types of pressure transducers were utilized: Endevco 8530B (surface mounted) and MSI EBP-100 (suspended in the cranium). The surface mounted pressure transducers were screwed into manually drilled and tapped holes into the skull and sealed with silicone glue. The single MSI pressure transducer was passed through and fastened to an M8 cord grip screwed into a hole on the posterior fixation plate (Figure 3-19, Figure 3-24).



*Figure 3-24: Endevco, surface mounted, pressure transducers (green arrows) were attached directly to the skull. The MSI, suspended, pressure transducer (red arrow) was passed through an M8 cord grip on the posterior fixation plate.*

### **Attachment of Rotation Coupling Hardware**

The rotation coupling hardware (Figure 3-3) facilitated the attachment of the head specimen to the RTD (Figure 3-25). Note that the hardware was designed such that the head began initially inverted (perpendicular to the ground) for all rotation direction conditions.

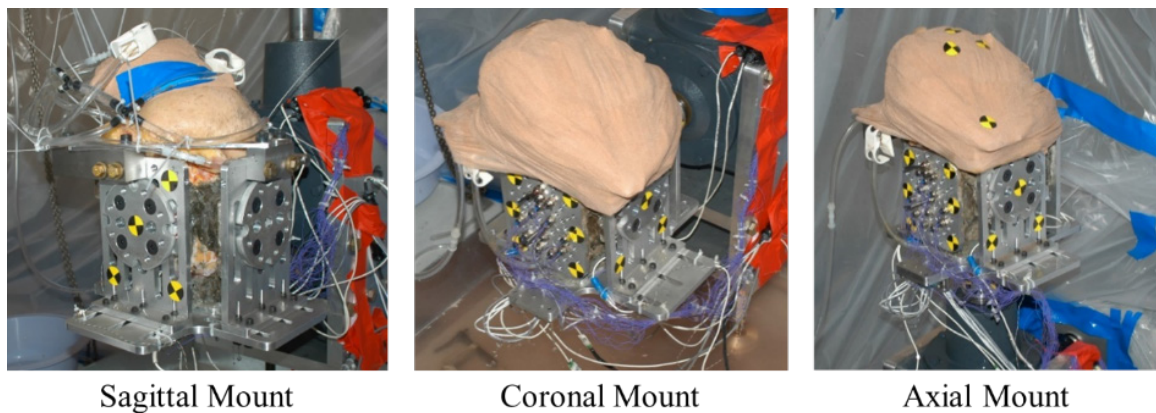


*Figure 3-25: Sagittal, coronal, and axial mounting configurations.*

## **Preparation and Testing Timeline**

Specimen preparation and testing for the pilot specimen was completed within 60 hours p.m., well within the goal of 72 hours. A post-test autopsy was conducted to investigate the specimen physically after each test, typically 6-8 days p.m.

## **INSTRUMENTATION**

### **Sonomicrometry**

Sonomicrometry data was recorded using a 32-channel TRX-USB Acquisition System (Sonometrics Corporation, London, Ontario, Canada). The associated SonoLab software was used to monitor and collect all crystal pair differences, and to set the acquisition parameters. Data were collected from 50 ms before to 500 ms after the trigger signal and were collected at a sampling rate of 560 Hz for the sagittal and coronal rotations, and a rate of 709 Hz for the axial rotations. Before and after each test, static sonomicrometry data was collected to confirm that all receivers returned to their original position and that the crystals did not damage the brain tissue during testing or slip out of position.

### **Kinematic Measurements**

Six degree-of-freedom (DOF) head kinematic measurements were acquired using a sensor array consisting of three Endevco 7264B-500 linear accelerometers (Meggitt Sensing Systems, Irvine, CA) and three ARS PRO-8k angular rate sensors (Diversified Technical Systems Inc., Seal Beach, CA), which was rigidly mounted to the head. An angular rate sensor was mounted to the drive drum for system diagnostic purposes. A SlicePRO data acquisition system (Diversified Technical Systems Inc., Seal Beach, CA) was used to acquire the data at a sampling rate of 10 kHz with an anti-aliasing filter of 2900 Hz. A summary of the kinematic instrument list is in Table 3-2.

Table 3-2: Head kinematic sensor list

| CHANNEL | MEASURAND           | UNITS | SENSOR LOCATION | MANUFACTURER | MODEL #   |
|---------|---------------------|-------|-----------------|--------------|-----------|
| 1       | Linear Acceleration | g's   | Head fixture    | Endevco      | 7264B-500 |
| 2       | Linear Acceleration | g's   | Head fixture    | Endevco      | 7264B-500 |
| 3       | Linear Acceleration | g's   | Head fixture    | Endevco      | 7264B-500 |
| 4       | Angular Velocity    | rad/s | Head fixture    | DTS          | ARS-8K    |
| 5       | Angular Velocity    | rad/s | Head fixture    | DTS          | ARS-8K    |
| 6       | Angular Velocity    | rad/s | Head fixture    | DTS          | ARS-8K    |
| 10      | Angular Velocity    | rad/s | RTD Drum        | DTS          | ARS-8k    |

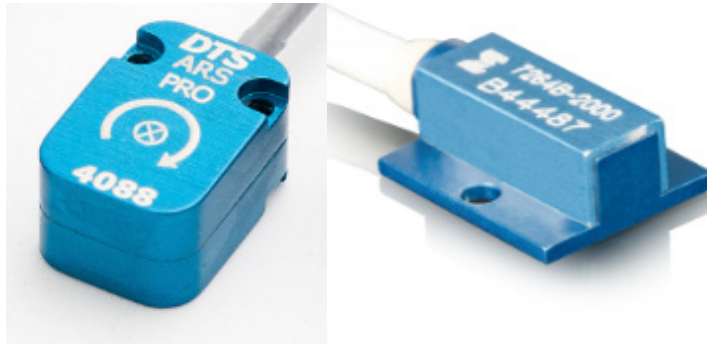


Figure 3-26: The sensors affixed to the head fixture and RTD include: DTS ARS-8k (left), Endevco 7264B-500 (right).

### **Pressure Measurements**

Intracranial pressure was measured using five surface-mounted pressure transducers fixed to the skull and two insertable pressure transducers suspended in the cranial cavity (Table 3-3).

The pressure transducer measurements were collected with the same data acquisition system and parameters as the kinematic measurements. The pressure transducers were automatically debiased to 0 psi during diagnostics after already being inserted in the perfused head.

Table 3-3: Pressure sensor list

| Channel | Measurand | Units | Manufacturer | Model # |
|---------|-----------|-------|--------------|---------|
| 11      | Pressure  | psi   | Endevco      | 8530B   |
| 12      | Pressure  | psi   | Endevco      | 8530B   |
| 14      | Pressure  | psi   | Endevco      | 8530B   |
| 15      | Pressure  | psi   | Endevco      | 8530B   |
| 17      | Pressure  | psi   | MSI          | EPB-100 |



Figure 3-27: The pressure transducers used in the head included: Endevco 8530B (left) and MSI EPB-100 (right).

### **High-Speed Video**

High-speed video was obtained using a NAC MEMRECAM GX1 monochromatic cameras (NAC Image Technology, CA, USA). The camera was placed orthogonal to the through-shaft of the RTD to capture head sagittal and coronal rotations. The video was collected at 1000 frames per second for a period of 50 ms before to 250 ms after the onset of the rotation pulse.

A trigger output from the DSD was used to trigger data acquisition, video capture, and sonomicrometry data. A custom made trigger box was used to send signals to SlicePro, the camera, and the sonomicrometry device simultaneously.

## DATA ANALYSIS

### Sonomicrometry

Data for each transmitter to receiver crystal pair was visualized and processed with SonoSOFT software (Sonometrics Corporation, London, Ontario, Canada). In total, for eight transmitter crystals and 24 receiving crystals, there are 192 possible distance traces for each test. The data is trimmed to the proper time range and manually examined for artifacts and signal error. The largest source of error sonomicrometry is noise in the form of outliers or level shifts (Figure 3-28). A processing method recommended by the manufacturer was used to correct both of these artifacts for each data channel.

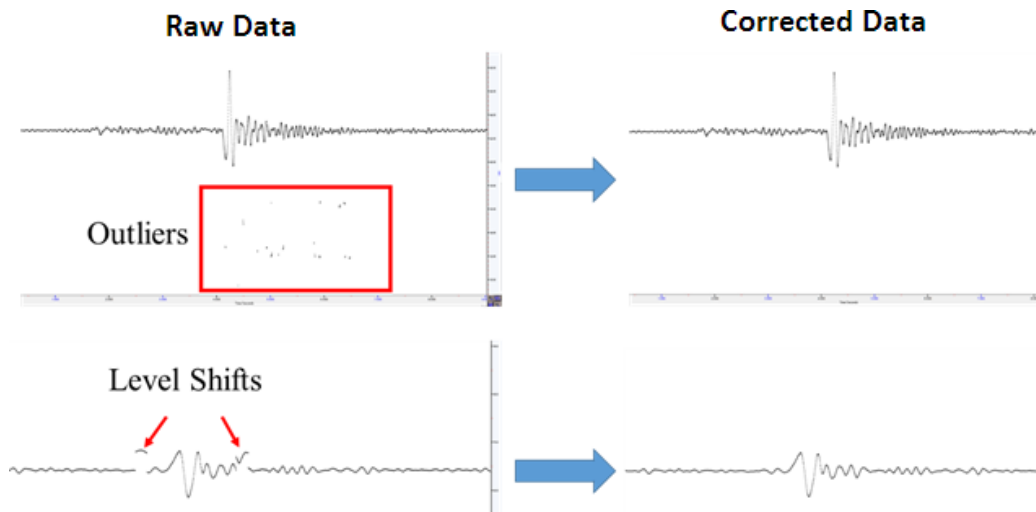


*Figure 3-28: Outliers (top) and level shifts (bottom) in raw (left) and corrected (right) distance traces. Outliers were removed, and level shifts were corrected by manually shifting the data.*

In several cases, the distance traces were either too noisy or not available because the transmitted pulse was not received (this was expected for transmitter-receiver pairs that exceeded the maximum distance previously determined). These traces were marked as “bad” and not considered for trilateration (Figure 3-29).

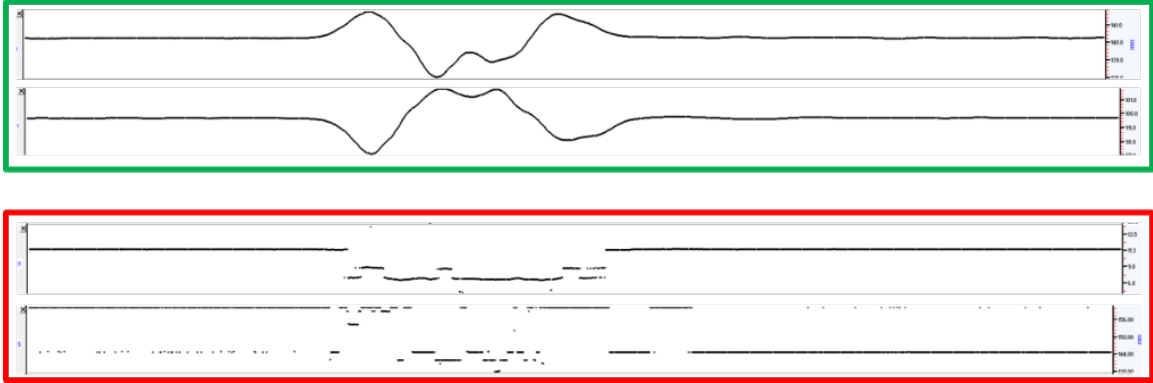


Figure 3-29: “Good” (top, green) and “bad” (bottom, red) traces. Bad traces were omitted when performing trilateration.

Once the data was processed and all “good” traces were identified, trilateration was utilized to determine the 3D coordinate time-history of each receiver crystal relative to the reference frame defined by the fixed transmitting crystals. Trilateration uses the geometry of spheres to determine the absolute location of a point based on distance measurements. The speed of sound was defined as 1540 m/s for all computations. This value was found by optimizing the static sonomicrometry distances measured at the beginning of testing to those observed from CT images. This value is consistent with the speed of sound values reported in the literature for brain tissue (Kremkau et al., 1981).

In preliminary work, the software package SonoXYZ (SonoXYZ, Sonometrics Corporation, London, Ontario, Canada) was used for the trilateration of receiving crystals (Alshareef et al., 2018). This software uses a multidimensional scaling algorithm to optimize the calculated crystal coordinates based on the measured distances, with an internal optimization routine to incorporate redundant information (i.e., when more than three signals are available for a receiver). The algorithm, however, was developed for cardiac biomechanics experiments and was not suitable for the brain deformation dataset as a result of different assumptions and boundary conditions. An investigation into various

trilateration algorithms is presented in Chapter 4, to identify the most suitable algorithm for brain deformation sonomicrometry experiments. The specific application of the identified algorithm to the brain deformation dataset is presented in Chapter 5.

### **Kinematic Measurements**

The head kinematics data were processed in MATLAB using a custom script. The data were imported and de-biased by subtracting the average of the first 50 pre-trigger points. All data were transformed to the local head coordinate system as defined by SAE J211 (SAE, 2007) standard. The linear acceleration was filtered with a CFC 1000 filter, and the angular velocity was filtered with a CFC 60 filter. Angular acceleration was calculated by differentiating the filtered angular velocity data using a central difference with a time step equal to that of the sampling rate.

The data was transformed to the CG of the head, as defined anatomically using the rectangular fixation plates during the preparation procedure. The procedure is as follows:

- 1- The linear acceleration of the 6 DOF cube was converted to units of  $m/s^2$  and was then transformed to the center of the cube by accounting for the off-axis angular velocities.
- 2- The 6 DOF cube was affixed to an instrumentation plate, located on the outside of the head fixture. A transformation matrix,  $\mathbf{P}$ , was computed to transform the kinematic data from the 6 DOF cube to a common point on the instrumentation plate.
- 3- To transform the data from the instrumentation plate to the head CG, a ROMER Arm was used to measure points outlining the left, right, and anterior linkage plates and the points outlining the position of the instrumentation plate. The head CG was

determined as the intersection between the normal vector of the anterior plate midpoint and the vector connecting the midpoints of the left and right linkage plates. In this global ROMER Arm coordinate system, a transformation matrix was computed defining the head coordinate system at the head CG,  $\mathbf{K}$ , and the common point on the instrumentation plate,  $\mathbf{B}$ . The final transformation matrix to transform data from the cube center to the head CG is defined as  $\mathbf{M} = \mathbf{K}^{-1} * \mathbf{B} * \mathbf{P}$ . The following matrices are an example for the pilot specimen, 846.

$$\mathbf{P} = \begin{bmatrix} -1 & 0 & 0 & 0.0152 \\ 0 & -1 & 0 & 0.0152 \\ 0 & 0 & 1 & -0.0197 \\ 0 & 0 & 0 & 1 \end{bmatrix}$$

$$\mathbf{B} = \begin{bmatrix} 0.0118 & 0.0114 & 0.999 & -0.0155 \\ -0.7645 & 0.6447 & 0.0017 & 0.2641 \\ -0.6446 & -0.7644 & 0.0163 & 0.9082 \\ 0 & 0 & 0 & 1 \end{bmatrix}$$

$$\mathbf{K} = \begin{bmatrix} 0.0236 & -0.0008 & 0.9997 & 0.1067 \\ -0.7616 & 0.6477 & 0.0185 & 0.1842 \\ -0.6476 & -0.7619 & 0.0147 & 0.7907 \\ 0 & 0 & 0 & 1 \end{bmatrix}$$

$$\mathbf{M} = \begin{bmatrix} -0.999 & -0.004 & 0.012 & -0.1245 \\ 0.004 & -0.999 & -0.012 & -0.0222 \\ 0.012 & -0.012 & 0.999 & -0.1387 \\ 0 & 0 & 0 & 1 \end{bmatrix}$$

- 4- The data was transformed by first transforming the angular velocity, angular acceleration, and linear acceleration using the 3x3 rotational component of  $\mathbf{M}$ ,  $\mathbf{M}_R$ . The linear acceleration data was then calculated using rigid body motion equations using the 3x1 translational component of  $\mathbf{M}$ ,  $\mathbf{M}_x$ .

$$a_{head} = \mathbf{M}_R * a_{cube}$$

$$\omega_{head} = \mathbf{M}_R * \omega_{cube}$$

$$\alpha_{head} = \mathbf{M}_R * \alpha_{cube}$$

$$a_{head} = a_{cube} - \omega_{head} \times (\omega_{head} \times \mathbf{M}_x) - \alpha_{head} \times \mathbf{M}_x$$

## **Statistical Methods**

Repeatability and comparisons between signals were assessed using a cross-correlation analysis tool (CORA) (Gehre et al., 2009) which scores the similarity of two signals based on phase, shape, and magnitude (equally weighted). A perfect correlation (i.e., two equal signals) results in a score of 1, which a score of 0 corresponds to a bad match between the two signals. A root mean squared (RMS) difference was also calculated for the repeatability of the applied head kinematics.

## **TARGET TEST MATRIX**

Tests were performed by applying pure rotational kinematics directly to the specimen's head about the three orthogonal axes defined by the local head coordinate system. The target rotational velocity pulses were approximately sinusoidal, with four different combinations of pulse magnitude (20 and 40 rad/s) and duration (30 and 60 ms). The pulses were chosen to reflect magnitudes and duration associated with injurious brain deformation in automotive impact environments, resulting in twelve test conditions, consisting of three directions and four pulses. For the current chapter, which only includes a pilot specimen, a single specimen was tested in all 12 test conditions (Table 3-4). Following positive results in the first set of tests, it was decided to perform repeats of each of the 40 rad/s, 30 ms tests to observe repeatability.

Table 3-4: Target Test Condition Matrix\*

|   | Plane    | Magnitude | Duration | Test Number |
|---|----------|-----------|----------|-------------|
|  | Sagittal | 20 rad/s  | 60 ms    | 1           |
|   |          |           | 30 ms    | 2           |
|   |          | 40 rad/s  | 60 ms    | 3           |
|   |          |           | 30 ms    | 4           |
|  | Coronal  | 20 rad/s  | 60 ms    | 5           |
|   |          |           | 30 ms    | 6           |
|   |          | 40 rad/s  | 60 ms    | 7           |
|   |          |           | 30 ms    | 8           |
|  | Axial    | 20 rad/s  | 60 ms    | 9           |
|   |          |           | 30 ms    | 10          |
|   |          | 40 rad/s  | 60 ms    | 11          |
|   |          |           | 30 ms    | 12          |

\* Note: Following positive results in the first set of tests, repeats of each of the 40 rad/s, 30 ms tests in the pilot specimen were performed to observe repeatability.

## RESULTS

All preparation and testing of the pilot PMHS specimen were completed within 56 hours post mortem. The static sonomicrometry data was used to calculate the difference in transmitter-receiver pair distances before and after every test to ensure that the crystals returned to their initial state. On average, all crystal pairs returned to a position measuring within  $0.075 \pm 0.032$  mm of the pre-test distance. The following results include data from pilot specimen to highlight aspects of the methodology. All other data and summary analyses are presented in Chapter 5.

### Head Kinematics

There were minimal linear acceleration and off-axis rotation of the head for all loading severities. The angular velocity and angular acceleration traces for the primary plane of rotation for all of the loading cases are shown in Figure 3-30. The average CORA

score for the repeated tests was 0.93 with a standard deviation of 0.05. The root mean squared differences for those applied angular velocities was  $1.3 \text{ rad/s} \pm 0.68 \text{ rad/s}$  for the 40 rad/s (nominal) tests. The angular velocity pulses for the axial rotations are depicted in Figure 3-30.

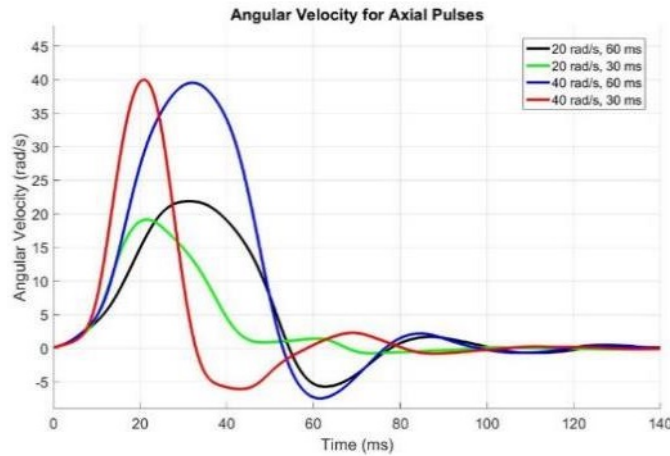


Figure 3-30: Angular velocity for the four cases of the test matrix for the axial head rotations.

Plots of the 6DOF kinematics for the sagittal 20 rad/s, 60 ms test tests, including linear acceleration, angular velocity, and angular acceleration transformed to the local head coordinate system is shown in Figure 3-31.

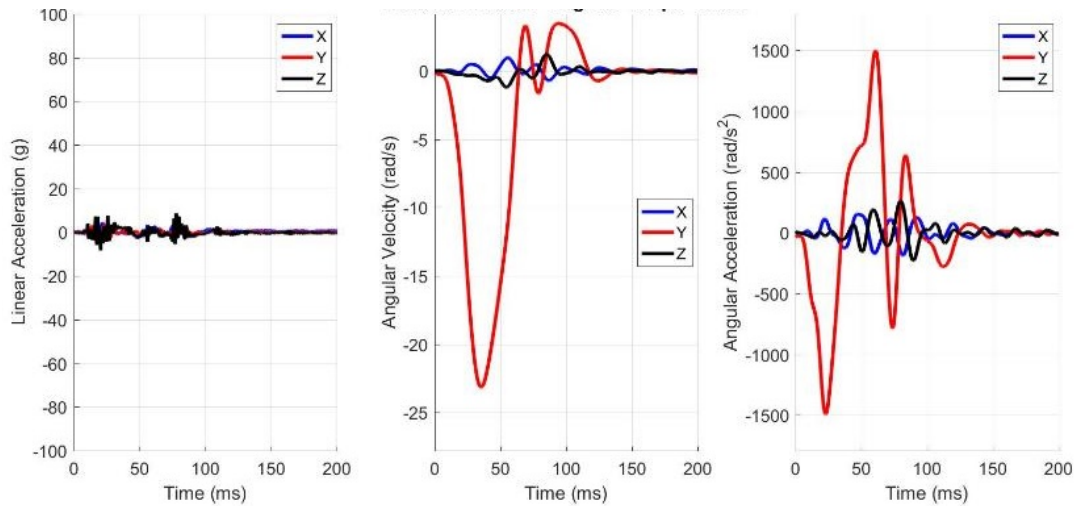


Figure 3-31: Six degree of freedom linear acceleration (left), angular velocity (middle), and angular acceleration (right) transformed to the local head coordinate system for specimen 846 for the sagittal 20 rad/s, 30 ms case.

## Intra-Cranial Pressure

Plots of intra-cranial pressure measurements for the sagittal tests for the pilot specimen presented in Figure 3-32. Pressure changes observed in the first specimen were negligible (less than 20 kPa) regardless of rotation severity. Pressure transducers were also used in the second specimen (Chapter 5) but were omitted in subsequent tests due to insignificant magnitudes of pressure.

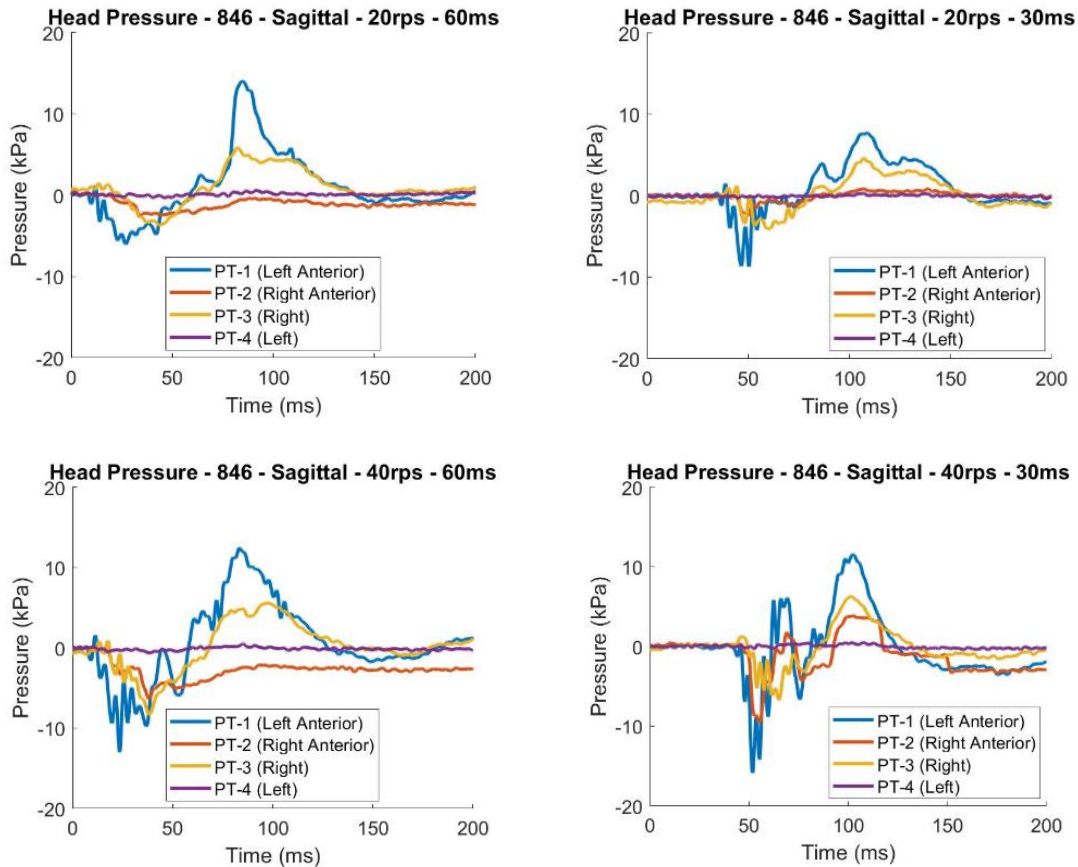
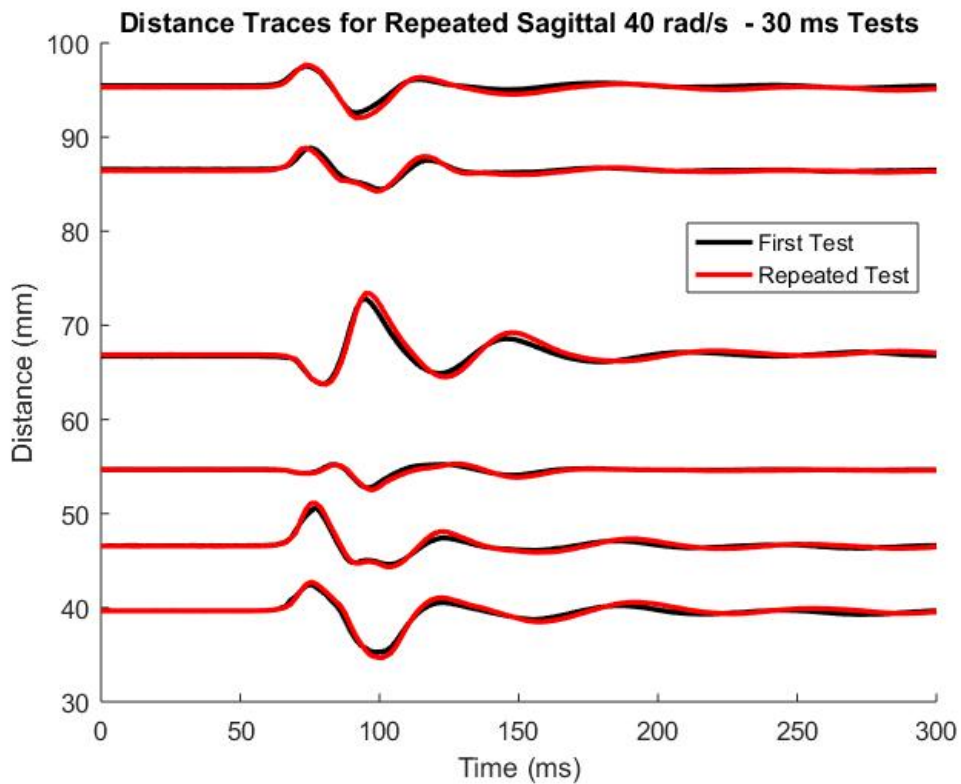


Figure 3-32: Intra-cranial pressure measurements for all sagittal cases for specimen 846.

## Sonomicrometry

The initial coordinates for each receiver and transmitter were obtained from the CT images and transformed to the head coordinate system following sonomicrometry instrumentation. During insertion, receivers 19, 21, 22, 26, and 32 were damaged, and

signals obtained from these receivers were unusable, yielding a total of 19 usable receivers. Figure 3-23 shows the positions of each receiver projected to the three anatomical planes. Select processed distance-time histories are shown for illustration in Figure 3-33 for the repeated 40 rad/s, 30 ms tests in all three directions. The average CORA score for the repeatability of the crystal responses was  $0.999 \pm 0.001$ .



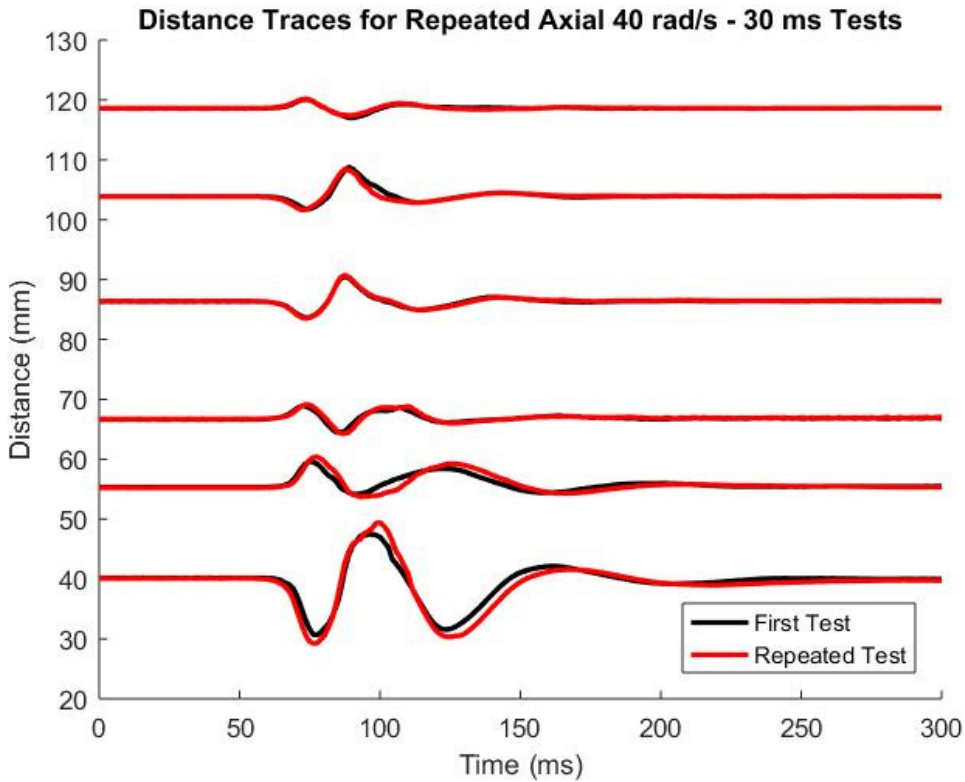
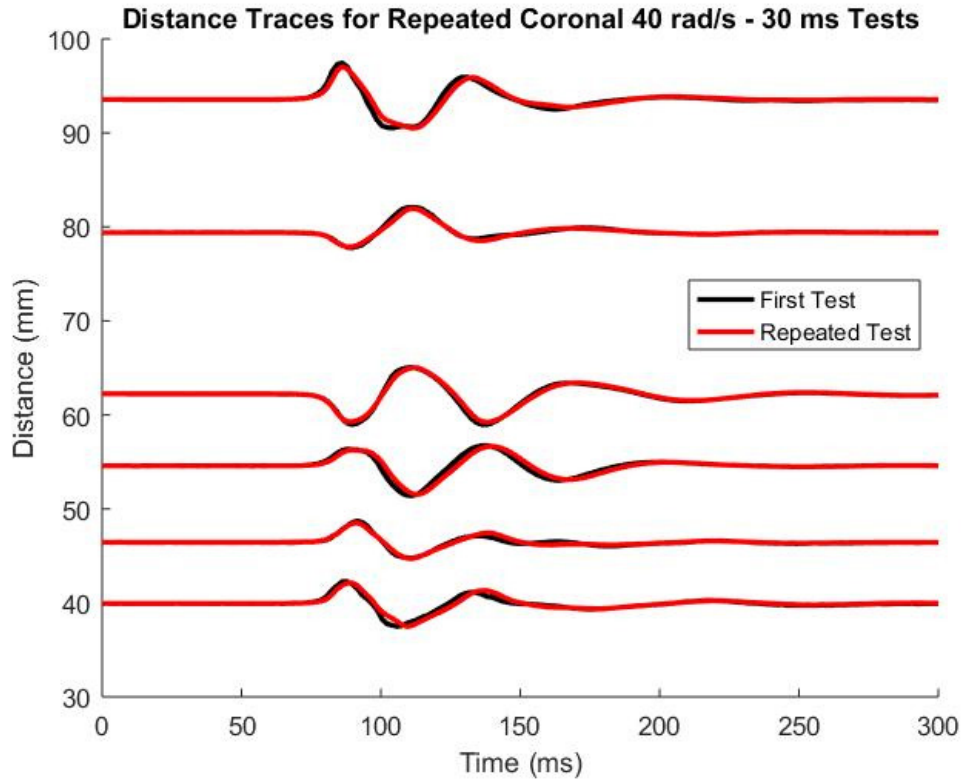


Figure 3-33: Select distance traces for the repeated axial 40 rad/s, 30 m/s pulses.

Trilateration was used to calculate the 3D displacement-time histories for each receiver. Crystal trajectories in the coronal plane during each coronal test are shown in Figure 3-34. Figure 3-35 depicts the trilaterated displacement plots for receivers 9, 16, and 13 for each coronal test.

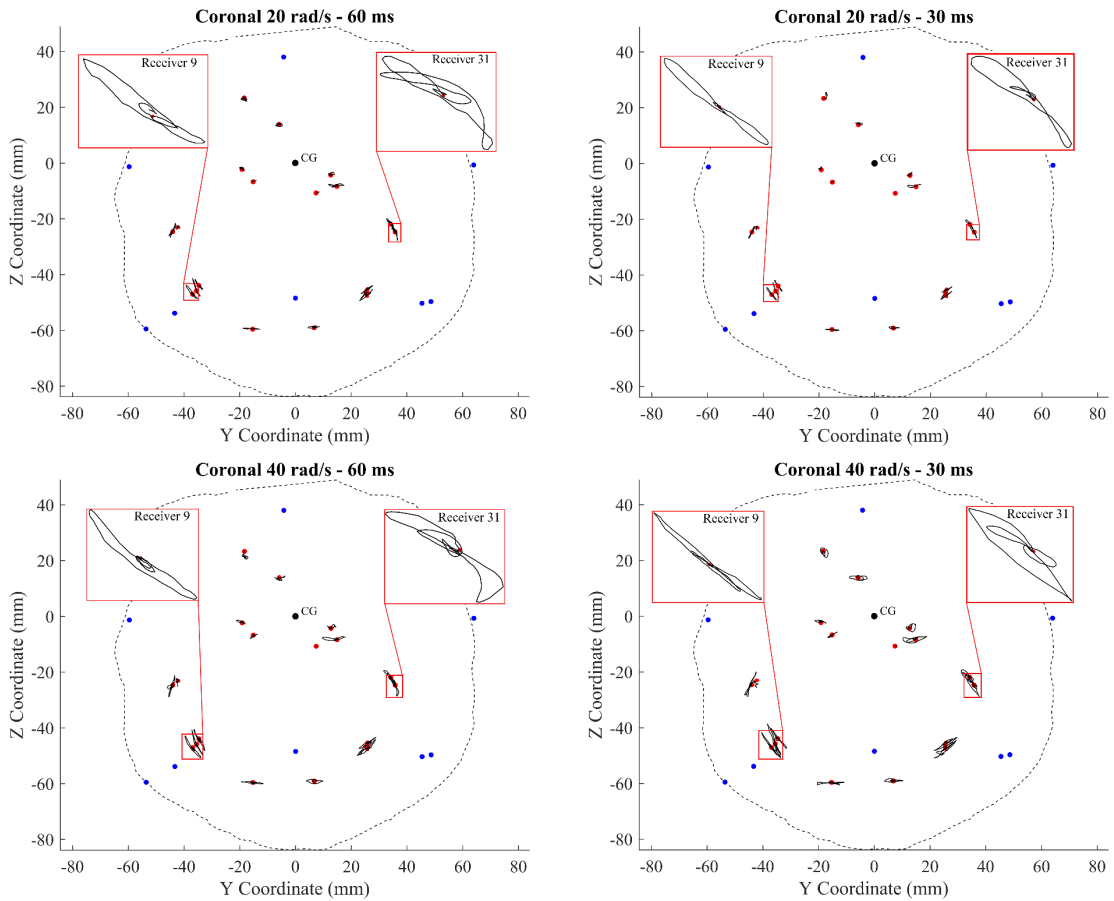


Figure 3-34: Trilaterated receiver trajectories in the coronal plane for the coronal tests. Dots indicate the initial receiver and transmitter positions. A detailed view of receivers 9 and 31 are shown on the top.

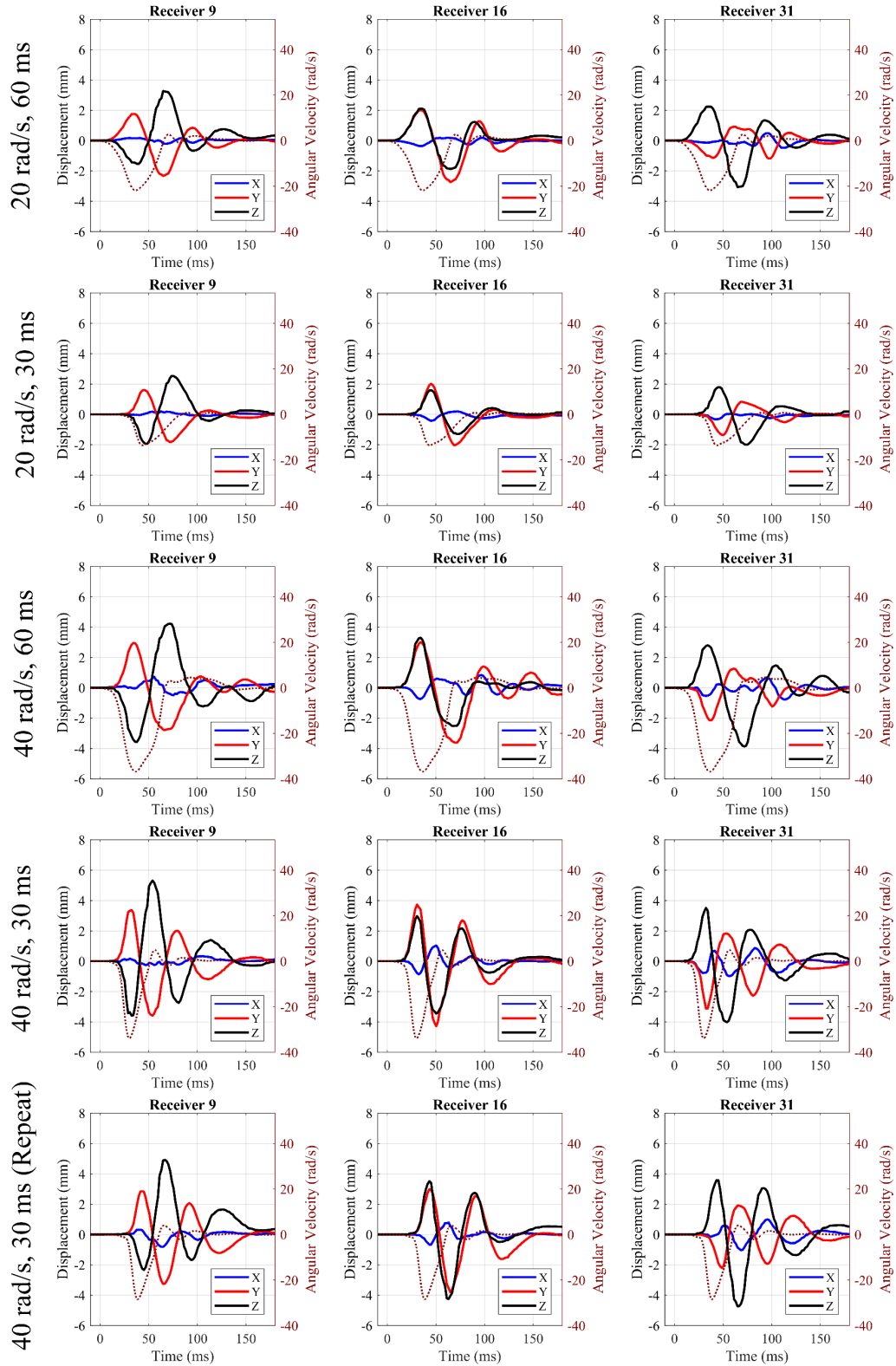


Figure 3-35: Trilaterated displacement results for receivers 9, 16, and 31 for the coronal tests. The applied angular velocity pulses (dashed line) are overlaid.

## DISCUSSION

A reliable and repeatable methodology to measure human brain deformation is essential to understanding the biomechanics of the brain and validating FE brain models. In this chapter, a new methodology using sonomicrometry has been developed for quantifying dynamic, 3D brain deformation during rotational loading of the head. This study is the first to capture whole brain deformation fields due to controlled, pure rotational loading in multiple directions using a human PMHS specimen. While brain deformations at injurious levels have been quantified in the past using bi-planar X-ray, the sonomicrometry method presents substantial improvements.

The primary disadvantage of bi-planar X-ray is the requirement for constant line-of-sight of the embedded NDT. Not only does this have implications on mounting hardware and test fixture design, but also on the number and placement of the NDTs throughout the brain. As such, only a planar alignment or regional cluster of all NDTs can be used in bi-planar X-ray tests and specific NDT configurations are required for each direction of rotation or impact. Therefore, the utility of each specimen is limited. Sonomicrometry is capable of measuring brain deformation without these line-of-sight limitations. Provided that the sonomicrometry crystals can communicate with one another, a large number of them can be distributed in multiple, overlapping planes throughout the brain volume facilitating the mapping of 3D whole brain deformation. There is no line-of-sight limitation with the fixation hardware. The use of sonomicrometry does not impose constraints on the loading conditions and ensuing head trajectories, as long as there is enough slack in the crystal wires to remain plugged into the data acquisition system. The ability to test in all directions increases the utility of each specimen, reducing the cost and time needed to

obtain the 3D experimental data required to develop model validation targets. Furthermore, sonomicrometry is an improvement on the spatial accuracy of the displacement measurements and is not subject to limitations with camera resolution, image distortion, parallax, and errors encountered in coordinate system transformation.

In the pilot study, a total of 15 tests in three directions were performed on a single specimen, spanning a range of angular velocities and durations. The rotational pulses applied to the head-neck specimen were informed by work done by Gabler et al. (Gabler et al., 2017), which examined brain deformation from nearly 1000 reconstructed sled and crash tests using a human finite element brain model. The reconstructed cases span a range of plausible head kinematics, from non-injury to concussion to moderate and severe TBI, based on kinematic injury criteria (Rowson and Duma, 2013; Takhounts et al., 2013a; Gabler et al., 2016a, 2017; Sanchez et al., 2017). Gabler et al. found that in most real-world impact environments, maximum brain deformation depends on the magnitude of angular velocity and angular acceleration (or rotation duration). From the deformation profiles, two peak angular velocities (20 and 40 rad/s) and two impact durations (30 and 60 ms) were chosen to cover loading conditions observed in automotive and sports impacts associated with mild-to-moderate risk of injury.

Experiments seeking to produce reference data for FE model validation should use well-controlled, repeatable input conditions that are readily implementable in FE models. Results from inconsistent loading conditions (e.g., impactor tests where the pulse is dependent on the mechanical behavior of the specimen) using multiple specimens cannot be readily combined into an average dataset. The RTD was designed to apply pure, controlled, and repeatable rotational motion directly to the skull with the intent of

comparing the biomechanics across different PMHS. A cross-correlation analysis of the repeat kinematic traces using CORA (Gehre et al., 2009) found a score of  $0.93 \pm 0.05$ , showing excellent repeatability of the RTD input kinematics. A root mean squared difference across time for the repeated pulses in all directions yielded an average of 1.3 rad/s  $\pm$  0.68 rad/s for the 40 rad/s tests. While the motion was constrained to the rotation in one direction, the system is a physical one with eccentricities, including the neck mass (with inconsistent inertias for each specimen and each loading direction) and an estimated axis of rotation of the head-neck specimen, that lead to off-axis loads and small linear accelerations. The off-axis rotations were 3-12% of the maximum angular velocity in the primary loading directions (an average of 6.75%). Linear acceleration time-histories contained noise spikes reaching up to 100g. However, since these linear accelerations occurred over small durations (1-2ms), and when filtered at an appropriate frequency (300 Hz), the magnitude of linear accelerations was below 15g for all tests.

For all static data acquired before and after tests, the receivers returned to within  $0.075 \pm 0.032$  mm of their original location. This result indicates two key findings. First, the sonomicrometry crystals did not slip relative to the surrounding tissue they were embedded in, and thus were representative of the displacement of the surrounding tissue. This finding also validates the crystal insertion methodology, which allowed for significant slack in the wires connected to the crystals to allow for freedom of movement with the brain. If tethering had occurred due to the wires, the crystals would slip relative to the brain and not return to the original position. Second, the loading conditions applied to the PMHS head, although at potentially injurious levels, did not result in gross structural damage to the parenchyma or supporting tissues. This lack of damage confirms that the cadaveric tissue

integrity remained intact throughout testing and that the techniques used to embed the crystals did not result in a loss of brain elasticity. It is important to clarify that the lack of structural damage does not necessarily mean that these loading conditions would not result in physiological brain injury in a living human. Mild TBI injuries typically present without observable physical damage or gross tissue disruption (Gennarelli et al., 1972).

The return of the crystals to their original position allowed for the testing of multiple rotation severities in all three planes, indicating the tissue was not damaged, and each test began with the same initial brain position. A second 40 rad/s, 30 ms test was conducted for each axis of rotation to assess the repeatability of the proposed test conditions and sonomicrometry methods. Excellent repeatability, with an average CORA cross-correlation score of  $0.999 \pm 0.001$ , was observed in the distance measurements and both sets of results were nearly identical in shape, phase, and magnitude (Figure 3-33). This repeatability also translated to the trilaterated displacements and receiver trajectories (Figure 3-35).

Trilateration was used to determine three dimensional displacement time histories for each receiver. While the algorithm provided excellent results for most tests (Figure 3-35 and Figure 3-34), there were one or two cases where the trilateration solution failed to converge properly despite the availability of good distance traces for that receiver. This uncertainty was evident when the final trilaterated displacement did not return to its original position ( $\sim 0$  mm) despite that the individual distance traces between pairs of sensors returned to zero. These errors are likely indicative of a limitation in the trilateration algorithms utilized in the SonoXYZ software for this particular application of the sonomicrometry instrumentation. A more robust trilateration methodology was

investigated in Chapter 4, and the data from the pilot specimen were re-analyzed using the updated algorithm in Chapter 5.

Three-dimensional whole brain deformation data is critical for understanding the fundamental mechanical response of the brain. A diffuse array of crystals in the brain allows for the quantification of parameters describing the motion of individual crystals, such as peak-to-peak displacement, duration, and frequency of the transient motion, and the lag time between the head and brain motions as well as regionally-dependent trends. The ability to test one head in all directions and loading severities also allows for comparisons of these parameters for the same crystals across head angular velocity magnitude, duration, and direction of head motion without preparation or specimen variability. For example, peak-to-peak displacements, defined as the maximum point-to-point displacement during the trajectory of each crystal, as large as 11, 12, and 23 mm were observed in the coronal, sagittal, and axial tests, respectively. The transient response of the brain was observed to last between 100 – 200 ms after the initiation of rotation, suggesting a mechanical vulnerability of the brain to additional superimposed loading. The crystal trajectories typically formed an arcing path in the plane of rotation (Figure 3-34). While some regions experienced large deformations, others saw little to no movement of the brain crystals, which suggests the brain deforms around an axis that is not coincident with the axis of rotation applied to the head. These observations suggest the potential for regions of vulnerability of the brain, which may be sensitive to direction, magnitude, and duration of loading.

While Hardy (Hardy et al., 2001, 2007) was able to quantify brain deformation, it is difficult to conduct any comparison of the two datasets. The applied head kinematics in

this study were purely rotational, while Hardy conducted a series of impacts with resulting linear and rotational head kinematics. This study also utilized a single specimen to test all head directions, while Hardy needed multiple specimens to test in different directions. The brain markers in the Hardy tests were at different locations compared to this study, and they were clustered within limited volumes of the brain. Additionally, the neck was constrained in the Hardy studies while the head was impacted, whereas this study allows the neck to move with the head. A constrained boundary condition at the neck could potentially influence the deformation of the inferior regions of the brain due to pulling through the cervical spine and spinal cord. This constraint may be representative of injurious impacts, but may not be ideal for controlled tests designed for FE model validation.

An important consideration in the methodology development was the measurement of the deformation of the brain relative to the skull. The use of sonomicrometry crystals affixed to the inner skull allows for the trilateration of crystal dynamic displacements independent of the rigid body motion of the head. While the quantified deformation of the brain may contain rigid body motion (of the brain relative of the skull) at low magnitudes of deformation (Laksari et al., 2012), the confinement of the brain with pressurized CSF in the skull is unlikely to result in any rigid body motion of the brain at the loading rates applied. As mentioned in Chapter 2, the brain's shear modulus is much lower than its bulk modulus, leading to a higher likelihood of shearing deformation than bulk motion of the tissue, especially under rotational loading. Regardless of whether the brain exhibits rigid body motion within the skull, the brain displacement data is still applicable for validation of FE brain models.

## CONCLUSION

The availability of accurate, 3D deformation data of the human brain will help improve the biofidelity of FE brain models and will lead to better techniques for predicting and mitigating concussion risk. This chapter provides a comprehensive methodology utilizing controlled mechanical input and sonomicrometry to measure 3D whole brain motion in dynamic head rotation tests. This methodology provides significant advantages over previous experiments, including:

- 3D motion capture of up to twenty-four sonomicrometry crystals within the brain without the need for bi-planar X-ray
- Ability to prepare and test a PMHS specimen rapidly post-mortem, preserving tissue integrity
- Ability to test all three planes of rotation with no sensor adjustment, and minimal mechanical adjustments
- Repeatable, pure rotational inputs to vary the magnitude and duration of the head kinematics
- Repeatable brain motion measurements, as evidenced by the return of the crystals to their initial position and matching responses in the repeated test case.

The ability to apply a pure rotation to the head and accurately measure 3D brain deformation in a repeatable and timely manner for various loading severities and directions allows for the collection of an extensive dataset of human brain deformation. The pilot specimen was used to validate and refine the methodology, in order to conduct experiments on additional specimens. The trilateration algorithm implemented for the pilot specimen, however, resulted in uncertainties in the calculated 3D motion of the crystals. Since

trilateration has not been used for brain deformation using sonomicrometry, an investigation and optimization of the trilateration technique were required to ensure the accuracy of the experimental brain deformation data.

## **CHAPTER 4: TRILATERATION METHODOLOGY**

The sonomicrometry technique is a reliable, accurate, and repeatable methodology to acquire in situ human brain deformation. The acquired distance data, however, has to be converted to dynamic position and displacement to be able to draw conclusions about the biomechanics of the brain and provide an FE validation dataset. Trilateration is typically used to convert a set of distances of a point to spatial coordinates. The objective of this chapter was to compare eight trilateration and Kalman filtering algorithms to determine the most suitable method for sonomicrometry trilateration. The algorithms were tested using experimental brain deformation sonomicrometry data in which random measurement errors were intentionally introduced to evaluate the effect on position error. A parameter sensitivity study was also conducted to optimize the algorithms to the simulated data. The Kalman filtering method was the most suitable for tracking dynamic brain deformation using sonomicrometry because it provided an accurate estimation of dynamic position and the estimated position was insensitive to the choice of initial parameters. The contributions of this study will provide a set of algorithms that can be implemented in positioning applications and a recommendation for an algorithm for use in other sonomicrometry experiments. Portions of this chapter were published previously (Alshareef et al., 2019. Application of Trilateration and Kalman Filtering Algorithms to Track Dynamic Brain Deformation Using Sonomicrometry. *Biomedical Signal Processing and Control*), and were adapted for this dissertation.

### **INTRODUCTION**

Sonomicrometry has become a proven technique in the field of biomechanics to track the dynamic motion of tissue or other objects. The technology has been extensively used

for various *in vivo* and *in situ* biomedical research applications for the last 30 years for high-rate internal motion tracking in cardiac mechanics (Dione et al., 1997; Van Trigt et al., 1981; Sarazan and Schweitz, 2009; Fomovsky et al., 2012; Holmes, 2004), animal biomechanics (Augustyniak et al., 2001; Carroll, 2004; Kaya et al., 2002), and clinical applications (Bebek and Cavusoglu, 2007; Brown Jr et al., 1999; Horiuchi et al., 2012; Larsson et al., 2015). In this dissertation, sonomicrometry has been extended to measure human brain deformation using a human cadaveric head specimen instrumented with an array of 32 small, neutrally-dense sonomicrometry crystals. The sonomicrometry technique was found to generate good quality signals between crystal pairs, demonstrated excellent repeatability, and captured accurate displacement measurements. While the quality of the sonomicrometry distance measurements was excellent, the preliminary trilateration algorithm used to find the spatial motion of each receiver crystal from a set of measured point-to-point distances resulted in uncertainties in the 3D motion dataset.

Trilateration has become ubiquitous in many applications including wireless positioning (Yim et al., 2008; Xu et al., 2016; Li et al., 2017), global positioning systems (GPS) (Bajaj et al., 2002; Fang, 1986; Rahman, 2012), and robotics (Borenstein et al., 1997; Thomas and Ros, 2005; Zhou, 2009). The method uses the measured distances from a set of reference points (with known positions) to a mobile point of interest (with unknown position) and uses the intersection of spheres created using the distances to determine the position of the mobile point. There are many algorithms, some as simple as finding a geometric intersection using equations of a sphere, and more complex ones that involve the minimization of error in the measured distances to find the most likely solution (Murphy and Hereman, 1995).

Additional work in positioning and position tracking has utilized Kalman filtering (Grewal, 2011), especially in wireless position estimation (Yim et al., 2008; Subhan et al., 2013; Kotanen et al., 2003), GPS positioning (Crassidis, 2006; Hide et al., 2004), and clinical applications (Bader et al., 2007; Senesh and Wolf, 2009; Shakarami et al., 2018). Kalman filtering is an algorithm that uses measurements (such as distances) associated with a variable (such as position) over time, which contain inherent errors or inaccuracies, to determine an estimate of the unknown variable. While Kalman filtering cannot find the spatial position of a point independent of time history like conventional trilateration algorithms, it holds an advantage in that it considers measurement error in the estimated variable across time in its tracking algorithm instead of treating each time point independently. Kalman filtering has not been implemented in the published literature for a sonomicrometry trilateration application.

The objective of this study was to find the most suitable method for determining the spatial position of sonomicrometry crystals embedded in a dynamically deforming brain. The first aim was to implement various algorithms involving trilateration and Kalman filtering that are currently used in positioning and tracking technology. The second aim was to investigate the effectiveness of these algorithms in calculating crystal position across time. These aims were accomplished using simulated brain deformation data in which various types and magnitudes of errors were introduced intentionally.

## **METHODS**

### **Sonomicrometry**

Previous biomechanics applications of sonomicrometry typically utilize transmitters to measure the distance between tissue-embedded receiving crystals to quantify the motion

of the tissue. The use of sonomicrometry in the brain presents unique challenges for the setup of transmitters and receivers, as well as for the conversion of individual transmitter-receiver distances to position and motion in 3D (Alshareef et al., 2018). Transmitting crystals are located at the surface of the skull, and move rigidly with the skull so that they are fixed in the skull coordinate system. Receiving crystals are implanted into brain tissue and move with the deforming brain relative to the skull coordinate system. Absolute distance errors in the sonomicrometry method are typically 2% - 6% of the measured distance (Meoli et al., 1998), which is approximately the diameter of a crystal. Errors in the absolute distance are usually due to errors in the assumed acoustic speed of sound, which underscores the importance of calibrating the initial position in trilateration, which can be accomplished using computed tomography (CT) scans (Alshareef et al., 2018). The absolute error is not prominent in receiver displacement measurements, where the sonomicrometry resolution is  $\pm 0.024$  mm (Dione et al., 1997).

### **Trilateration**

Trilateration is used to determine the position of the mobile receiver crystal using the sonomicrometry distance measurement between the receiver and a set of the fixed transmitter crystals. By utilizing spheres with radii of each distance from the receiver to all transmitters, the common intersection point of all spheres can be found to determine the spatial position of the receiver (Figure 4-1). For a given system, there are  $M$  receivers ( $R_1 - R_M$ ) located at a position  $(x_i, y_i, z_i)$  for  $i = 1:M$  that can move in time with the brain tissue. Additionally, there are  $N$  transmitting crystals ( $T_1 - T_N$ ) with known positions  $(X_j, Y_j, Z_j)$ , for  $j = 1:N$  that are fixed to the skull. At a given moment in time, the point-to-point distance between the receiver  $R_i$  and the transmitter  $T_j$  is recorded ( $r_{ij}$ ). The position

of receiver  $R_i$  is located at the intersection of the spheres with radius  $r_{ij}$  and satisfies the distance measurements between the receiver and each transmitter.

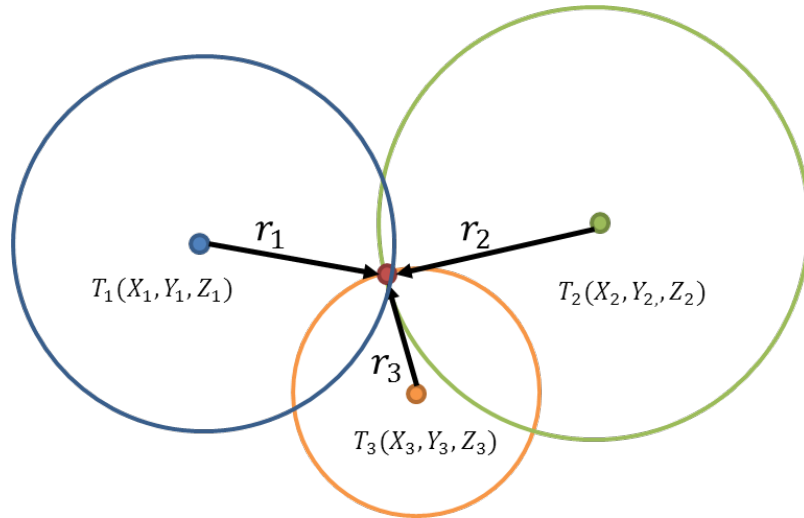


*Figure 4-1: The trilateration algorithm depicted using three transmitting points and one receiver point in the same plane. Three transmitters are shown ( $T_1, T_2, T_3$ ) with their associated positions and distances away from the receiver.*

A minimum of four transmitter distances is needed for trilateration to find the 3D position of each receiver. Each point-to-point measurement can contain error in the distances, which can result in multiple or no intersection points among the spheres. Measurement errors are propagated to the estimated position solution, and a substantial error in at least one distance can have a significant effect on the calculated trilateration position. In cases where a receiver has more than four transmitter distances, the redundant measurements can reduce the effect of measurements errors, using probabilistic or predictive algorithms.

### **Linear Trilateration Methods**

The following algorithm equations will include the solution for each receiver independently. For each receiver, the square distance to each transmitter at each time step is defined by:

$$r_j^2 = (x - X_j)^2 + (y - Y_j)^2 + (z - Z_j)^2 \quad (4-1)$$

Equation (4-1) can be linearized into the matrix form  $\mathbf{A}\vec{x} = \vec{b}$  for each receiver by subtracting the squared distance for each transmitter-receiver ( $j = 2:N$ ) from the first pair ( $j = 1$ ):

$$\mathbf{A} = 2 \begin{bmatrix} X_2 - X_1 & Y_2 - Y_1 & Z_2 - Z_1 \\ \vdots & \vdots & \vdots \\ X_N - X_1 & Y_N - Y_1 & Z_N - Z_1 \end{bmatrix}, \quad \vec{x} = \begin{bmatrix} x \\ y \\ z \end{bmatrix} \quad (4-2)$$

$$\vec{b} = \begin{bmatrix} (X_2^2 - X_1^2) + (Y_2^2 - Y_1^2) + (Z_2^2 - Z_1^2) - (r_2^2 - r_1^2) \\ \vdots \\ (X_N^2 - X_1^2) + (Y_N^2 - Y_1^2) + (Z_N^2 - Z_1^2) - (r_N^2 - r_1^2) \end{bmatrix}$$

The location of the receiver,  $\vec{x}$ , can be found independent of the other receivers through a linear least squares (LLS) solution, which uses the minimum of the sum of square residuals (Murphy and Hereman, 1995). This method yields (4-3), which can be solved at each time step independently to find the dynamic spatial position of each receiver during its motion.

$$\vec{x} = (\mathbf{A}^T \mathbf{A})^{-1} \mathbf{A}^T \vec{b} \quad (4-3)$$

In the case that the  $[\mathbf{A}^T \mathbf{A}]$  matrix is singular or poorly conditioned, other techniques can be employed. The normalized QR decomposition of  $\mathbf{A}$  can be used to find the solution, as seen in (4-4) and (4-5). This technique is abbreviated as LLS-QR.

$$\mathbf{A} = \mathbf{QR} \quad (4-4)$$

$$\vec{x} = (\mathbf{R})^{-1} \mathbf{Q}^T \vec{b} \quad (4-5)$$

An enhancement to the linear least squares approach in this case could also be employed in the form of a weighting factor representing the covariance of the  $\vec{b}$  vector (Guvenc et al., 2008). The solution becomes the form given in (4-6), where  $\mathbf{W}$ , the

weighting factor, is a diagonal matrix that contains the distances,  $r_j$ , from the receiver to all transmitters. This technique is abbreviated as LLS-W.

$$\mathbf{W} = \text{diag}(r_j) \quad (4-6)$$

$$\vec{x} = (\mathbf{A}^T \mathbf{W}^{-1} \mathbf{A})^{-1} \mathbf{A}^T \mathbf{W}^{-1} \vec{b}$$

### **Non-Linear Trilateration Methods**

A non-linear least squares (NLLS) approach can account for measurement errors by assuming an inherent error in the signals. Letting  $r_j$  denote the measured distance between the receiver and transmitter  $j$  containing some error, and  $\hat{r}_j$  denote the true distance, the sum of square errors between the true and measured distances, defined as  $F$ , can be minimized (4-7).

$$F(x, y, z) = \sum_{j=1}^N (\hat{r}_j - r_j)^2 = \sum_{j=1}^N f_j(x, y, z)^2 \quad (4-7)$$

$$\text{Where, } f_j(x, y, z) = \hat{r}_j - r_j$$

The solution to minimize the sum of squared errors can be implemented in many ways. An iterative Newton method was implemented in this study, which requires an initial position guess and either a number of maximum iterations or an error threshold. By differentiating (7) with respect to each coordinate  $(x, y, z)$ , (4-8) was obtained (with similar equations for  $y$  and  $z$ ). Note that only the differential in the  $x$ -direction is shown below.

$$\frac{\partial F}{\partial x} = 2 \sum_{j=1}^N f_j \frac{\partial f_j}{\partial x} \quad (4-8)$$

Introducing the vectors  $\vec{f}$  and  $\vec{g}$ , and the Jacobian matrix  $\mathbf{J}$ , lead to the following formulation in (4-9).

$$\vec{g} = 2\mathbf{J}^T \vec{f} \quad (4-9)$$

Where,

$$\mathbf{J} = \begin{bmatrix} \frac{\partial f_1}{\partial x} & \frac{\partial f_1}{\partial y} & \frac{\partial f_1}{\partial z} \\ \vdots & \vdots & \vdots \\ \frac{\partial f_N}{\partial x} & \frac{\partial f_N}{\partial y} & \frac{\partial f_N}{\partial z} \end{bmatrix}, \vec{f} = \begin{bmatrix} f_1 \\ \vdots \\ f_N \end{bmatrix}, \vec{g} = \begin{bmatrix} \frac{\partial F}{\partial x} \\ \frac{\partial F}{\partial y} \\ \frac{\partial F}{\partial z} \end{bmatrix}$$

The Newton method approximation iteratively finds a solution by using the previous iteration solution and the matrices defined above.  $\tilde{\mathbf{x}}$  is defined as the approximate solution and  $k$  is the iteration count (4-10).  $\tilde{\mathbf{x}}_{\{1\}}$  is the initial guess.

$$\tilde{\mathbf{x}}_{\{k+1\}} = \tilde{\mathbf{x}}_{\{k\}} - (\mathbf{J}_{\{k\}}^T \mathbf{J}_{\{k\}})^{-1} \mathbf{J}_{\{k\}}^T \vec{f}_{\{k\}} \quad (4-10)$$

### **Maximum Likelihood Estimate (MLE) Trilateration Method**

While the three linear trilateration methods (LLS, LLS-QR, LLS-W) and the nonlinear method (NLLS) can yield a good estimation given a low level of noise in the signals, they do not take into account the type or distribution of noise present in the signals. For example, the NLLS method assumes that there is noise in the estimated position  $\vec{\mathbf{x}}$ , but does not assume a noise in the individual distances between the receiver and each transmitter. In biomechanics experiments, this noise can result from many sources, including acoustic reflections or tissue discontinuities. Maximum likelihood estimation (MLE) methods have been developed to address this problem, by assuming that each distance between a transmitter-receiver pair contains an error with a Gaussian normal distribution  $N(0, \sigma^2)$ , such that the error has a mean of 0 and a constant variance,  $\sigma^2$ . A major distinction between MLE and the previous methods is that it assumes that each distance from the transmitters to a receiver are independent of one another. There are many MLE algorithms in the

literature, with certain conditions and error assumptions. The one used in this study was a distance-based MLE method devised by Xu et al. (2016) adapted to three dimensions.

Using the same transmitter-receiver scenario and the above assumptions, the marginal probability density function (denoted by  $m$ ) for the error in the distances is defined in (4-11).

$$m_j(r_j) = \frac{1}{\sqrt{2\pi}\sigma\hat{r}_j} \exp\left[-\frac{(r_j - \hat{r}_j)^2}{2\sigma^2\hat{r}_j^2}\right] \quad (4-11)$$

The corresponding likelihood function is shown in (4-12).

$$\ln[m(r_1, r_2, \dots, r_N)] = -\sum_{j=1}^N \ln(\hat{r}_j) - \sum_{j=1}^N \frac{(r_j - \hat{r}_j)^2}{2\sigma^2\hat{r}_j^2} - N\ln(\sqrt{2\pi}\sigma) \quad (4-12)$$

MLE finds the position of the receiver by maximizing the likelihood function (12). There are multiple ways to solve the function. However, a method based on the first-order optimality method will be used in this study (Xu et al., 2016). This method begins by minimizing the following objective function in (4-13).

$$m(x, y, z) = \ln\left(\sqrt{(x - \tilde{x})^2 + (y - \tilde{y})^2 + (z - \tilde{z})^2}\right) + \frac{(r - \sqrt{(x - \tilde{x})^2 + (y - \tilde{y})^2 + (z - \tilde{z})^2})^2}{2\sigma^2((x - \tilde{x})^2 + (y - \tilde{y})^2 + (z - \tilde{z})^2)^2} \quad (4-13)$$

By taking the partial derivative of (4-13) with respect to  $x$ ,  $y$ , and  $z$ , and then setting the partial derivative equal to 0 yields (4-14)-(4-16). These equations can be minimized to find the receiver position.

$$\sum_{j=1}^N \left[ \frac{x - \tilde{x}_j}{(x - \tilde{x}_j)^2 + (y - \tilde{y}_j)^2 + (z - \tilde{z}_j)^2} + \frac{r_j(x - \tilde{x}_j)(\sqrt{(x - \tilde{x})^2 + (y - \tilde{y})^2 + (z - \tilde{z})^2} - r_j)}{\sigma^2((x - \tilde{x})^2 + (y - \tilde{y})^2 + (z - \tilde{z})^2)^2} \right] \quad (4-14)$$

$$\sum_{j=1}^N \left[ \frac{y - \tilde{y}_j}{(x - \tilde{x}_j)^2 + (y - \tilde{y}_j)^2 + (z - \tilde{z}_j)^2} + \frac{r_j(y - \tilde{y}_j)(\sqrt{(x - \tilde{x})^2 + (y - \tilde{y})^2 + (z - \tilde{z})^2} - r_j)}{\sigma^2((x - \tilde{x})^2 + (y - \tilde{y})^2 + (z - \tilde{z})^2)^2} \right] \quad (4-15)$$

$$\sum_{j=1}^N \left[ \frac{z - \tilde{z}_j}{(x - \tilde{x}_j)^2 + (y - \tilde{y}_j)^2 + (z - \tilde{z}_j)^2} + \frac{r_j(z - \tilde{z}_j)(\sqrt{(x - \tilde{x})^2 + (y - \tilde{y})^2 + (z - \tilde{z})^2} - r_j)}{\sigma^2((x - \tilde{x})^2 + (y - \tilde{y})^2 + (z - \tilde{z})^2)^2} \right] \quad (4-16)$$

Other methods can be used to find the MLE solution, such as weighting specific transmitter-receiver pairs if certain pairs contain higher levels of noise. However, the proposed solution presented in the equations above will be used by optimizing only one parameter, the  $\sigma^2$  error assumption.

### **Kalman Filtering Trilateration Method**

The five trilateration methods presented thus far (LLS, LLS-QR, LLS-W, NLLS, MLE) do not consider the motion of the receiver in time when determining the position (i.e., the solution to the current position is independent on the previous position). While some of the methods, such as MLE and NLLS, consider an error in the physical distance, they ignore any temporal errors in the motion of the receiver. Kalman filtering differs in that it iteratively estimates the spatial position of the receivers based on the position at the previous time step. Therefore, it assumes an error in the initial guess (from the previous

time point) and an error in the measured distances (at the current time point), allowing for as a more reliable estimation across time. The disadvantage of using a Kalman filter is that it cannot localize or trilaterate the crystal position at the first time step. Therefore, the receiver position at the first time step has to be known, or it has to be found using another trilateration method, such as NLLS or MLE.

The basic Kalman filter assumes a linear form of the prediction and measurement variables. Since trilateration is a non-linear problem (4-1), local linearization has to be applied within the Kalman filter process. This linearization changes the filter to an extended Kalman Filter (EKF) (Julier and Uhlmann, 2004), which contains real-time linearization of the prediction and allows the measurement to be able to update the estimated position iteratively. The following process, which was derived from Yim et al. (Yim et al., 2008, 2010), explains EKF applied to the sonomicrometry distance data.

Let  $x$ ,  $\tilde{x}$ , and  $X_i$  denote the 3D position of the true location of the receiver, the estimated location of the receiver, and the position of each transmitter,  $i$ , respectively. Each iteration in the Kalman filter will be denoted by the subscript  $k$ . Since the transmitters are fixed, their position does not depend on time or the EKF iteration.

$$x_k \sim (x_k, y_k, z_k)$$

$$\tilde{x}_k \sim (\tilde{x}_k, \tilde{y}_k, \tilde{z}_k)$$

$$X_i \sim (X_i, Y_i, Z_i)$$

Assume that the estimated position of the receiver has an error,  $w$ , and that the distance measurements,  $r$ , contain an error,  $v$ . Both of these errors are assumed to be normally-distributed Gaussian white noise with a mean of zero and assumed variance.

$$x_k = x_{k-1} + w_k \tag{4-17}$$

$$r_k = h_k(x_k) + v_k$$

Where,

$$h_k(x_k) = \sqrt{(x_k - X_j)^2 + (y_k - Y_j)^2 + (z_k - Z_j)^2} \quad (4-18)$$

Let the distributions of  $w$  and  $v$  be defined as  $p(w) \sim N(0, Q)$  and  $p(v) \sim N(0, R)$ . If the receiver was fixed and not moving over time, the value of  $Q$  would be 0 and there would only be error in the measurement ( $R$ ). This is similar to the assumption that other positioning algorithms, like MLE or NLLS, utilize. The linearization for the EKF occurs to convert the estimated position  $\tilde{x}_k$  to distances, using (4-19):

$$h(x_k) \approx h(\tilde{x}_k) + \mathbf{H}_k w_k x_k \quad (4-19)$$

Where  $\mathbf{H}_k$  is the Jacobian of the estimated distances (4-20).

$$\mathbf{H}_k = \left[ \frac{\partial h}{\partial x} \right]_{x=\tilde{x}_k} \quad (4-20)$$

Each row of  $H_k$  corresponds to the associated transmitter, as defined in (4-21):

$$H_{kj} = \frac{\tilde{x}_k - X_j}{h_j(\tilde{x}_k)} \quad (4-21)$$

For each iteration in the EKF procedure, initial values must be defined for the position ( $\tilde{x}_k$ ) and the two error variances ( $R$  and  $Q$ ). The variance  $R$  will be chosen as a constant value and will not change with each EKF iteration. The variance  $Q$  is used to calculate the matrix  $\mathbf{P}$  at the first iteration of the EKF. Since  $P$ , which represents the error of the prediction, is updated at every EKF iteration, an initial value of the diagonal values of  $\mathbf{P}$  will be chosen. For each iteration of the EKF, the initial known position  $\hat{x}_k$  will be updated and used as the initial estimate for the next iteration. These variables are used to calculate the Kalman Gain ( $\mathbf{K}$ ), which is equivalent to a weighting function that changes the

estimated position  $\tilde{x}_k$  depending on the errors in the prediction and measurement. The following steps are taken at each iteration:

$$\text{Step 1: } \tilde{x}_k = \tilde{x}_{k-1}, \mathbf{P}_k = \mathbf{P}_{k-1}$$

$$\text{Step 2: } \mathbf{K}_k = \mathbf{P}_k \mathbf{H}_k^T (\mathbf{H}_k \mathbf{P}_k \mathbf{H}_k^T + \mathbf{R}_k)^{-1}$$

$$\text{Step 3: } \tilde{x}_k = \tilde{x}_k + \mathbf{K}_k (r_k - h(\tilde{x}_k))$$

$$\text{Step 4: } \mathbf{P}_k = (\mathbf{I} - \mathbf{K}_k \mathbf{H}_k) \mathbf{P}_k (\mathbf{I} - \mathbf{K}_k \mathbf{H}_k)^T + \mathbf{K}_k \mathbf{R}_k \mathbf{K}_k^T$$

$$\text{Step 5: } \tilde{x}_{k-1} = \tilde{x}_k, \mathbf{P}_{k-1} = \mathbf{P}_k$$

The steps are repeated until either the maximum number of iterations ( $k$ ) or a tolerance threshold is achieved. For this study, the maximum number of iterations was set to 100. A tolerance using the sum of all matrix components of the Kalman Gain ( $\mathbf{K}$ ) being less than 0.01 was also implemented.

The initial guess for the EKF algorithm can either be a known position, a predicted position from a trilateration algorithm, or a prediction position based on the physical system. For this study, three EKF algorithms will be analyzed based on the different initial guesses. The Kalman-MLE method will use the estimate from the MLE algorithm for the initial estimate in the first time step and use the position from the previous step as the initial estimate for subsequent time steps. The Kalman-CT method will use the receiver position observed in the pre-test CT scan as the initial estimate in the first time step and use the position from the previous step as the initial estimate for subsequent time steps. The Kalman-V method will use the CT position as the initial estimate for the first two timesteps and use an estimate of the receiver velocity calculated by the change in position between previous two steps to calculate the initial position estimate for all subsequent timesteps.

### 3D Receiver Motion Simulation

To test out the trilateration and Kalman filtering methods using real biomechanical data, one receiver embedded in a brain during a coronal rotation of the head (Alshareef et al., 2018) was used to simulate the proposed methods (data from the pilot specimen, Chapter 3). The 3D displacement of the receiver is shown in Figure 4-2, and for this analysis, was considered to be the motion related to the true position of the receiver,  $x(t)$ . The fixed positions of the eight transmitters and the initial position of the receiver are given in Table 4-1. Positions are based on the skull anatomical reference frame.

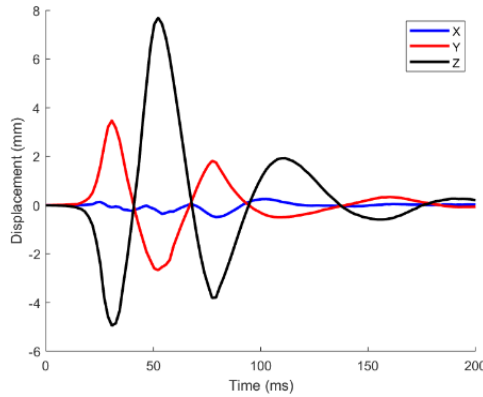


Figure 4-2: Simulated 3D displacement of an arbitrary receiver

Table 4-1: Positions for all transmitters (Tx) used in the trilateration simulation. The initial position of the receiver is listed in the last row.

| Crystal               | X (mm)       | Y (mm)        | Z (mm)        |
|-----------------------|--------------|---------------|---------------|
| Tx-1                  | 0.11         | -55.10        | -1.32         |
| Tx-2                  | 65.74        | 4.56          | -48.45        |
| Tx-3                  | 40.32        | -38.77        | -53.87        |
| Tx-4                  | -34.06       | 53.19         | -49.69        |
| Tx-5                  | -0.018       | 68.52         | -0.70         |
| Tx-6                  | -22.97       | -49.06        | -59.51        |
| Tx-7                  | 26.82        | 49.95         | -50.32        |
| Tx-8                  | -56.14       | 0.33          | 37.99         |
| <b>Receiver (t=0)</b> | <b>14.03</b> | <b>-30.99</b> | <b>-45.79</b> |

The true distance measurements were then intentionally modified to account for measurement errors potentially encountered in sonomicrometry signals to obtain a set of hypothetical measurements,  $\tilde{r}_j(t)$ . Two types of measurement errors were introduced: noise error and bias error. Noise errors can occur in sonomicrometry data from electrical noise, acoustic reflections, or delayed wave front triggering (Dione et al., 1997; Van Trigt et al., 1981; Meoli et al., 1998). Noise error was introduced in the simulated measurement data by multiplying each data point across time, for each transmitter-receiver pair, by a random variable of up to 5% (-2.5% to +2.5%) of the initial magnitude of the true distance. Bias error can occur in sonomicrometry data from an error in the speed of sound defined for the tissue, CT measurement of the initial position, and in level shifts that occur as a result of the chosen receiver wavefront triggering sensitivity (Dione et al., 1997; Van Trigt et al., 1981; Meoli et al., 1998). Bias error was introduced by adding a constant random value to the entire distance signal of up to 10% (-5% to 5%) of the initial magnitude of the true distance. It is important to note that the magnitude of the errors introduced into this simulated sonomicrometry data was typically an order of magnitude larger than what was seen in the experimental signals (noise errors of 0.2-0.8% and bias errors of 2-6%) in order to test each of the trilateration algorithms.

Simulations were conducted with either noise error only, bias error only, or a combination of both error types. Example distance traces for all transmitter (Tx) for the receiver (Rx) with both error types are shown in Figure 4-3.

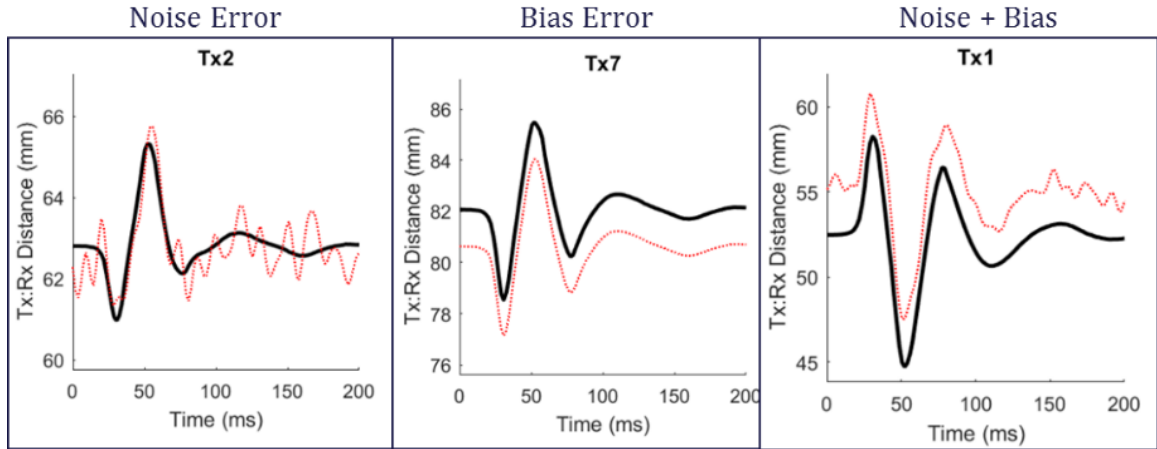


Figure 4-3: Example distance traces from select transmitters (Tx) to the receiver (Rx) with the true distance (black), and distance with the error introduced (red) for noisy only (left), bias only (middle), and both types of error (right).

A total of eight methods will be compared for the sonomicrometry trilateration scenario presented, including LLS, LLS-QR, LLS-W, NLLS, MLE, Kalman-MLE, Kalman-CT, and Kalman-V. For methods with a user-defined parameter, a sensitivity analysis will be conducted to determine suitable ranges of values for the combined noise and error condition. For the MLE method, the variance  $\sigma$  will be varied from 0.01 to 0.5. For the Kalman methods,  $R$  will be varied from 0.0001 to 0.5, and  $P$  will be varied from 0.01 to 200 mm.

To simulate the effectiveness of each trilateration and Kalman filtering algorithm, MATLAB (Mathworks Inc., MA, USA) was used to implement the positioning algorithms and calculate the estimated position. Random error (noise only, bias only, or noise and bias) was added to each of the eight transmitter distances to the receiver for each simulation. Each technique was then used to calculate the estimated position of the receiver across time,  $\tilde{x}$ . The estimated position and the true position,  $x$ , were compared using four error metrics. For all trilateration methods (except Kalman filtering), an initial position error was found by calculating the distance between the estimated initial position (at the

first time point) and the true initial position. For all methods, the other three error metrics were the root mean squared (RMS) errors for the position ( $\tilde{x} - x$ ), displacement ( $\Delta\tilde{x} - \Delta x$ ), and distance error for all transmitters ( $\tilde{r}_i - r_i$ ). The error calculations for all methods are included in (4-22)-(4-25). Errors were calculated for 100 iterations of simulated data, and a mean and standard deviation was calculated for all error types for each method. The number of iterations (100) was chosen based on a convergence study with iteration counts ranging from 5-1000.

$$Err_{initial} = \tilde{x}_{x,y,z} - x_{x,y,z} \quad (4-22)$$

$$Err_{position} = \sqrt{\text{mean} \left[ \left( \tilde{x}_{x,y,z}(t) - x_{x,y,z}(t) \right)^2 \right]} \quad (4-23)$$

$$Err_{displacement} = \sqrt{\text{mean} \left[ \left( \Delta\tilde{x}_{x,y,z}(t) - \Delta x_{x,y,z}(t) \right)^2 \right]} \quad (4-24)$$

$$Err_{distances} = \frac{1}{N} \sum_{i=1}^N \sqrt{\text{mean} \left[ \left( \tilde{r}_i(t) - r_i(t) \right)^2 \right]} \quad (4-25)$$

## RESULTS

### Parameter Sensitivity Analysis

A combined noise and bias error were introduced into the sonomicrometry signals to optimize the parameters. For MLE, the  $\sigma$  value sensitivity results are given in Figure 4-4. All of the errors were relatively constant until a  $\sigma=0.15$ . The Kalman-MLE method was not affected by the choice of  $\sigma$ . A value of  $\sigma=0.15$  was chosen as a result of the optimization. The optimization of the Kalman parameters included P (the error in the prediction/initial guess) and R (the error in the distance measurements). For both parameters, the trilateration solutions and errors were insensitive to their chosen values

across the three Kalman methods. Therefore, values of  $P=100$  mm and  $R=0.1$  were chosen as a result of the optimization.

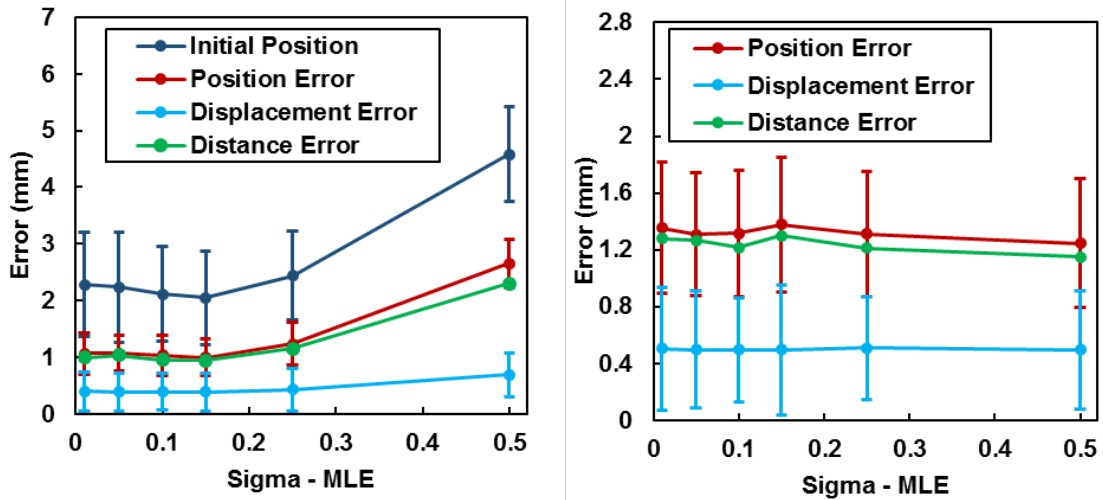


Figure 4-4: Parameter optimization for  $\sigma^2$  for the MLE (left) and Kalman-MLE algorithm (right).

### Initial Position Error

The trilateration algorithms were investigated for accuracy in determining initial position, with the known position (based on CT) as the initial guess. For the five algorithms capable of calculating the initial position (LLS, LLS-QR, LLS-W, NLLS, MLE), a depiction of the results from one simulation and mean error for all three error conditions are shown in Figure 4-5. The MLE method had the least error for all cases. The error for the MLE method ranged from an average of 0.88 mm for the ‘noise only’ condition to 2.23 mm for the ‘noise and bias’ condition. The three LLS methods performed the poorest among the different methods and had similar errors across all conditions.

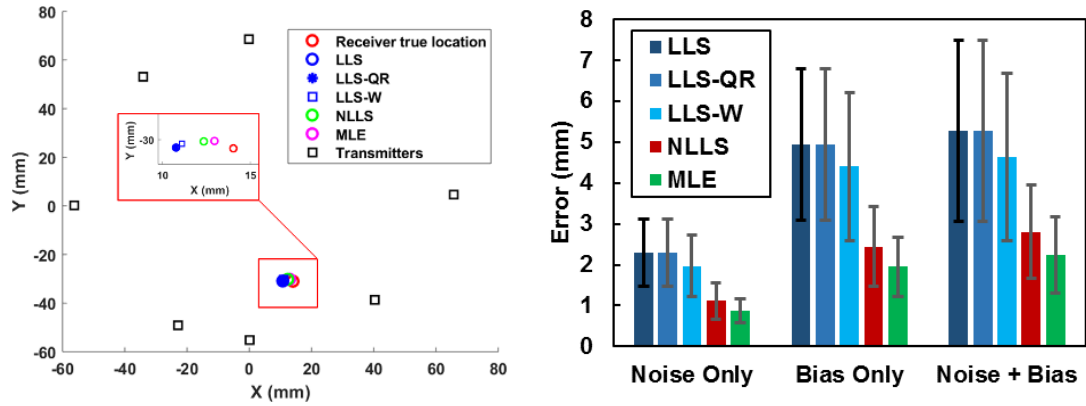


Figure 4-5: The initial positions estimation for the LLS methods, NLLS, and MLE are shown for one iteration (left). The average error (right) is lowest for the MLE and NLLS methods.

### Dynamic Error Analysis

The trilateration and Kalman filtering algorithms were simulated under three error conditions. The results from one simulation with the ‘noise and bias’ error condition is shown in Figure 4-6 for the LLS, MLE, and Kalman-CT methods. The remaining methods resulted in estimates that were identical to the other LLS or Kalman methods.

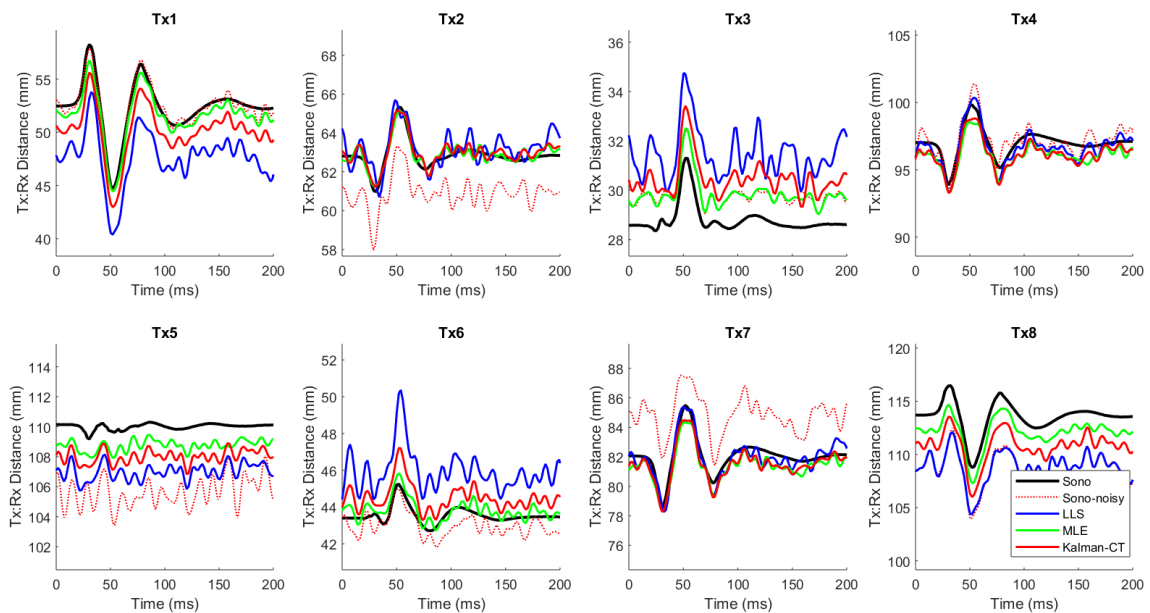


Figure 4-6: Distance results from one iteration of a simulation with the ‘noise and bias’ error condition. The plots show the distance from each transmitter to the receiver with the true distance (sono), noisy distance (sono-noisy), and the LLS, MLE (after tuning), and Kalman-CT methods.

To quantify which algorithms estimated the closest position to the true receiver position, all algorithms were compared using the three dynamic error metrics (position, displacement, and distance error) under the three simulated measurements error conditions. The three LLS methods had similar results across all error metrics, with consistently higher errors than the other algorithms (Figure 4-7). MLE performed the best across the error metrics and conditions, with the NLLS and Kalman methods approximately having the same values. All of the Kalman methods, regardless of initial guess, had the same average error, close in value to the NLLS method.

Under the applied measurement errors in this analysis, the displacement error ranged from 0.1 mm to 0.9 mm, which represents 0.7% - 6.9% of the peak-to-peak displacement of the receiver. The position and distance errors were approximately the same across all algorithms, with the NLLS, MLE, and Kalman filtering algorithms having the least error. The input noise was quantified using the same distance RMS error metrics and is shown in Figure 4-7. The level of error using the LLS methods was approximately the same as the level of error introduced into the measurement signals, while the NLLS, MLE, and Kalman filtering algorithms provided demonstrated a reduced solution error relative to the input signal error (40% - 72%).

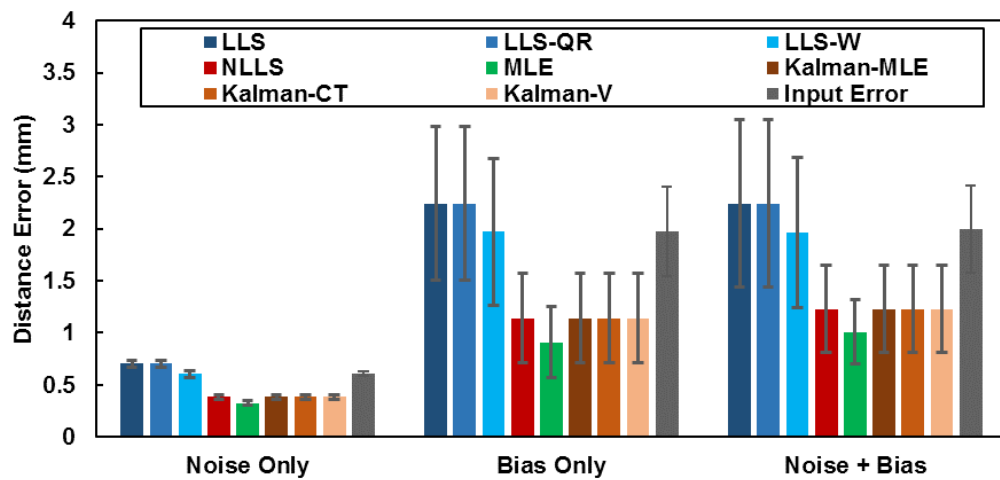
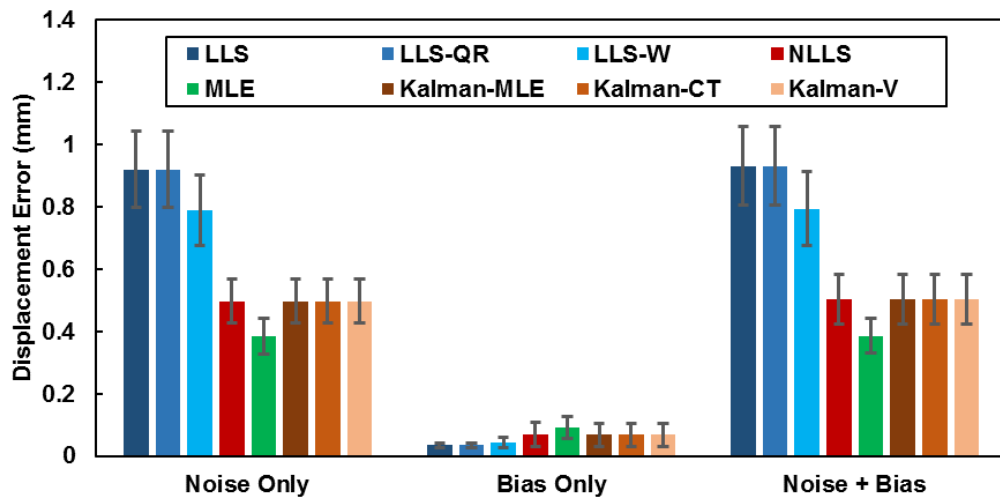
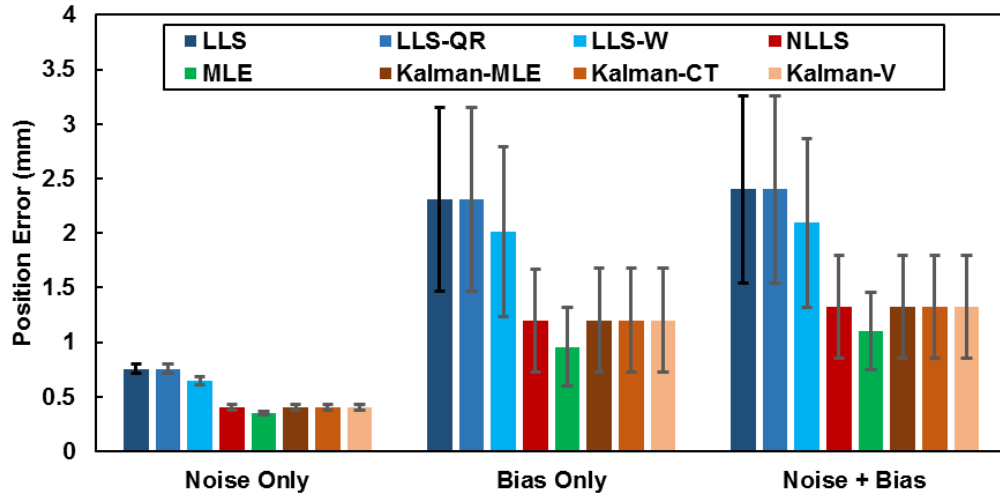


Figure 4-7: Comparison of trilateration and Kalman filtering algorithms for position error (top), displacement error (middle), and distance error (bottom) for the three error metrics.

## DISCUSSION

### Application of Trilateration Algorithms to Sonomicrometry

Trilateration algorithms are typically used in applications related to large-field tracking and positioning, such as a GPS or wireless positioning within a building. While trilateration algorithms have been used with sonomicrometry data, this is the first study to compare various algorithms to the trilateration problem in biomechanics to determine their accuracy. The sonomicrometry environment is unique in that distances are small (20-200 mm), and the types of signal error differ from traditional positioning applications. This chapter investigated three signal error conditions, including ‘noise only,’ ‘bias only,’ and ‘noise and bias’ to create a representative set of dynamic signals with error much higher than typically encountered for brain sonomicrometry signals. It is important to note that the errors introduced in the simulated curves in this study are an overestimate of the noise in the sonomicrometry brain signals. The initial position error, Figure 4-5, ranged from 0.5 - 10 mm, representing a 1-10% error in the magnitude of the true distances. The dynamic RMS errors metrics for all algorithms ranged from 0.1 mm to 3 mm, which is similar to the diameter of the receivers. Even when simulating data with high amounts of noise in the simulated data, the average RMS error was less than the diameter of the receiver.

While all of the algorithms yielded results within a reasonable percentage of the true values, the non-linear methods provided much better estimates across all metrics. The different linear methods (LLS) provided comparable results, with the weighted LLS (LLS-W) showing improved estimates than the original LLS or the QR decomposition. The NNLS, MLE, and Kalman methods showed similar error results, with the MLE having slightly lower mean values across all error metrics. For the Kalman methods, there were

no differences across the three methods with different choices of initial guesses. This result indicates that the choice of initial guess for the Kalman filtering algorithm is not important for the simulated application.

### **Parameter Sensitivity**

The parameter sensitivity for the MLE and Kalman filtering methods was conducted to identify if the trilaterated solution was sensitive to the initial parameters and to determine the best parameters for this application. The  $\sigma$  value for the MLE method, which is the variance of the assumed error in the distances, can be thought of as a radius around the initial guess for where the estimated MLE position may be. If the value is too small, the solution may be incorrect and may be unstable across time points when estimating the position of dynamic data. If the value of  $\sigma$  is too large, the result will be inaccurate and may drift further from the true solution. The sensitivity study supports this observation by showing that there is a slight decrease as  $\sigma$  increases to a value of 0.15 (Figure 4-4). Above this threshold, the errors rise in magnitude across all metrics. This trend may be specific to the particular data used in this study. When applied to a larger dataset of similar sonomicrometry data, the convergence point was found to differ across signals. Therefore,  $\sigma$  needs to be optimized for the errors in each distance signal. While a value of 0.15 was suitable for most sonometric brain deformation data, an optimization should be done for representative signals in each dataset.

The parameter sensitivity for the Kalman filtering algorithm included  $P$ , which represents the error in the prediction, and  $R$ , which represents the measurement error. The sensitivity analysis showed that neither parameter affected the predicted solution of the Kalman filter and the error metrics were insensitive to changes in  $P$  and  $R$  across a wide

range of values. This is likely due to the way the algorithm uses and updates these parameters in the steps outlined in the methods. The value of  $P$  is updated for every iteration of the Kalman filter based on how close the prediction or initial guess was to the value predicted by the distance measurements. In previous studies that use Kalman filtering for wireless positioning, it was recommended that the initial choice of  $P$  is a value much higher than the estimated error in the prediction (Yim et al., 2008). Although the value of  $R$  was not updated in the Kalman filter for each iteration, it is used to calculate the Kalman gain ( $K$ , step 2) and to update the value of  $P$  (step 4). The Kalman gain is similar to a joint probability distribution between the prediction and the measurement errors, and it was used to update the estimated position based on the data and the values of  $P$  and  $R$ . While a change in  $R$  does not change the final solution, it may take more EKF iterations to reach the same solution with a higher value of  $R$ .

### **Optimal Algorithms for Brain Sonomicrometry**

Estimating dynamic position for crystals using sonomicrometry is very important to the field of brain injury biomechanics, as it provides a reliable and robust approach to measure brain deformation caused by head impact to quantify head impact severity. The displacements of the embedded crystals are used as a benchmark to validate computational models of the brain, which are then used in injury prediction, helmet development, and the development of injury risk curves. This study was performed to find the most accurate and suitable algorithm given the scarcity and importance of this experimental dataset.

While all of the algorithms, except for the LLS methods, yielded similar results in terms of error, Kalman filtering (using the CT position as the initial guess) was the recommended method for trilaterating brain sonomicrometry data. The MLE and NLLS

methods were similarly accurate but needed *a priori* optimization or constraint for each test or set of tests. Additionally, these two methods treat each time point independently, while the Kalman filter considers temporal variations in error. The sonomicrometry signals in the brain are usually smooth and do not have spikes in magnitude across time, as a result of the compliance and viscoelastic mater properties of the brain. Kalman filtering can help alleviate the uncertainties in the measurement introduced by outliers or magnitude spikes at individual time points that can result in non-physical position estimates. The Kalman filter was also insensitive to user-defined initialization parameters, so the algorithm does not have to be optimized before every dataset. If the initial position at the first time point is not known, it is recommended that the MLE or NLLS method be used to determine the initial position for the Kalman filter.

## **CONCLUSION**

Trilateration and Kalman filtering algorithms have been used in many fields, including sonomicrometry, to find the dynamic position of objects given redundant distance data that often include noise. Eight trilateration and Kalman filtering methods were evaluated to identify the one most suitable for trilaterating dynamic brain sonomicrometry data. While the non-linear, MLE, and Kalman filtering trilateration methods yielded the least error (40% - 72% reduction in input distance error), the Kalman filtering algorithm was recommended for use in sonomicrometry due to its accuracy and insensitivity to initial parameters.

The brain deformation data acquired using sonomicrometry for the pilot specimen (chapter 3) contained uncertainties in the 3D solution. After optimizing the trilateration solution, the data from the pilot specimen can be accurately converted to spatial brain

deformation data. The experimental methodology and the optimized trilateration algorithms allow for the collection of a comprehensive dataset of human brain deformation. An additional five specimens will be tested with the same test matrix. The dataset of six specimens will be used to investigate the dependence of brain deformation on rotation severity, loading direction, and brain region.

## **CHAPTER 5: HUMAN BRAIN DEFORMATION DATASET**

The development of a robust trilateration algorithm to determine the dynamic position of sonomicrometry crystals embedded in the brain allows for large-scale investigations into the biomechanics of the brain. Along with the methodology developed in chapter 3, the trilateration method can be used to generate a dataset of human brain deformation with multiple specimens to be able to investigate the dependence of brain deformation on input kinematics and brain anatomy. The brain deformation dataset is also crucial to the validation of FE brain models, which have been instrumental in understanding brain injury and developing injury mitigation systems. The objective of this study was to apply the sonomicrometry methodology to measure brain deformation by generating a comprehensive dataset of human brain deformation under rotational loading. Dynamic brain deformation was measured for six specimens with four loading severities in the three directions of rotation, for a total of twelve tests per specimen. Testing for all specimens was completed 42-72 hours post-mortem. The final dataset contains approximately 5,000 individual crystal displacement curves. The data presented in this chapter will provide valuable insight into fundamental brain biomechanics that has only been theorized using computational models. Additionally, the data will provide a comprehensive set of experimental targets for more rigorous model validation during the development of the next generation of finite element brain models. A paper titled “Human Brain Deformation During Dynamic Rotation of the Head” is currently in draft, with a target journal of “Journal of Neurotrauma.”

## INTRODUCTION

In the past two decades, there have been numerous FE models of the brain developed in the literature (Giudice et al., 2018a). The models allow for regional and macroscopic investigations into the brain response under a wide variety of loading conditions and severities that would not otherwise be possible experimentally. The biofidelity of these models in predicting the deformation of the brain is requisite for their role in predicting and mitigating TBI. Verifying the fidelity of these models relies on comparing the deformation responses to reference data measuring brain motion during dynamic experiments.

Most of the original injury criteria, such as the Head Injury Criterion (Versace, 1971), were developed using only linear acceleration loading. As a result, most previous attempts to quantify brain motion biomechanics under impact loading have focused on impacts resulting in linear translation of the head. Such studies have formed the basis of current tools for evaluating the safety protective equipments such as helmets (Giudice et al., 2018b; Panzer et al., 2018) and automotive restraint systems (Newman et al., 2000; Rowson and Duma, 2013; Takhounts et al., 2013a; Versace, 1971). Despite the historical focus on linear head acceleration, rotational impact has long been theorized to be a primary mechanism of TBI (Holbourn, 1943).

Few methods are available to measure 3D motion of the brain during dynamic rotation of the head. Measuring human brain deformation has been explored using magnetic resonance imaging (MRI) (Bayly et al., 2005; Feng et al., 2010; Knutsen et al., 2014; Sabet, Christoforou, Zatlín, Genin, & Bayly, 2008), and bi-planar X-ray imaging (Hardy et al., 2007; Nusholtz et al., 1984; Stalnaker et al., 1977). While the bi-planar X-ray

methodology provided good quality data for FE model validation, the method has inherent limitations arising from line-of-sight requirements and other factors (Alshareef et al., 2018).

A new methodology using sonomicrometry was described in Chapter 3 as an alternative to high-speed radiography. Sonomicrometry uses ultrasound time-of-flight to dynamically measure distances between pairs of small piezoelectric crystals implanted within a tissue. Sonomicrometry does not have line-of-sight limitations, which allows for a larger number of crystals to be tracked in the brain, and it allows for testing under multiple directions and loading conditions for each specimen. This methodology was demonstrated using a pilot specimen. The specimen was subjected to dynamic rotation tests that were applied about the three principal directions (sagittal, coronal, axial), with angular velocity pulses ranging from 20-40 rad/s, with durations of 30-60 ms and angular accelerations from 600-5500 rad/s<sup>2</sup>. The sonomicrometry and experimental techniques were able to reliably and repeatedly capture three-dimensional dynamic *in situ* whole brain deformation during the dynamic head rotation tests.

The objective of this study was to apply the methodology of sonomicrometry and trilateration developed in Chapter 3 and 4 to generate a reference dataset of human brain deformation under rotational loading with multiple specimens, to form the basis for biofidelity evaluation of human FE brain models. A secondary aim was to examine the relationship between brain deformation, loading magnitude and duration, and the direction of rotation. The data presented in this study will provide valuable insight on fundamental brain biomechanics that has only been theorized using computer models and will provide

a comprehensive set of experimental targets for more rigorous model validation during the development of the next generation of finite element brain models.

## **METHODS**

Six head/brain specimens of post mortem human surrogates (PMHS, cadavers) were tested using the methodology described in Chapter 3. A comprehensive description of the methodology used to measure brain deformation, including the test device, specimen preparation, and use of sonomicrometry can be found in the referenced chapter. A concise explanation of the methods that include any changes relevant to the full dataset of six specimens is presented below.

### **Specimen Acquisition and Information**

All tissue donation, testing, and handling procedures were approved by the University of Virginia Institutional Review Board – Human Surrogate Use (IRB-HSU) Committee. Exclusion criteria for the acquisition of the specimens included any factors that may have compromised the anatomy or material properties of the skull or brain tissue, and included any diagnosed skull lesions or trauma, neurological disease, or neurological lesions. All specimens were also screened for bloodborne pathogens (HIV, Hepatitis B & C). The donated PMHS were acquired unembalmed, never frozen, 10-24 hours post-mortem. General PMHS information is presented in Tables 5-1 and 5-2.

Pre-test radiographs of the specimens confirmed no abnormalities of the skull and cranial space. For four of the specimens (896, 900, 902, 904) T1-weighted Magnetic Resonance Imaging (MRI) scans of the brain were also obtained to acquire subject-specific brain anatomy (Table 5-1). Head-neck specimens were then procured at or around the first thoracic vertebra for specimen preparation.

Table 5-1: Specimen information and identification number (ID) for all tested PMHS.

| Specimen ID | Age (yrs.) | Sex    | Cause of Death           | Imaging | Testing Complete* (hrs.) |
|-------------|------------|--------|--------------------------|---------|--------------------------|
| 846         | 53         | Male   | Congestive heart failure | CT      | 56                       |
| 896         | 57         | Female | Esophageal cancer        | CT, MRI | 42                       |
| 900         | 66         | Female | Carcinoma                | CT, MRI | 72                       |
| 902         | 61         | Female | Cardiac arrest           | CT, MRI | 64                       |
| 903         | 80         | Female | Cardiac arrest           | CT      | 54                       |
| 904         | 67         | Male   | Colon cancer             | CT, MRI | 63                       |

\* Indicates hour post-mortem

Table 5-2: PMHS anthropometry and mass measurements.

| Anthropometric Measurement                      |                                 | 846  | 896  | 900  | 902  | 903  | 904  | Average      |
|---|---------------------------------|------|------|------|------|------|------|--------------|
| Whole Body                                      | Stature (cm)                    | 173  | 163  | 165  | 168  | 156  | 177  | 167 ± 8      |
|   | Mass (kg)                       | 116  | 31.1 | 56.2 | 97.1 | 90.2 | 54.9 | 74.3 ± 31.9  |
|   | BMI                             | 38.8 | 11.7 | 20.6 | 34.4 | 37.1 | 17.5 | 26.7 ± 11.5  |
| Skull   | Circumference (mm)              | 510  | 500  | 520  | 539  | 506  | 514  | 514.8 ± 13.7 |
|   | Length (A-P, mm)                | 172  | 176  | 184  | 181  | 180  | 186  | 179.8 ± 5.15 |
|   | Breadth (L-M, mm)               | 144  | 129  | 131  | 148  | 129  | 135  | 136.0 ± 8.15 |
|   | Height (Vertex-Mentum, mm)      | 240  | 196  | 230  | 226  | 220  | 234  | 224.3 ± 15.5 |
|   | Height (Vertex-Occiput, mm)     | 156  | 135  | 146  | 137  | 130  | 153  | 142.8 ± 10.5 |
|   | Brow-to-Occiput Arc Length (mm) | 315  | 305  | 320  | 315  | 292  | 352  | 316.5 ± 20.1 |
| Mass  | Head/Neck (kg)                  | 7.79 | 3.35 | 4.53 | 4.11 | 4.09 | 4.73 | 4.44 ± 0.84  |
|   | Brain (kg)*                     | 1.27 | 1.21 | 1.34 | 1.30 | 1.11 | 1.49 | 1.28 ± 0.13  |
| Intracranial Volume (from CT, cm <sup>3</sup> ) |                                 | 1442 | 1435 | 1558 | 1481 | 1298 | 1692 | 1484 ± 132   |

\* Brain mass measured post-test during specimen dissection

## Specimen Preparation

All instrumentation and hardware installation were performed relative to the head center of gravity (CG) which was estimated based on anatomical landmarks according to the protocol outlined by Robbins (Robbins et al., 1983). The skull was denuded and secured to the head rotation fixture by plates that were attached to the superior, lateral, and posterior surfaces using a custom-built fixation jig. Artificial cerebrospinal fluid (aCSF), with a constant pressure of approximately 78 mmHg (Hardy et al., 2001) was used to provide constant perfusion (Sugawara et al., 1996) throughout testing. The perfusion inlets were

through the carotid arteries and ports at the sagittal sinus and occiput, and the fluid drained through the jugular veins and the spinal cord.

Sonomicrometry crystals (Sonometrics Corporation, London, Ontario, Canada) were implanted to quantify brain deformation in response to head rotations. A total of 40 crystals were utilized, with transmitting crystals affixed to the inner skull and receiving crystals inserted in the brain tissue. An array of 30 crystals were inserted into the brain using a stereotactic cannula system. The positions of the crystals were controlled by a guide plate that was fixed to the posterior surface of the skull. Only 24 of the 30 receivers were used during the tests (acquisition system capacity), with the additional six serving as backups in the case of noisy or non-functioning crystals. The chosen crystal positions were designed to avoid skull boundaries and ventricles while maximizing dispersion throughout the brain. Wire slack was intentionally introduced during insertion to ensure crystals do not displace during the testing relative to the brain tissue.

An array of 10 sonomicrometry crystals were rigidly coupled to the inner surface of the skull with the primary function of transmitting ultrasound pulses. The transmitters were fixed to the skull in locations that were designed to encompass all the receivers while ensuring that all receivers measured at least four transmitting signals. Only 8 of the ten transmitters were used during testing, with backups in the case of improperly placed or non-functioning crystals. After the installation of the sonomicrometry sensors, computed tomography (CT) images were acquired at a resolution of 0.625 mm to determine the initial coordinates of each receiver and transmitter relative to the head CG (Figure 5-1). Perfusion was applied during CT scans to ensure that the intracranial space was fully perfused and to obtain an accurate measurement of the initial position of all implanted sensors. A post-test

CT scan was also collected without mounting hardware to obtain a clean image of the cranium. An autopsy was also conducted for each specimen 6-8 days p.m. to investigate structural and anatomical variation among specimens (summary observations are presented in Appendix A).

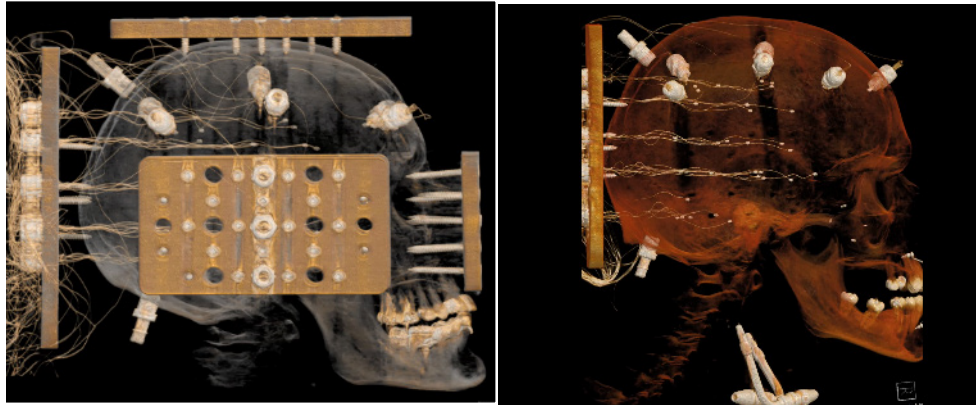


*Figure 5-1: Representative CT images following the specimen preparation and crystal insertion procedure. Specimen 903 (left) includes the mounting plates and instrumentation plate. Specimen 904 (right) shows the transmitters affixed to the skull, the receivers in the brain (note that slack is intentionally introduced in the wires during insertion), and the perfusion ports in the carotid arteries and occipital skull.*

### **Test Fixture and Matrix**

A custom-built rotational test device was designed to apply controlled and repeatable rotations to the head in the sagittal (posterior to anterior rotation), coronal (right to left rotation), and axial directions. The RTD used a cable-drive system to translate the linear output of the actuator into a rotational pulse. In all rotation directions, the head was inverted at the initiation of every test to allow for consistent perfusion. The rotation was applied through the head CG, and the specimen returned to its initial position after every test.

Four rotational severities were tested and consisted of haversine pulses with a peak angular velocity of 20 or 40 rad/s and duration of 30 or 60 ms. Peak angular accelerations ranged from 600 to 5500 rad/s<sup>2</sup>. The four severities were applied in each of the three anatomical axes for a total of twelve tests per specimen.

## **Head Kinematics**

The 6DOF kinematics of the head were measured using an array consisting of three Endevco 7264B-500 linear accelerometers (Meggitt Sensing Systems, Irvine, CA) and three angular rate sensors (ARS), ARS PRO-8k angular rate sensors (Diversified Technical Systems Inc., Seal Beach, CA). The sensor array was rigidly mounted to the head mounting plates. The array kinematics were transformed to the head coordinate system according to SAE J211 standards (1995). A SlicePRO data acquisition system (Diversified Technical Systems Inc., Seal Beach, CA) was used to acquire the data at a sampling rate of 10 kHz with an anti-aliasing filter of 2900 Hz. The linear acceleration data were filtered with a CFC 180 filter, and the angular velocity was filtered with a CFC 60 filter. Angular acceleration was calculated by differentiating the filtered angular velocity data. The peak angular velocity and pulse duration of every test for each specimen was calculated from the measured head kinematics.

## **Sonomicrometry Acquisition and Data Processing**

Sonomicrometry data was recorded using a 32-channel TRX-USB Acquisition System (Sonometrics Corporation, London, Ontario, Canada). Unfiltered data were collected at a sampling rate of 600 Hz for all tests, except for the pilot specimen. There were a total of 192 distance traces for each test. Before and after each test, static sonomicrometry data were collected to confirm that all receivers had returned to their original position. Sonomicrometry data were processed according to the manufacturer's recommendation to remove outliers and level shifts in the signals. Excessively noisy signals were removed and not included in subsequent analyses.

## **Sonomicrometry Trilateration**

Trilateration was utilized to determine the 3D coordinate time-history of each receiver crystal relative to the reference frame defined by the fixed transmitting crystals. The method uses the geometry of spheres to determine the absolute location of a point based on multiple distance measurements from fixed transmitters. Each distance trace was adjusted using an offset distance such that the initial position matched the corresponding distance measured in the CT images.

Once the data were processed and all ‘good’ traces were identified, trilateration was utilized to determine the 3-D coordinates of the receiving crystals relative to the reference frame defined by the fixed skull crystals. A custom script was written in MATLAB (Mathworks Inc., MA, USA) to trilaterate the displacement of each crystal using Kalman filtering. Kalman filtering iteratively estimates the position of receivers based on the distances at the next time step, assuming errors in the measured distances, allowing for a more accurate and reliable solution. The Kalman filtering algorithm was investigated for use in brain sonomicrometry among eight trilateration methods and yielded the most accurate and robust results (Chapter 4). All analyses were performed using a brain tissue speed of sound of 1540 m/s, which was chosen by optimizing distances in the static sonomicrometry data compared to those measured from the pre-test CT images.

The initial position ( $\tilde{x}_k$ ) at the first timestep was defined at the initial CT position of each receiver. For each subsequent time step, the initial estimated position was the position predicted by EKF at the previous time step. After the EKF algorithm predicted the position of the receiver in the brain, a set of quality control procedures were used to ensure that the estimation was accurate and that no “bad” signals were present in the data. For each receiver, the estimated distances to each transmitter were calculated and compared to the

experimental sonomicrometry distances. The root mean square error (RMSE) between the predicted and measured distances for each transmitter-receiver pair was found. If the RMSE was greater than 0.5 mm, the pair was marked as “bad.” In addition to the RMSE calculation, each prediction was manually reviewed to check for large deviations, as compared to the experimental data. If any receiver-transmitter pairs were removed, the EKF algorithm was run again and a new solution was checked. If any receiver fell below 4 transmitter-receiver pairs, it was removed from the analysis.

The processing and trilateration workflow can be summarized in the following steps:

1. Traces were processed for outliers and level shifts and marked as “good.”
  - a. Traces that were too noisy or did not receive transmission were marked as “bad.”
2. Data were adjusted to a speed of sound of 1540 m/s (original, 1590 m/s).
3. The initial distances in the sonomicrometry data were shifted to the CT-determined distance.
4. The initial guess of the first time step in the EKF was defined as the CT receiver position.
5. Trilateration algorithm was executed using processed, “good” traces with adjusted initial distances at each time step. The prediction of the previous time step was used as the initial guess for the next time step.
6. The predicted distances to each transmitter were calculated across time and compared to the experimental distance measurements.
7. Any transmitter-receiver pair that had an RMSE greater than 0.5 mm was removed if there were more than four pairs used.

- a. Any receivers that had less than 4 “good” transmitter-receiver pairs were removed from the analysis.
8. The EKF algorithm was re-run with adjusted data, and the final solution was found.

### **Peak-to-Peak Deformation Statistics**

The peak-to-peak deformation of every crystal for each test and specimen was calculated using the maximum point-to-point displacement during the trajectory of each receiver. The maximum and average peak-to-peak were calculated for each test and specimen for a total of 72 data points. The dependence of brain deformation on head kinematics was found using a multiple regression analysis. For each axis (sagittal, coronal, and axial), a regression fit was found using the 24 data points in that axis. The multiple linear regression model is shown below and includes an interaction term.

$$Pk - Pk = A * \omega_{peak} + B * \Delta t + C * \omega_{peak} * \Delta t + D \quad (5-1)$$

where ‘ $\omega_{peak}$ ’ denotes the peak angular velocity (rad/s),  $\Delta t$  denotes the measured duration (ms), and A, B, C, and D are the regression coefficients.

### **Comparison to Kinematic Injury Criteria**

The peak-to-peak deformation of the crystals was also used to compare the predictions of various kinematics-based head and brain injury metrics. Thirteen injury metrics were evaluated in this analysis, which were selected based on their dependence on various linear and rotation head kinematics, including both acceleration and velocity. Some of the metrics were developed based on mechanics theory or computational methods, but most of them were formulated based on phenomenological experimental fits. Head kinematics were described by the directionally-dependent, time history vectors of linear acceleration, angular acceleration, and angular velocity.

The translational only injury criteria evaluated include the Gadd Severity Index (GSI) and the Head Injury Criteria (HIC). The combined translational and rotational kinematics metrics include the Combined Probability of Concussion (CPC), Generalized Acceleration Model for Brain Injury Threshold (GAMBIT), Head Impact Power (HIP), and Kleiven's Linear Combination (KLC). The rotational kinematic metrics include the Brain Injury Criteria (BrIC), Power Rotational Head Injury Criterion (PRHIC), Rotational Injury Criterion (RIC), Rotational Velocity Change Index (RVCI), Universal Brain Injury Criterion (UBrIC), Convolution of Impulse response for Brain Injury Criterion (CIBIC), and Diffuse Axonal Multi-Axis General Evaluation (DAMAGE). Brief descriptions of each metric and the head kinematics utilized are specified in Table 5-3; specific formulations and critical values can be found in the referenced literature.

The injury criteria were evaluated using the 6DOF kinematics from each test (twelve tests total) for each specimen, for a total of 72 points. The maximum peak-to-peak deformation for each test was associated with the prediction of the kinematics-based injury criteria. For all injury criteria, a higher score is either associated with a higher percent chance of injury or an increase in brain strain. For all 72 points, a linear regression (without an intercept) was evaluated to assess the correlation between the injury criteria and the experimental peak-to-peak deformation. The  $R^2$  value was used to assess the correlation.

Table 5-3: Overview of existing head kinematics-based brain injury criteria.

| Injury Metric | Type | Development Method | Type of Injury      | Direction Dependence | Reference                     |
|---------------|------|--------------------|---------------------|----------------------|-------------------------------|
| GSI           | T    | Experimental       | Skull Fracture, TBI | No                   | (Gadd, 1966)                  |
| HIC           | T    | Experimental       | Skull Fracture, TBI | No                   | (Versace, 1971)               |
| CPC           | T, R | Experimental       | Concussion          | No                   | (Rowson and Duma, 2013)       |
| GAMBIT        | T, R | Theoretical        | Concussion          | No                   | (Newman, 1986)                |
| HIP           | T, R | Theoretical        | Concussion          | Yes                  | (Newman et al., 2000)         |
| KLC           | T, R | Computational      | Concussion          | No                   | (Kleiven, 2007)               |
| BrIC          | R    | Computational      | DAI                 | Yes                  | (Takhounts et al., 2013a)     |
| PRHIC         | R    | Experimental       | Concussion          | No                   | (Kimpara et al., 2011)        |
| RIC           | R    | Experimental       | Concussion          | No                   | (Kimpara and Iwamoto, 2012)   |
| RVCI          | R    | Computational      | DAI                 | Yes                  | (Yanaoka et al., 2015)        |
| UBrIC         | R    | Computational      | DAI                 | Yes                  | (Gabler et al., 2018a)        |
| CIBIC         | R    | Computational      | DAI                 | Yes                  | (Takahashi and Yanaoka, 2017) |
| DAMAGE        | R    | Theoretical        | DAI                 | Yes                  | (Gabler et al., 2018b)        |

\* T = Translational. R = Rotational.

## RESULTS

All specimen preparation and testing were completed within 72 hours post-mortem. There were a total of 72 tests conducted on a total of six specimens. The dataset included three-dimensional displacements for 1652 receivers, which corresponded to approximately 5000 response curves for motion in the orthogonal directions of motion (x, y, z).

## Rotational Head Kinematics

The target maximum rotational velocities were 20 rad/s and 40 rad/s, with durations of 30 and 60 ms. There were minimal linear accelerations and off-axis rotations of the head for all loading severities. Due to differences in the inertia of each specimen, there were slight variations in the head kinematics, predominantly in the sagittal and coronal directions. Measured head kinematics of all specimens for the axial 40 rad/s – 30 ms target rotations are shown in Figure 5-2. The average peak linear acceleration, angular velocity, angular acceleration, and duration are given in Table 5-4. A summary of the measured head kinematics for every test is included in Appendix C.

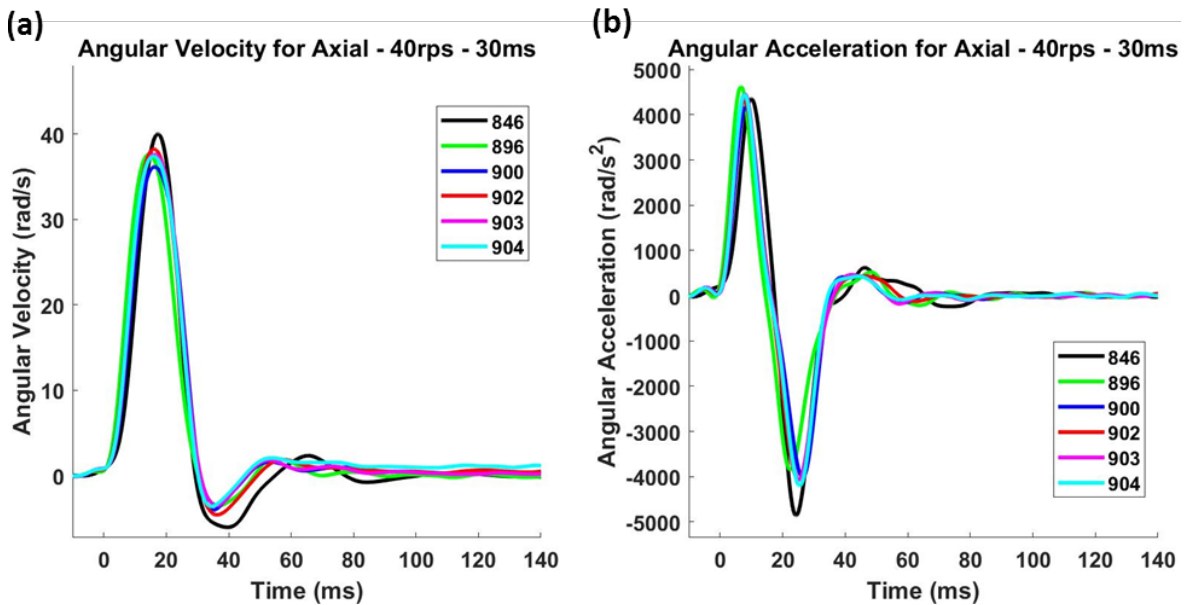


Figure 5-2: Angular velocity (a) and angular acceleration (b) plots for the axial – 40 rad/s – 30 ms rotation for all specimens.

Table 5-4: Summary of peak linear and angular head kinematic for all specimens. Means and standard deviations are shown.

|                 | Test       | Max LAC (g) | Max ARS (rad/s) | Duration (ms) | Max AAC (rad/s <sup>2</sup> ) |
|-----------------|------------|-------------|-----------------|---------------|-------------------------------|
| <b>Sagittal</b> | 20rps-60ms | 3.5 ± 0.6   | 23.1 ± 1.5      | 58.9 ± 3.0    | 1641 ± 291                    |
|                 | 20rps-30ms | 6.9 ± 2.1   | 16.7 ± 3.1      | 38.2 ± 12.2   | 1908 ± 574                    |
|                 | 40rps-60ms | 9.4 ± 2.3   | 43.6 ± 2.7      | 54.5 ± 4.0    | 3753 ± 692                    |
|                 | 40rps-30ms | 16.7 ± 6.5  | 39.9 ± 2.3      | 33.1 ± 2.0    | 5209 ± 525                    |
| <b>Coronal</b>  | 20rps-60ms | 4.6 ± 1.3   | 23.7 ± 1.5      | 62.2 ± 2.7    | 1455 ± 266                    |
|                 | 20rps-30ms | 7.8 ± 3.4   | 15.9 ± 2.3      | 40.4 ± 7.1    | 1527 ± 355                    |
|                 | 40rps-60ms | 10.7 ± 2.3  | 42.2 ± 2.9      | 60.6 ± 2.4    | 3826 ± 731                    |
|                 | 40rps-30ms | 18.0 ± 6.7  | 33.8 ± 3.1      | 35.7 ± 2.4    | 4342 ± 563                    |
| <b>Axial</b>    | 20rps-60ms | 4.6 ± 2.3   | 22.8 ± 0.7      | 64.7 ± 8.6    | 1803 ± 102                    |
|                 | 20rps-30ms | 7.0 ± 2.0   | 17.7 ± 1.4      | 36.4 ± 12.5   | 2193 ± 188                    |
|                 | 40rps-60ms | 10.6 ± 3.7  | 43.4 ± 2.0      | 61.1 ± 5.9    | 3363 ± 79                     |
|                 | 40rps-30ms | 24.0 ± 9.6  | 37.8 ± 1.3      | 29.1 ± 0.5    | 4484 ± 236                    |

LAC = Linear Acceleration. ARS = Angular Velocity. AAC = Angular Acceleration

### **Brain Motion (Sonomicrometry)**

The trilaterated trajectories of the sonomicrometry crystals in the brain, similar temporally and spatially to the traces of the pilot specimen, are given in Appendix D. A digital data archive of the dataset, which includes Excel files with six DOF head kinematics, sonomicrometry crystal initial position in the head coordinate system, and sonomicrometry crystal displacements, are available through the National Highway and Traffic Safety Administration (NHTSA) biomechanics database.

Trajectories of all receivers for the 20 rad/s – 30ms and 40 rad/s – 30ms tests for specimen 900 in the axial and sagittal directions, overlaid on an outline of the brain in the direction of rotation, are given in Figure 5-3. The brain motion in the plane of rotation follows a circular trajectory about a point, independent of the head CG. There was a larger magnitude of deformation for the 40 rad/s test as compared to the 20 rad/s rotation.

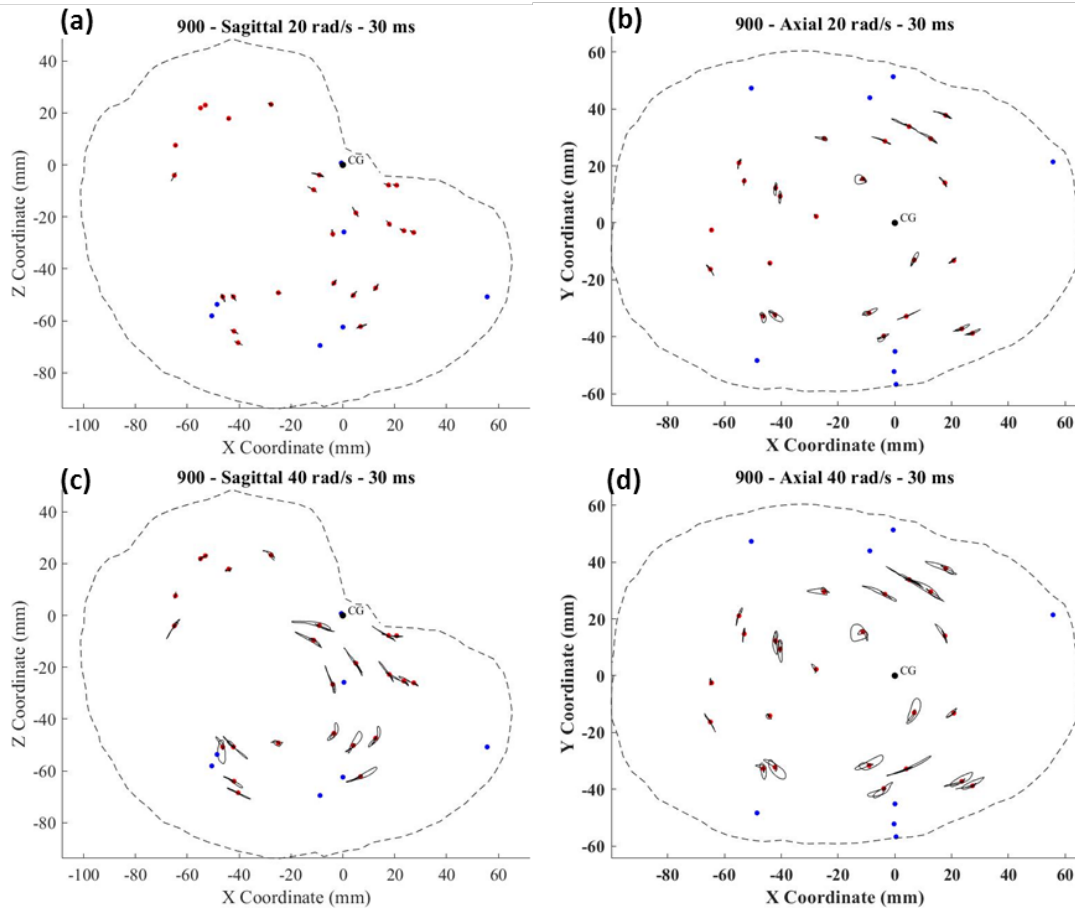


Figure 5-3: Trajectory plot for the 20 rad/s – 30ms (a-b) and 40 rad/s – 30ms (c-d) sagittal and axial tests for specimen 900. The red dots symbolize the initial position of each receiver. The black dot represents the CG of the head, about which the rotation was applied. Blue dots represent the transmitter crystals in the skull.

The peak-to-peak deformations for the 40 rad/s – 30 ms tests for each receiver for all specimens are shown in Figure 5-4. There was a spatial dependence of brain deformation, with receivers in the inferior brain regions, including the cerebellum and brainstem, experiencing low deformations across all rotation directions. There was also a directional dependence for the peak-to-peak motion of different regions of the brain. The peak-to-peak deformation of all receivers across all specimens and tests was quantified and is shown in a box plot in Figure 5-5. The maximum peak-to-peak deformation for every test for each specimen is included in Appendix C.

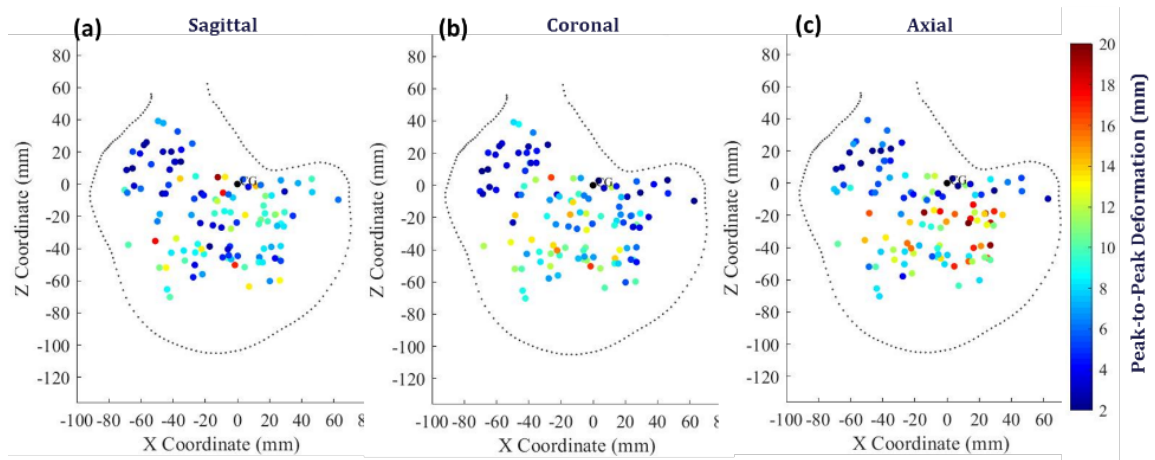


Figure 5-4: Peak-to-peak deformation of all crystals for all specimens for the axial – 40 rad/s – 30 ms tests in the sagittal (A), coronal (B), and axial (C) directions.

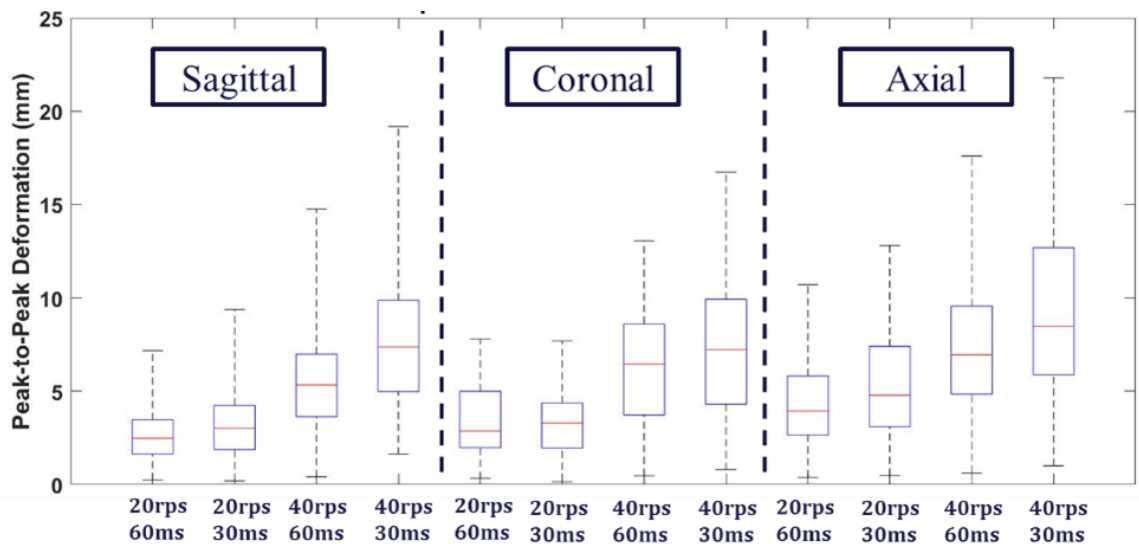


Figure 5-5: Box plots of peak-to-peak deformation for all specimens for each test. The blue boxes represent the 25<sup>th</sup> and 75<sup>th</sup> quartile values, the red line represents the median, and the dashed lines represent the maximum and minimum values.

### Peak-to-Peak Deformation Statistics

The maximum and mean peak-to-peak deformation for every test was utilized in a multiple linear regression to determine the dependence of brain deformation on angular head kinematics. For the maximum peak-to-peak deformation regression (Figure 5-6), the

model fits had an  $R^2$  ranging from 0.69-0.79. Coefficient values are presented in Table 5-5. The regressions showed a dependence of brain deformation on angular kinematics, with increasing angular velocity and decreased duration causing non-linear increases in maximum peak-to-peak deformation. The sagittal and coronal rotation directions had similar trends and magnitudes of peak-to-peak deformation, while the axial direction resulted in larger deformation for the same input kinematics.

For the mean peak-to-peak deformation regression (Figure 5-7), the model fits had an  $R^2$  ranging from 0.67-0.78. Coefficient values are presented in Table 5-6. The regressions showed a dependence of brain deformation on angular kinematics, with increasing angular velocity and decreased duration causing increases in maximum peak-to-peak deformation. Unlike the maximum peak-to-peak regression, the mean peak-to-peak showed similar deformations for the axial and coronal rotations and lower deformations for the sagittal rotation.

*Table 5-5: Regression coefficients, standard, and p-value for the regression of maximum peak-to-peak deformation to the varying head kinematic severities.*

| <b>DIRECTION</b> | <b>COEFFICIENT</b> | <b>ESTIMATE</b> | <b>STANDARD ERROR</b> | <b>P-VALUE</b> |
|------------------|--------------------|-----------------|-----------------------|----------------|
| <b>SAGITTAL</b>  | <i>A</i>           | 0.670           | 0.197                 | 0.003          |
|                  | <i>B</i>           | 0.103           | 0.135                 | 0.453          |
|                  | <i>C</i>           | -0.009          | 0.004                 | 0.055          |
|                  | <i>D</i>           | -4.534          | 6.125                 | 0.468          |
| <b>CORONAL</b>   | <i>A</i>           | 0.606           | 0.202                 | 0.007          |
|                  | <i>B</i>           | 0.052           | 0.121                 | 0.672          |
|                  | <i>C</i>           | -0.007          | 0.004                 | 0.097          |
|                  | <i>D</i>           | -1.787          | 6.071                 | 0.772          |
| <b>AXIAL</b>     | <i>A</i>           | 0.519           | 0.135                 | 0.001          |
|                  | <i>B</i>           | -0.015          | 0.083                 | 0.859          |
|                  | <i>C</i>           | -0.004          | 0.003                 | 0.118          |
|                  | <i>D</i>           | 4.116           | 4.187                 | 0.337          |

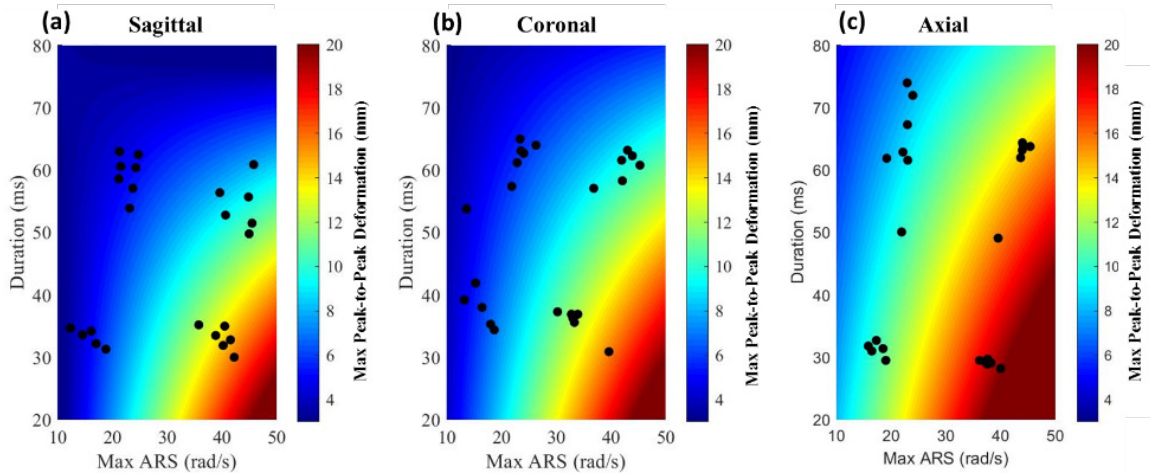


Figure 5-6: Surface plots depicting the results of the multiple linear regression of maximum peak-to-peak deformation using the maximum angular velocity (ARS) and duration for the sagittal (a), coronal (b), and axial (c) tests. The black dots correspond to the data points used in the regression fit. The sagittal regression model had an  $R^2$  of 0.691. The coronal regression model had an  $R^2$  of 0.693. The sagittal regression model had an  $R^2$  of 0.795.

Table 5-6: Regression coefficients, standard, and p-value for the regression of mean peak-to-peak deformation to the varying head kinematic severities.

| DIRECTION | COEFFICIENT | ESTIMATE | STANDARD ERROR | P-VALUE |
|-----------|-------------|----------|----------------|---------|
| SAGITTAL  | A           | 0.355    | 0.104          | 0.003   |
|           | B           | 0.055    | 0.071          | 0.447   |
|           | C           | -0.005   | 0.002          | 0.057   |
|           | D           | -2.388   | 3.250          | 0.471   |
| CORONAL   | A           | 0.346    | 0.101          | 0.003   |
|           | B           | 0.015    | 0.060          | 0.802   |
|           | C           | -0.004   | 0.002          | 0.085   |
|           | D           | -0.495   | 3.020          | 0.871   |
| AXIAL     | A           | 0.265    | 0.091          | 0.009   |
|           | B           | -0.003   | 0.056          | 0.963   |
|           | C           | -0.002   | 0.057          | 0.220   |
|           | D           | 1.845    | 2.842          | 0.524   |

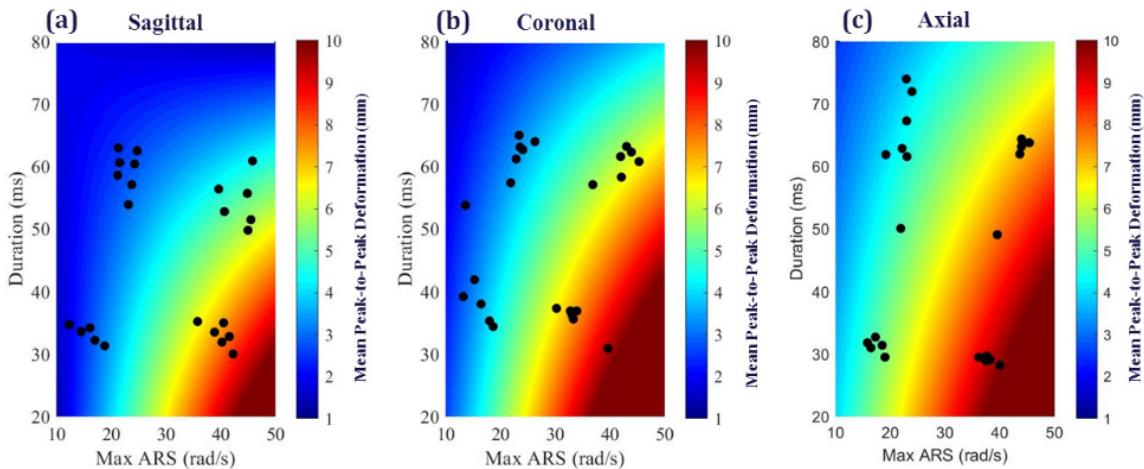


Figure 5-7: Surface plots depicting the results of the multiple linear regression of mean peak-to-peak deformation using the maximum angular velocity (ARS) and duration for the sagittal (a), coronal (b), and axial (c) tests. The black dots correspond to the data points used in the regression fit. The sagittal regression model had an  $R^2$  of 0.692. The coronal regression model had an  $R^2$  of 0.780. The axial regression model had an  $R^2$  of 0.675.

### **Comparison to Kinematics-Based Injury Criteria**

Thirteen kinematics-based injury criteria were compared to the maximum peak-to-peak deformation of all the specimens to assess their efficacy in predicting experimental brain deformation severity (Table 5-7). The translational injury criteria (GSI and HIC) had low correlations to the deformation. The combined rotational and translational criteria had good results for GAMBIT and HIP, but KLC had the lowest correlation of all injury criteria. For the rotational kinematics criteria, PRHIC had the lowest score, similar in magnitude to the translation criteria. RIC and RVCI (which was compared using its development with MPS and CSDM) performed similarly to the combined rotational and translational metrics. The best performing metrics were the most recently developed rotational kinematic metrics, including UBrIC (MPS-based), DAMAGE, and CIBIC. The best performing metric was CIBIC with an  $R^2$  of 0.744.

The injury criteria were also compared to mean peak-to-peak deformation, which takes into account the deformation of all receivers in the brain for all tests, instead of only

the maximum deformation. The correlation to the mean deformation was similar or lower for all injury criteria.

*Table 5-7: Correlation of kinematics-based injury criteria to maximum and mean peak-to-peak deformation. For criteria that include an associated risk of mTBI (AIS2+), a regression analysis is also conducted for the injury risk and deformation metrics.*

| <i>Criteria</i>      | <b>Criteria Value</b>                    |   | <b>Criteria Injury Prediction (AIS2+)</b> |   |
|----------------------|--|---|---|---|
|                      | <b>Max Peak-to-Peak <math>R^2</math></b> | <b>Mean Peak-to-Peak <math>R^2</math></b> | <b>Max Peak-to-Peak <math>R^2</math></b>  | <b>Mean Peak-to-Peak <math>R^2</math></b> |
| <i>GSI</i>           | 0.558                                    | 0.582                                     | N/A                                       | N/A                                       |
| <i>HIC</i>           | 0.557                                    | 0.580                                     | 0.459                                     | 0.468                                     |
| <i>CPC</i>           | 0.093                                    | 0.097                                     | 0.560                                     | 0.570                                     |
| <i>GAMBIT</i>        | 0.640                                    | 0.686                                     | 0.594                                     | 0.608                                     |
| <i>HIP</i>           | 0.660                                    | 0.660                                     | 0.499                                     | 0.519                                     |
| <i>KLC</i>           | 0.454                                    | 0.492                                     | N/A                                       | N/A                                       |
| <i>BRIC</i>          | 0.585                                    | 0.556                                     | 0.652                                     | 0.630                                     |
| <i>PRHIC</i>         | 0.573                                    | 0.559                                     | N/A                                       | N/A                                       |
| <i>RIC</i>           | 0.649                                    | 0.654                                     | 0.502                                     | 0.506                                     |
| <i>RVCI (MPS)</i>    | 0.649                                    | 0.682                                     | N/A                                       | N/A                                       |
| <i>RVCI (CSDM)</i>   | 0.619                                    | 0.606                                     | N/A                                       | N/A                                       |
| <i>U-BRIC (MPS)</i>  | 0.700                                    | 0.630                                     | N/A                                       | N/A                                       |
| <i>U-BRIC (CSDM)</i> | 0.623                                    | 0.587                                     | N/A                                       | N/A                                       |
| <i>CIBIC</i>         | 0.744                                    | 0.695                                     | N/A                                       | N/A                                       |
| <i>DAMAGE</i>        | 0.705                                    | 0.643                                     | N/A                                       | N/A                                       |

## DISCUSSION

An understanding of the biomechanics of the brain during injurious loading of the head is essential to predicting and mitigating injury. A human brain deformation dataset with accurate, repeatable, and well-defined loading conditions has represented a significant need

in the TBI biomechanics field. Expanding on a methodology developed in Chapter 3, this study generated a dataset of human brain deformation with six subjects varying in sex, age, and anthropometry. The dataset contains approximately 5000 brain motion traces that can each be used to improve and validate FE brain models.

### **Brain Biomechanics**

An extensive dataset of human brain deformation allows for insight into brain biomechanics that has previously relied on animal experiments and FE models. While previous human brain deformation experiments conducted a breadth of tests and severities with different specimens (Hardy et al., 2007), this is the first dataset to produce data for multiple loading directions and severities for the same set of specimens. This dataset allows for comparisons for the same point in the brain across different angular velocity, loading duration, and rotation direction. As observed in Figure 5-5, the axial rotation direction caused the largest maximum and average Pk-Pk deformation for all four loading severities. The sagittal and coronal directions had similar Pk-Pk deformation magnitudes, with the sagittal direction resulting in slightly greater maximum deformations. The spatial distribution of Pk-Pk deformations also differed across rotation axes, with the sagittal and coronal directions causing larger deformation in the inferior regions of the brain than the axial direction (Figure 5-4). All rotation directions experienced the largest deformations in the mid-cerebrum. The brain deformations also depended on the angular velocity and duration of the head rotation pulse (Figure 5-6). Increasing angular velocity and decreasing pulse duration resulted in larger maximum Pk-Pk deformations across all loading directions.

The regression analysis used to investigate the dependence on brain deformation on head angular velocity is simplistic, and was used in this study only to show a dependence on head rotational kinematics, not to predict or interpolate brain deformation at various magnitudes and duration of angular velocity. Although each regression had a high  $R^2$  value, only 24 data points were used to create each regression fit. Additionally, a more complex model could be used to fit the data, such as using a multi-body model (Gabler et al., 2018b), but these were not investigated in this study. The quantification of peak-to-peak deformation was also limited to the spatial distribution of crystals in each specimen. Since there was variability in crystal placement, differences in peak-to-peak deformation could be attributed to the sampled brain regions, and not the angular kinematics. These limitations prevent the use of the regression surface (Figure 5-6) to interpolate brain deformation or to predict injury risk.

### **Rotational Pulse Severities**

The rotational severities applied to the specimens were chosen to represent head impact conditions observed in automotive and sports impacts associated with mild-to-moderate risk of TBI. Based on a rotational brain injury criterion that utilizes head kinematics as the predictor (Brain Rotational Injury Criteria – BrIC (Takhounts et al., 2013a), the risk of AIS 2+ brain injury for the pulses in this study ranged from 4.3% to 99.3% risk. The correlation between human brain deformation and associated head impact severity has only been investigated using FE models. While this study provides a limited set of four severities across three loading directions, it is a valuable initial step into improving the link between head kinematics, brain deformation, and clinical injury risk. Statistically significant conclusions that relate rotational severity to brain deformation can

be made (Figure 5-6), but a wider range of severities is needed to allow for a better understanding of the link between rotational pulse severity and human brain deformation.

### **Finite Element Model Validation**

Direct measurement of tissue-level deformation of the brain under head impact, outside of controlled laboratory experiments, remains elusive and challenging. Anatomically-detailed FE models provide a valuable alternative and have been vital to approximating the temporal and spatial mechanical behavior of the brain. These models allow for a cost-effective investigation of the brain response under various loading conditions at a level that is not possible using cadaveric or human experiments. They have been created to predict injury using strain-based injury metrics, influencing governmental automotive safety standards and product development across multiple industries. It is essential to validate the brain deformation predicted by these models using human brain motion under repeatable injurious loading conditions. The availability of this digital dataset of human brain deformation with precise measurement location and six DOF loading conditions, as well as similar loading conditions for multiple specimens, allows for thorough and rigorous validation of FE models. The biofidelity of these models is of utmost importance to the TBI field, and meticulous comparison of model-simulated brain motion to this human experimental brain motion is essential.

### **Extension of Sonomicrometry Method**

One of the most prominent debates in the field of TBI injury biomechanics has been on the roles of linear and rotational kinematics on brain injury. However, due to the incompressible nature of the brain tissue and closed volume of the skull, the prevailing hypothesis is that rotational, not linear, kinematics are responsible for the shear

deformations of the brain tissue that lead to the diffuse injuries associated with TBI. While this concept has been demonstrated using computational brain models (Gabler et al., 2018a; Giudice et al., 2018a; Takhounts et al., 2013a), this is the first experimental dataset to demonstrate large magnitudes of brain deformation during dynamic head rotation. The sonomicrometry methodology developed in this project provides a unique platform for investigating the influence of head kinematics on the ensuing brain deformation in a controlled and repeatable manner. To expand this line of research, future investigations may be performed in pure linear loading conditions or combined rotational and linear loading conditions using the platform developed in this study to examine the relative contributions of each type of loading to brain deformation.

One of the major questions in the field of brain biomechanics is the response of the brain due to multiple impacts. The results of this study show that the brain remains in transient motion up to 100-200 ms after the onset of head rotation. In automotive and sports impacts, the head is often impacted multiple times in the span of 100 – 200 ms due to the chaotic nature of these environments. It is unclear how the brain responds to second impacts while it is still in transient motion. Such impacts could have a superposing effect on brain deformation, leading to exacerbated injury risk. The experimental methodology presented here provides a potential opportunity to study such events in a controlled, repeatable manner.

The sonomicrometry method can also be extended to animal models, allowing correlation of brain deformation to clinical injury. Matched-pair testing may then be performed with sonomicrometry and survival cohorts receiving identical loading to identify injury prediction metrics and pathological outcomes. Such studies would help to

“close the loop” that has existed between biomechanical input, brain deformation, and injury.

## **CONCLUSION**

The sonomicrometry method was utilized to generate a dataset of human brain deformation containing six specimens, twelve test severities, and approximately 5000 individual brain deformation traces. The peak-to-peak deformation of the brain demonstrates the dependence of brain deformation on rotation severity, loading direction, and location within the brain. This brain deformation dataset can be used to investigate fundamental brain mechanics, create kinematics injury criteria for safety standards, and develop and re-validate FE brain models.

The availability of a dataset of human brain deformation with specimens tested with repeatable loading conditions allows for the aggregation of the data into an average specimen response. Average data corridors are typically used in biomechanics to aggregate the data from multiple specimens into an average that describes the intra-population variability. Since this is the first series of experiments to test the same specimens under multiple severities, aggregated data corridors can be created with the six specimens in the dataset. The average response is also useful to the validation of FE brain models; FE models created to represent population average, such as a 50<sup>th</sup> percentile male, could be validated using the corridors.

## **CHAPTER 6: AVERAGE DATA CORRIDORS**

The *in situ* human brain deformation dataset generated in this dissertation provides a valuable tool for understanding the mechanics of the brain and validating FE models of the brain based on individual specimen response. However, typical FE models are constructed to represent a specific anthropometry or subset of a population, such as a 50<sup>th</sup> percentile male. The experimental data used to validate the response of FE models are often combined into average data corridors that represent the population response by taking into account variations among the individual specimens. An aggregation of the data into average response corridors will also provide insight into intra-population variances in the dataset, given the range of specimen anthropometry, anatomy, and biological characteristics. There are currently no reported average data corridors for human brain deformation. To create the first brain deformation average response corridors, new techniques are required to aggregate this type of data given some differences in the tests among the specimens. This chapter will focus on the development of the brain deformation average data corridors from the six specimens available in the dataset from Chapter 5.

### **INTRODUCTION**

Average data corridors are commonly developed in injury biomechanics to represent a population response from a set of experimental tests. They are used primarily in the development of physical models for injury, such as anthropomorphic test devices or dummies, and in the validation of FE models. The experimental response is typically two-dimensional (e.g., force or displacement versus time) and includes variations in the magnitude, shape, and temporal behavior of the signal (Lessley et al., 2004). Much like one-dimensional data that uses an average and a standard deviation to represent the

variability of a response, average data corridors use a dynamic average and standard deviation to incorporate population difference into the corridor response. The creation of average data corridors is difficult for dynamic biomechanics data due to variations in the response spatially and temporally (Ash et al., 2012; Kim et al., 2013). There are also variations in the testing procedure and specimen characteristics that can exacerbate the difficulties in creating an average dataset. The variation stems from specimen anatomy and anthropometry as well as the experimental variation inherent to complex preparation and testing procedures.

Corridors are typically used in the validation of FE models to provide a reasonable target for comparing a specific model to an aggregate set of data. Ideally, the data represents a population response, by incorporating samples from the target population. FE models of the brain are used to simulate the response of the brain under a variety of loading conditions and for a wide range of subjects (Giudice et al., 2018a). Most of the developed FE models of the brain are generated to represent the response of a specific gross anthropometry (e.g., a 50<sup>th</sup> percentile male), even though there are differences in neuroanatomy, age, sex, and material response across individuals. Of the sixteen FE brain models developed in the last two decades, only two have been models created with a subject-specific framework that allows for the reconstruction of impacts specific to an individual (Ghajari et al., 2017; Giudice et al., 2018a; Miller et al., 2016).

The FE models created to represent a target population based on a specific anthropometry, such as the GHMBC (Mao et al., 2013) and SIMon (Takhounts et al., 2008b) models representing a 50<sup>th</sup> percentile male, are typically validated using data from multiple tests, with each test representing the response of a single specimen from the Hardy

et al. (2007) dataset. Only three to five individual tests from the 62-test Hardy dataset have been used in the validation of most of these models (Miller et al., 2016; Takhounts et al., 2008b). While the models can arguably be validated to the specimen with the closest anthropometry or target population characteristics, they must also be compared to an average population response. Previous brain deformation datasets could not aggregate data from multiple specimens into a population response because of the inconsistent loading conditions and differences in impact direction associated with the Hardy et al. (2001) methodology (Alshareef et al., 2018).

An extensive amount of preliminary work for the sonomicrometry brain deformation dataset was done to match loading kinematics, crystal placement, and experimental procedures. Despite these considerations, variation across specimens was inevitable. The techniques typically used in injury biomechanics to generate corridors (Kim et al., 2013; Lessley et al., 2004) are insufficient for the sonomicrometry brain deformation data because they do not account for differences in loading condition or sensor placement. New techniques are required to aggregate the sonomicrometry brain deformation dataset into average response corridors.

The objective of this chapter is to combine the dataset of six specimens to generate average data corridors for brain deformation. The methods section will focus on using various numerical and statistical procedures to account for inherent variation in the specimens, as well as variation introduced in the experimental procedure. The contribution of this study will be an average response of human brain deformation, consisting of twelve loading conditions that can be used to validate FE brain models and to better understand intra-population variations in brain response.

## **METHODS**

The three major categories of variation across the specimens include head loading kinematics, cranial geometry, and initial crystal position (or placement). The following sections will explain the techniques used to account for the effect of each of the three sources on the average brain deformation response. The techniques were implemented in sequential order, starting with the variation in head kinematics to ensure that all loading severities were matched to a common severity of head rotation. Next, the differences in subject anthropometry and geometry were accounted for using a position and displacement registration technique. Finally, the initial positions of the crystals were interpolated using an inverse weighting method to generate brain deformation corridors using the six specimens. While the presented method was intended to remove testing differences across specimens, the final corridors included the inherent specimen variability caused by population differences, such as internal neuroanatomy, age, sex, and brain material properties.

### **Variation in Loading Kinematics**

During the specimen testing procedure (Chapter 3), each head-neck specimen was procured at the spinal T1 level to maintain similar size and mass of each specimen. There were differences in specimen inertial properties, however, because of the denuding procedure and specimen anthropometry variations. Although the RTD runs on a closed-loop feedback, the PID for this device was tuned to a specific inertia. Thus, deviations from the tuned inertia resulted in differences in the input rotational kinematics controlled by the RTD, which varied by  $6.26\% \pm 4.78\%$  in the magnitude of the peak angular velocity and  $4.72\% \pm 2.61\%$  in pulse duration across all specimens except 846. The inertial properties

of each specimen also governed the overshoot present in the deceleration phase as the head comes to a stop, which ranged from 0.5-8% of the magnitude of the maximum angular velocity, most prominently in the 30 ms duration tests. The RTD was re-tuned after the first specimen (846) to allow for better control of inertial differences and to minimize overshoot, which resulted in similar input kinematics for the remaining five specimens. Summaries of head kinematics for all specimens are presented in Appendix C.

To account for the variation in loading kinematics, linear state-space transfer functions were generated in MATLAB (Mathworks Inc., MA, USA) to adjust each crystal displacement time-history to common loading input. The transfer function was generated by creating a data object in MATLAB (function “iddata”) using the angular velocity in the direction of motion as the input and the sonomicrometry trilaterated displacement as the output. Next, the “tfest” function was used to predict a transfer function between the input and output data. The default “tfest” function was modified to fit the numerator and denominator of the transfer function using a non-linear least squares fitting function with enforced stability (“lsqnonlin” with “Levenberg-Marquardt” algorithm.). The choice of the number of zeros and poles in the predicted transfer function was optimized for a number of poles and zeros between 2 and 4, with a constraint that the number of zeros could not be greater than the number of poles. The final number of poles and zeros was the combination with the minimum normalized root mean square error (NRMSE) between the original displacement data and the predicted displacement using the transfer function (with original kinematics) normalized by the maximum magnitude of the signal. The NRMSE is subtracted from a value of 1 so that the metric ranges from a value of negative infinity (bad fit) to a value of 1 (perfect fit). A unique transfer function was created for every

direction of motion (x, y, z) for every crystal for all tests. In addition to the sum of square error, a Correlation and Analysis (CORA) (Gehre et al., 2009) score was used to assess the quality of the simulated response of the transfer function.

Although the transfer function yielded a good fit for most brain deformation displacements, there were cases with unstable transfer functions or a low NRMS. An unstable transfer function may drastically alter the shape and magnitude of the brain deformation response. A threshold was used to determine whether the transfer function should be used instead of the original data. To ensure the quality of data, an NRMSE threshold of 60% was used to determine if the normalized data (using the transfer function) was used. If the NRMS was below the threshold, the original, unscaled brain deformation response was used.

A common set of head kinematics was required for the corridors to normalize the brain deformation response of each specimen. For each of the five specimens after the RTD was re-tuned (896, 900, 902, 903, and 904), each kinematic pulse was scaled in magnitude to match either 20 rad/s or 40 rad/s and scaled in time duration to match either 30 or 60 ms. The two scale factors were applied to each of the twelve kinematic severities for each test. The common kinematic input was chosen to be the average of the scaled kinematics of the five specimens. The scaled traces were averaged for each test severity for a total of twelve common scaled kinematic curves. The common kinematic input for each severity was used as the input to the transfer function for every crystal in each direction for each specimen.

### **Variation in Head Anthropometry**

There were variations among the specimens in the shape and size of the brain and cranium. Even in specimens with similar whole-body anthropometry, differences were

present in the volume, length, width, and height of the intra-cranial space. The specimen anthropometry information and head measurements are presented in Chapter 5.

While simple linear scaling techniques can be utilized to account for variations in the head across specimens, they will not account for shape differences in skull geometry. A morphing technique was developed to account for these differences and normalize the locations and displacements of all crystals to a common brain anthropometric space. This procedure is similar to normalization spaces used to register images in Magnetic Resonance Imaging (MRI) (Avants et al., 2011). The common normalization space used in this study was the inner cranial geometry of the GHBMC M50 v4.4 finite element model, although any common parametric space could be utilized (such as another FE brain model). An overview of the registration methodology for the receiver positions and displacement for each specimen is shown in Figure 6-1. An in-depth explanation of the morphing methodology is presented in Appendix B.

The technique used to morph each skull to the common space was based on a morphing technique by Park et al. (2018). First, the geometry of the inner skull of the specimen was created by segmenting the skull from the CT scan. Then, the segmented geometry was aligned and linearly scaled to the target geometry of the GHBMC skull manually, and then the two surfaces were aligned using an iterative closest point approximation (Besl and McKay, 1992). Next, the segmented specimen CT inner skull was mapped to the GHBMC skull surface using an iterative registration method (Burr's elastic registration, Bryan et al. 2010) to match the external geometry of the two surfaces. The same transformation in this step was then applied to the initial crystal positions and the crystal displacement (at each time point) using a thin-plate spline method with a radial basis function. The method

interpolates the 3D morphing function based on the surface registration (Rohr et al. 2001) to obtain the receiver positions and displacements in the GHBMC brain registration space. This normalization process was applied to the data that had already been adjusted using the kinematic transfer function, yielding data that had been normalized to the same input kinematics and the same anthropometric space.

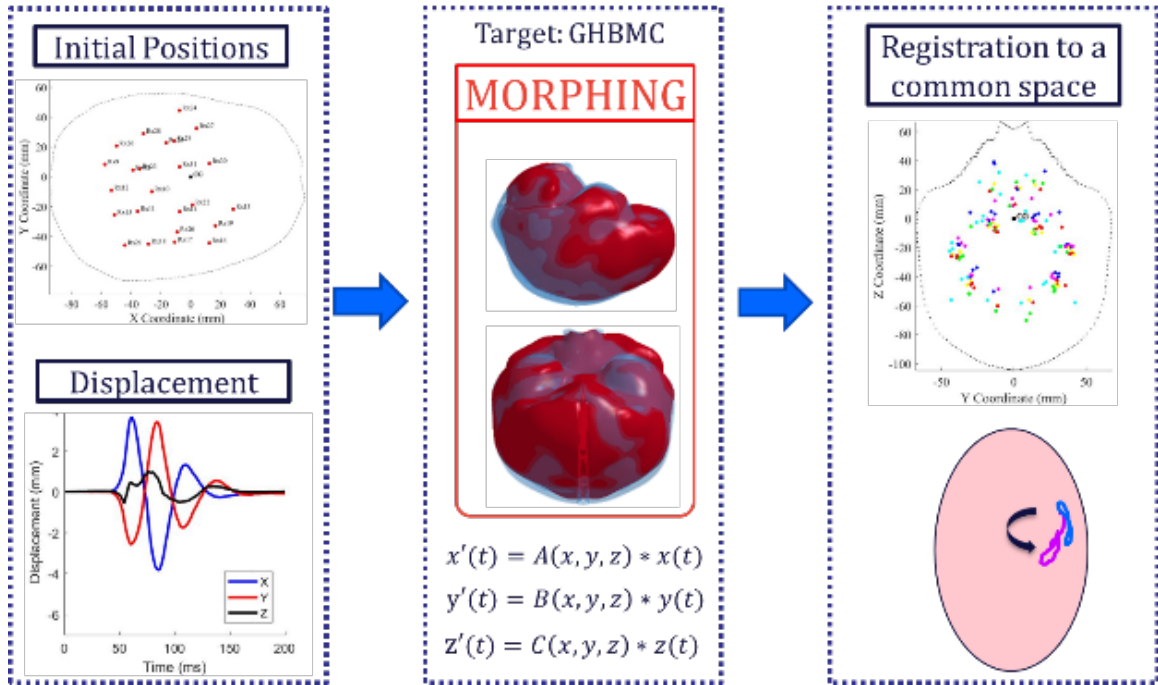


Figure 6-1: A morphing registration method was used to account for anthropometric differences among specimens. The cranium shape of each specimen was registered to a common 3D parametric space, chosen to be the GHBMC brain model, using a surface registration methodology. The registration parameters in each direction (A, B, and C) are used to map the position and displacement to the parametric space.

### **Variation in Initial Crystal Position**

After normalizing the initial position of every receiver to a common anthropometric space, there were still differences in the initial positions of each receiver among specimens due to differences in placement during specimen preparation or due to the use of extra crystals to replace non-functioning crystals. To generate average displacement corridors that combine the brain deformation results of all specimens, the responses of equivalent

receivers for each specimen must be combined. Ideally, the same receiver (e.g., Rx-9) would be combined for all specimens to calculate the average response. The normalized positions of all receivers relative to the outline GHBMC brain are shown in Figure 6-2.

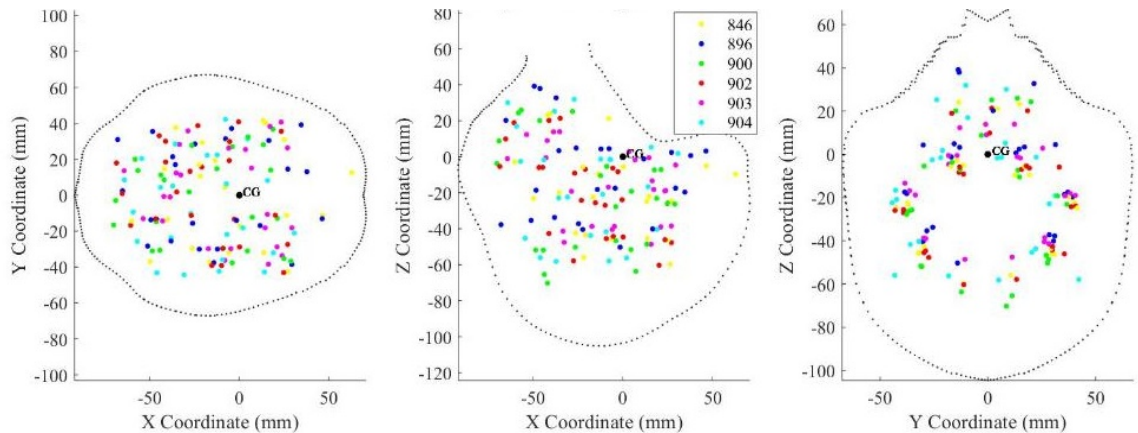


Figure 6-2: Normalized crystal position for all specimens.

Three methods were investigated to aggregate the responses of the various crystal positions in the registered brain space: an organized grid method (grid), a cluster method using all receivers (cluster-all), and an optimized cluster method after removing outliers (cluster-optimized). The grid method utilized an iterative grid of points to span the range of receiver positions in all three dimensions. The grid was composed of 50 points dispersed throughout the normalized anthropometric space, encompassing the location of all crystals used in all of the tested specimens. The grid is shown in Figure 6-4. An advantage of using the grid point approach is the ability to generate reliable corridors at a large number of discrete points in the brain while still utilizing information from a majority of the crystals and all of the specimens. The disadvantage of this method is the non-unique nature of the solutions at each discrete point. Depending on the spatial interpolation method used to determine the response at each grid point, the displacements may represent the response of a region of points, not only the discrete point chosen for this analysis.

The cluster methods utilized the initial receiver positions of all specimens to generate 24 points that represent the average position of the receiver. In the cluster-all method, the positions for the equivalent receivers of all specimens were averaged to find a mean position. The cluster-all points are shown in Figure 6-4. The advantage of this method is that the points used in the corridor development represent the variation in the placement of the receivers during the experiments. The disadvantage is that an outlier or large variance in receiver placement can cause cluster point positions to be in positions with no nearby receivers. A solution to this problem was implemented in the third method (cluster-optimized) by manually removing up to two outlier receivers (based on position), if necessary, from the calculation of the average position in every cluster. An example of this process is shown in Figure 6-3. For the receiver in Figure 6-3A, the position of the receiver for all specimens was within a tight cluster of points. The receiver in Figure 6-3B, however, included one outlier for specimen 904. The position of the receiver from specimen 904 was removed and the average position was calculated for the remaining five specimens. This process is only employed to calculate the average position, not to discard the displacement data from that receiver. The corridor points generated using the cluster-optimized method are shown in Figure 6-4. An advantage of the cluster-optimized method is a set of cluster points that have a tight set of experimental points surrounding them, which will allow for a more reliable corridor calculation. A disadvantage is that, unlike the grid method, there are only 24 discrete points used to generate corridors.

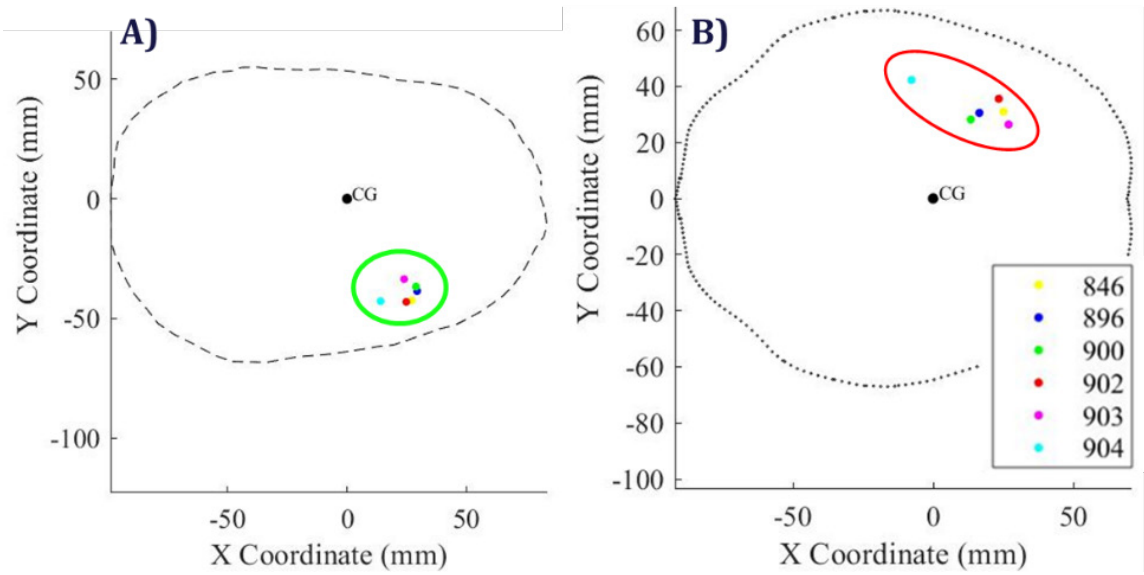
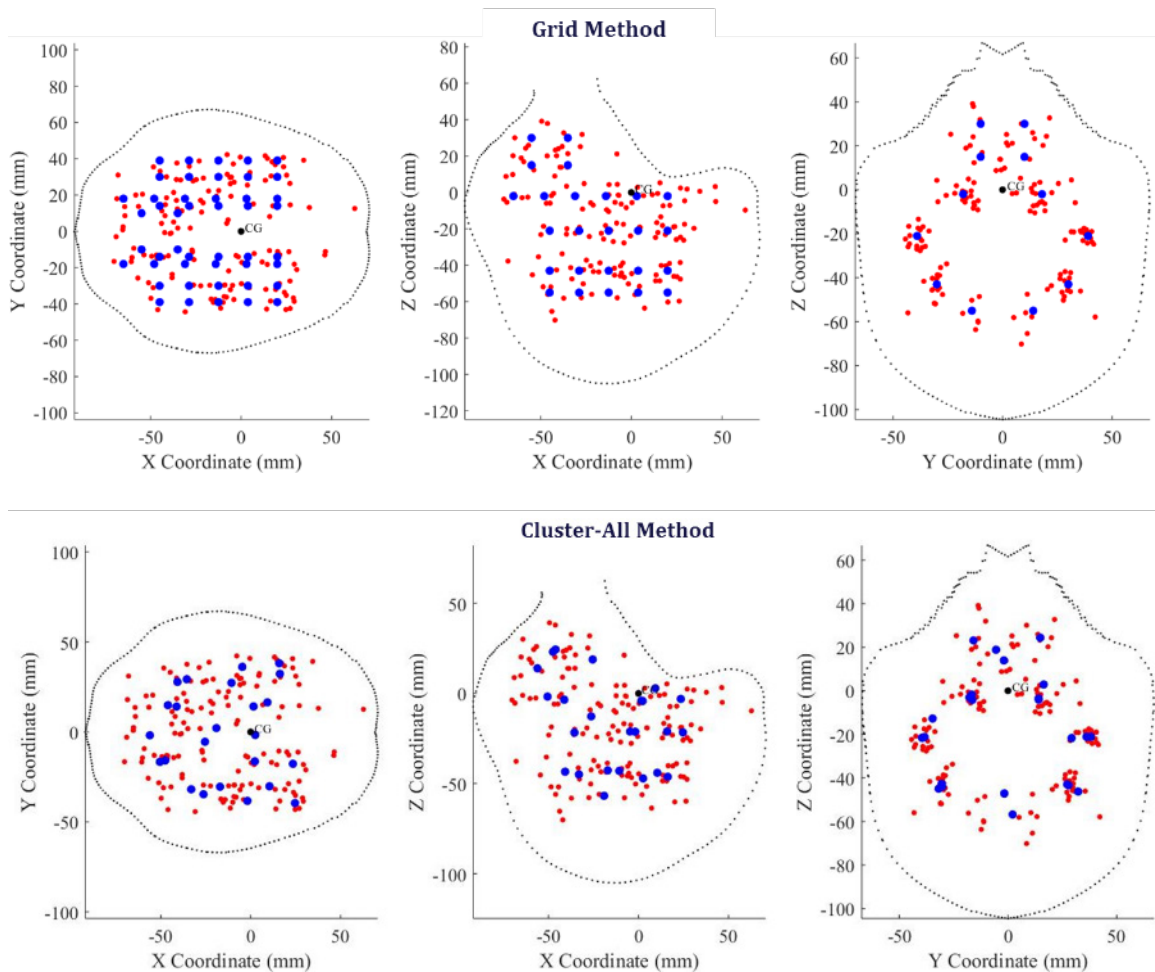


Figure 6-3: Depiction of the optimization of the cluster positions. For cases where all specimens had a tight clustering of normalized positions (A), no receivers were removed. For cases where there are outliers (B), up to two receivers were removed from the cluster point average position.



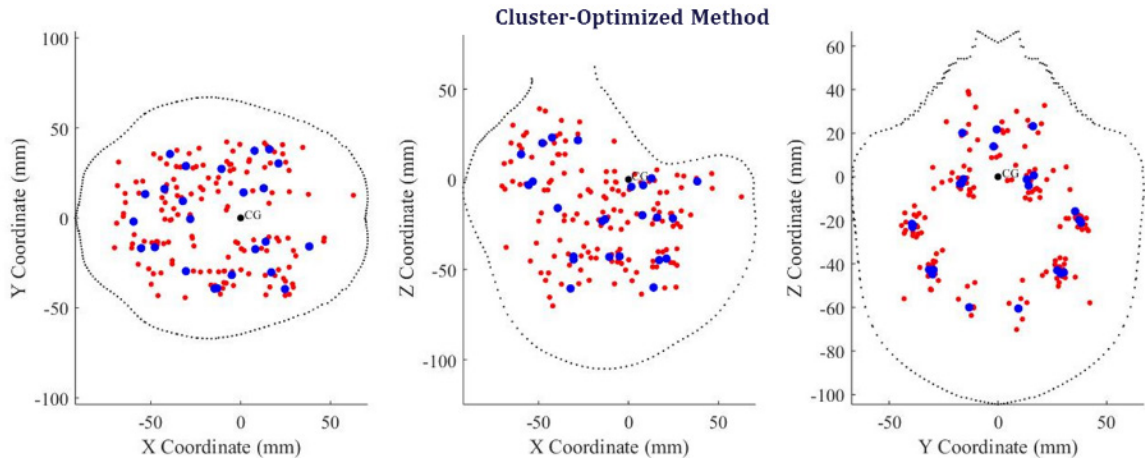


Figure 6-4: Methods of generating discrete points for brain deformation corridor development. In the grid method, points were generated using a spatial grid. Normalized receiver locations are indicated in red. Sample points for the corridors are shown in blue. For the cluster-all method, an average of equivalent receivers was taken for all specimens to generate the corridor points. For the cluster-optimized method, outliers from the cluster-all method were removed to generate average positions based on a subset of specimens.

### **Scattered Data Interpolation**

For each of the twelve test conditions, the response of each corridor point to the common kinematic input was calculated by aggregating the response of nearby crystal responses. For each corridor point, the nearest six crystals from all subjects, by distance, were found and their response was aggregated using an inverse distance weighting (IDW) approach. IDW has been used as an interpolation technique at discrete points with unknown responses for irregularly spaced data in climate map estimation (Babak and Deutsch, 2009; Nalder and Wein, 1998) and computational mechanics (Li et al., 2000; Lukaszyk, 2004). The distance metric used in IDW is usually the Minkowski metric, given in (6-1), describing the distance ( $d_i$ ) between the unknown point ( $M$ ) and each of the known experiment points ( $N_i$ ). The Euclidean distance is a special case of the Minkowski metric where  $p = 2$ .

$$d_i^{(p)} = \left[ \sum (M_{(x,y,z)} - N_{i(x,y,z)})^p \right]^{1/p} \quad (6-1)$$

In the simplest formulation, introduced by Shepard (1968) (Shepard, 1968), the weighting factor is the inverse of the distance from the corridor point to the nearby experimental data points. An exponent is applied to the distance term ( $u$ ) and must be optimized to the given data ((6-2). The Liszka (1984)(Liszka, 1984) weighting factor includes an error term ( $\delta$ ) derived through a Taylor series expansion of assumed errors at the experimental points ((6-3). In Lukaszyk (2004)(Lukaszyk, 2004), the experimental points are presumed to contain an error with an assumed distribution ((6-4).

$$w_i = \frac{1}{[d_i^{(p)}]^u} \quad (6-2)$$

$$w_i = \frac{1}{[d_i^{(p)} + \delta^2]^3} \quad (6-3)$$

$$w_i = \frac{1}{[D_{NN}^{(p)}]^u}, \text{ where} \quad (6-4)$$

$$D_{NN}^{(p)} = d_i + \frac{2s}{\sqrt{\pi}} \exp\left(-\frac{d_i^2}{2s^2}\right) - d_i \operatorname{erfc}\left(\frac{d_i}{2s}\right)$$

The distance weights ( $w$ ) is a vector describing the weighted contribution of each of the experimental points. In this study, the six closest receivers to each corridor point were chosen to calculate the weighted response, representing the number of specimens in the dataset. A distance-weighted average ((6-5) and standard deviation ((6-6) were used to generate an average response and standard deviation corridor for each grid or cluster point. The corridor response for each of the twelve kinematic test conditions was defined as the average response with a +1 and -1 standard deviation corridor for each of the corridor points.

$$X_{avg} = \frac{\sum_{i=1}^6 X_i * w_i}{\sum_{i=1}^6 w_i} \quad (6-5)$$

$$X_{std} = \sqrt{\frac{\sum_{i=1}^6 (X_i - X_{avg})^2 * w_i}{5 * \sum_{i=1}^6 w_i}} \quad (6-6)$$

### **Validation and Optimization**

The GHBMCM FE brain model was utilized to validate and optimize the parameters of the IDW methodology as well as the choice of the corridor point method (grid or cluster). The normalized receiver locations of all specimens, a total of 144 receivers, were compared to the position of the nodes of the FE model, relative to the CG. The corresponding nodes for the corridor points, for the grid and cluster methods, were determined in the same manner. The models were simulated under three rotation conditions, 40 rad/s – 60 ms for the sagittal, coronal, and axial directions.

The data aggregation was conducted on the three simulated models for all of the corridor point methods (grid, cluster-all, and cluster-optimized) and the three IDW methods, including an optimization of the variables  $p$  and  $u$ . An RMS error was quantified between the true FE brain deformation result at the corresponding corridor points, and the predicted FE brain deformation result using the IDW methods. The maximum standard deviation across the dynamic brain deformation signal was also used as a metric of corridor fit. An average of the RMS error and maximum standard deviation was taken across all corresponding corridor points to determine the best method or optimize the parameters.

## **RESULTS**

### **Kinematic Transfer Functions**

The common head kinematics generated from the average, scaled kinematics (in both magnitude and time) were smooth and yielded a representative curve for every rotation direction. An example of the axial 40 rad/s, 30 ms case is presented in Figure 6-6. All of the common head kinematic loading cases are presented in Appendix E.

The numerical transfer functions used to predict the displacement of each sonomicrometry brain deformation signal in response to the common scaled kinematics were simulated with the original data to ensure the stability and reliability of each transfer function. Any transfer functions with an NRMS error less than 60% were not used and the original sonomicrometry data was not altered. An example of the transfer function prediction for two receivers is given in Figure 6-5.

The average CORA score for all receivers for all test for each specimen was calculated and is shown in Figure 6-7. Overall, all transfer functions had an average score of 0.88-0.92, indicating an excellent transfer function prediction to the original data. Once the transfer functions were created and validated, they were used to generate scaled responses for each crystal for each test for every specimen.

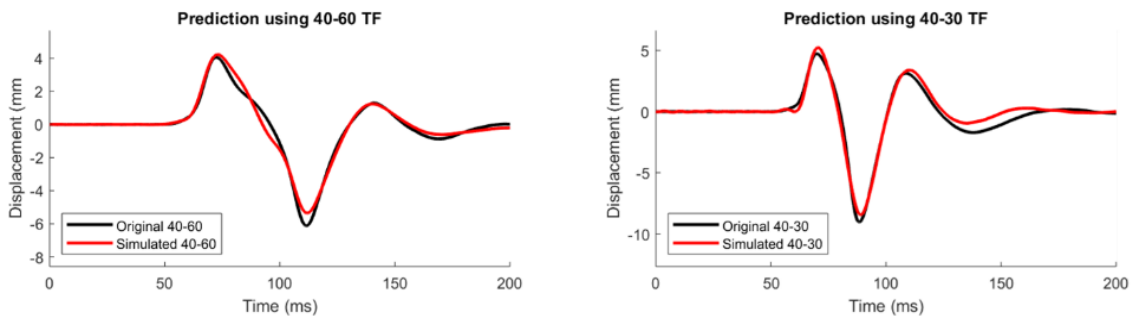


*Figure 6-5: The transfer function prediction for the x-axis deformation two receivers for the sagittal 40 rad/s – 60 ms (left) and the sagittal 40 rad/s – 30 ms (right) tests.*

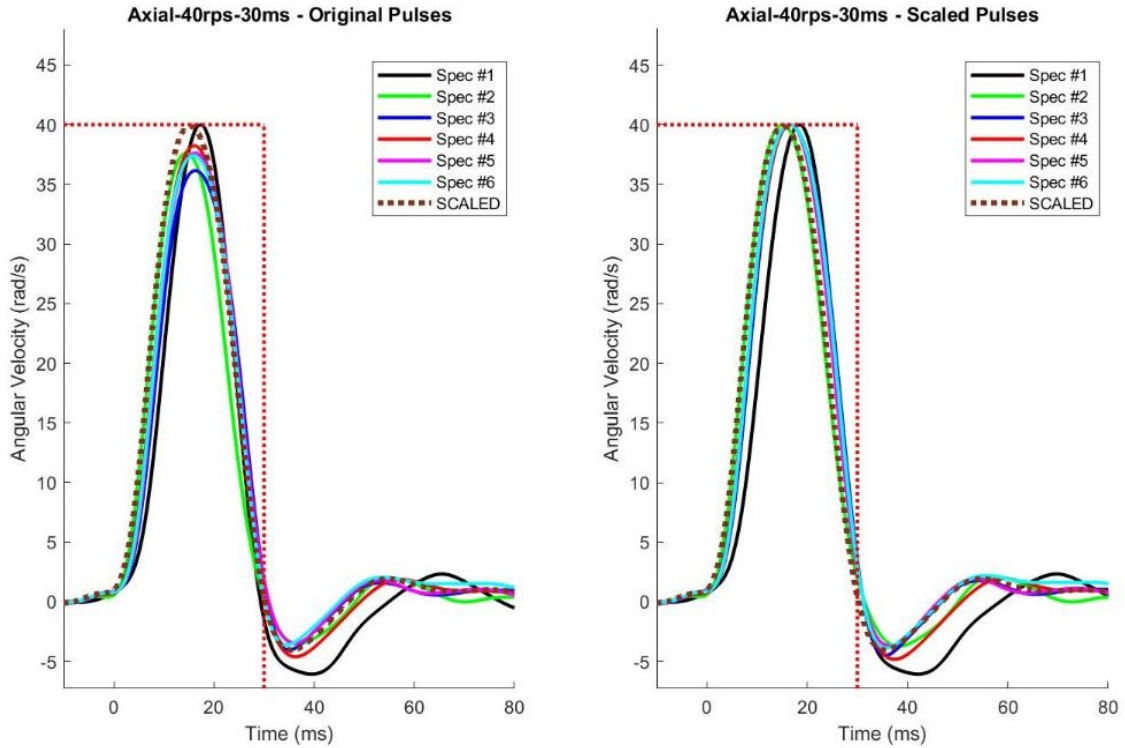


Figure 6-6: The common input of the scaled kinematics for the axial – 40 rad/s – 30 ms test, with the original pulses (left) and the scaled pulses (right). The average common loading kinematics is denoted by the dashed red curve, denoted by “SCALED”. The red dotted lines indicate the target magnitude and duration of the rotation.

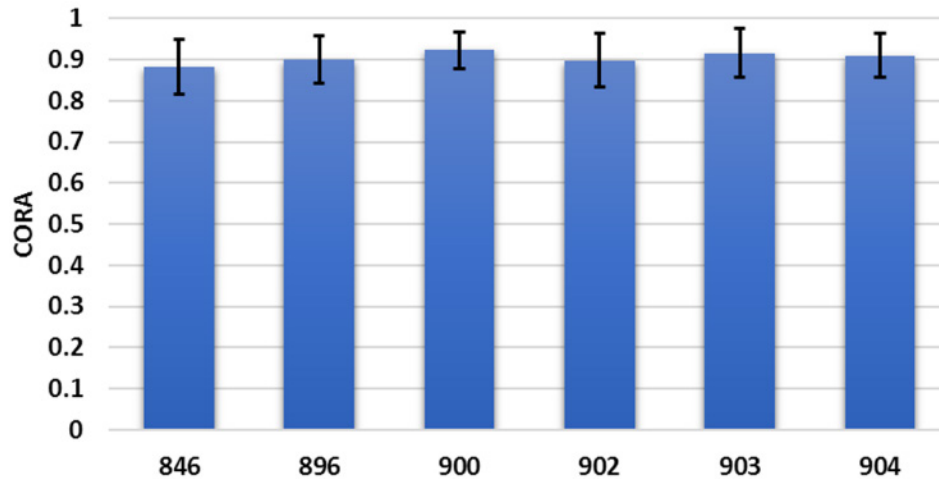
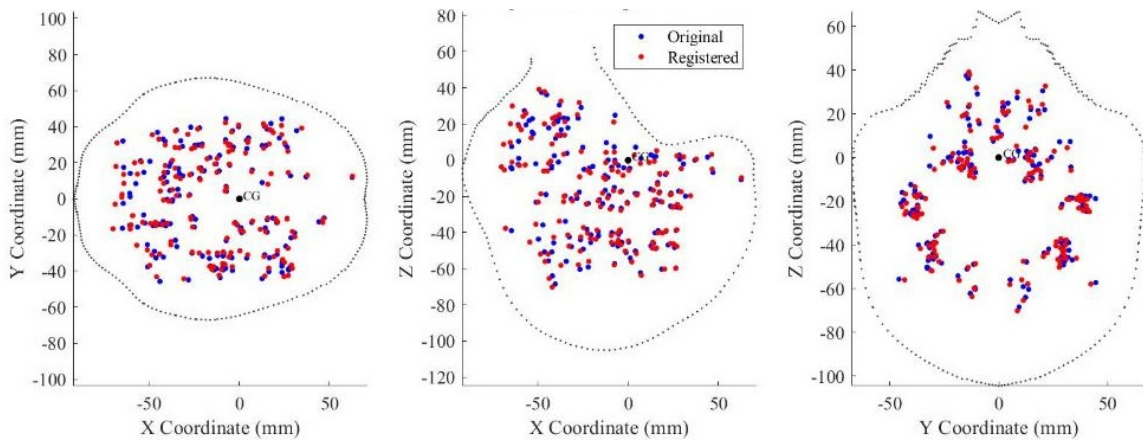


Figure 6-7: Average CORA scores for the simulated transfer function brain deformation response using the original kinematics. Data was averaged ( $\pm 1$  SD) across all axes for all crystals for all loading severities.

## Normalized Position and Displacement Registration

The normalization of the initial position of all receivers for each specimen was conducted through a registration process to account for shape and geometric differences among specimens. Generally, the registration process did not significantly alter the initial position of crystals (Figure 6-8). All of the receiver initial positions were shifted by less than 10 mm.



*Figure 6-8: Original (blue) and registered (red) initial positions of all receivers for all specimens. The cranium outline is the GHMBC inner skull outline, which used the parametric space for the registration.*

The registration process was also applied to the dynamic displacement response of each receiver. Comparable the initial position registration, the registration process did not significantly alter the brain deformation response of each receiver (Figure 6-9).

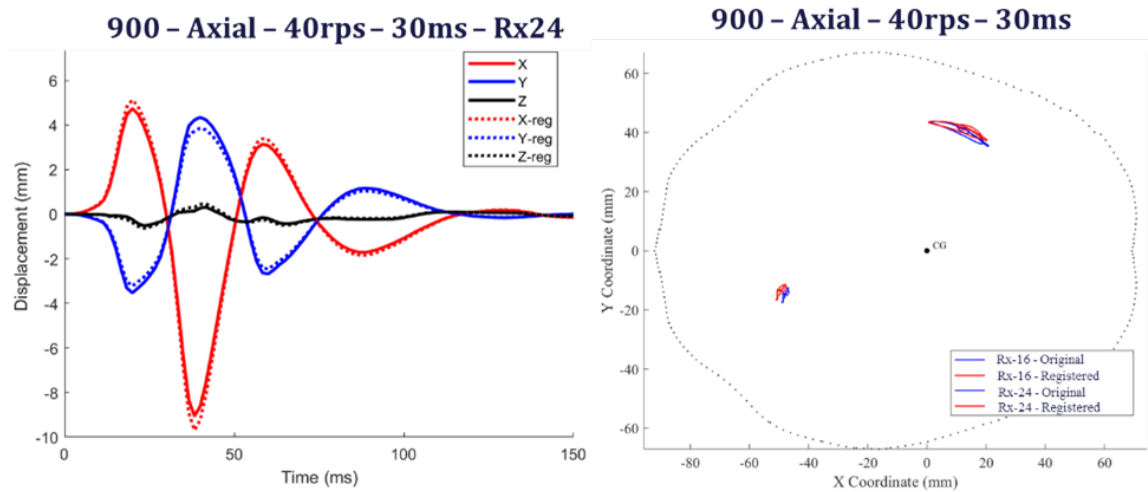


Figure 6-9: The normalized displacement for receiver (Rx) 24 for specimen 900 under the axial – 40 rad/s – 30 ms tests did not change significantly from the original displacements (left). The trajectory of receivers 16 and 24 are shown in the axial plane (right).

### **Validation and Optimization of Corridor Methods**

The GHBM brain model was used to validate and optimize the average data corridor creation methods. For the IDW methods, the  $p$  parameter was optimized using the average RMS error between the true FE response and the predicted response. The lowest RMS error was for  $p = 2$ , which is the Euclidean distance. An optimization was also conducted for the power ( $u$ ) term of the weighting factor ( $w$ ). The power optimization results for the grid and cluster-optimized methods are depicted in Figure 6-10. The RMS error in the x-deformation was largest, followed by y and z. There were few differences between the Shepard and Lukaszuk IDW algorithms. The minimum RMS error occurred at approximately  $u = 3$ , which is the power value used in the Lyszka method if  $\delta = 0$ . An optimization of the assumed error ( $\delta$ ) showed that  $\delta = 0$  resulted in the lowest RMS error.

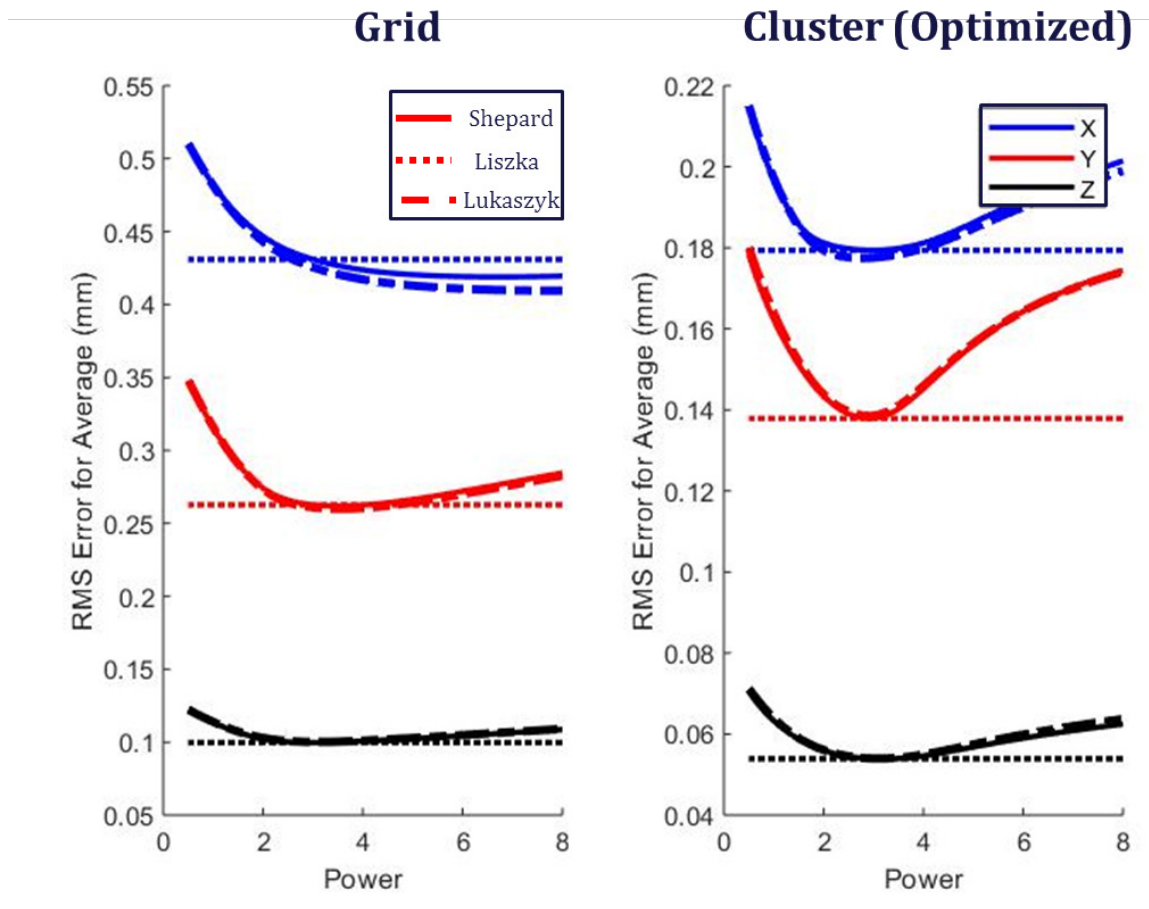


Figure 6-10: Optimization of the power ( $u$ ) parameter for the Shepard and Lukaszyk IDW methods using the grid (left) and cluster-optimized (right) methods.

Using the Shepard IDW method with  $p = 2$  and  $u = 3$ , the GHBMC model was simulated for the three corridor point generation methods under the sagittal, coronal, and axial 40 rad/s – 60 ms rotation severity. The RMS error for each axis of deformation is shown in Figure 6-11. For each loading severity and axis of deformation, the cluster-optimized method resulted in the lowest average RMS error. The grid and cluster-all methods had similar error magnitudes across the loading directions and axes of deformation.

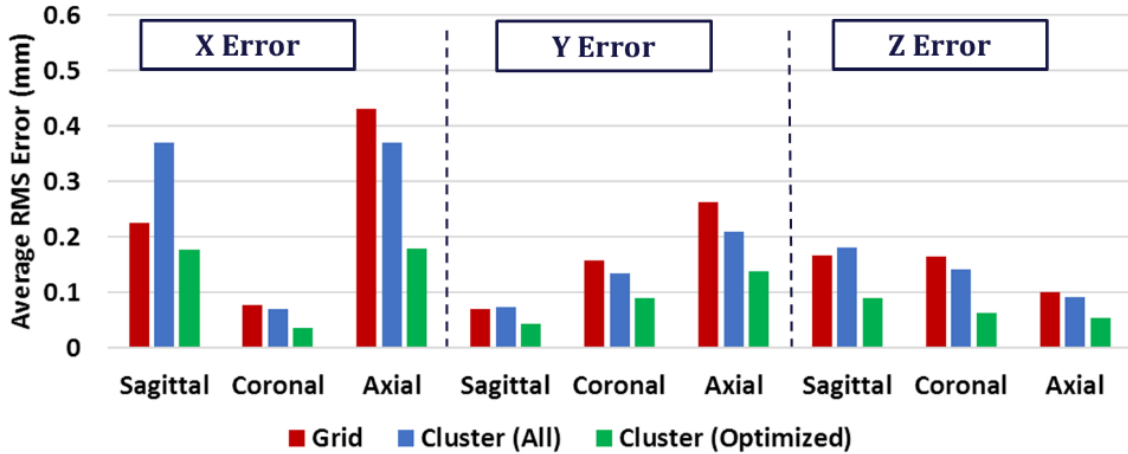
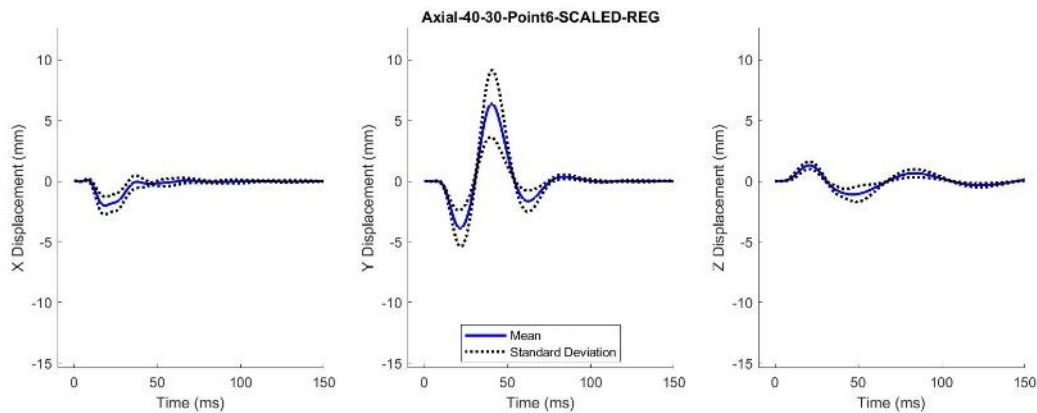


Figure 6-11: Average RMS error between the true FE brain deformation response at the corridor points and the predicted response using the IDW interpolation. The error in each motion axis ( $x$ ,  $y$ , and  $z$ ) is shown for rotational loading in each direction (sagittal, coronal, and axial) for the 40 rad/s – 60 ms tests.

### Aggregated Displacement Corridors

After validation and optimization of the IDW and discrete point distribution method, the final displacement corridors were generated using the Shepard IDW method with  $p = 2$  and  $u = 3$ , and using the cluster-optimized method. The final corridors are calculated after scaling the data using the kinematic transfer function, then normalizing to a common anthropometric space (GHBMC brain), and lastly using the IDW method to average nearby data points. The displacement corridors for the Axial – 40 rad/s – 30 ms for selected cluster points are depicted in Figure 6-12.



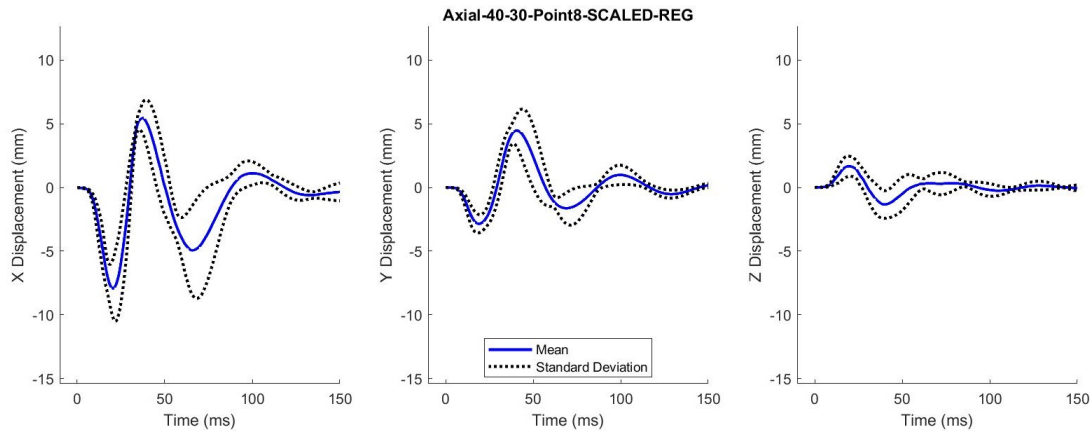


Figure 6-12: The final corridors for selected grid points for the Axial – 40 rad/s – 30 ms case. The final corridors are calculated after scaling the data using the kinematic transfer function, then normalizing to the common anthropometric space.

## DISCUSSION

The generation of a dataset of human brain deformation with multiple specimens under consistent loading conditions and loading severities for each specimen allows for the aggregation of *in situ* human brain deformation data. There were differences in each specimen, arising from anatomical differences such as inertia and anthropometry as well as dissimilarities in test setup due to specimen preparation procedures. The three major areas of variation addressed in this study are differences in loading kinematics, cranial anthropometry, and sonomicrometry receiver initial position. Several techniques were introduced and validated in this study that are not typically implemented in the generation of biomechanical data corridors. The use of these techniques allows for the aggregation of a dataset that contains some inconsistencies and allows for the generation of the first average displacement corridors of human brain deformation. Refinement and extension of these methods are possible for their application to brain deformation data or other biomechanical experiments.

The use of transfer functions, through physical representations such as a multi-body (e.g., spring-damper) model, to extrapolate the response of a mechanical system is common for engineered materials with highly characterized responses. The use of analytical multi-body models has also recently been used to model the maximum strain response of FE brain models (Gabler et al., 2017, 2018b). In most cases, these linear transfer models were an efficient and accurate approach to represent the response of the crystals to head motion, and the transfer functions were able to simulate the original brain deformation response with average CORA scores of approximately 0.9. Each transfer function was inspected to ensure the accuracy and stability of the simulated response. However, the use of transfer functions in this study to normalize data to a common kinematic input was limited to small changes between the original and scaled kinematics, primarily due to the linear nature of the transfer function. Thus, each transfer function was only applicable to the specific crystal under the kinematic severity that was used to develop it, and could not be applied to dissimilar kinematics. Future work should investigate non-linear techniques to fit the response of each specimen or each receiver across a range of severities. These non-linear techniques can include physics-based approaches such as quasi-linear viscoelastic multi-body models.

The registration and morphing method was used to account for differences in the initial position and dynamic displacement due to the variation in cranial anthropometry. The morphing technique was adopted from similar work to create subject-specific models of the human femur (Bryan et al. 2010; Park et al. 2017) and was used in this dissertation to account for subject variability when evaluating FE brain models (Chapter 6). The application of this technique to register the position and displacement of each receiver is a

new approach to normalizing human brain deformation data based on anthropometry. Similar techniques are used in the registration of human brain MRI images to a common ‘space’ or template (Avants et al., 2011), which allows for geometric evaluations across a population. The approach employed in this study uses the GHBMC brain model as the template or registration space for all of the specimens. The choice of this template is arbitrary, and the methodology could be applied to any FE model or parametric space. The registration and morphing techniques utilized the segmented CT scans of each specimen to map the deviations in the initial position and Cartesian displacement to the normalized space. While there were small differences in the initial position and smaller differences in the displacement, after normalization, this step was important for removing any bias in the data due to specimen anthropometry.

Although the preparation procedures included many precautions to ensure similar placement of crystals within every specimen, differences in initial position after normalization complicate the averaging of the deformation response across the specimens. These differences could have occurred from the specimen anthropometry as well as experimental error associated with the insertion process. The creation of discrete points within the range of receivers for all specimens allows for an averaging of the deformation response as well as the initial crystal position. Three methods of discrete corridor point generation were studied: grid, cluster-all, and cluster-optimized methods. While each method has its advantages and drawbacks, the cluster-optimized method resulted in the best visual distribution of corridor points as well as the lowest RMS error when the methods were simulated using the GHBMC brain model.

The other aspect of predicting the response at discrete points from a dataset of irregularly scattered data is the averaging method. IDW has been used since its introduction by Shepard (1968) in many fields spanning mechanics to climate and geology using a simple and computationally efficient approach. The method has been evaluated and adapted to include error assumptions and parameters (Liszka, 1984; Lukaszuk, 2004). Three IDW methods were evaluated in this study, but the original Shepard formulation was the most accurate. The parameters of the formulation were optimized using the GHBMC FE brain model. While any technique used to interpolate data can include non-unique solutions because of regions that have similar distances to the same experimental points, IDW provides a valuable approximating method for averaging brain displacement data. Other interpolation approaches, such as finite element methods, may be applicable, but the sparsity of the spatial distribution of the receivers introduce errors in the predicted response.

The GHBMC FE brain model was used to validate and optimize the discrete corridor point generation and the IDW method. There are a few limitations to this approach, namely the assumption that the mechanics and interpolation results of the model match that of the human brain. It was documented that the response of the GHBMC brain model (Chapter 6) may not be entirely representative of the human brain, with some notable differences in simulated material properties and internal anatomy. The use of the model in the context of this study, however, was only to inform the choice of several techniques and parameters. The model was not used in the creation of the aggregate corridors or the averaging method. This provides an aggregated dataset that was validated with a mechanically-based FE model but does not use the model response to bias the data. The lack of metrics to evaluate

the goodness-of-fit of a biomechanical data corridor makes it challenging to validate the methodology in other ways. This approach could be incorporated in future work regarding the recommended procedures for validating or optimizing the methodology for creating average data corridors.

## **CONCLUSION**

Average data corridors are typically used in biomechanics to represent an aggregated population response and to validate FE models. This study introduced the first average data corridors for *in situ* human brain deformation, using a dataset of six specimens and twelve rotational severities. Several techniques were introduced to account for specimen and experimental differences, and to normalize the average data corridors to a common kinematic input and common anthropometric space. The validation of these techniques provides a reliable set of brain deformation corridors as well as methods for more robust and reliable biomechanical corridor creation.

The generation of the sonomicrometry brain deformation dataset and average data corridors presents an opportunity to evaluate and validate FE brain models. There is no standard method to account for anatomical differences between the models and individual specimens. The variation in skull geometry can cause inconsistencies when choosing corresponding nodal points in the model to compare to the sonomicrometry crystal responses. It can also cause differences in brain motion and strain metrics. An investigation into the appropriate methods to evaluate models is needed to ensure consistent and objective validation of FE brain models.

## **CHAPTER 7: FINITE ELEMENT MODEL EVALUATION**

One of the difficulties of validating the biofidelity of FE brain models to brain deformation data is the variation of geometry between the model and the specimens in the experimental dataset. This variation can cause inconsistencies when validating FE models, and there is no consensus on a standard method to evaluate the biofidelity of computational brain models. This chapter will focus on using the experimental dataset from Chapter 5 and the average data corridors from Chapter 6 to identify best practices when validating FE brain models. The focus will be on geometry, with four different evaluation methods used to assess the biofidelity of two commonly used FE brain models.

### **INTRODUCTION**

The study of the biomechanics of the brain during impact is essential to understanding and preventing TBI. Kinematic injury criteria that utilize the motion of the head to predict injury to the brain have typically been employed to evaluate the effectiveness of vehicles (2015) and helmets (Hodgson, 1975) as well as predict brain injury during real-time events (Duma et al., 2005). Many recent kinematic brain injury criteria have been developed using a combination of reconstructed impacts in FE models, using tissue-level metrics as correlates to injury (Gabler et al., 2018b; Takhounts et al., 2013a). Tissue-level injury criteria delve deeper into brain mechanics by assessing the relationship between the biomechanics of the brain, with a metric such as strain, to injury. Direct measurement of tissue-level deformation of the brain during head impact is challenging, and anatomically-detailed FE models provide a valuable alternative. FE brain models have been vital to investigating TBI mechanisms, assessing injury risk and safety gear, and developing brain

injury criteria based on external head kinematics (Gabler et al., 2016a, 2017; Sanchez et al., 2017; Takhounts et al., 2013a).

FE models provide an advantage over kinematics-based metrics because of their ability to measure complex patterns in the temporal and spatial mechanical response of the brain instead of using a relationship between peak kinematics and brain deformation (Elkin et al., 2018; Sanchez et al., 2017). These models allow for the in-depth investigation of the brain response under various loading conditions at a level that is not possible using cadaveric or human experiments. They have been created to predict injury using summary strain-based injury metrics such as maximum principal strain (MPS) and the cumulative strain damage measurement (CSDM) (Gabler et al., 2016a; Kleiven, 2007; Sanchez et al., 2017; Takhounts et al., 2013a; Zhang et al., 2004). Although these injury metrics and models are computationally-based, they are considered the state-of-the-art method for evaluating a large number of head impacts and kinematics in an attempt to relate head motion to injury (Deck and Willinger, 2009).

To be able to make significant conclusions about tissue-level deformation, the biomechanical response of the model must match as closely as possible to real-world human brain deformation. Although many of the models are validated using the same single dataset of human brain deformation, the results of the models can vary significantly among models (Giudice et al., 2018a). A recent analytical review of FE brain models suggests that the factors affecting the output of these models include material properties, geometry differences, the size, type, and quality of the mesh, and FE parameters such as hourglass control (Giudice et al., 2018a). Additionally, the models are often simulated under conditions that vary from the head kinematic impacts they were validated against

(direct impact versus rotational loading), raising questions about the applicability of the models and what conclusions can be drawn from the results.

Improvements in computational capabilities and the availability of early brain deformation datasets (Hardy et al., 2001, 2007) have allowed for the creation of multiple FE brain models. Given the importance of these models in influencing standards of safety and product development across multiple industries, it is essential to validate the brain deformation predicted by these models using human brain motion under repeatable loading conditions that are causative of injury. Most of the FE models in the literature are validated based on one or two datasets available for brain models consisting of two types of response: the Hardy brain motion datasets (Hardy et al., 2001, 2007) and the preceding brain pressure datasets by Nahum (Nahum et al., 1977) and Trosseille (Trosseille et al., 1992). While the pressure datasets provide a reasonable metric to validate the volumetric loading experienced by the brain, they are not useful as an injury correlate (as shown for the pressure data collected in Chapter 3).

Additionally, there is no standard method for evaluating FE brain models. While most of the models use a small subset of the Hardy dataset, there is a lack of consistency in how the models are evaluated. Miller et al. (2017) (Miller et al., 2017) performed evaluations of several FE brain models in comparison to a subset of the Hardy dataset. The Miller study found that the models yielded a cross-correlation score (CORA) (Gehre et al., 2009)) between 0.26-0.41. The study did not account for differences in specimen geometry and picked nodal points that were closest to the absolute marker location. Displacement was only compared in the plane of testing (x-z or y-z) with each test in the Hardy dataset conducted on a different specimen, preventing the validation of the models across different

impact directions using the same specimen. There is a need for a standard method to evaluate and score the response of the FE brain models to a consistent and more substantial dataset.

The objective of this chapter is to evaluate the brain deformation response of widely used FE models of the brain in comparison to the experimental dataset collected in Chapter 5. The models will be compared to each specimen individually using four techniques of geometric normalization. Finally, the models will be evaluated using the average data corridors developed in Chapter 6. The contribution of this study will be a recommended method of evaluating the biofidelity of FE brain models.

## **METHODS**

Two FE brain models, the GHMC detailed M50 (Mao et al., 2013) (v4.3) and SIMon (Takhounts et al., 2008a), were evaluated to assess the biofidelity of brain deformation (Figure 7-1). All experimental test cases were simulated by prescribing the experimental kinematics collected in reference to the head center of gravity (CG) to the FE model through a rigidized dura (Gabler et al., 2016a). The response of the brain models was assessed by comparing the motion of the receivers from the sonomicrometry experiments (Chapter 5) to the motion of the corresponding model nodes. The x, y, and z displacements of all implanted brain crystals were compared for each test for a total of approximately 5000 individual trace validation comparisons.

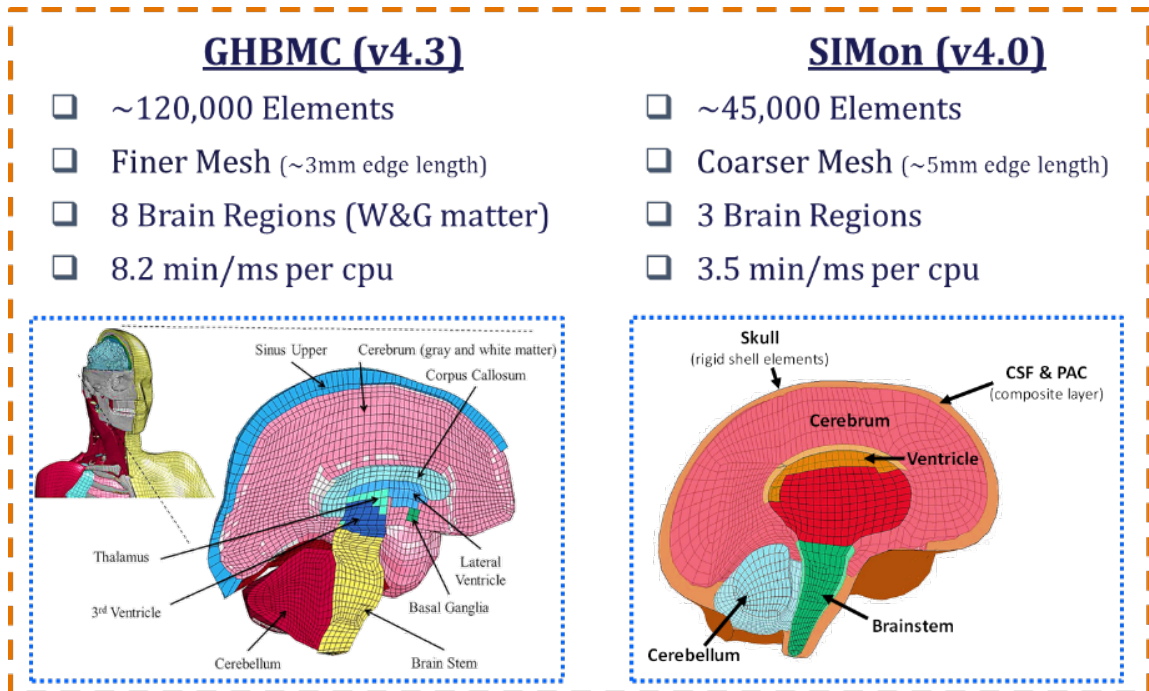


*Figure 7-1: Depiction of the GHBMC and SIMon FE brain models, with geometric and anatomical characteristics as well as computational efficiency for each model.*

### **Comparison Methods**

Given the anatomical differences between the FE brain models and the cadaveric specimens (Table 7-1), four methods were implemented for model evaluation:

- 1) Using the **absolute** coordinates of the initial crystal position relative to the head CG to identify the corresponding model node.
- 2) Using the **relative** coordinates based on the maximum length (x), width (y), and height (z) of the head to identify the corresponding node.
- 3) Geometrically **scaling** the dimensions of the FE models to those of the cadaveric head and using the initial crystal positions to identify the corresponding model node.

- 4) **Morphing** the FE model based on the CT of the inner skull to match the anthropometry of each specimen and using the initial crystal positions to identify the corresponding model node.

The absolute method utilized the baseline GHBMC and SIMon models. The coordinates of the receivers for each specimen were found in the model relative to the model center of gravity (CG). The absolute comparison method did not account for the geometry of the specimen, with each node identified as the closest by distance to the corresponding sonomicrometry receiver position. The relative method also utilized the baseline FE model but used a scaled position for each receiver position to find the corresponding node. The coordinate (x, y, z) of each receiver was scaled by the ratio of length (x), width (y), and height (z) of the model and specimen (Table 7-1) to obtain scaled positions. The scaled receiver positions were then compared to the baseline model coordinates to find the closest corresponding nodes. The scaled receiver positions were generated for each specimen for both GHBMC and SIMon.

*Table 7-1: Specimen anthropometry relative to the GHBMC and SIMon FE models.*

| Measurement                    | Specimen 846 | Specimen 896 | Specimen 900 | Specimen 902 | Specimen 903 | Specimen 904 | Specimen Average | GHBMC | SIMon |
|--------------------------------|--------------|--------------|--------------|--------------|--------------|--------------|------------------|-------|-------|
| <b>Length x (mm)</b>           | 159.6        | 169.6        | 169.2        | 168.3        | 164.5        | 176.5        | 168.0 ± 5.6      | 164.9 | 166.5 |
| <b>Width y (mm)</b>            | 133.4        | 126.6        | 124.2        | 137.3        | 123.3        | 130.6        | 129.2 ± 5.5      | 134.4 | 135.3 |
| <b>Height z (mm)</b>           | 138.7        | 134.3        | 146.7        | 135.5        | 137.9        | 148.6        | 140.3 ± 5.9      | 143.7 | 135.6 |
| <b>Volume (cm<sup>3</sup>)</b> | 1442         | 1435         | 1558         | 1481         | 1298         | 1692         | 1484 ± 132       | 1569  | 1527  |

The scaled method utilized modified, scaled versions of the FE models, which were obtained by geometrically scaling the original model in each direction (x, y, z) by the ratios used in the relative comparison methods for each coordinate. A total of twelve scaled models were generated for each specimen for both GHBMC and SIMon. The

corresponding nodes from the ‘absolute’ comparison method were used to compare the FE response to the sonomicrometry experiments.

A morphing technique was implemented to precisely match the external geometry of the FE brain models to the target specimen. A technique utilized and adapted by Park (2017) (Park et al., 2017) was extended to the brain and included four main steps: 1) Surface preparation and segmentation, 2) rigid body alignment and scaling, 3) surface registration, and 4) volume morphing and evaluation. An in-depth explanation of the morphing methodology is presented in Appendix B.

The FE models were prepared by extracting the outermost layer of the model: the dura for GHBMC and the inner skull for SIMon. This surface will be used to match to the segmented specimen geometry. The morphing method was applied to generate a 3D model mesh that matches the external surface of each specimen. After the morphed model was obtained, the normalized Jacobian ratio of all elements was quantified to ensure comparable element quality of the morphed model to the original FE brain models. A depiction of the specimen 846 morphed GHBMC model along with the normalized Jacobian ratio is shown in Figure 7-2. The nodes corresponding to each receiver in the experimental dataset were chosen by finding the node with the least distance away from the crystal position relative to the CG.

The morphing process for the SIMon model required an additional step. Due to the coarser mesh (larger element size) for SIMon, the registration and 3D morphing process resulted in inverted elements, penetration across different parts, and negative volume errors when simulated. To fix this problem, each hexahedral element in the mesh was split into eight elements to generate a hex-split model with an average element size of  $1.07 \pm 0.39$

mm (original:  $2.07 \pm 0.77$  mm). The hex-split model was then used to generate a morphed surface and 3D model. The extra nodes from the hex-split model were then deleted, and the morphed model contained only the nodes (now morphed) and elements from the original model. A depiction of the specimen 902 morphed SIMon model along with the normalized Jacobian ratio is shown in Figure 7-2. A specimen-specific model was generated for each specimen for both GHBMC and SIMon for a total of twelve models.

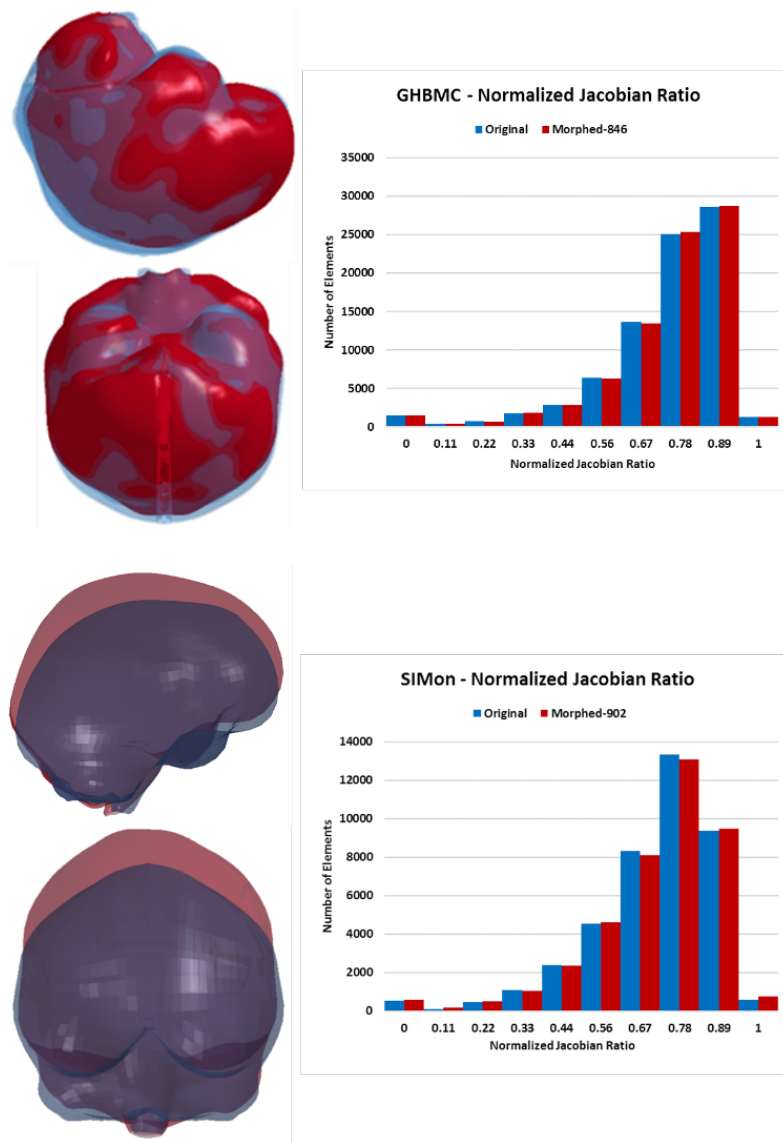
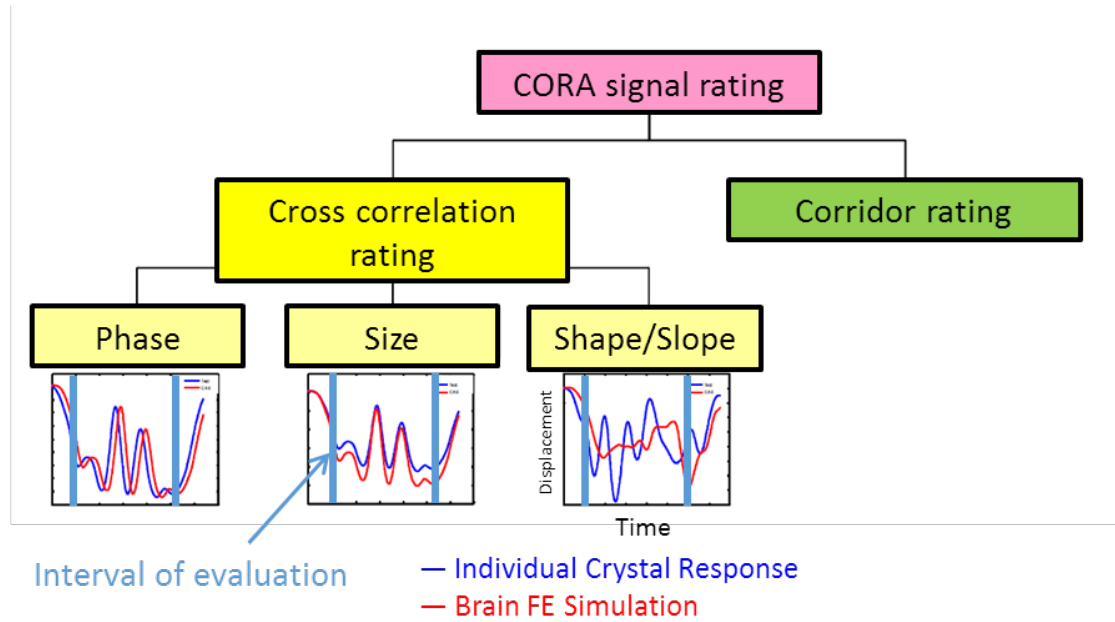


Figure 7-2: The original (blue) and morphed (red) GHBMC FE model for specimen 846 (top) and the SIMon FE brain model for specimen 904 (bottom).

## Model Evaluation

Model biofidelity was quantified using a signal cross-correlation score, CORA (Gehre et al., 2009). The CORA score, depicted in Figure 7-3, uses an average of three ratings between 0 and 1, for the phase, size, and progression comparison between the two signals. A separate corridor rating is discarded for the individual specimen comparisons.



*Figure 7-3: Depiction of the CORA cross-correlation metric to evaluate the similarity between two signals. The phase, size, and shape are equally weighted for an overall maximum score of 1. The corridor rating is discarded for the individual specimen evaluations.*

A weighted averaging was applied to obtain a single representative objective rating for each 3-D signal (Wu et al., 2019). The weighted CORA score was calculated by weighting the component CORA scores ( $CORA_{x,y,z}$ ) by the maximum peak-to-peak displacement in the three axes ( $d_x$ ,  $d_y$ ,  $d_z$ ), formulated in the equation below. For each validation case, an overall score was computed by averaging the individual weighted CORA scores for each receiver.

$$\text{Weighted CORA} = \frac{d_x \times \text{CORA}_x + d_y \times \text{CORA}_y + d_z \times \text{CORA}_z}{d_x + d_y + d_z}$$

### **FE Model Evaluation to Corridors**

In addition to evaluating the models in comparison to each specimen, the two FE models were evaluated for biofidelity against the brain deformation corridors developed from the six specimens (Chapter 5). For each model, the corresponding cluster points were found by finding the nearest node in the FE brain model to each grid point. The head kinematics were simulated by applying the common scaled kinematics in the same manner as the individual evaluation method. The x, y, and z displacements of all grid points were compared for each test for a total of approximately 850 corridor comparisons. Model corridor biofidelity was quantified using the weighted CORA metric by comparing the average response of the grid point to the FE model response. The corridor rating was quantified by comparing the model response within the corridor boundaries, defined by the standard deviation of the average response. A detailed description of this calculation can be found in Gehre et al. (2009) (Gehre et al., 2009). The overall CORA score for each cluster point is the mean of the weighted CORA score and the corridor score. For each loading case, an overall score was computed by averaging the individual signal overall scores for all cluster points.

### **Strain Calculation**

Tissue-level strain metrics are often used to correlate FE model simulations to injury outcome (Gabler et al., 2018b). The most common strain metrics are maximum principal strain (MPS) and the cumulative damage strain measure (CSDM). The MPS was calculated using the maximum value of maximum principal strain for all elements in the brain over the entire kinematic time history (Takhounts et al., 2008a). Although many studies have

used the maximum element MPS value (Kleiven, 2007; Takhounts et al., 2013a; Yanaoka et al., 2015), the 95th percentile value (ranked by element) was used as a correlate to maximum brain strain to avoid computational instabilities that may arise from the element with the maximum principal strain (Gabler et al., 2016a; Panzer, 2012). The 50<sup>th</sup> percentile value (ranked by element) was also calculated to serve as mean strain value, similar to the mean peak-to-peak deformation calculated in Chapter 5. CSDM is the cumulative volume fraction of elements that sustain an MPS that exceeds a threshold value. A threshold of 25% MPS was used for CSDM in this study because it was shown by Takhounts et al. (2013) (Takhounts et al., 2013a) to be the best indicator of DAI. A depiction of the calculation of the percentile MPS values and CSDM are shown in Figure 7-4.

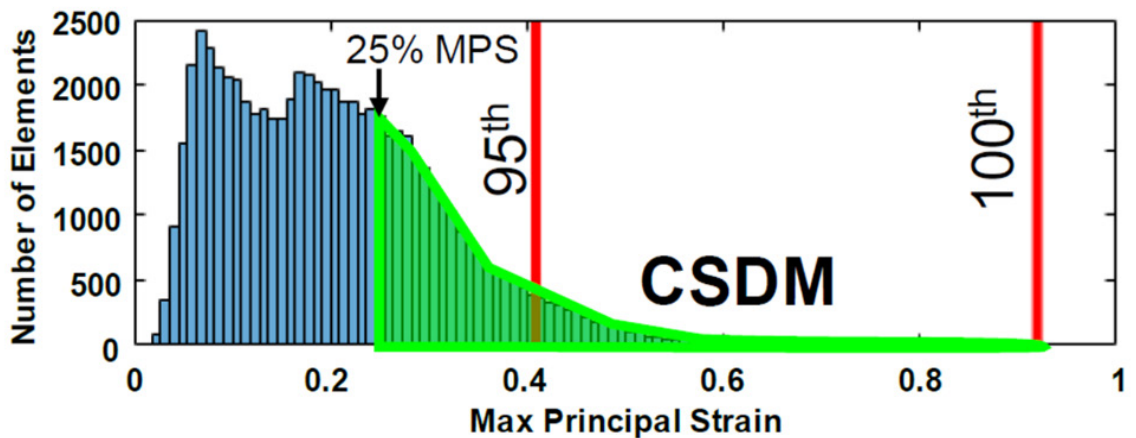


*Figure 7-4: Distribution of the maximum MPS across elements for a single head rotation. Solid red lines indicate the 95th and 100th percentile MPS. The green highlighted region indicates the elements that have achieved an MPS of at least 25% during the impact, which are included in the CSDM calculation.*

The 50<sup>th</sup> and 95<sup>th</sup> percentile MPS and CSDM strain metrics were calculated for each kinematic severity for all models (absolute/relative, scaled and morphed) to compare the effect of each method on tissue-level strain. The strain metrics were also compared to the maximum and mean peak-to-peak deformation (Chapter 5) to investigate the effectiveness of the strain metrics in predicting *in situ* human brain deformation.

## RESULTS

### Individual Specimen Evaluation

The nodal response of each simulated specimen loading condition was compared to the corresponding sonomicrometry data. An example of this response is given in Figure 7-5. The weighted CORA scores for the GHBMC simulations for all loading conditions for specimen 900 are depicted in Figure 7-6. The CORA scores for the other specimens are presented in Appendix F.

The weighted CORA scores for all loading conditions for each specimen were averaged to determine differences between the comparison methods. The averages and standard deviations are shown in Figure 7-7.

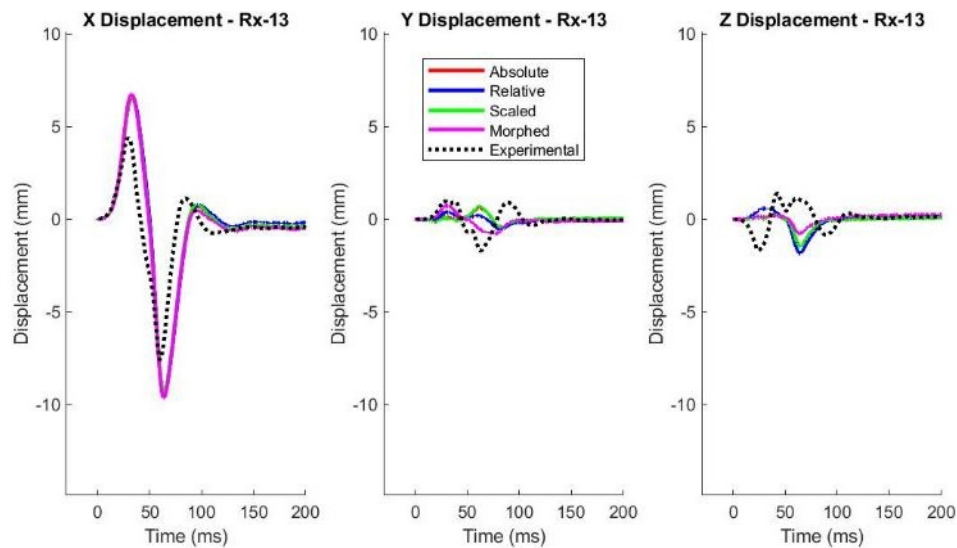


*Figure 7-5: Response of the GHBMC model for receiver 13 for the sagittal, 40 rad/s, 60 ms case. All four comparison methods are shown with the sonomicrometry experimental data.*

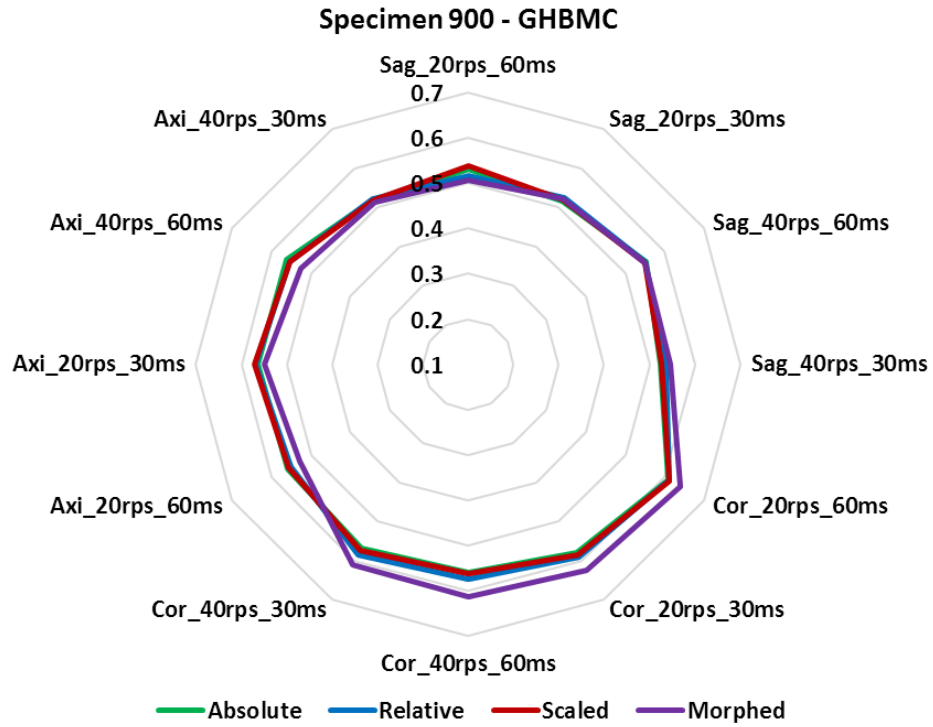


Figure 7-6: The weighted CORA for all rotational loading conditions in the sagittal (sag), coronal (cor), and axial (axi) directions for specimen 900 for GHBMC.

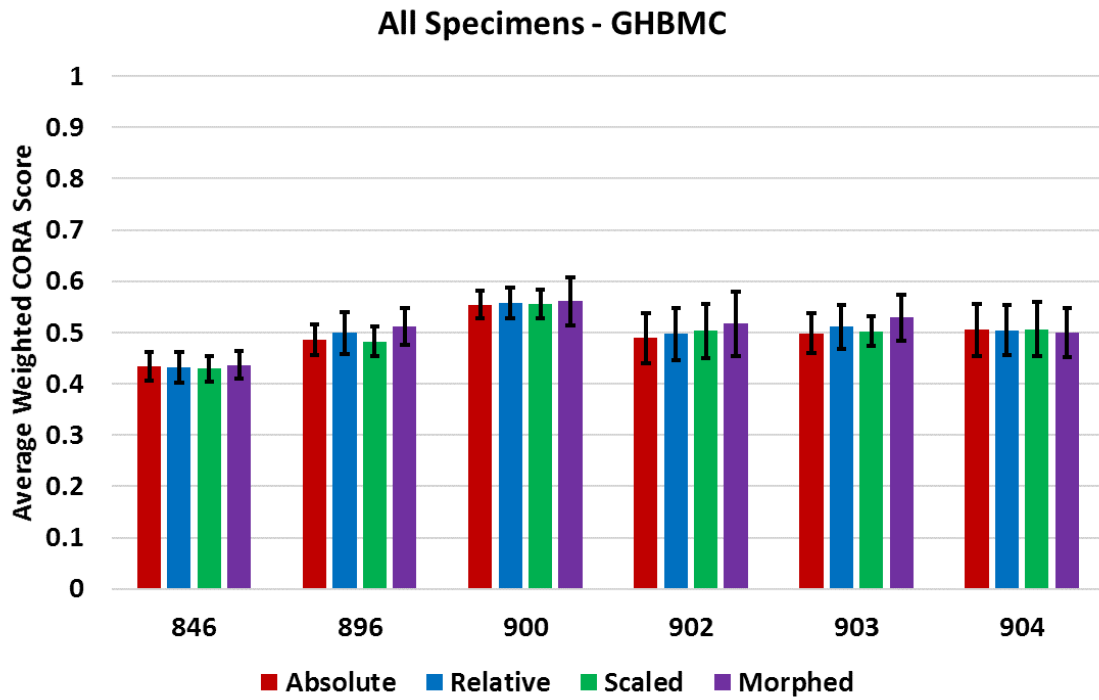
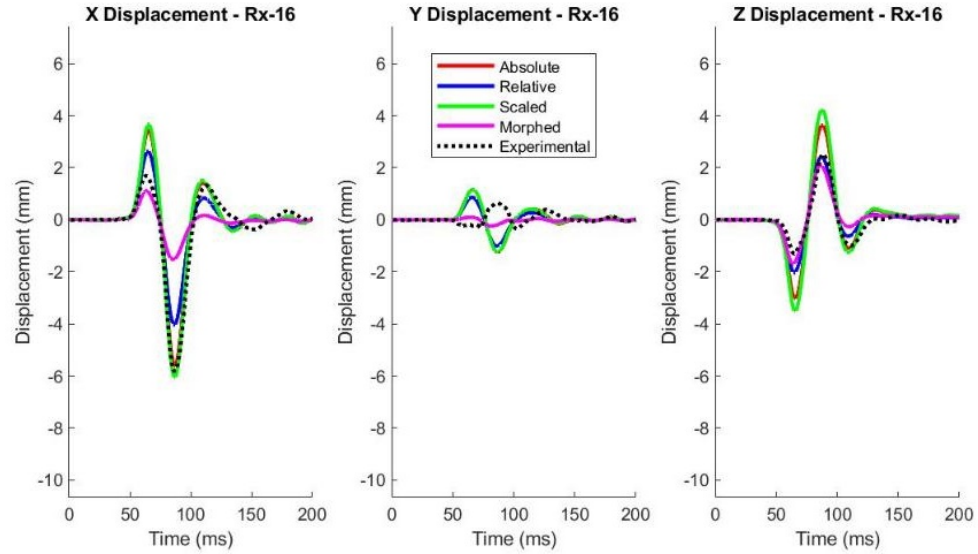


Figure 7-7: The average weighted CORA in the GHBMC simulations for all specimens.

For the SIMon FE brain model, the nodal response of each simulated specimen loading condition was compared to the corresponding sonomicrometry data. An example of this response is given in Figure 7-8.



*Figure 7-8: Response of the SIMon model for receiver 16 for the sagittal, 40 rad/s, 30 ms case. All four comparison methods are shown with the sonomicrometry experimental data.*

The weighted CORA scores for the GHBM simulations for all loading conditions for specimen 900 are depicted in Figure 7-9. The CORA scores for the other specimens are presented in Appendix F. The weighted CORA scores for all loading conditions for each specimen were averaged to determine differences between the comparison methods. The averages and standard deviations are shown in Figure 7-10.

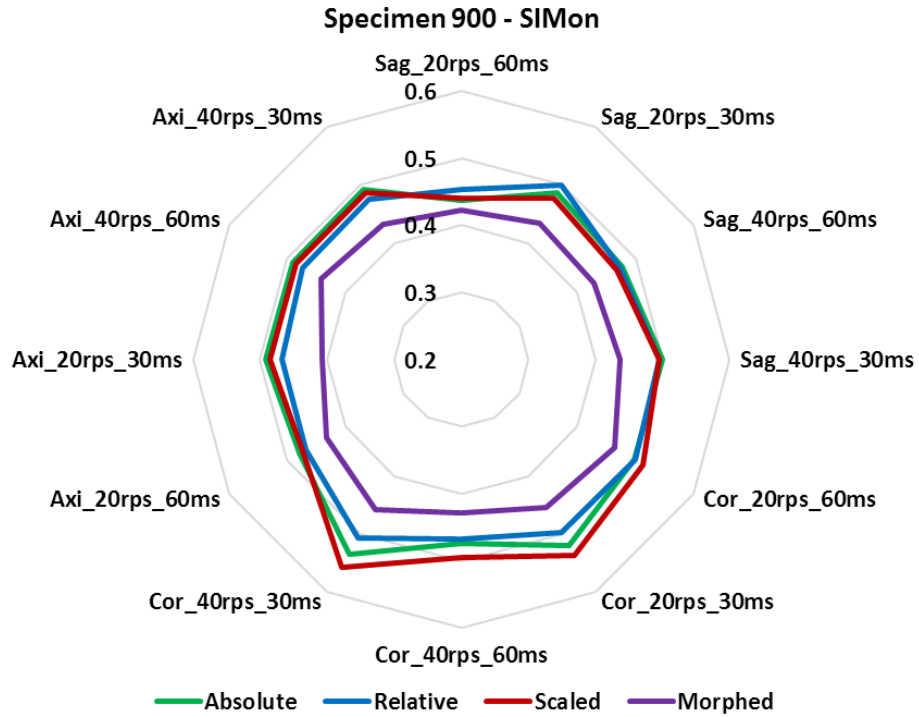


Figure 7-9: The weighted CORA for all loading conditions for specimen 900 for the SIMon model.

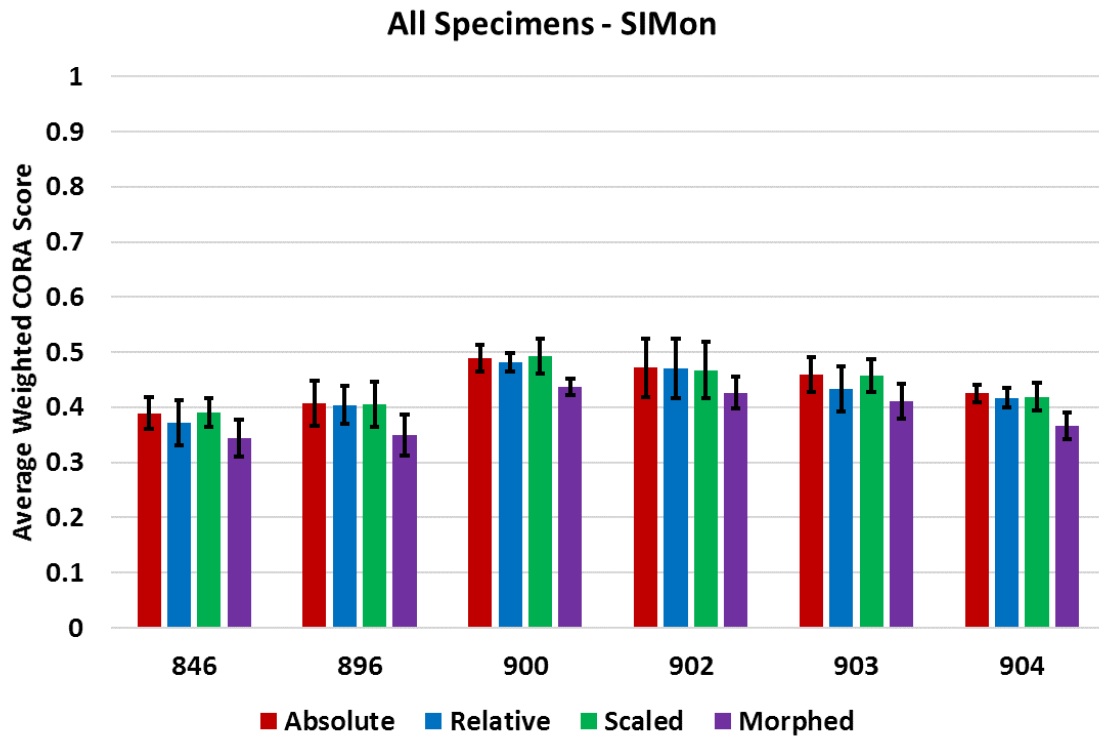


Figure 7-10: The average weighted CORA for all specimens for the GHMBC model.

The performance of the GHBMC and SIMon models did not significantly depend on the comparison method, except for the morphed SIMon model, which had a lower average weighted CORA score for all specimens. The performance of the GHBMC and SIMon models were compared relative to each other (Figure 7-11). The GHBMC model had a larger average CORA score across all specimens, and the difference was more pronounced for the ‘morphed’ comparison method.

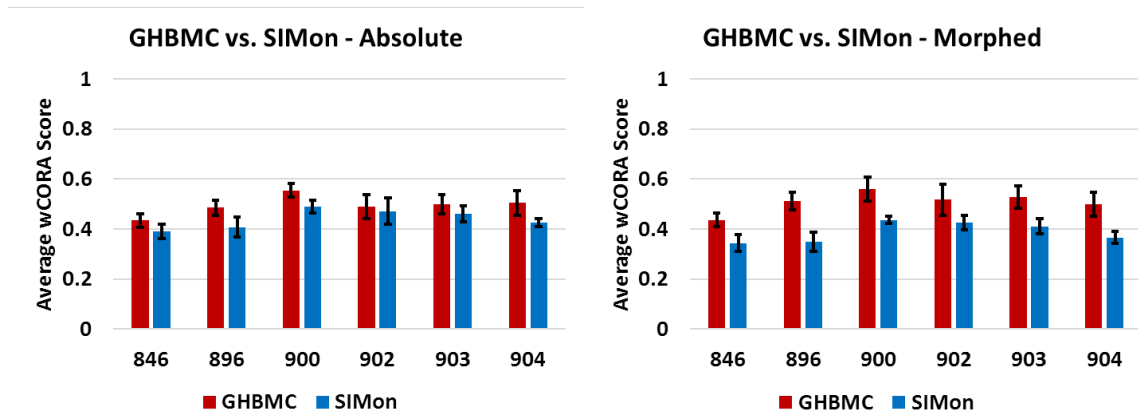


Figure 7-11: The average weighted CORA for all specimens for GHBMC and SIMon for the ‘absolute’ and ‘morphed’ comparison methods.

### Corridor Evaluation

The response of each model simulated with the scaled loading kinematics was compared to the cluster point corridor responses. The weighted CORA was calculated as well as a weighted corridor response. An overall weighted score was calculated as the average of these two scores. For both models, the weighted CORA scores in all loading conditions are shown in Figure 7-12. The overall CORA scores for the corridors were of similar magnitudes to the average overall CORA scores from the individual comparisons, with scores ranging from 0.45-0.64 for GHBMC and 0.42-59 for SIMon.

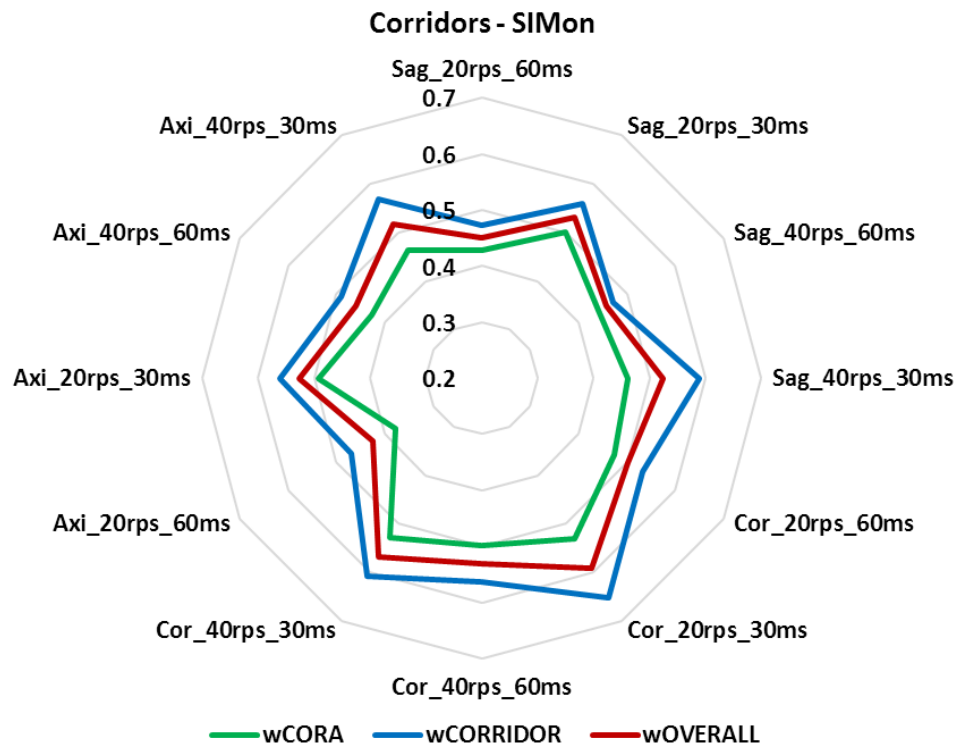
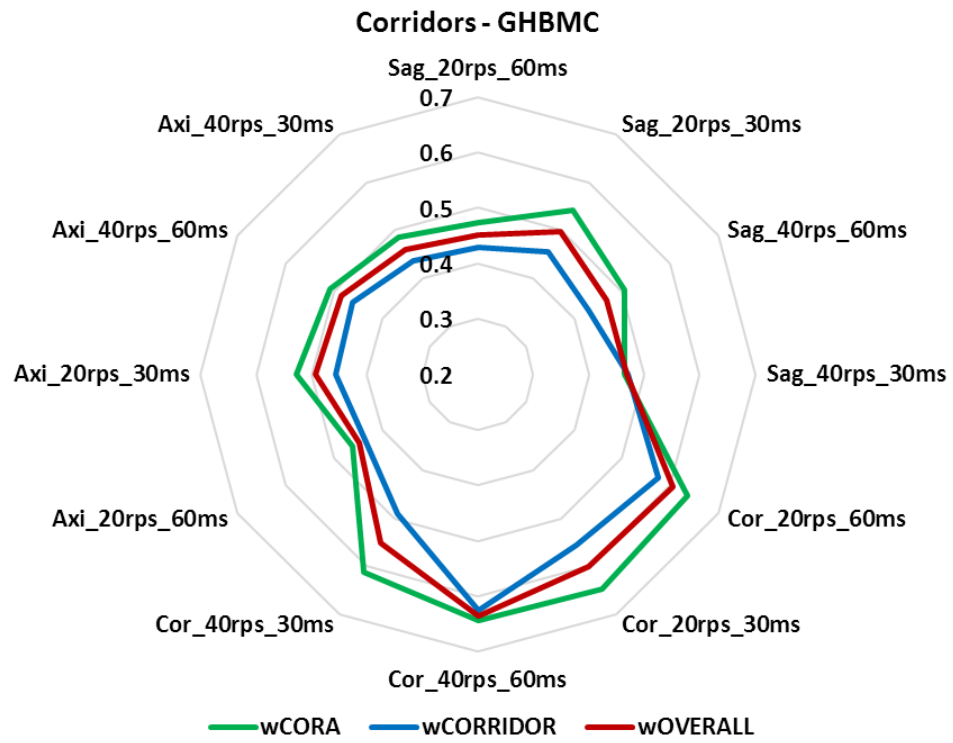


Figure 7-12: The weighted CORA, weighted corridor score, and the weighted overall score for the GHBM (top) and SIMon (bottom) models compared to the brain deformation corridors.

## Strain Results

The MPS-95<sup>th</sup>, MPS-50<sup>th</sup>, and CSDM were quantified for all of the individual specimen simulations for the three geometries (original, scaled, and morphed models). The MPS for the different geometries for specimen 904 for the axial, 40 rad/s – 30 ms simulation are depicted in Figure 7-13. The strain results of the scaled and morphed model were compared to the original model by calculating the difference in strain then averaging the difference across all test severities for all specimens. The average and standard deviation for each metric for the GHBMCM and SIMon models are presented in Figure 7-14. The scaled models experienced some difference in strain, likely depending on the size difference between the model and specimen. The morphed models experienced more significant deviations in strain values, most prominently for the MPS-95<sup>th</sup> and CSDM results. The results were similar for both the GHBMCM and SIMon models.

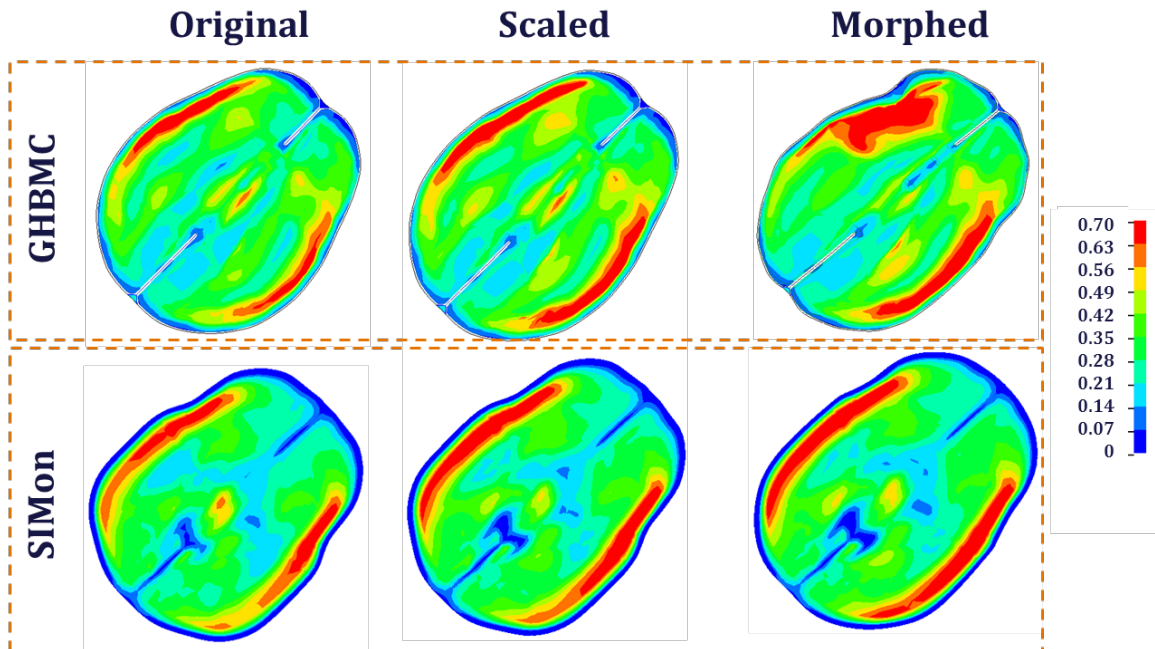


Figure 7-13: The maximum principal strain for the original, scaled, and morphed models for specimen 904 for the axial, 40 rad/s – 30 ms simulation.

## Effect of Model Geometry on Strain Metrics

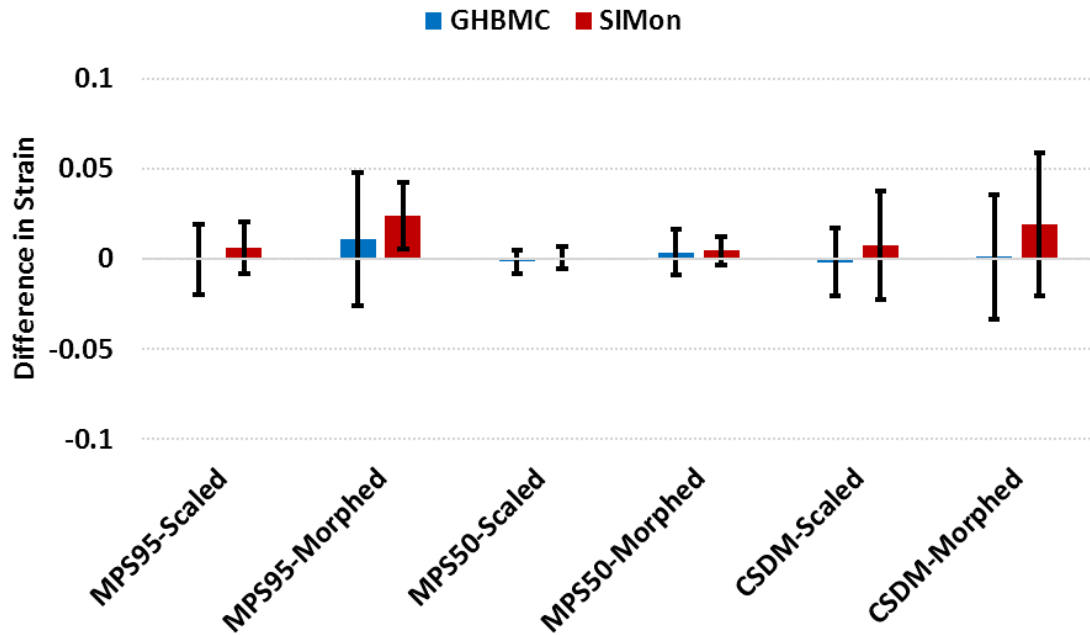
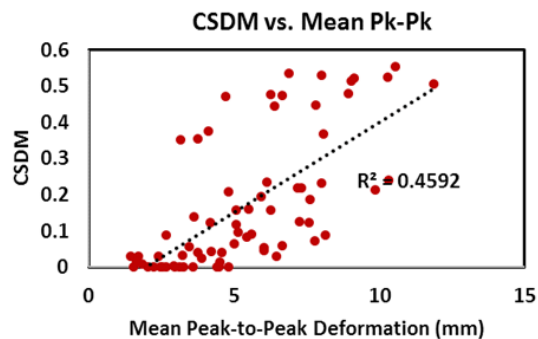
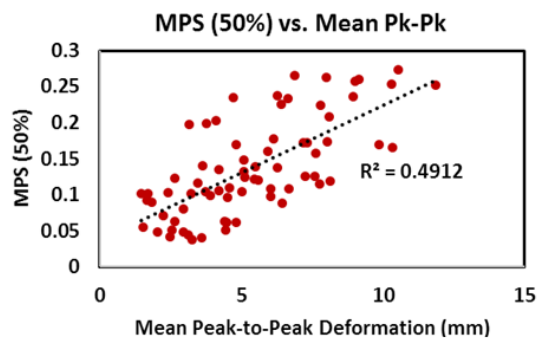
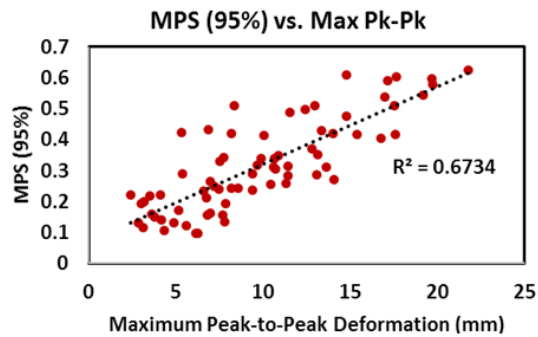


Figure 7-14: The difference in strain for the scaled and morphed (relative to the baseline) GHBMC and SIMon FE brain models. The 95<sup>th</sup> percentile MPS (MPS95), 50<sup>th</sup> percentile MPS (MPS50), and CSDM are shown for each model.

The strain results for all tests and specimens were also correlated through a linear regression analysis to the maximum and mean peak-to-peak results presented in Chapter 5. Based on the theoretical underpinnings of the MPS and CSDM calculation, the MPS-95<sup>th</sup> value should correlate to the maximum peak-to-peak deformation, while the MPS-50<sup>th</sup> and CSDM values should correlate to the mean peak-to-peak deformation. The regression results for the GHBMC and SIMon models are presented in Figure 7-15. The  $R^2$  values ranged from 0.46-0.74 for all pair-wise comparisons of the three strain metrics and two peak-to-peak metrics. The best fit occurred between the SIMon model MPS-95<sup>th</sup> and maximum peak-to-peak deformation. While the CSDM regressions had reasonable  $R^2$  values, many simulations had CSDM values close to 0 due to the 25% strain threshold.

## GHBMC



## SIMon

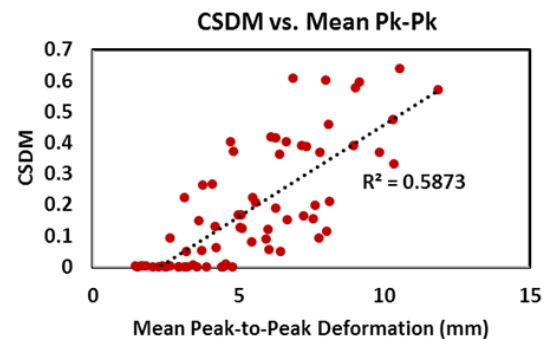
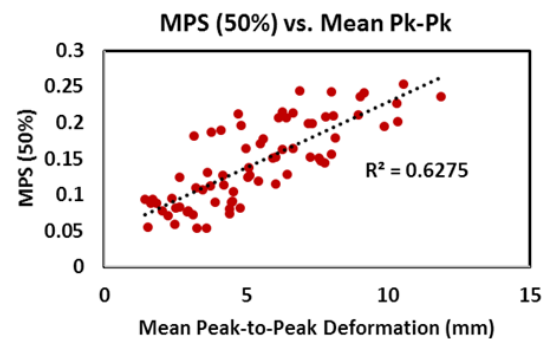
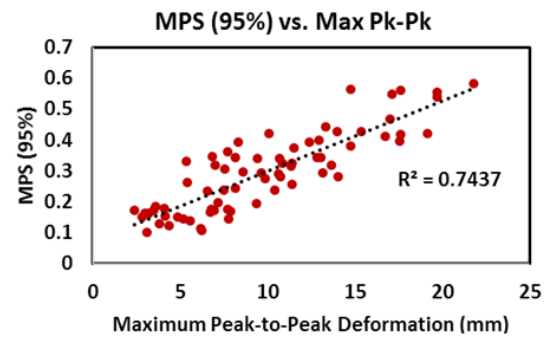


Figure 7-15: The correlation between tissue-level strain metrics (MPS-95<sup>th</sup>, MPS-50<sup>th</sup>, and CSDM) and experimental peak-to-peak brain deformation was investigated using linear regression for the GHBMC and SIMon models. The resulting best fit line (dashed) and correlation coefficient ( $R^2$ ) are plotted along with the data points (red).

## DISCUSSION

In this chapter, the evaluation of FE brain model biofidelity was investigated using various techniques to account for differences between specimen anthropometry and model geometry. Two widely used FE brain models, GHBMC and SIMon, were evaluated using the methods to determine best practices when evaluating FE models. The brain deformation

results of the models were compared to the sonomicrometry brain deformation dataset and the average response corridors generated in this dissertation. The strain results of the models were also used to compare the geometric comparison methods, and were compared to the experimental peak-to-peak brain deformation results. In general, there were no significant differences in the geometric methods, except for the morphed SIMon model. The average weighted CORA scores for all specimens ranged from 0.4-0.61 for GHBMc and from 0.34-0.53 for SIMon. The strain results showed some differences for the morphed models as compared to the original models, indicating the importance of a geometric match between the model and validation data. The correlation between FE model maximum strain metrics and the experimental peak-to-peak deformation was reasonable, with correlation coefficients as high as 0.74.

The four comparisons implemented to account for specimen anthropometry when evaluating FE models have not been used in the brain biomechanics field. The only previous dataset included many specimens, but there were no 3D brain or cranial scans available to study the effects of brain anthropometry on the biofidelity evaluations. The advantages of the sonomicrometry dataset also include the availability of CT, and in some cases, MRI scans of the tested specimen, in addition to digitally available 3D brain deformation data for each specimen under multiple severities. These scans allow for a thorough comparison of model evaluation methods. The GHBMc model showed small differences in the average weighted CORA across comparison methods, which could be because of small differences in geometry between the model and the specimens (Table 7-1, Figure 7-2). The SIMon model had similar results for the absolute, relative, and scaled comparison methods, but had lower average weighted CORA scores for the morphed

model. This difference is likely due to the height ( $z$ ) of the model, which is smaller than most of the specimens (Table 7-1, Figure 7-2). In specimens 900 and 904, where there were the largest differences in height between SIMon and the specimens, the morphed model had the poorest results.

Although the comparison methods were similar in overall average CORA scores, there may be local differences in motion that lead to better regional matches of brain deformation. The differences may inform predictions of brain deformation through tissue-level strain metrics. As shown in Figure 7-14, there were differences as large as 0.1 strain for the morphed models. The average CORA score may not reflect differences in deformation or strain, but the difference in strain emphasizes the importance of matching the FE brain model to the specimen or subject. To remove the effects of geometric differences between the model and experiments, the recommended method to evaluate models is to match the geometries through morphing. If morphing is not possible, the scaled model comparison method is recommended to account for size differences.

The morphing methodology implemented to account for specimen anthropometry provides an important advancement in FE brain modeling. The technique facilitates matching the exact inner cranium shape of the model and specimens, not only the size and volume. The average minimum distance between the surface of the FE model and surface of each specimen CT was less than 1 mm. While morphing has been attempted through conventional control point morphing (Horgan and Gilchrist, 2004; Li et al., 2011) and the generation of new voxel models (Ghajari et al., 2017; Miller et al., 2016), the use of an automated process of picking and registering control points is essential in generating an accurate specimen-specific model. The researcher does not have to manually select control

points, which can be laborious and error-prone. Instead, all of the nodes of the specimen geometry and model are used as control points, to automatically generate a smooth, accurate morphed model. A limitation of the morphing methodology for FE brain models is that it does not address the differences in internal anatomy between subjects, such as ventricle size, regional organization of brain regions, and size of the brain. The morphing methodology only registers the outside surface, consequently the internal anatomy is scaled according to the surface. Future methods that incorporate subject-specific morphing or model development of the brain using MRI scans are needed to accurately model and predict subject-specific brain injury.

The biofidelity of the models, with CORA scores as high as 0.6, could be improved. While the GHBMC model had slightly larger CORA values, it was difficult to assign a recommendation for either model in their performance as compared to the experimental data. It was also challenging to comment on a threshold value for a ‘good’ score in FE brain modeling. While a CORA value of 0.9 is typically used in biomechanics to assign an excellent match between the model and the experimental data (Gehre et al., 2009), such a high CORA value can be achieved when comparing metrics with low subject variability. FE models of the brain have variations in population differences, material differences, and FE implementation. A material sensitivity study will be presented in Chapter 8 to elucidate some of these differences, as well as a regional investigation of material changes that can improve the CORA scores of the models.

In addition to the individual specimen evaluations, the models were compared to the average data corridors in order to investigate their biofidelity to data that includes population variances in brain deformation. The models performed similarly to the

individual specimen data, with overall CORA scores ranging from 0.38-0.64. This result indicates that the corridors may be used as a supplement to individual specimen evaluations to assess the response to the population. If the corridors were the only method of evaluating the biofidelity of FE brain models, the scores may be inflated because many of the corridor displacements are around 0 mm displacement. This inflation can cause a model with an overly stiff response (low displacement) to have a large CORA corridor score, thus, inflating the overall CORA score.

A limitation in the evaluation of the FE brain models is the use of CORA to evaluate FE brain model biofidelity. CORA and similar cross-correlation tools have become standard in injury biomechanics to quantify FE model biofidelity to experimental results. While the CORA scores are beneficial in providing a generalized cross-correlation rating that includes magnitudes, phase, and slope differences between the two signals, it has limitations for evaluating differences between signals with small differences. When the CORA scores are averaged, the score may not capture subtle variation in brain deformation response as compared to the experimental data. Thus, CORA may, on average, be similar across multiple tests, but other metrics like peak-to-peak deformation or the transient duration of brain deformation may capture variations in biofidelity. An investigation into an optimal biofidelity rating or a set of parameters to evaluate model response is needed to minimize the confounding effects of the CORA rating.

The relationship between the models and experimental data extends to the strain metrics typically used to relate FE model results to clinical or real-world prediction of injury and product safety. Ideally, the strain metrics would match the experimental peak-to-peak brain deformation results. While there were good agreements between these

metrics, there were still discrepancies in the experimental deformation and the strain metrics (Figure 7-15). While it is not currently possible to conclude why the strain metrics are not very predictive of *in situ* brain deformation based on the linear regression results, the correlation provides a baseline for investigating the relationship between strain and brain deformation. The discrepancies are most likely due to the limited spatial sampling of the sonomicrometry experimental points within the brain, but model biofidelity and any computational methods confound those limitations. A regional analysis of largest strain, along with regions of largest peak-to-peak deformation may help explain differences or contribute to improving the model through a localized analysis of biofidelity.

## **CONCLUSION**

Two widely used FE brain models were evaluated in comparison to the experimental brain deformation dataset using four comparison methods to account for specimen anthropometry. The morphing method provided a reliable and accurate technique for morphing FE brain models. There were minimal differences across the comparison methods, but there were differences in strain metrics. The morphed model is recommended for use in biomechanics evaluation of FE models to minimize the differences between the model and specimen. Individual evaluations of each specimen are recommended to accurately measure the biofidelity of the models, with the corridor assessment used as a supplementary validation method.

The biofidelity scores for the models provided mixed results, with a need for further improvement of model response in comparison to the sonomicrometry brain deformation dataset. The material properties of the model can be optimized to improve the model response. To efficiently predict the optimal material properties of the brain models, a

sensitivity analysis can be used to investigate the spatial distribution of the effects of material property changes on brain deformation. The sensitivity analysis can then be used to predict calibrated material properties in an attempt to improve model biofidelity.

## **CHAPTER 8: FE MODEL MATERIAL SENSITIVITY**

The focus of this chapter is on understanding the sensitivity of the deformations of the GHBM and SIMon brain models when changing their baseline material parameters. These models were partially validated using previous experimental datasets and were evaluated in this dissertation (Chapter 7) in comparison to the sonomicrometry brain deformation dataset. The models showed mixed validation results. There are methods to improve the models, such as adjusting the material properties of the brain and surrounding structures. The goal of this chapter is to identify the first order sensitivity of all materials in the GHBM and SIMon FE brain models. The contributions of the sensitivity analysis will assist in the secondary goal of improving the biofidelity of the SIMon model by calibrating its material properties.

### **INTRODUCTION**

FE models of the brain are used extensively for TBI prediction, safety assessment, and mechanical investigations of brain trauma (Gabler et al., 2018b; Ji et al., 2015; Sanchez et al., 2017; Takhounts et al., 2008a). The limiting factor of FE brain models, however, is the validation data used to evaluate their biofidelity. The sonomicrometry experimental data generated in this dissertation provides a valuable tool for evaluating and improving the biofidelity of FE brain models. Two models, GHBM (Mao et al., 2013) and SIMon (Takhounts et al., 2008a), were evaluated in Chapter 7 to determine a baseline biofidelity evaluation for each model. The models provided CORA scores ranging from 0.42 to 0.64, indicating an adequate fit to the brain deformation data and the need for improvement.

While the geometric comparisons did not significantly change the validation scores, changes to the material properties could improve the biofidelity of these models. The

properties implemented in FE brain models are typically chosen through a combination of *ex situ* mechanical tests of brain tissue (Kleiven, 2007; Mao et al., 2013; Wu et al., 2019) and a calibration of the FE brain material properties to the Hardy (2007) brain deformation dataset. Although there have been many studies on the mechanical properties of the brain, there is a large range of values reported in the literature: the complex shear modulus spans three orders of magnitude and ranges from 0.1 to 100 kPa, and the damping coefficient (tan-delta) spans 0.1 to 4 (Figure 8-1).

The sonomicrometry dataset generated in this dissertation provides an accurate measurement of brain deformation at numerous locations within the brain. The regional distribution of crystals embedded in the brain and the plethora of data available present an opportunity for the calibration of material properties of various brain regions to the experimental dataset. Some FE brain model developers have attempted to tune the material properties of the model to match experimental brain deformation. Deck and Willinger (2009) conducted simulations of a model with six different material implementations to study their effects on brain deformation and intra-cranial pressure (Deck and Willinger, 2009). Miller et al. (2016) partially calibrated the material properties of an FE brain model, with the brain modeled as one material, to the brain deformation response of three brain deformation tests from the Hardy dataset (Miller et al., 2016). The final calibrated properties resulted in a CORA score of 0.426. Other studies have calibrated specific brain FE materials such as the brain's bulk modulus (Ganpule et al., 2018).

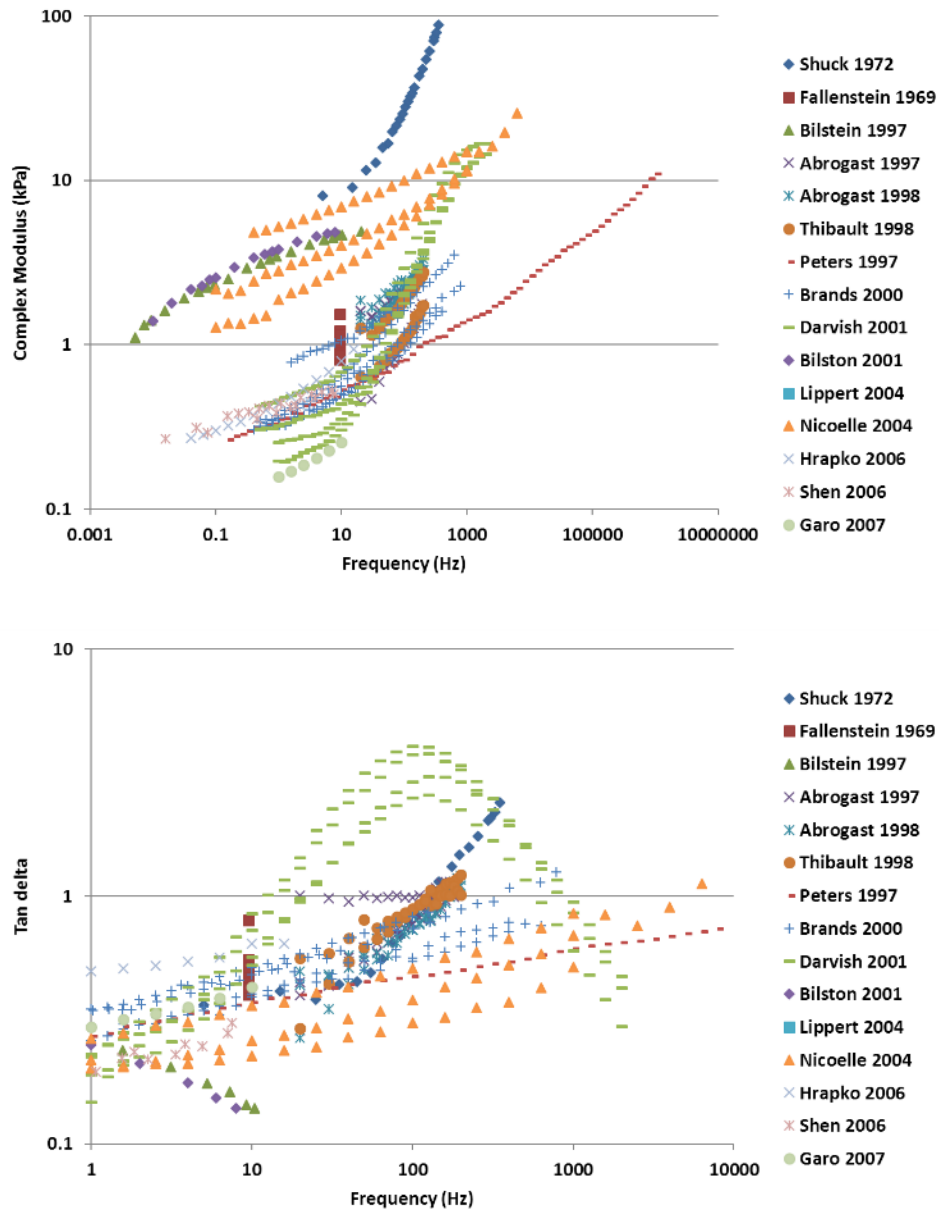


Figure 8-1: Reported material properties for brain tissue for the complex modulus and tan-delta (Panzer, 2012).

Before optimizing the material properties of FE brain models, it is important to investigate the effect of the material parameters on brain deformation response. Parts of the brain may be more sensitive to specific material property changes, and understanding the spatial distribution of the effects of those changes can assist in predicting calibrated material properties. Additionally, multiple parameters within each material model could

potentially be calibrated in an FE model. An optimization of all parameters to experimental data with multiple loading directions and severities is computationally expensive. A material sensitivity analysis will provide an informed choice of material parameters to optimize the model instead of using an unstructured calibration of all material parameters. This approach will reduce computational cost and will provide a methodology for improving already developed FE models.

The first aim of this chapter is to identify material parameters that affect brain motion and the spatial distribution of that effect. Two FE models, GHBMC and SIMon, will be used in this study to conduct a material sensitivity analysis on all parts used to model the brain. A linear regression model will be developed to identify the significance of each material property on the brain deformation response throughout the brain. The second aim will be to use the regression model to predict a set of new material parameters that will improve the accuracy of the model response. The models will then be calibrated with the new material properties to improve their biofidelity in comparison to the sonomicrometry dataset.

## **METHODS**

A computational study for the GHBMC and SIMon FE brain models was performed to determine the effect of material property changes on brain deformation. There were two material constitutive models used for all brain parts that were analyzed in this study, linear elastic or linear viscoelastic (VE). The linear VE constitutive model used in the GHBMC and SIMon models is the standard linear solid (SLS), which contains one time constant in the viscoelastic formulation. A single order parametric analysis (changing only one

material property for each simulation) of the materials was conducted under loading conditions representative of the sonomicrometry dataset.

### **Material Parameters**

For the linear elastic FE brain material parts, three parameters define the material response, including the density, Poisson's ratio, and the stiffness (Young's modulus). It is often assumed that the density and Poisson's ratio do not vary significantly for different brain parts due to the high water content and incompressible nature of brain tissue. The only parameter that is believed to contribute to the tissue deformation response is the material stiffness, which was varied to determine its effect on the brain deformation response. Two simulations were run for each elastic material, one with 200% stiffness and the other with 50% stiffness as compared to the baseline model (Table 8-1). The baseline model is defined as the original GHBMC brain model with no geometric or material changes.

For the linear viscoelastic materials, the parameters that govern the material response include the bulk modulus and the viscoelastic parameters. The bulk modulus was not altered in this analysis due to its relative magnitude (three orders of magnitude larger than the shear modulus) and high water content of brain tissue. A recent study of the bulk modulus of the brain showed that brain deformation was insensitive to changes in the parameter within an order of magnitude (Ganpule et al., 2018). Three material parameters control the stiffness and viscoelasticity of the SLS constitutive model: the short-term shear modulus ( $G_0$ ), the time constant ( $\tau$ ), and the long-term shear modulus ( $G_\infty$ ). These three parameters were combined into the storage ( $G'$ ) and loss ( $G''$ ) moduli, which depend on the frequency of deformation ( $\omega$ ). The storage and loss moduli were then used to calculate

the complex modulus ( $G^*$ ) and tan-delta ( $\tan[\delta]$ ). The complex modulus represents the shear stiffness of the viscoelastic material, while  $\tan(\delta)$  represents the damping of the linear viscoelastic material. The formulations are given in the equations below.

$$E' = \frac{G_\infty + (G_\infty + G_0)\omega^2\tau^2}{1 + \omega^2\tau^2} \quad (8-1)$$

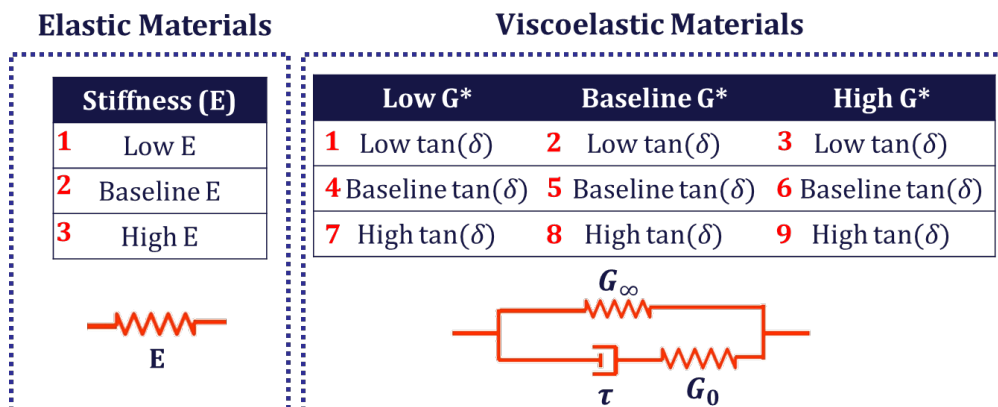
$$E'' = \frac{\omega\tau G_0}{1 + \omega^2\tau^2} \quad (8-2)$$

$$G^* = \sqrt{G'^2 + G''^2} \quad (8-3)$$

$$\tan(\delta) = \frac{E''}{E'} \quad (8-4)$$

To determine the sensitivity of brain deformation to the linear VE parameters, the complex modulus was varied from its baseline value to a ‘high’ value that is 200% of the baseline and ‘low’ value that is 50% of the baseline. The same percentage changes were applied to the damping ( $\tan[\delta]$ ). Nine sensitivity conditions were simulated for each linear VE material, with a combination of low, baseline, and high complex modulus and  $\tan[\delta]$ . The simulation matrix for each linear VE material can be found in Table 8-1. A depiction of the material sensitivity for the white matter viscoelastic material of the GHBMC model is shown in Figure 8-2.

*Table 8-1: Material sensitivity matrix for each the FE model materials. The elastic materials have one parameter, the Young’s modulus or stiffness of the material. The viscoelastic materials have two parameters, the complex modulus ( $G^*$ ) and damping coefficient ( $\tan[\delta]$ ).*



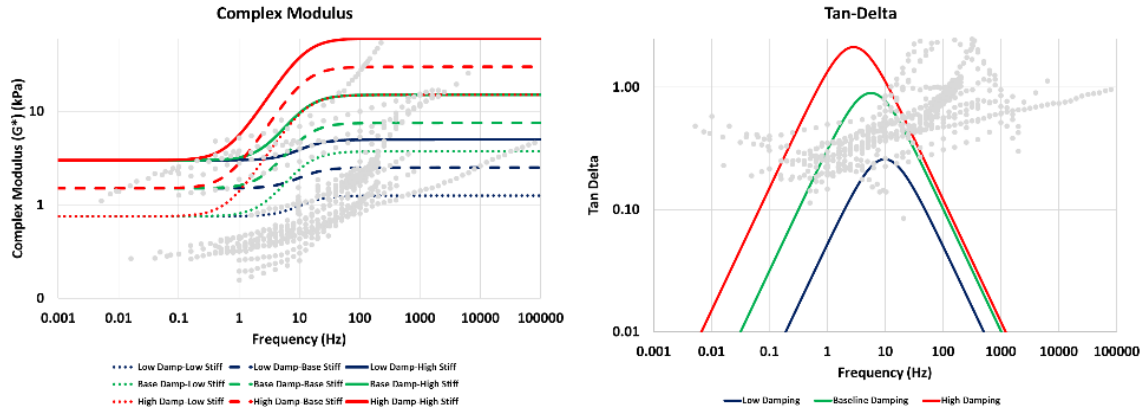


Figure 8-2: The material sensitivity parameters for the cerebrum white and cerebellum parts of the GHBMC model, with the complex modulus (left) and  $\tan(\delta)$  (right). Gray dots indicate literature material properties.

For the GHBMC model, there were six parts with linear elastic material properties with two simulations each. These include the dura, falx, pia mater, arachnoid, tentorium, and the brainstem cap. There were eight parts with LVE material properties with eight simulations each: cerebrum gray, cerebrum white, cerebellum, thalamus, brainstem, basal ganglia, corpus callosum, and the CSF/ventricles. For the SIMon model, there were two parts with elastic material properties: the falx-tentorium and the foramen. There were four parts with VE material properties: cerebrum, cerebellum, brainstem, and CSF. The original material properties and the range of properties used in the sensitivity analysis are shown in Figure 8-2.

The kinematic loading conditions used in the sensitivity study simulations were the 40 rad/s, 60 ms pulses from specimen 846. To evaluate the material sensitivity in all three directions, simulations were run in the sagittal, coronal, and axial directions, using the respective 40 rad/s, 60 ms pulses from specimen 846. The final simulations matrix included 231 simulations for GHBMC and 111 for SIMon for a total of 342 sensitivity analysis simulations (Table 8-3).

Table 8-2: Original material properties for the GHBMC and SIMon models. The range of material properties used in the sensitivity analysis are given in parentheses.

| Model | Part  | Material Type | Short-term Shear Modulus (kPa) | Long-term Shear Modulus (kPa) | Time Constant (ms) | Young's Modulus (MPa) |
|-------|---|---------------|--------------------------------|-------------------------------|--------------------|-----------------------|
| GHBMC | Cerebrum Gray, Cerebellum, Thalamus, Brainstem, Basal Ganglia | Linear VE     | 6 (1 - 48)                     | 1.2 (0.6 - 2.4)               | 0.0125             | --                    |
|       | Corpus Callosum, Cerebrum White                               | Linear VE     | 7.5 (1.25 - 60)                | 1.5 (0.75 - 3)                | 0.0125             | --                    |
|       | CSF, Ventricles   | Linear VE     | 0.5 (0.16 - 4)                 | 0.1 (0.05 - 0.2)              | 0.0125             | --                    |
|       | Dura, Tentorium, Brainstem Cap                                | Elastic       | --                             | --                            | --                 | 31.5 (15.75 - 63)     |
|       | Falx, Pia Mater   | Elastic       | --                             | --                            | --                 | 12.5 (6.25 - 25)      |
|       | Arachnoid   | Elastic       | --                             | --                            | --                 | 12 (6 - 24)           |
| SIMon | Cerebrum, Cerebellum, Brainstem                               | Linear VE     | 1.66 (0.6 - 15.73)             | 0.928 (0.46 - 1.86)           | 59                 | --                    |
|       | CSF   | Linear VE     | 100 (16.7 - 800)               | 20 (10 - 40)                  | 10                 | --                    |
|       | Falx, Tentorium   | Elastic       | --                             | --                            | --                 | 31.5 (15.75 - 63)     |
|       | Foramen   | Elastic       | --                             | --                            | --                 | 6933 (3467 - 13867)   |

Table 8-3: Simulation matrix for each of the GHBMC and SIMon FE brain models. GHBMC included fourteen parts, and SIMon included six parts for the sensitivity analysis for a total of 342 simulations.

| Model        | Part   | Material Type       | Number of Parts | Sensitivity Cases | Head Rotations | Total Models |
|--------------|--|---------------------|-----------------|-------------------|----------------|--------------|
| GHBMC        | Baseline   | N/A                 | 1               | 1                 | 3              | 3            |
|              | Cerebrum Gray, Cerebellum, Thalamus, Brainstem, Basal Ganglia, Corpus Callosum, Cerebrum White | Linear Viscoelastic | 7               | 8                 | 3              | 168          |
|              | CSF, Ventricles  | Linear Viscoelastic | 1               | 8                 | 3              | 24           |
|              | Brainstem cap  | Elastic             | 1               | 2                 | 3              | 6            |
|              | Dura   | Elastic             | 1               | 2                 | 3              | 6            |
|              | Falx, Pia Mater  | Elastic             | 2               | 2                 | 3              | 12           |
|              | Arachnoid  | Elastic             | 1               | 2                 | 3              | 6            |
|              | Tentorium  | Elastic             | 1               | 2                 | 3              | 6            |
| SIMon        | Baseline   | N/A                 | 1               | 1                 | 3              | 3            |
|              | Cerebrum, cerebellum, brainstem  | Linear Viscoelastic | 3               | 8                 | 3              | 72           |
|              | PAC-CSF  | Linear Viscoelastic | 1               | 8                 | 3              | 24           |
|              | Falx, Tentorium  | Elastic             | 1               | 2                 | 3              | 6            |
|              | Foramen-Magnum   | Elastic             | 1               | 2                 | 3              | 6            |
| <b>TOTAL</b> |  |                     |                 |                   |                | <b>342</b>   |

## Sensitivity Evaluation

To investigate the effects of the sensitivity of changes in material properties on brain deformation, peak-to-peak deformation of all of the nodes of each model was quantified. The peak-to-peak deformation of every node for each sensitivity simulation was calculated using the maximum point-to-point displacement during the trajectory of each node. The change in peak-to-peak deformation, as compared to the baseline model, was quantified to

determine the effect of material changes on the models. The inclusion of all nodes in this analysis, not just the corresponding nodes to the sonomicrometry experiments, allows for a spatial sensitivity analysis that determined which materials affect specific regions of the brain. There were a total of 72,564 brain nodes in the GHBMC model and 33,445 brain nodes in the SIMon model.

To determine the effect of each material on the model response, a multiple linear regression was conducted for each node in each model. The regression model used the change in peak-to-peak deformation of the node as the output, and each material was used as an input to the linear regression. The material properties were assigned a value of 0 for the baseline model, a value of 1 for the model with a 200% increase (high), and a value of -1 for the model with a 50% decrease (low). The change in peak-to-peak deformation was 0 mm for the baseline model. It was calculated relative to the baseline for the low and high sensitivity models. The multiple linear regression included one term for each linear elastic material (the stiffness) and two terms for each linear viscoelastic material. The GHBMC model had 22 terms in the regression, and SIMon had 10 terms. A generalized equation for each node ( $i$ ) in response to each material parameters ( $x_m$ ), with coefficients ( $A_m$ ), is given in the equation below. The intercept term was set to 0.

$$[Pk - Pk]_i = \sum A_m x_m \quad (8-5)$$

Threshold values for the input peak-to-peak deformation, the regression p-value, and the coefficients were used to remove insignificant terms from the analysis. All changes in peak-to-peak deformation less than 0.25 mm were excluded, and no regression was conducted for that node. The 0.25 mm threshold was chosen to remove nodes with small changes in brain motion relative to the changes in material properties. If the regression was

calculated, any coefficient that was not significant (with a p-value greater than 0.05) was assigned a value of 0. Additionally, any coefficient magnitude ( $A_m$ ) less than 0.1 was not meaningful due to the small effect of brain deformation in the range of the material property changes, and was assigned a value of 0. The regression analysis was conducted for each of the three loading directions (sagittal, coronal, and axial).

### **Model Material Calibration**

The sensitivity regression model was utilized to optimize the results of the models to better fit the experimental brain deformation data. The following method was applied to the data from a single specimen only. The model was optimized by finding the 24 corresponding nodes, using the absolute comparison method (Chapter 7) for the specimen. The regression equations for each of the 24 nodes were then used to construct a linearized matrix form of the formulation, where the vector  $\vec{b}$  is the change in peak-to-peak deformation.

$$\mathbf{A}\vec{x} = \vec{b} \quad (8-6)$$

The sizes of  $\mathbf{A}$  and  $\vec{b}$  depend on the data used to predict the optimal material properties. If all three rotations (sagittal, coronal, and axial) were used for the optimization of a single specimen, the  $\mathbf{A}$  was a 72x22 matrix and  $\vec{b}$  was a 72x1 vector. The vector  $\vec{x}$  represents the number of materials and was a 22x1 vector. The equation was solved using the following equation to predict the optimal material properties.

$$\vec{x} = \mathbf{A}^{-1}\vec{b} \quad (8-7)$$

The tuned material properties incorporated in the model and simulations were run for the 40 rad/s, 60 ms loading condition in all three directions to verify the model

improvement. Once the model parameters were calibrated to the three loading conditions, the remaining nine rotations were simulated and evaluated.

## RESULTS

### GHBMC Material Sensitivity

The brain deformation sensitivity to each material was investigated using the loading kinematics from specimen 846. The 40 rad/s, 60 ms loading condition was simulated in the three loading directions (sagittal, coronal, and axial), and each material was simulated with either two material changes for elastic properties or eight material properties for LVE materials. The change in peak-to-peak deformation for all nodes experiencing a peak-to-peak deformation difference greater than 0.25 mm is presented in Figure 8-3 for the cerebrum gray and brainstem parts of the GHBMC model for the high damping, high stiffness case.

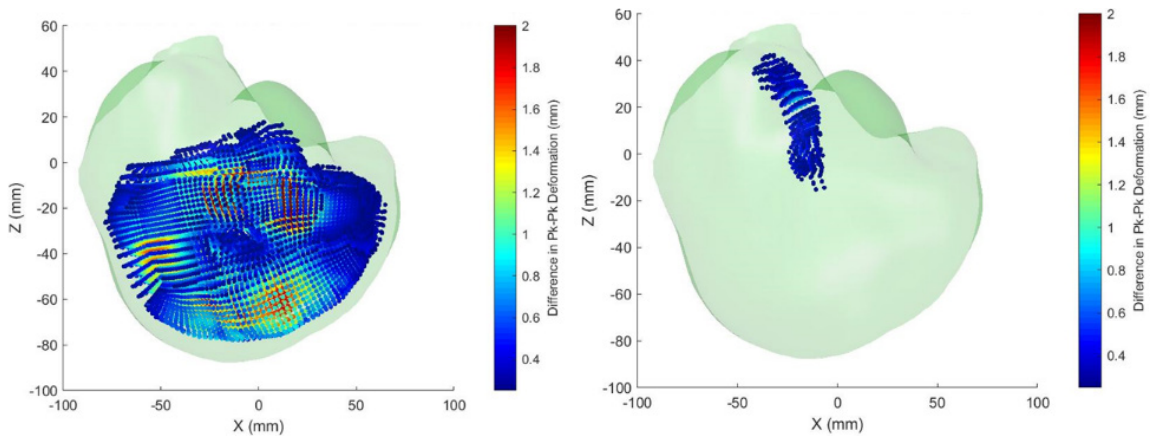


*Figure 8-3: The sensitivity of the cerebrum gray and brainstem parts of the GHBMC model for the high damping, high stiffness case under sagittal rotation. The change in peak-to-peak deformation, relative to the baseline model is shown in color for all nodes with a magnitude greater than 0.25 mm.*

The regression analysis of the sensitivity study allows for the compilation of data from the material changes (two cases for each elastic material and eight cases for each viscoelastic material) into a single coefficient for each node. The regression coefficient

indicates the magnitude and increase or decrease of the peak-to-peak deformation of each node in response to the material change. An example of the coefficients for the cerebrum gray in response to changes in the complex modulus ( $G^*$ ) is shown in Figure 8-4. The regression plots of all the materials are presented in Appendix G. To investigate whether each material parameter affected the model, the maximum of the absolute value of regression coefficients across all nodes for each material parameter was calculated and is depicted in Figure 8-5. Some materials, including the dura, spinal cap, CSF, and thalamus had very low or insignificant regression coefficients, indicating small contributions to the deformation response. Certain membranes, including the arachnoid and pia, had a significant effect on peak-to-peak deformation. Most of the brain parts affected the nodes within the specific parts, such as the brainstem or cerebellum, with the most significant effects stemming from changes in the cerebrum gray and white matter.

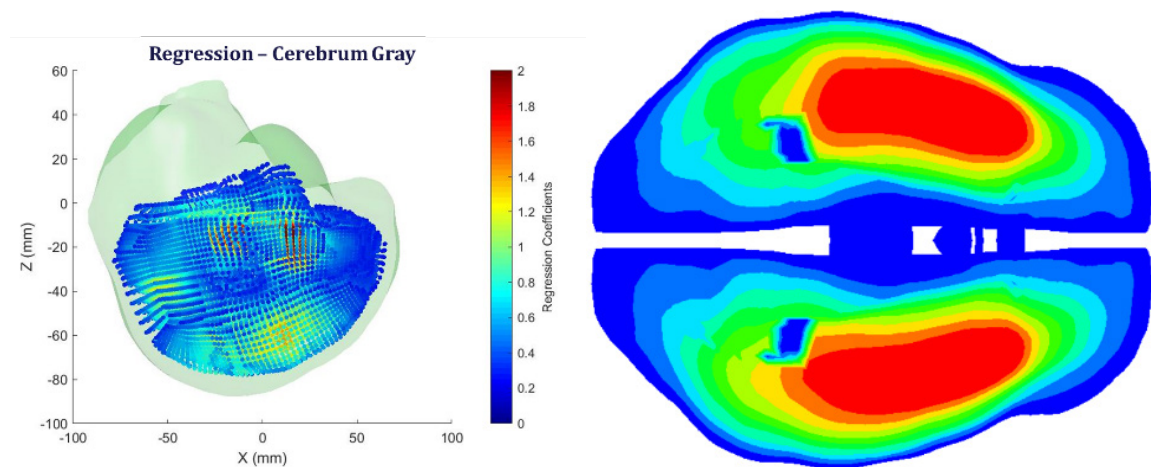


*Figure 8-4: The absolute value of the significant regression coefficients ( $p$ -value  $< 0.05$  and  $|A_i| > 0.1$ ) of the cerebrum gray of the GHBMC model for the sagittal rotation are shown for all nodes in response changes in the complex modulus (left). A superior-inferior slice view ( $z = -20$  mm) of the distribution of the regression coefficients is shown on the right.*

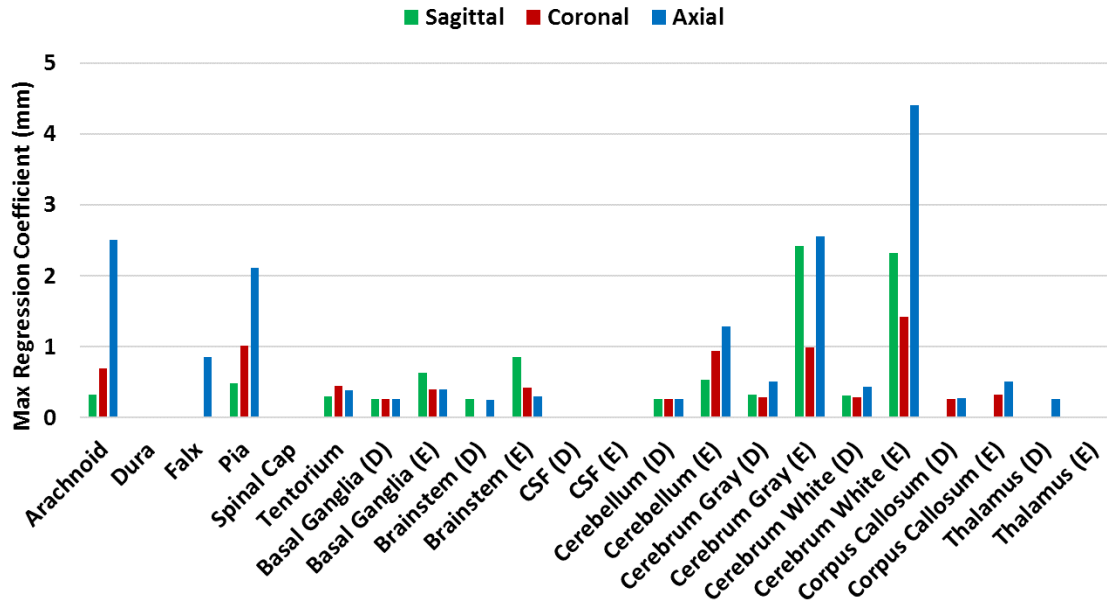


Figure 8-5: The maximum of the absolute value of the regression coefficients across all nodes of the GHBMC model are shown for each of the three rotation directions. For viscoelastic material, the damping (D) and complex modulus (E) are separated for each material.

### SIMon Material Sensitivity

A similar analysis was conducted for the SIMon brain model materials. The differences in peak-to-peak deformation for the CSF and the cerebellum under the baseline damping, high stiffness condition for the sagittal rotations are depicted in Figure 8-6.

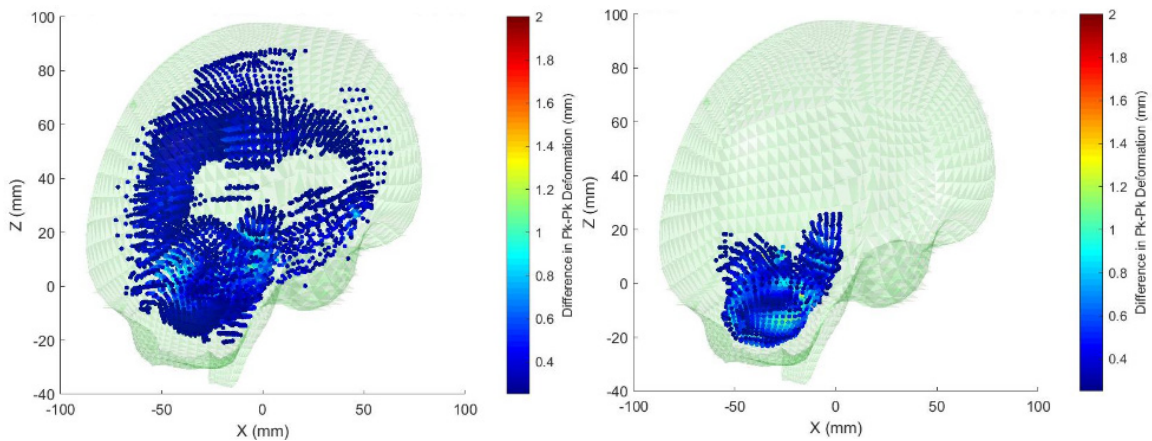
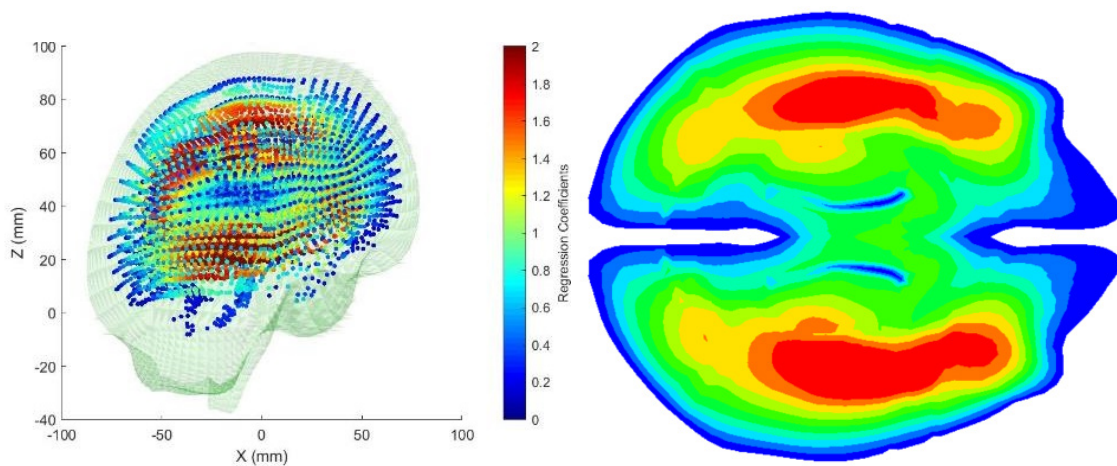


Figure 8-6: The sensitivity of the CSF and cerebellum parts of the SIMon model for the baseline damping, high stiffness case under sagittal rotation. The change in peak-to-peak deformation, relative to the baseline model is shown for all nodes with a magnitude greater than 0.25 mm.

The regression analysis showed similar results to the GHBMC models. For the brainstem, cerebellum, and brainstem parts, the regression coefficients were significant for nodes within the corresponding parts for each material. The cerebrum regression results for the complex modulus parameters are depicted in Figure 8-7. The regression plots of all the materials are presented in Appendix G. The CSF and falx/tentorium materials also affected the deformation response at brain regions neighboring those parts. The foramen did not have any significant regression coefficients. The maximum of the absolute value of regression coefficients across all nodes for each material parameter was calculated and is shown in Figure 8-8.



*Figure 8-7: The absolute value of the significant regression coefficients ( $p$ -value  $< 0.05$  and  $|A_i| > 0.1$ ) of the cerebrum of the SIMon model for the sagittal rotation are shown for all nodes in response changes in the complex modulus (left). A superior-inferior slice view ( $z = 30$  mm) of the distribution of the regression coefficients is shown on the right.*

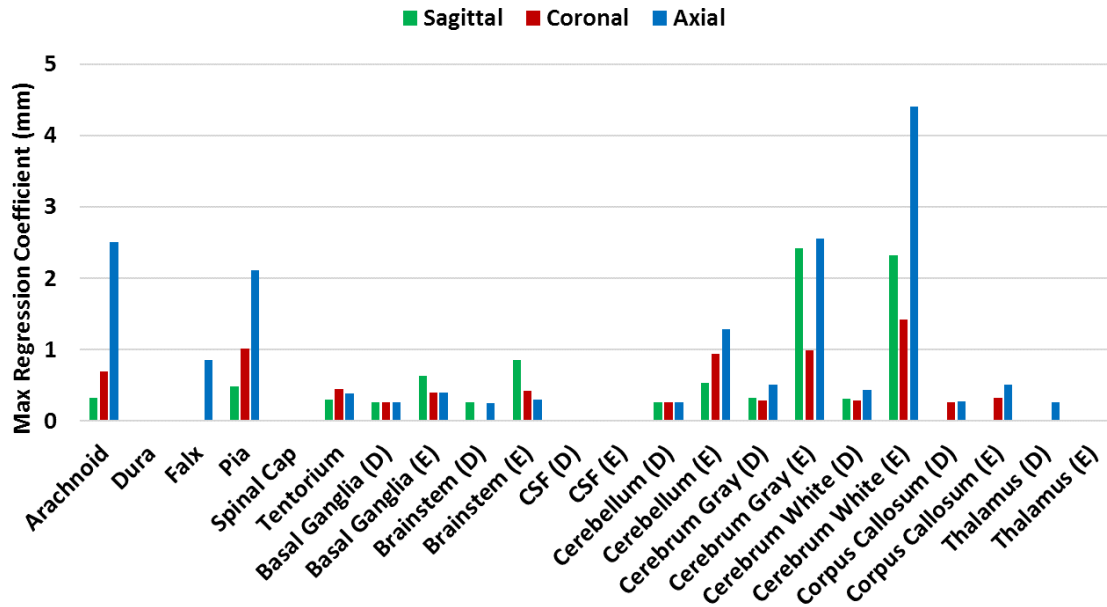


Figure 8-8: The maximum of the absolute value of the regression coefficients across all nodes of the SIMon model are shown for each of the three rotation directions. For viscoelastic material, the damping (D), and complex modulus (E) are separated for each material.

### **Model Improvement**

The calibration procedure was initially implemented using the GHBM model, but it was discovered that the linear VE time constant implemented in the model (0.0125 ms) is three orders of magnitude lower than the reported time constant of 12.5 ms (Mao et al., 2013). Thus, the damping parameters in the sensitivity analysis exhibited little to no effect on the peak-to-peak deformation due to the wrong time constant. The regression fit, consequently, was not able to correctly predict the calibrated material properties.

Nevertheless, the prediction of the linear regression was used to calibrate the stiffness of the model using the data from specimen 846. The predicted normalized parameters for the pia (-4.0), cerebrum gray (-0.2) and cerebrum white (2.4) were changed in the model, with all other material parameters remaining the same. An example trace for the axial rotation (40 rad/s – 60 ms) with the original and calibrated FE response shown in

comparison to the sonomicrometry data in Figure 8-9. The CORA scores of the calibrated model were within 0.1 of the original model. Although the CORA score did not show any differences, the difference in peak-to-peak deformation between the FE models and the sonomicrometry brain deformation data showed an improved regression prediction. The averages of the absolute value of the peak-to-peak deformation differences are depicted in Figure 8-10.

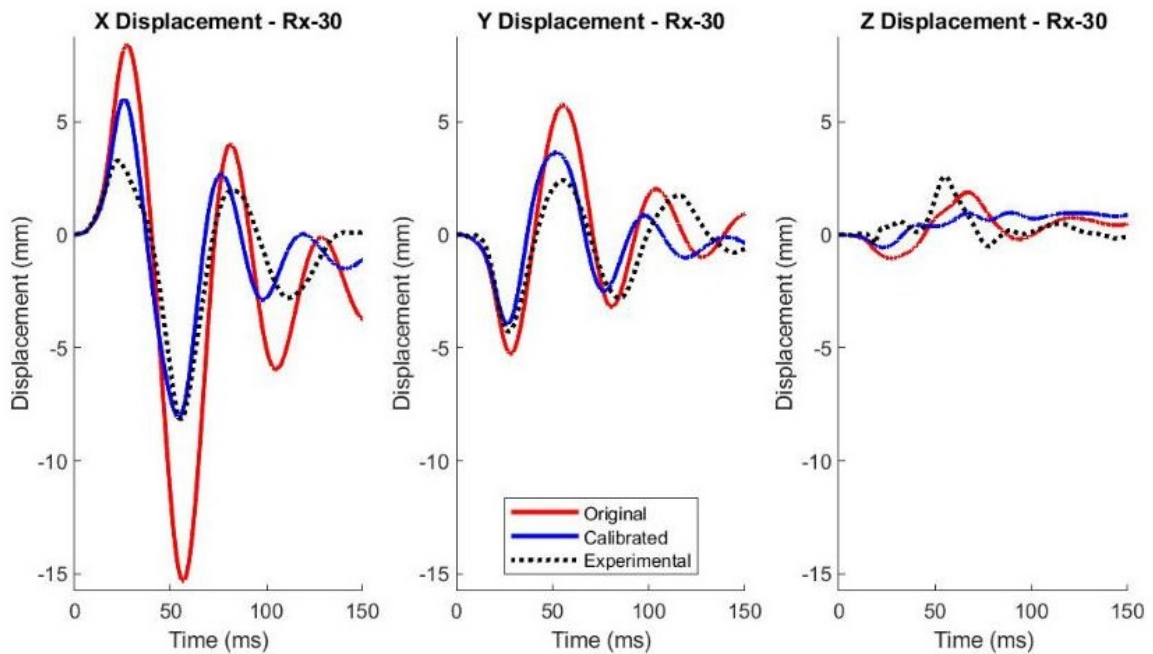
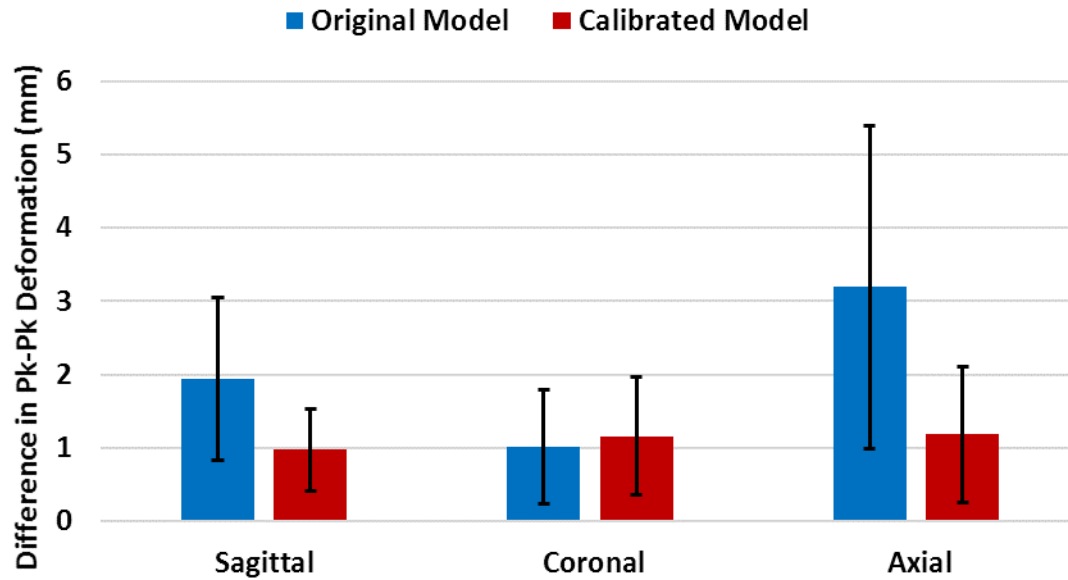


Figure 8-9: The effect of the calibrated material properties for specimen 846 for the axial – 40 rad/s – 60ms rotation.

## GHBMC Optimization



*Figure 8-10: The difference in peak-to-peak deformation between the GHBMC model and sonomicrometry data for the three rotation directions. The calibrated model resulted in lower average differences in peak-to-peak deformation for the sagittal and axial rotations.*

The calibration procedure could not be fully validated using the GHBMC model due to an issue in the linear VE time constant. The SIMon model was calibrated using the same procedure for specimen 900 in an attempt to predict material properties that will improve the CORA validation score. The improvement in weighted CORA from the calibrated material properties is shown in Figure 8-11. CORA scores increased by 0.05 – 0.1 across all directions of rotation for the tests used to calibrate the material properties. For the remaining tests, there were improvements in the sagittal and coronal tests, while the axial rotations had approximately similar scores to the original model.

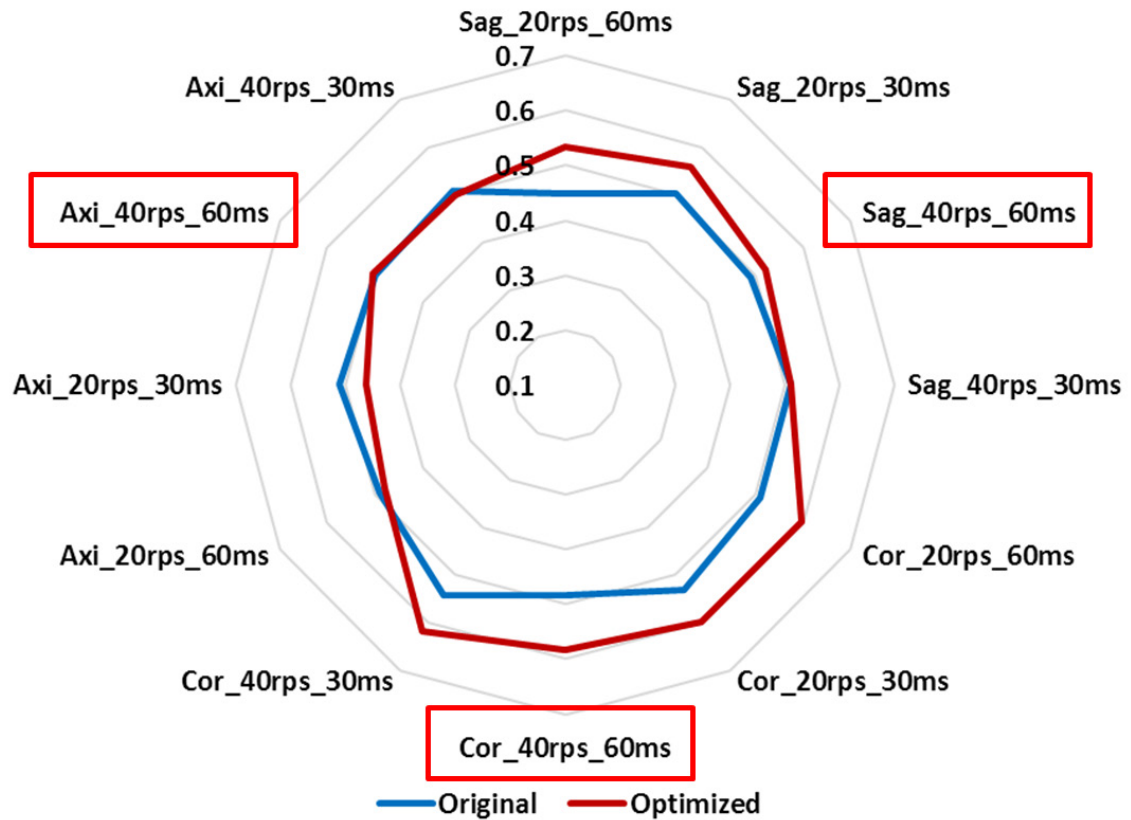


Figure 8-11: The weighted CORA score of the original and calibrated SIMon model in comparison to the specimen 900 brain deformation data for all tests. The tests used to calibrate the material properties are shown with red boxes.

## DISCUSSION

The biofidelity of the deformation response of FE brain models is essential to their predictions of TBI. Calibration of the material parameters can improve model performance relative to the sonomicrometry brain deformation dataset. Since there was a broad range of reported mechanical properties for brain tissue, the parameters implemented in any model must be validated for that model based on the computational methods. A first-order sensitivity study was conducted in this chapter to elucidate the effects of brain and meningeal material parameters on the brain deformation response. The sensitivity provides valuable information on what parameters can be changed to optimize the model. An

example of this optimization was conducted using the GHBMCM and SIMon model, and the sensitivity results provided an informed guess into the optimal material properties. The optimized GHBMCM/SIMon model yielded a better biofidelity score, with CORA scores increases up to 0.1 for the axial 40 rad/s, 60 ms rotation.

### **FE Sensitivity**

The results of the sensitivity analyses provide insight into the parameters that have a significant effect on the model response. For the GHBMCM model, most of the significant material parameters affected the parts using that material, and the effect did not extend to nodes in other regions. For example, the brainstem stiffness parameter affects a subset of nodes within the brainstem part and does not affect any nodes in the cerebellum or midbrain. There were minimal effects on brain deformation for smaller regions of the brain, including the thalamus, corpus callosum, and basal ganglia, possibly due to the magnitude of stiffness chosen and the small volume of those parts. The SIMon model exhibited similar trends, with the cerebrum, brainstem, and cerebellum affecting a majority of the nodes within the respective parts.

The CSF material properties showed contrasting trends in the models. For the GHBMCM model, the CSF and ventricle spaces did not affect brain deformation. The CSF of the SIMon model had a significant effect on the surrounding regions. The difference was likely due to the computational methods implemented for the CSF part. The GHBMCM CSF and ventricles were modeled as a solid part with a Young's modulus, while SIMon employs a fluid material (with zero stiffness) for the ventricles. The CSF in SIMon was modeled as a linear viscoelastic solid to represent the effective stiffness of the pia-arachnoid complex (Takhounts et al., 2008a). The SIMon ventricles were not analyzed in the sensitivity

analysis, but the effect of the CSF on brain deformation was likely a consequence of the modeling approach of the CSF layer, which includes the influence of the meninges.

The meningeal layers of the models affect regions that were close to the surface of the part, with no effect on nodes deep within the brain parenchyma. These membranes serve to encompass and link parts of the brain to the inner skull and other brain regions. The contribution of the meninges on brain deformation can be explained by the interfaces between the meninges and brain modeled as tied nodes. The pia and arachnoid of the GHBM model, for example, may have a small tethering effect on nearby brain nodes depending on their stiffness and direction of motion. The falx of the GHBM model affects only in axial rotation, while the tentorium contributed in all three rotation directions. The SIMon model also exhibits contributions from the meninges, with the falx-tentorium parts affecting the brain deformation of nearby regions. The effect of the arachnoid and pia was included in the CSF component. For both models, the membrane at the inferior edge of the brainstem (the foramen/spinal cap) was a necessary modeling technique to create an accurate boundary condition for the model without including the spinal cord. The stiffness of this membrane did not affect the brain deformation of either model.

A multiple linear regression elucidated the effects of the material parameters on brain deformation. A regression consolidated the effects of the sensitivity study into a simple and computationally efficient analysis of the significant material parameters. Instead of analyzing each of the eight cases associated with a linear viscoelastic material, the significant material properties can be statistically determined for each node of the model. Peak-to-peak deformation was the chosen output of this analysis to match the deformation response of the models, although different parameters could be utilized, such as peak-to-

peak deformation in each direction (x, y, z) or the duration of brain motion. The regression delves deeper into the material properties of the brain, providing insight into future avenues of experimental and FE model optimization. One of the least characterized tissues in the brain is the meninges, especially the pia and arachnoid. The bovine pia-arachnoid complex has been characterized under tensile (Jin et al., 2006) and shear (Jin et al., 2011) loading, with Young's moduli of 6.75-40.19 MPa shear moduli of 11.73-22.37 kPa under various strain rates. Recent experiments on the spinal cord and pia-arachnoid complex showed a viscoelastic response of the meninges with a much stiffer response of the meninges than the spinal cord (Ramo et al., 2018). A better characterization of the human brain pia-arachnoid complex will improve its FE representation in human brain models.

A limitation of this analysis is the specificity of the results to each model, given the differences in boundary conditions and computational methods utilized for each FE brain model. The results of the sensitivity analysis cannot be used to make conclusions about the contributions of specific material properties to brain deformation or injury, only to the predicted brain deformation of the model. This distinction is important due to the methods used to create FE brain models, where differences in mesh size, hourglass control, and various other parameters can have an effect on the brain response (Giudice et al., 2018a). One example of a modeling choice that may affect the response of the brain is how the skull-brain boundary is simulated. The two models used in this study used a continuous mesh with shared nodes to model the meninges and brain. This layer is typically modeled as a solid with a low stiffness to allow the brain to slide relative to the skull (mimicking the CSF and arachnoid space). Other approaches to model the skull-brain boundary are available including sliding contact boundaries with or without a friction coefficient (Dixit

and Liu, 2017). Although more computational parameters are introduced when changing the internal boundary conditions, a sliding interface should be investigated in future optimization of FE brain models to more accurately represent the mechanics of brain motion.

### **FE Model Improvement**

The regression analysis can identify experimental needs as well as predict properties based on biofidelic brain deformation. The results for each node allow for an optimization of the model response to the peak-to-peak deformation response. A simple linear matrix form of the optimization was utilized to predict the change in material properties that will tune the model to match the sonomicrometry data. This optimization may not be perfect depending on the chosen regression output (peak-to-peak deformation), but it allows for an informed prediction of material parameters. This method of optimization reduces the computational cost and provides future techniques of optimizing the model based on various regression outputs.

FE model optimization using the results of the sensitivity analysis was demonstrated in this study with the GHBMC and SIMon models. In the first calibration of material parameters using the regression model for the GHBMC model, the difference in peak-to-peak deformation between the model and sonomicrometry dataset was used to predict calibrated material properties. While the CORA scores did not increase, there was a reduction in the difference in peak-to-peak deformation between the model and data. The lack of change in the CORA scores was likely due to the choice of peak-to-peak deformation as the regression output. Other parameters should be investigated to align

more closely with the desired CORA biofidelity rating, such as peak-to-peak deformation in each direction or the duration of brain deformation for each crystal.

Another limitation in improving the models was the use of CORA to evaluate FE brain model biofidelity. CORA and similar cross-correlation tools have become standard in injury biomechanics to quantify FE model biofidelity to experimental results. While the CORA scores are beneficial in providing a generalized cross-correlation rating that includes magnitudes, phase, and slope differences between the two signals, it has limitations for evaluating differences between signals with small differences. When the CORA scores of multiple signals are averaged, the score may not capture subtle improvements in the model's response. Thus, a material property calibration may yield a better match in peak-to-peak deformation, but the average CORA scores may remain the same. An investigation into an optimal biofidelity rating or a set of parameters to evaluate model response is needed to minimize the confounding effects of the CORA rating.

An issue with the published version of the GHBMC model prevented an ideal calibration using the regression analysis. While Mao et al. (2013) report a time constant of 12.5 ms for all linear viscoelastic materials, the model files contain a time constant of 0.0125 ms, three orders of magnitude lower. The short time constant means that the mechanical behavior of the brain is essentially elastic and governed only by the long-term shear modulus ( $G_t$ ). This error was observed in the sensitivity analysis, where the damping parameters exhibited little to no effect on the peak-to-peak deformation due to the wrong time constant. The regression fit, consequently, was not able to predict calibrated material properties with an improved CORA score. It is unclear what the correct time constant should be, as a preliminary evaluation of the model response using the reported time

constant of 12.5 ms yields lower CORA scores in comparison to the sonomicrometry dataset than 0.0125 ms. Once the correct parameter is identified by the developers, the new model can be evaluated and a sensitivity analysis can be conducted. Alternatively, more advanced versions of this model (Wu et al., 2019) can be used for material calibration.

## **CONCLUSION**

A sensitivity analysis of the mechanical properties of the GHBMC and SIMon models elucidated the influence of material parameters on brain deformation at every node in the FE brain. A linear regression provided a statistical method to determine and visualize the significant material properties. The sensitivity results can inform future experiments of brain mechanical properties, in addition to optimizing the material parameters of existing models. The GHBMC and SIMon models were calibrated based on the regression analysis of the nodes corresponding to the sonomicrometry experiments. The optimization was expedient in predicting the material properties of the model and improved the biofidelity score of the SIMon model.

## **CHAPTER 9: CONCLUSIONS**

Traumatic brain injuries (TBI) are one of the most common but least understood injuries to the body, with an estimated 1.7 million TBIs occur annually in the United States. Finite element (FE) models of the brain have been crucial for understanding brain injury and developing injury mitigation systems; however, the experimental brain deformation data currently used to validate these models are limited. The objective of this dissertation is to advance the current state of research of TBI mechanics by improving the experimental understanding of brain deformation under rotational loading and improving the biofidelity of FE brain modeling capabilities. This dissertation will include research using both experimental and computational methods. The experimental phase will focus on developing a methodology to measure *in-situ* human brain motion under rotational loading, and on using the methodology to build a dataset of brain deformation. The computational phase will focus on developing a methodology to evaluate FE brain models in comparison to experimental data, and on a framework to optimize the material properties of the models to better match the brain deformation data.

### **SUMMARY AND MAJOR CONTRIBUTIONS**

Accurately quantifying brain motion is crucial for understanding and modeling the mechanics of the human brain. Our understanding of human brain mechanics is primarily informed by animal models, mechanical property experiments of brain tissue, and computational models. In particular, FE models of the brain have become ubiquitous in research aimed at predicting and mitigating TBI. The validation of FE brain models to human brain deformation data is requisite for their efficacy and capacity to predict injury

and assist in the design of safety equipment. Some datasets of human brain deformation exist, but they include limitations that preclude their use for FE model validation.

There has been a need in the field of TBI biomechanics for a dataset of brain deformation under dynamic rotational loading, as well as recommended methods for evaluating FE model biofidelity for brain deformation response. The goal of this dissertation was to address these needs by improving the understanding and modeling of human brain deformation under rotational loading. This dissertation addresses not only gaps in experimental work by the meticulous development of a methodology and dataset quantifying *in situ* human brain deformation but also addresses uncertainties in FE model biofidelity by introducing recommended methods of model evaluation and optimization. The main contribution of this work will be a digital dataset of brain deformation, including average data corridors, that facilitates and outlines best practices for the evaluation of FE brain models (available through the NHTSA database).

A major contribution of this dissertation is the methodology for measuring human brain deformation under rotational loading. The experiments represent the first test series to use sonomicrometry to quantify three-dimensional brain deformation during rotational loading of the head. Sonomicrometry presents numerous advantages over bi-planar X-ray. First, sonomicrometry is capable of recording data in three dimensions with no line-of-sight limitations, and no constraints on the direction or type of motion that is applied during the test. Additionally, it can record the entirety of the event, as long as necessary to capture the whole transient response. This was an improvement over bi-planar X-ray, which constrains the observable results to a very limited test volume, often limiting the duration over which target trajectory data may be collected.

The dataset of six specimens under various loading conditions represents another significant contribution of this dissertation. In addition to FE model evaluation and optimization, the dataset allows for the experimental investigation of brain mechanics. Several analyses were conducted in this dissertation, such as quantifying peak-to-peak deformation and its dependence on loading severity and direction. Future investigations should include metrics such as the duration of brain deformation, the lag between skull and brain motion, and the natural frequency of brain deformation. There are also interesting features of the data, such as the center of rotation of the brain relative to the head CG, which can elucidate regions of risk relevant to TBI.

The average data corridors serve as an extension of the dataset to show intra-population differences in brain response and to provide a supplemental set of FE model evaluation targets. The various techniques employed in creating the first reported brain deformation data corridors provide a new approach to averaging biomechanical data. With the presumption that the data contains discrepancies from population and experimental differences, techniques typically used in other scientific fields were optimized and validated for their use in the corridor creation, including linear transfer functions, position and displacement registration, and inverse distance weighting. While these techniques may not apply to every experiment, they provide opportunities for enhancing current averaging methods for other biomechanics studies. An FE model was used to validate the procedures, but its use was limited to optimization of the parameters and validation of the methods.

The computational phase of this dissertation provided an opportunity for the direct translation of experimental procedures to FE models, without digitization of data or uncertainties about the test procedure or data analysis. The contributions of the

computational work were a method of evaluating models to this dataset, given differences in specimen and model anthropometry. The morphing of FE models to match the exact inner skull anatomy of the specimens was a valuable contribution for model development and evaluation. The morphing method allows researchers to minimize discrepancies in the model response due to differences in specimen geometry, without the need to manually choose control points. The technique can be used for existing FE models, such as its use in the creation of a GHBMC model with embedded axons (Wu et al., 2019), as well the development of subject-specific FE brain models. Additionally, a sensitivity analysis and model optimization was conducted to demonstrate methods for identifying and optimizing material properties to match the brain deformation data. While only two models were utilized in this analysis, the method should be applied to every existing model, as well as any newly developed FE brain models.

A summary of the methodological and technological advancements that have resulted from this dissertation are presented below:

- Demonstrated that sonomicrometry is capable of capturing the 3D motion of the brain in a highly repeatable manner, with spatial and temporal precision sufficient to fully capture both the short-term and long-term transient mechanical response of the brain in these tests.
- Developed and verified a method to record 3D brain motion at numerous points throughout the brain using trilaterated sonomicrometry.
- Recorded 3D brain motion data (and accompanying head kinematics) for 12 test conditions (varying direction, magnitude, and pulse duration) for six specimens.

- Generated a substantial dataset of *in situ* brain deformation for individual validation of finite element models, totaling 5000 brain deformation time-histories.
- Developed the first set of brain deformation average data corridors for the validation of generalized finite element models.
- Evaluated the biofidelity of the GHBMC and SIMon FE brain models to the dataset by accounting for geometric differences between the specimens and model, including the development of a brain morphing methodology.
- Conducted a sensitivity analysis and linear regression of the brain material properties for the GHBMC and SIMon models.
- Calibrated the GHBMC/SIMon model using a computationally-efficient approach, by using the results of the FE model.

## **LESSONS LEARNED**

### **Measuring Brain Deformation**

The dataset generated from this test series demonstrates that the displacement measurements obtained using sonomicrometry were highly repeatable, exhibit consistently high quality in spatial precision and the signal to noise ratio, and were able to record 3D motion data at a sampling rate that was more than adequate to capture the dynamic and transient response of the brain in these tests. These results suggest that sonomicrometry was a robust and reliable tool for quantifying 3D brain deformation in dynamic loading conditions, and is recommended for future tests to quantify brain deformation.

A limitation of any method used to measure brain deformation at discrete locations is the inability to quantify strain across the brain. The sonomicrometry dataset yielded a sufficient spatial resolution of crystals, but the data is too dispersed to be able to accurately

measure 3D strain. The scope of this work was to measure brain deformation, which has typically been used to validate FE brain models. Since most studies use strain as the primary correlate to injury, future methods to quantify strain may provide improved validation targets. Currently, no methods exist with a sufficient sampling frequency to quantify brain deformation or strain in cadaveric specimens.

### **Intracranial Pressure Measurements**

Intracranial pressure was relatively low in the loading conditions used in this study. Also, there was little variation in pressure response with increasing loading severity (Chapter 3). For these reasons, and given the added complexity and preparation time associated with the pressure transducers compared to the limited information gained, it is recommended that future tests studying pure rotational loading do not include intracranial pressure transducer measurements. There were also head injury criteria and FE models that utilize brain pressure either as an injury metric or validation target. While pressure can be correlated with focal injuries occurring from impact loading, this study demonstrates that rotational loading associated with diffuse TBI does not generate appreciable intra-cranial pressures.

### **Validating Finite Element Models**

One of the main objectives of this study was to develop brain deformation data for the validation of FE models of the brain. The brain deformation data was delivered and presented in two forms as individual test data (specific to each specimen with respect to anatomy, receiver locations, and input kinematics) and aggregated corridors (data normalized to the same anatomy, receiver locations, and input kinematics). While either data set could be used for FE model validation, the individual test data should be the first

choice for model validation. Although this requires simulating each experiment separately, the individual data is the most accurate due to possible errors introduced in the data aggregation method. Furthermore, using a morphed brain model is recommended when evaluating the specimens tested. A morphed model reduces variability in brain deformation and strain measurements introduced due to differences in the size and shape of the skull (Chapter 7). If morphing is not possible, simply scaling the brain model dimensions (x, y, z) separately to roughly match the specimen anthropometry is preferred in the case that there are significant differences between model and specimen anthropometries. It is recommended that a comparison of the model response to the average data corridors be used as a final verification of the model validation procedure, not in lieu of using the individual specimen data. To summarize, the various model validation procedures are:

A. Comparing the morphed model response to individual test data

- This requires many simulations (for full validation, 12 tests x 6 specimens = 72 simulations)
- Minimizes the influence of model geometry

B. Comparing the scaled model response to individual test data

- This requires many simulations (for full validation, 12 tests x 6 specimens = 72 simulations)
- Influence of model geometry compared to the tested specimens can be moderate

C. Comparing the unscaled/unmorphed model response to the individual test data

- This requires many simulations (for full validation, 12 tests x 6 specimens = 72 simulations)

- Influence of model geometry compared to tested specimens can be large

#### D. Comparing the model response to the response corridors

- Requires fewer simulations (12 tests x 1 normalized specimen = 12 simulations)
- Influence of model geometry compared to the normalized geometry (GHBMC brain model) can be moderate
- Possible error introduced by the steps required to aggregate data may introduce error into the corridors and influence model validation
- Model can be morphed or scaled to the GHBMC brain geometry to minimize the influence of geometric differences

The Hardy dataset has been used in the validation of most published FE brain models. The dataset provides an alternative brain deformation dataset to validate FE models, but is limited to blunt impacts to the head and to a small set of tests per specimen. It is recommended only as a supplementary check of the validation conducted using the sonomicrometry dataset, or if validating the use of an FE model in different injury mechanics, such as coup-countercoup or impact cases. The Hardy dataset is not representative of diffuse brain deformation caused by rotational loading, and FE model developers should be cautious in optimizing such a model to that dataset.

## **FUTURE WORK**

This work represents the first test series to use sonomicrometry to quantify three-dimensional brain deformation during rotational loading of the head. The objectives set forth in this dissertation have been satisfied, and this work represents a necessary improvement to the TBI mechanics field. However, other questions remain in this field that

were not addressed in this study. Through a better understanding of brain deformation, improvements to computational modeling capabilities will be made. These improvements, however, are limited by the uncertain relationship between the deformation of the brain and the associated injury. Future work must investigate such relationships to better correlate brain deformation to pathological and clinical outcomes.

### **Animal Models**

One of the main benefits of animal models of TBI is the possibility of performing *in vivo* survival studies under injurious loading conditions that cannot be performed in human volunteers. By extending the sonomicrometry technique to animal models, it will be possible to empirically quantify the brain deformation under injurious loading. Matched-pair testing can then be performed with sonomicrometry and survival cohorts receiving identical biomechanical loading. Brain deformation in a sonomicrometry cohort can then be matched to injury seen in the survival cohort, which can be assessed using functional behavioral examinations, advanced imaging techniques (fMRI, PET) as well as post-mortem histological analyses. These studies would help to “close the loop” that has existed between biomechanical input, brain deformation, and injury.

The animal models most appropriate for the application of sonomicrometry are the ferret and pig because smaller animals lack an appropriate brain size for instrumentation with transmitters and receivers. The pig model is especially attractive as a next step as it would be possible to adapt the existing rotational test device setup for a porcine model. While the rotational rates needed for a pig model (>80 rad/s) are higher than that of the human due to the pigs smaller brain, the lower cephalus mass means it may be possible to achieve the higher kinematics using the current device with some modifications. The

smaller brain of the ferret would require the development of a smaller system to achieve the correspondingly higher rotational velocities for injurious loading ( $>150$  rad/s), but require lower torque to generate those speeds. The future development of these animal models offers a pathway to direct linkage of brain deformation and injurious outcomes.

### **Translational and Combined Rotational/Translational Loading**

One of the most prominent debates in the field of TBI injury biomechanics has been the roles of linear and rotational kinematics on brain injury. However, due to the incompressible nature of the brain tissue and closed volume of the skull, the prevailing hypothesis is that rotational kinematics, and not linear, are responsible for the shear deformations of the brain tissue that lead to the diffuse injuries associated with TBI. While this concept has been demonstrated using computational brain models (Gabler et al., 2016c, 2016b, 2018a; Giudice et al., 2018c; Takhounts et al., 2013b), there are currently no experimental data to directly rule out the influence of linear kinematics on brain deformation. However, due to the robust nature of the sonomicrometry method developed and utilized in this project, the role of linear kinematics on brain deformation could be investigated using a modified test apparatus. The sonomicrometry methodology developed in this project provides a unique platform for investigating the influence of head kinematics on the ensuing brain deformation in a controlled and repeatable manner.

### **Multiple Impact Loading**

One of the major questions in the field of brain biomechanics is the response of the brain to multiple impacts. In automotive and sports impacts, the head is often impacted multiple times in the span of 100-200 ms due to the chaotic nature of vehicle collisions and sports environments. It is unclear how the brain responds to secondary impacts, while it is

still in transient motion. Such impacts could have an exacerbated effect on brain deformation, leading to worse injuries. Additionally, multiple impacts happening with larger time differences, such as a few hours or days, could also be investigated using sonomicrometry. If the first impact affects the mechanical properties of the brain, secondary impacts could result in higher deformations, even for the same input kinematics. The sonomicrometry brain deformation methodology presents a unique opportunity to study such events in a controlled, repeatable manner to be able to understand the complex mechanics of the brain.

## **PUBLISHED WORK AND CONTRIBUTIONS**

The research in this dissertation has been and will be disseminated into the scientific literature through the following work. The methodology developed has led to contributions for the use of the sonomicrometry technique to measure brain deformation in animal and physical models. There are also affiliated contributions to studies of modeling axons within human FE brain models and subject-specific modeling of the brain.

## **PEER-REVIEWED PUBLICATIONS**

- **Alshareef A**, Giudice JS, Forman J, Salzar RS, Panzer MB. (2018). A Novel Method for Quantifying Human In Situ Whole Brain Deformation Under Rotational Loading Using Sonomicrometry. *Journal of Neurotrauma*, 35 (5), pg.780-789.
- **Alshareef A**, Giudice JS, Forman J, Shedd D, Wu T, Reynier K, and Panzer MB. (2019). Application of Trilateration and Kalman Filtering Algorithms to Track Dynamic Brain Deformation Using Sonomicrometry. *Biomedical Signal Processing and Control*. (under review).
- **Alshareef A**, Giudice JS, Forman J, Shedd D, Reynier K, Wu T, Sochor S, Sochor MR, Salzar RS, and Panzer MB. (2019). Human Brain Deformation During Dynamic Head Rotation. *Journal of Neurotrauma*. (Drafted).
- **Alshareef A**, Giudice JS, Forman J, Shedd D, Reynier K, Wu T, and Panzer MB. (2019). Human Brain Deformation During Controlled Dynamic Rotation of the Head. *The 2019 International Research Council on Biomechanics of Injury*. Florence, Italy.
- **Alshareef A**, Giudice JS, Forman J, Panzer MB. (2017). Evaluating the Biofidelity of Human Brain Finite Element Models Using Sonomicrometry Data. *The 2017 International Research Council on Biomechanics of Injury*. Antwerp, Belgium.
- Giudice JS, **Alshareef A**, Forman J, Panzer MB. (2017). Measuring 3D Brain Deformation During Dynamic Head Motion Using Sonomicrometry. *The 2017 International Research Council on Biomechanics of Injury*. Antwerp, Belgium.

## PATENTS

- Panzer MB, Forman JL, Giudice JS, **Alshareef A**. U.S. Utility Patent Application Serial No. 15/879,649. Title: System, Method, and Computer Readable Medium for Quantifying Anatomical Device Deformation Under Load. Filed on January 25, 2018.
- Panzer MB, Forman JL, Giudice JS, **Alshareef A**. U.S. Provisional Patent Application Serial No. 62/620,166. Title: System and Method for Brain Deformation Headform Using Sonomicrometry. Filed on January 22, 2017.

## CONFERENCE PRESENTATIONS

- **Alshareef A**, Giudice JS, Forman J, Shedd D, Reynier K, Wu T, and Panzer MB. "Human Brain Deformation During Dynamic Rotation of the Head." *National Neurotrauma Symposium 2019*, Pittsburgh, PA. June 2019. (Poster)
- **Alshareef A**, Giudice JS, Forman J, Shedd D, Reynier K, Wu T, and Panzer MB. "Quantifying 3D Brain Deformation using Sonomicrometry During Dynamic Head Rotational Loading." *National Capital Area TBI Research Symposium*, Washington, DC. March 2019. (Platform)
- Forman J, **Alshareef A**, Giudice JS, Panzer MB. "Measuring 3D Brain Deformation During Dynamic Head Rotation Using Sonomicrometry." *JSAE IBEC Workshop*, Tokyo, Japan. May 2018. (Platform)
- **Alshareef A**, Giudice JS, Forman J, Panzer MB. "Quantifying the Biomechanical Response of the Human Brain During Head Rotational Loading." *NHTSA Human Subjects Workshop*, Charleston, SC. November 2017. (Platform)
- **Alshareef A**, Giudice JS, Forman J, Panzer MB. "Quantifying 3D Whole Brain Deformation Using Sonomicrometry During Dynamic Head Rotational Loading and Preliminary Assessment of Brain Finite Element Models." *Biomedical Engineering Society Annual Meeting*, Phoenix, AZ. October 2017. (Platform)
- **Alshareef A**, Giudice JS, Forman J, Panzer MB. "Quantifying Whole Brain Deformation Using Sonomicrometry and Comparison to Human Brain Finite Element Models." *US National Congress on Computational Mechanics*, Montreal, Canada. July 2017. (Platform)
- **Alshareef A**, Giudice JS, Forman J, Panzer MB. (2017). Quantifying 3D Whole Brain Deformation using Sonomicrometry During Dynamic Head Rotational Loading. *National Neurotrauma Symposium 2017*. Snowbird, UT. (Poster)

- Giudice JS, **Alshareef A**, Forman J, Panzer MB. "Three-dimensional brain deformation under dynamic head rotation and preliminary assessment of brain FE models." *The 2017 Association for the Advancement of Automotive Medicine Student Symposium*. Las Vegas, NV. (Platform)
- **Alshareef A**, Giudice JS, Forman J, Panzer MB. (2017). Using sonomicrometry data to evaluate the biomechanics of human brain finite element models. *The 2017 Military Health System Research Symposium*. Kissimmee, FL. (Poster)
- Giudice JS, **Alshareef A**, Forman J, Panzer MB. (2017). Measuring 3D deformation during dynamic head motion using sonomicrometry. *The 2017 Military Health System Research Symposium*. Kissimmee, FL. (Poster)
- Forman J, Giudice JS, **Alshareef A**, and Panzer MB. "Quantification of in situ whole brain deformation under rotational impact using sonomicrometry." *SAE Government/Industry Meeting*, Washington, DC. January 2017. (Platform)

## **AFFILIATED PUBLICATIONS AND CONTRIBUTIONS**

- Wu T, **Alshareef A**, Giudice JS, Panzer MB. (2019). "Explicit Modeling of White Matter Axonal Fiber Tracts in a Finite Element Brain Model." *Annals of Biomedical Engineering*, 1-15.
- Giudice JS, Zeng W, Wu T, **Alshareef A**, Shedd D, Panzer MB. (2018). "An Analytic Review of Numerical Methods for Finite Element Modeling of the Brain." *Annals of Biomedical Engineering*, pg. 1-18.
- Shedd DF, **Alshareef A**, Giudice JS, Reynier K, and Panzer MB. "Experimental Models of TBI using Novel Controlled Dynamic Rotation Devices." *The 2019 Military Health System Research Symposium*. (Poster)
- Wu T, **Alshareef A**, Giudice JS, and Panzer MB. "Investigation of Cross-Species Scaling Methods for Traumatic Brain Injury Using Finite Element Analysis." National Capital Area TBI Research Symposium 2019, Washington, DC. March 2019. (Poster)
- Giudice JS, **Alshareef A**, Wu T, and Panzer MB. "Investigating the Need for Subject-Specific Finite Element Brain Models." National Capital Area TBI Research Symposium 2019, Washington, DC. March 2019. (Poster)
- Singh A, **Alshareef A**, Panzer MB. "Analysis of Brain Tissue Simulants for Physical Models of Traumatic Brain Injury." Biomedical Engineering Society Annual Meeting, Atlanta, GA. October 2018. (Platform)

- Wu T, Antona-Makoshi J, **Alshareef A**, Panzer MB. "Investigating Cross-Species Scaling for Traumatic Brain Injuries Using Finite Element Analysis." National Neurotrauma Symposium 2018. Toronto, Canada. (Poster)
- Giudice JS, Wu T, **Alshareef A**, Panzer MB. "Development and Evaluation of a Subject-Specific Brain Injury Model." VPH 2018, Zaragoza, Spain. Sep 2018. (Platform)
- Wu T, Hajiaghamemar M, Antona-Makoshi J, **Alshareef A**, Margulies S, and Panzer MB. "Investigating Cross-Species Scaling for Traumatic Brain Injuries using Finite Element Analysis." World Congress of Biomechanics 2018, Dublin, Ireland. July 2018. (Platform)
- Wu T, Antona-Makoshi J, **Alshareef A**, Panzer MB. "*Investigating Cross-Species Scaling for Traumatic Brain Injuries using Finite Element Analysis.*" World Congress on Computational Mechanics 2018, New York, NY. July 2018. (Platform)
- Wu T, **Alshareef A**, Crandall JR, Panzer MB. "*Modeling Axonal Fibers of White Matter in Human Brain Finite Element Model.*" USNCTAM 2018, Evanston, IL. June 2018. (Platform)

## APPENDIX A: POST-TEST AUTOPSY NOTES

The head-brain specimens were dissected 6-8 days p.m. All the Fiberglas-embedded polyester resin (Bondo) was removed, and a craniectomy was performed along the axial plane. The average mass of the brain and all associated membranes was  $1.28 \pm 0.13$  kg.

For all specimens, the brain and dura were intact. No visible holes were observed in the brain due to crystal insertion or the experiments. No other gross damage was observed around the crystal insertion sites. Once the brain was extracted, the parenchyma remained intact. The brains were then dissected to examine the major brain structures (Figure A-1).

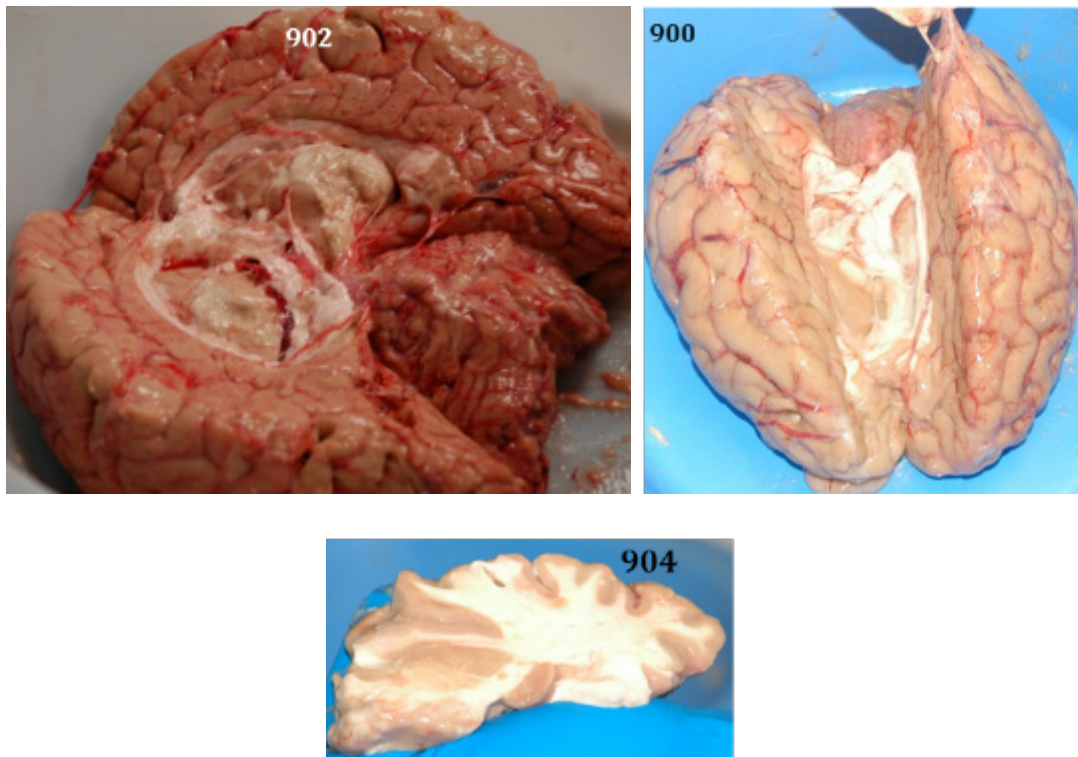


*Figure A-1: Brain regions and white/gray matter regions can be identified after brain extraction.*

The connection between the inner table of the skull and the dura varied among the specimens, with some having an inseparable attachment and others having a very loose attachment (Figure A-2). The dura was very well attached to the inferior skull regions in all specimens.

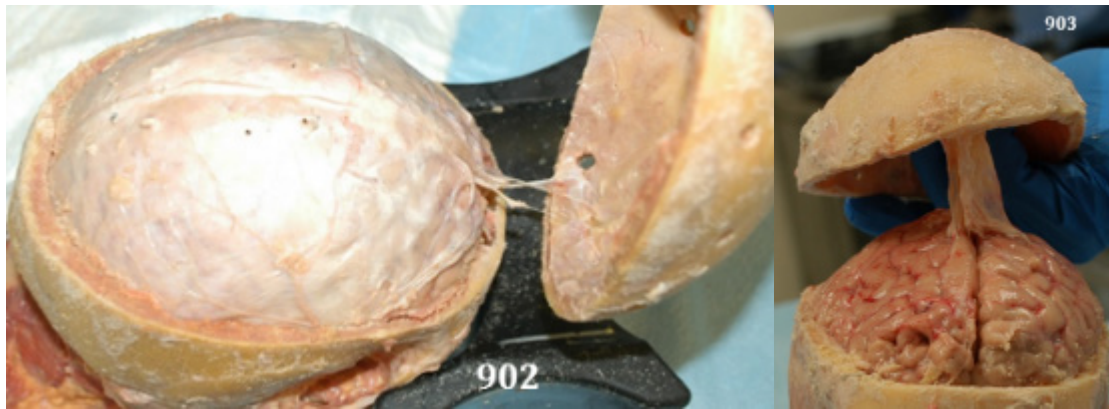


*Figure A-2: The dura attachment to the skull was very loose (left) or inseparable (right).*

There were differences in the dura's connection to the Crista Galli. In four specimens, the dura was well attached to the Crista Galli anteriorly and had to be cut with a scalpel. In two specimens, there was little to no connection, with the falx easily separable from the Crista Galli (Figure A-3).

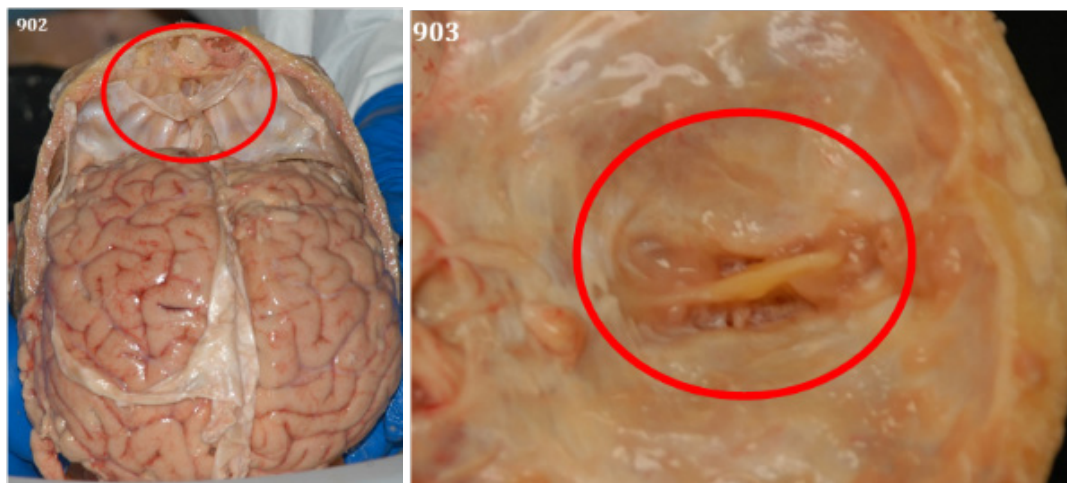


*Figure A-3: The dura was either very well connected to the Crista Galli (left) or not connected (right).*

Blunt dissection revealed a loose connection between the dura and the brain, with minimal disruption needed to separate the layers in all specimens (Figure A-4).

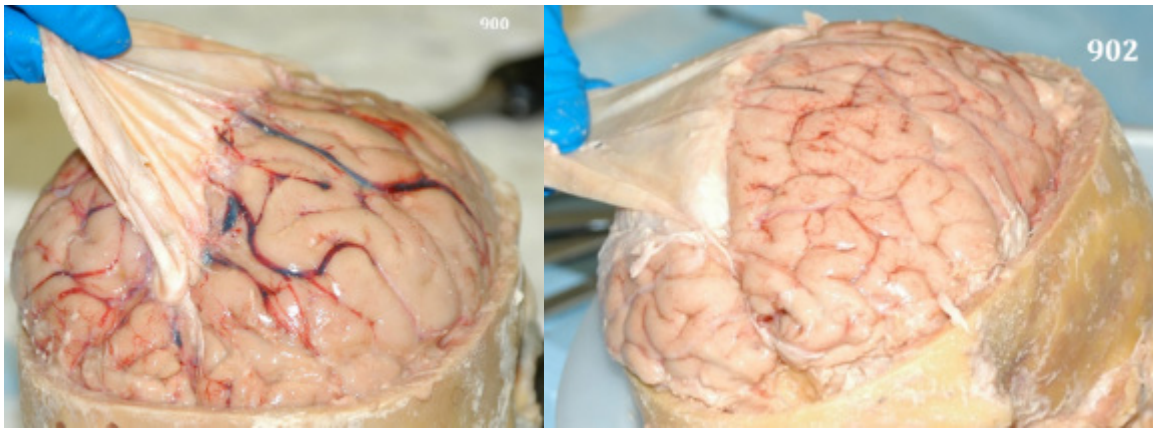


*Figure A-4: There was a loose connection between the dura and brain, except at the midline.*

There were also differences in the bony anatomy of the inner skull, with various regions exhibiting bone degeneration or bony spurs/protrusions (Figure A-5).

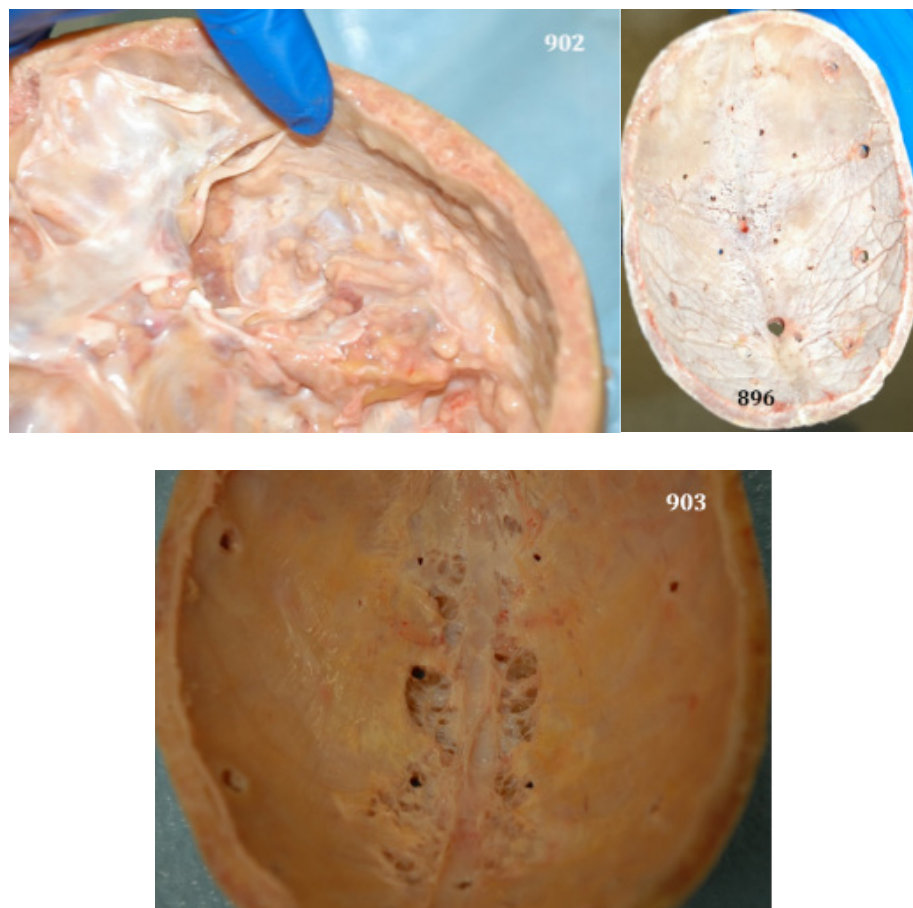


*Figure A-5: Differences in bony anatomy. Specimen 902 shows prominent bony spurs/protrusions, some of which were sharp to the touch. Specimen 903 and 896 show bone decay along the sagittal sinus.*

## APPENDIX B: MORPHING

A morphing technique was implemented to match the geometry of the specimens to a target geometry. A technique utilized and adapted by Park (2017) (Park et al., 2017) for the subject-specific FE modeling of human femurs was extended to the brain in order to accurately match the geometries. The morphing methodology involved four steps: FE model and specimen geometry preparation, rigid body alignment, surface registration, and 3D volume morphing (Figure B-1). The steps are applied below to morph a specimen geometry to the GHBMC brain model, but the same method can be applied to any FE model or parametric space.

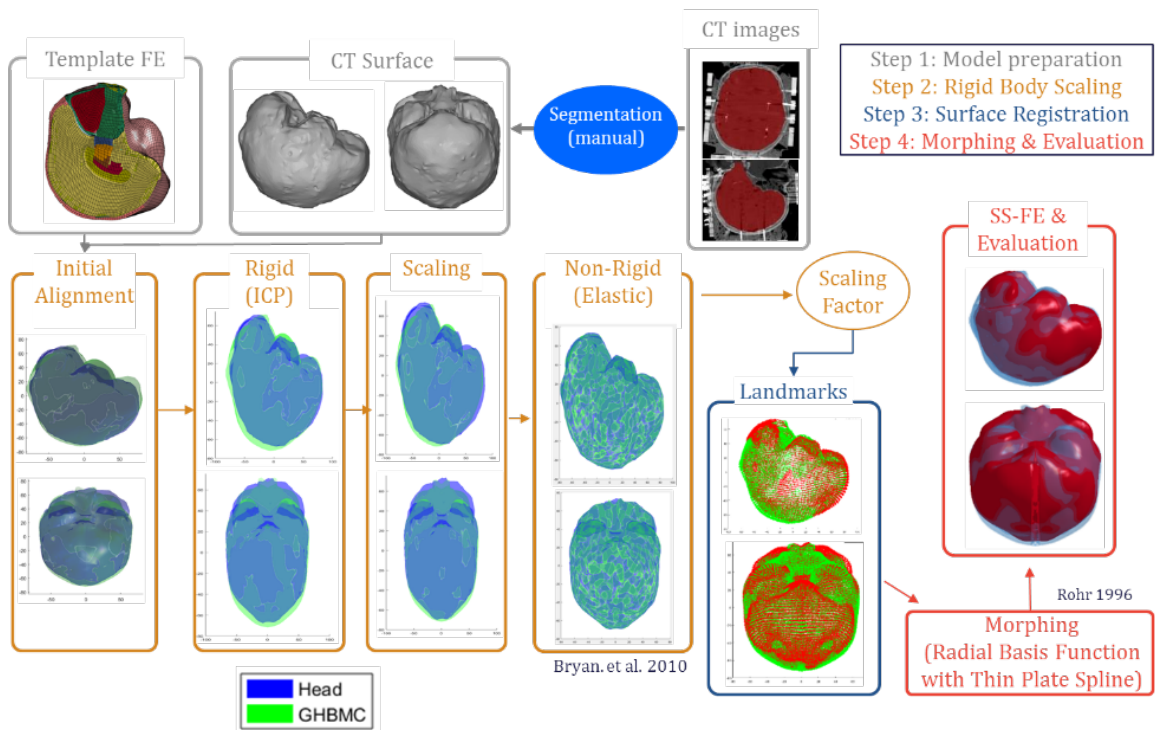


Figure B-1: Representation of the morphing process, with GHBMC as an example. The morphing process includes four main steps: 1) Surface preparation and segmentation, 2) rigid body alignment and scaling, 3) surface registration, and 4) volume morphing and evaluation.

In the preparation stage, the inner cranial geometry of the specimen was segmented from the computed tomography (CT) scans using Mimics 19.0 (Materialise, Plymouth,

MI). The segmented geometry included everything in the cranial vault up to the inner skull. A thresholding value was used to apply a mask to the desired geometry, followed by manual editing of the mask in areas with low-density trabecular bone and the inferior regions of the cranium and brainstem. The edited mask was used to extract the 3D brain geometry for each specimen. The target geometry can be prepared similarly. In the case of FE brain models, the target geometry was prepared by extracting the outermost layer of the model (the inner skull). This surface will be used to match to the segmented specimen geometry.

To align the two surfaces, the specimen geometry was first rotated and centered to match the coordinate system of the FE model. Once the two surfaces were close using manual rigid body rotation, an iterative closest point approximation (ICP, Besl and McKay, 1992) was used to match the initial rigid body position of the surfaces. The specimen geometry was then scaled to the target external geometry of the FE model in all three directions ( $x$ ,  $y$ ,  $z$ ) to minimize volume differences between the two geometries. The scaling factors were used to scale back the target geometry after the surface registration as to not affect the 3D volume morphing.

Next, control points were selected to map the FE model surface to the specimen surface. In typical biomechanical morphing techniques, control points were chosen based on automated spatial segmentation or a manual assignment based on prominent anatomical features. These methods were difficult for segmented brain CT scans because the shape of the brain may vary significantly and manual assignment of landmarks may lead to large user error. An example of this process is shown in Figure B-2. To minimize errors in the choice of landmarks, an iterative registration method based on the 3D generalization of

Burr's elastic registration (Bryan et al., 2010), was used to match the external geometry of the two surfaces. All of the points in each model, which were mapped in the registration, were utilized as landmarks to convert the FE model geometry to the specimen geometry using the registration algorithm. The accuracy of the registration method was evaluated using an average minimum distance error, the average distance between nodes on the target surface and the surface of the specimen geometry.



*Figure B-2: Control points for the morphing process can be chosen manually if the shape of the target and template geometry are similar or there are prominent landmarks available (left). Deviations in shape between the two surfaces can result in variability in the choice of surface landmarks (right).*

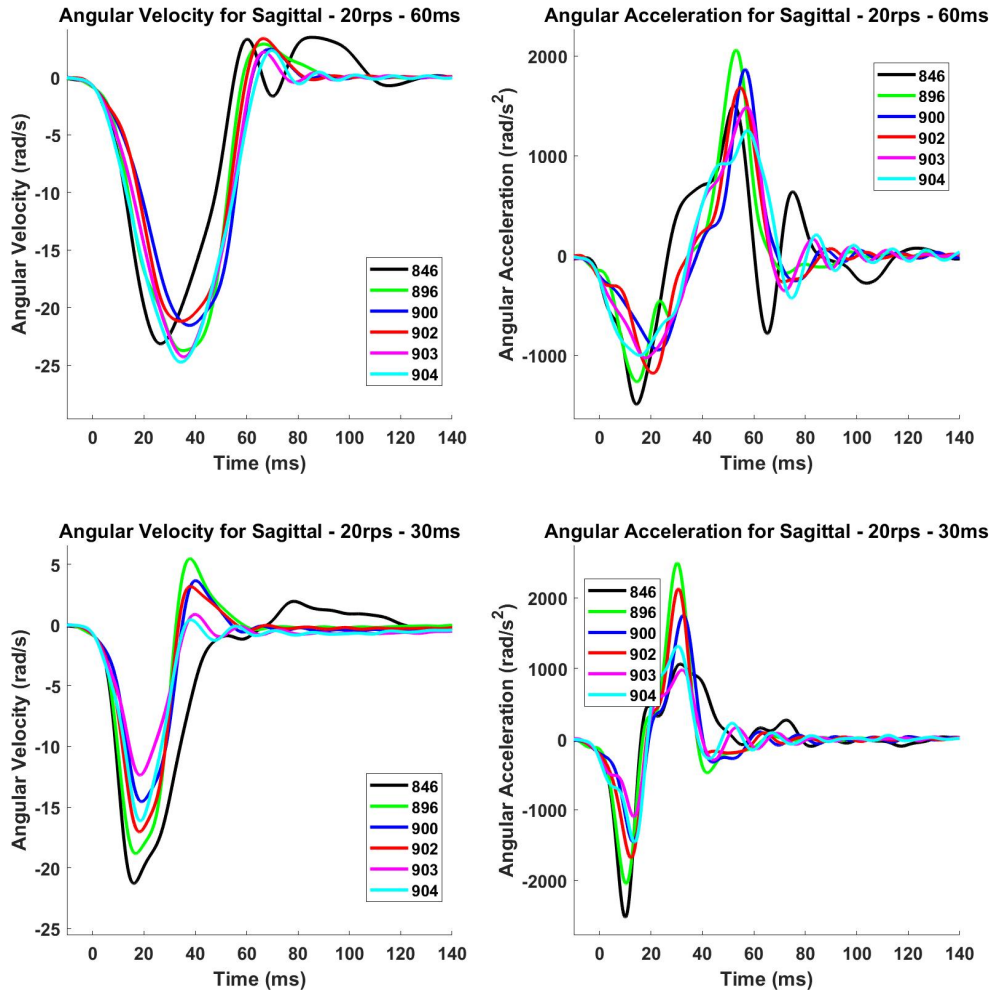
The transformations used to match the control points in the registration step were then applied to the internal nodes of the FE brain model to morph the 3D volume to the external geometry of the specimen using a thin-plate spline method with a radial basis function (Rohr et al., 2001), an extension of the original thin-plate spline proposed by Bookstein (1989) to take into account landmark localization errors. If the morphing is applied to an FE brain model, the normalized Jacobian ratio of all elements was quantified to ensure comparable element quality of the morphed model to the original FE brain models.

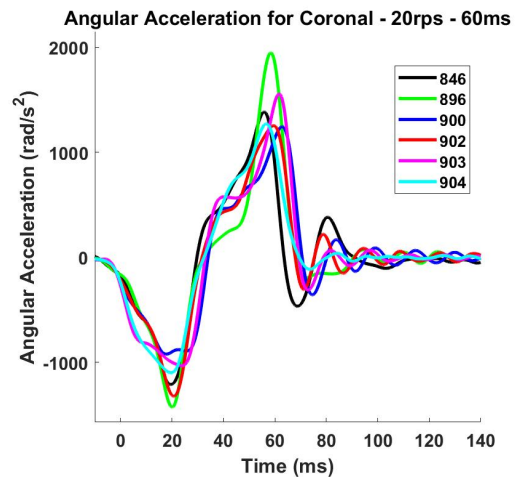
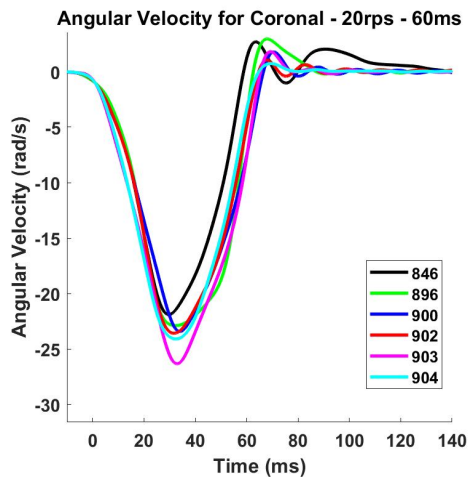
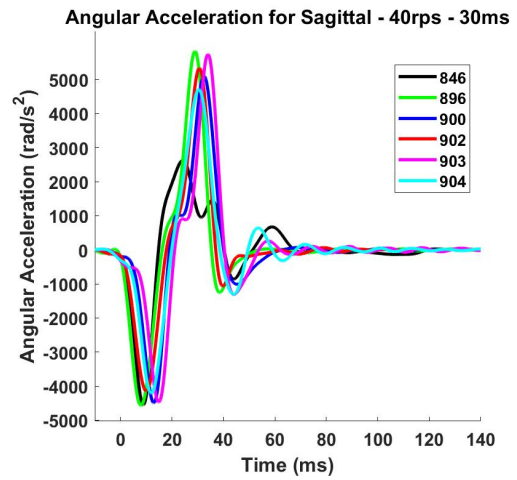
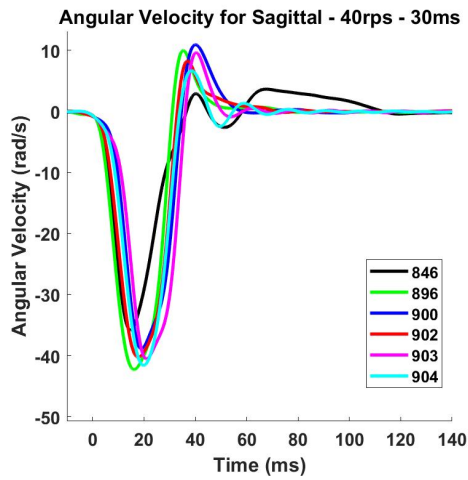
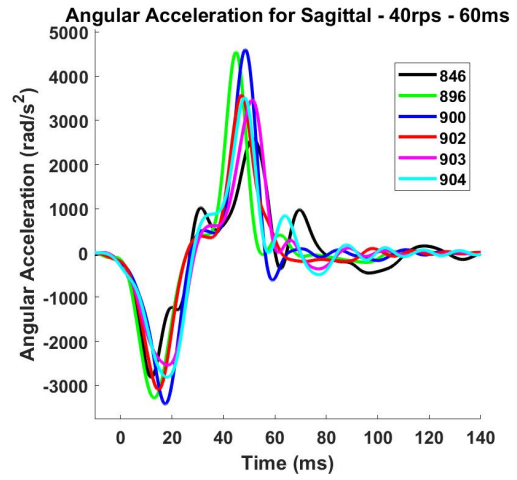
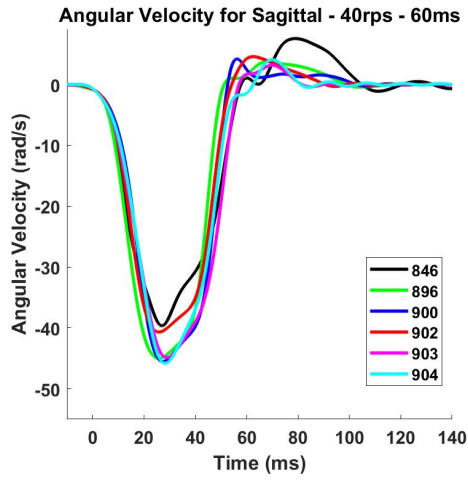
The morphing methodology implemented to account for specimen anthropometry provides an important advancement in FE brain modeling. The technique facilitates matching the exact inner cranium shape of the model and specimens, not only the size and

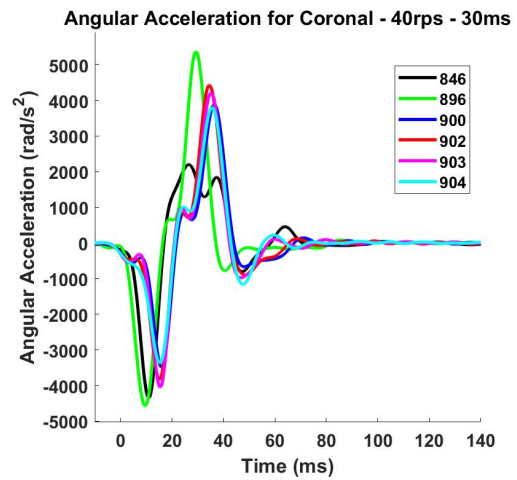
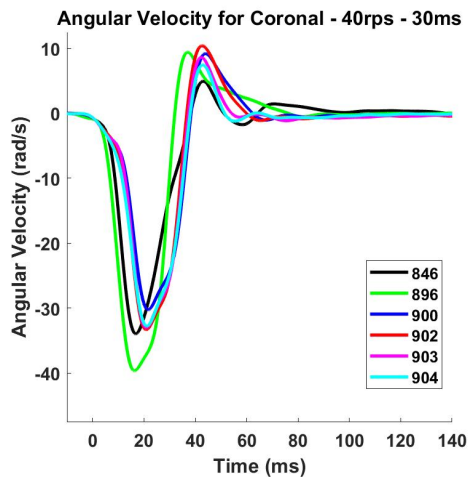
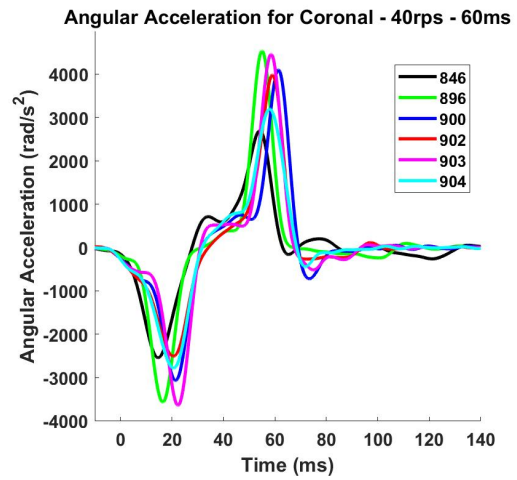
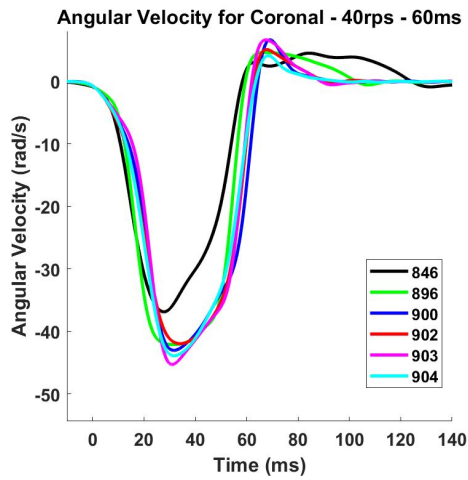
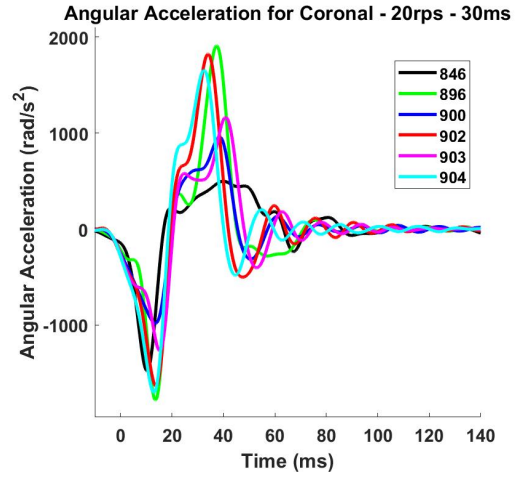
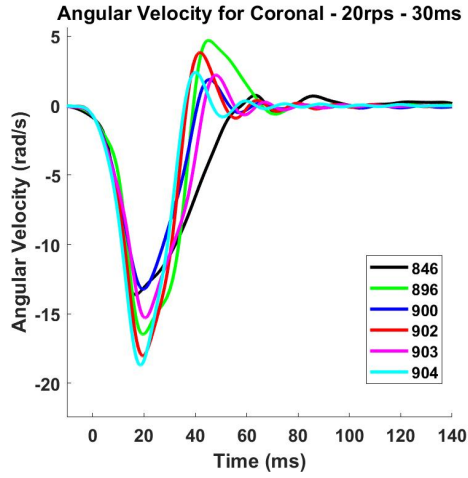
volume. The average minimum distance between the surface of the FE model and surface of each specimen CT was less than 1 mm. While morphing has been attempted through conventional control point morphing (Horgan and Gilchrist, 2004; Li et al., 2011) and the generation of new voxel models (Ghajari et al., 2017; Miller et al., 2016), the use of an automated process of picking and registering control points is important in generating an accurate specimen-specific model. The researcher does not have to manually select control points, which can be laborious and error-prone. Instead, all of the nodes of the specimen geometry and model are used as control points, to generate a smooth, accurate morphed model automatically. A limitation of the morphing methodology for FE brain models is that it does not address the differences in internal anatomy between subjects, such as ventricle size, regional organization of brain regions, and size of the brain. The morphing methodology only registers the outside surface. Consequently the internal anatomy is scaled according to the surface. Future methods that incorporate subject-specific morphing or model development of the brain using MRI scans are needed in order to accurately model and predict subject-specific brain injury.

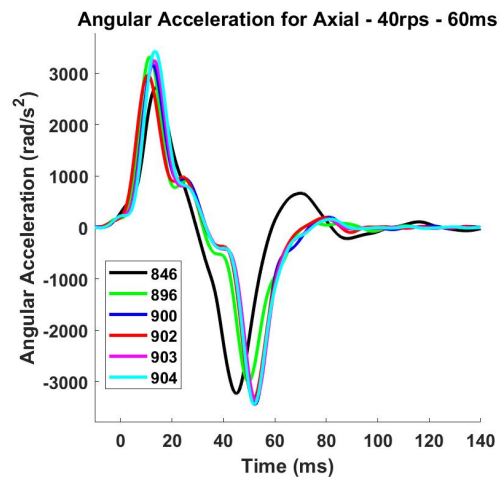
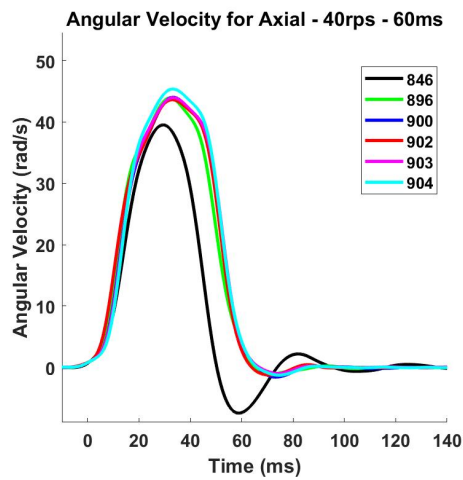
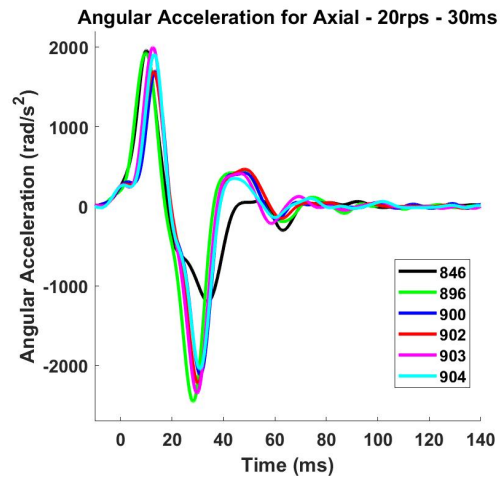
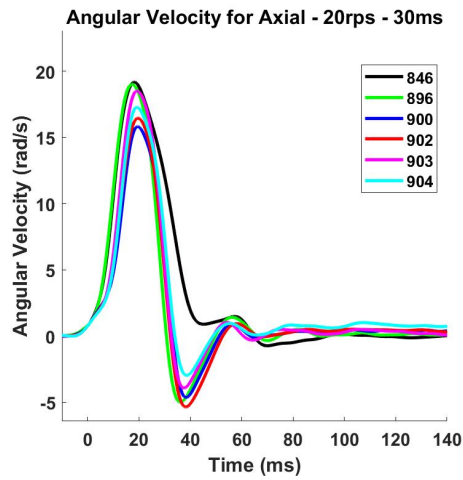
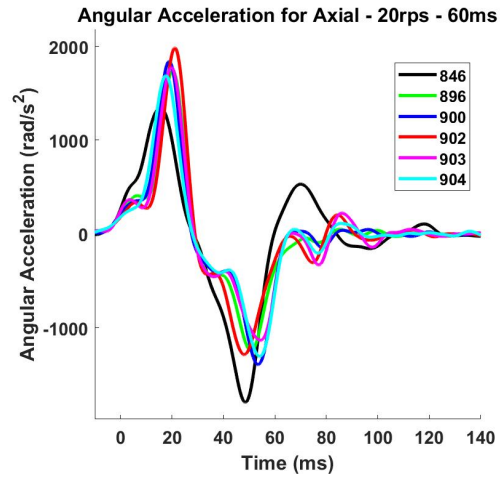
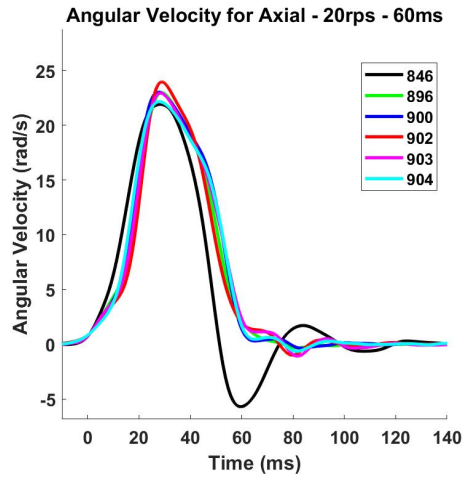
## APPENDIX C: DATASET SUMMARY

This appendix provides a summary of the kinematics and peak-to-peak deformation of the sonomicrometry dataset collected in Chapter 5. The following plots depict the angular velocity and angular acceleration traces for all specimens for each test condition.









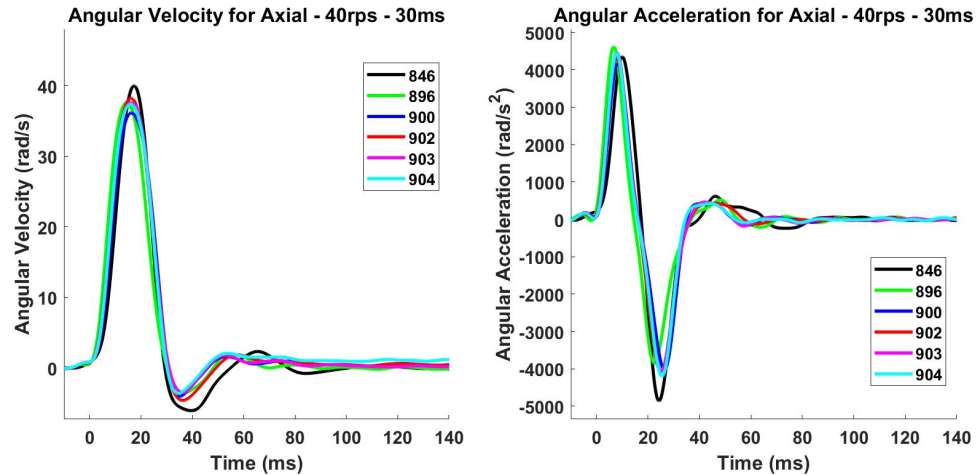


Figure C-1: Angular velocity and angular acceleration for each test severity.

The summary data include the peak linear acceleration (LAC), peak angular velocity (ARS), angular velocity duration, peak angular acceleration (AAC), and maximum/mean peak-to-peak deformation (Pk-Pk).

Table C-1: Summary of peak head kinematics and brain deformation for specimen 846.

| Specimen 846 | Test       | Max LAC (g) | Max ARS (rad/s) | Duration (ms) | Max AAC (rad/s <sup>2</sup> ) | Max Pk-Pk (mm) | Mean Pk-Pk (mm) |
|--------------|------------|-------------|-----------------|---------------|-------------------------------|----------------|-----------------|
| Sagittal     | 20rps-60ms | 4.34        | 23.16           | 53.9          | 1499.87                       | 6.74           | 3.89            |
|              | 20rps-30ms | 4.25        | 21.29           | 63.0          | 2520.53                       | 7.87           | 4.53            |
|              | 40rps-60ms | 10.12       | 39.64           | 56.4          | 2817.65                       | 9.86           | 5.94            |
|              | 40rps-30ms | 11.89       | 35.80           | 35.2          | 4546.77                       | 13.15          | 8.02            |
| Coronal      | 20rps-60ms | 4.65        | 21.89           | 57.4          | 1383.83                       | 7.80           | 4.43            |
|              | 20rps-30ms | 1.73        | 13.63           | 53.8          | 1476.63                       | 6.24           | 3.58            |
|              | 40rps-60ms | 8.04        | 36.88           | 57.1          | 2695.45                       | 10.69          | 6.45            |
|              | 40rps-30ms | 7.26        | 33.97           | 36.9          | 4342.96                       | 14.06          | 7.78            |
| Axial        | 20rps-60ms | 2.02        | 21.90           | 50.1          | 1793.82                       | 10.71          | 5.13            |
|              | 20rps-30ms | 4.87        | 19.18           | 61.9          | 1958.62                       | 11.40          | 5.44            |
|              | 40rps-60ms | 4.13        | 39.54           | 49.1          | 3233.82                       | 17.00          | 8.08            |
|              | 40rps-30ms | 12.86       | 40.00           | 28.2          | 4860.52                       | 21.78          | 10.55           |

Table C-2: Summary of peak head kinematics and brain deformation for specimen 896.

| Specimen 896    | Test       | Max LAC (g) | Max ARS (rad/s) | Duration (ms) | Max AAC (rad/s <sup>2</sup> ) | Max Pk-Pk (mm) | Mean Pk-Pk (mm) |
|-----------------|------------|-------------|-----------------|---------------|-------------------------------|----------------|-----------------|
| <b>Sagittal</b> | 20rps-60ms | 3.01        | 23.75           | 57.1          | 2060.53                       | 7.17           | 3.45            |
|                 | 20rps-30ms | 8.37        | 18.83           | 31.3          | 2492.08                       | 9.37           | 4.56            |
|                 | 40rps-60ms | 9.35        | 44.99           | 49.8          | 4546.46                       | 14.76          | 7.81            |
|                 | 40rps-30ms | 28.67       | 42.28           | 30.0          | 5828.44                       | 19.18          | 10.29           |
| <b>Coronal</b>  | 20rps-60ms | 6.09        | 22.89           | 61.2          | 1947.05                       | 6.96           | 4.47            |
|                 | 20rps-30ms | 9.97        | 16.48           | 38.0          | 1909.51                       | 7.69           | 4.80            |
|                 | 40rps-60ms | 13.65       | 42.11           | 58.3          | 4532.36                       | 13.05          | 8.13            |
|                 | 40rps-30ms | 23.59       | 39.65           | 30.9          | 5372.49                       | 16.74          | 10.34           |
| <b>Axial</b>    | 20rps-60ms | 7.18        | 22.97           | 67.3          | 1737.99                       | 10.41          | 6.04            |
|                 | 20rps-30ms | 10.18       | 19.01           | 29.5          | 2456.05                       | 12.80          | 7.62            |
|                 | 40rps-60ms | 14.01       | 43.94           | 63.2          | 3329.44                       | 17.59          | 9.85            |
|                 | 40rps-30ms | 38.09       | 37.62           | 28.9          | 4622.71                       | 19.71          | 11.86           |

Table C-3: Summary of peak head kinematics and brain deformation for specimen 900.

| Specimen 900    | Test       | Max LAC (g) | Max ARS (rad/s) | Duration (ms) | Max AAC (rad/s <sup>2</sup> ) | Max Pk-Pk (mm) | Mean Pk-Pk (mm) |
|-----------------|------------|-------------|-----------------|---------------|-------------------------------|----------------|-----------------|
| <b>Sagittal</b> | 20rps-60ms | 2.78        | 21.56           | 60.6          | 1865.24                       | 4.10           | 2.39            |
|                 | 20rps-30ms | 5.07        | 14.55           | 33.6          | 1751.78                       | 5.18           | 2.94            |
|                 | 40rps-60ms | 10.79       | 45.53           | 51.5          | 4599.98                       | 12.40          | 6.66            |
|                 | 40rps-30ms | 19.33       | 38.89           | 33.5          | 5098.65                       | 17.55          | 8.94            |
| <b>Coronal</b>  | 20rps-60ms | 3.84        | 23.42           | 65.0          | 1244.02                       | 5.60           | 3.13            |
|                 | 20rps-30ms | 5.60        | 13.23           | 39.2          | 984.28                        | 6.16           | 3.26            |
|                 | 40rps-60ms | 11.44       | 43.04           | 63.2          | 4098.11                       | 11.34          | 6.66            |
|                 | 40rps-30ms | 17.80       | 30.26           | 37.3          | 3884.38                       | 13.63          | 7.58            |
| <b>Axial</b>    | 20rps-60ms | 2.11        | 23.02           | 61.6          | 1840.71                       | 8.18           | 4.22            |
|                 | 20rps-30ms | 6.62        | 15.82           | 31.8          | 2118.13                       | 10.62          | 5.07            |
|                 | 40rps-60ms | 12.19       | 44.04           | 64.2          | 3447.11                       | 13.99          | 7.33            |
|                 | 40rps-30ms | 18.31       | 36.15           | 29.5          | 4182.85                       | 17.13          | 9.02            |

Table C-4: Summary of peak head kinematics and brain deformation for specimen 902.

| Specimen 902    | Test       | Max LAC (g) | Max ARS (rad/s) | Duration (ms) | Max AAC (rad/s <sup>2</sup> ) | Max Pk-Pk (mm) | Mean Pk-Pk (mm) |
|-----------------|------------|-------------|-----------------|---------------|-------------------------------|----------------|-----------------|
| <b>Sagittal</b> | 20rps-60ms | 3.65        | 21.19           | 58.6          | 1684.21                       | 2.41           | 1.45            |
|                 | 20rps-30ms | 8.68        | 17.04           | 32.2          | 2128.14                       | 3.00           | 1.83            |
|                 | 40rps-60ms | 12.23       | 40.69           | 52.8          | 3569.87                       | 5.34           | 3.14            |
|                 | 40rps-30ms | 12.66       | 40.26           | 31.9          | 5330.47                       | 8.33           | 4.72            |
| <b>Coronal</b>  | 20rps-60ms | 5.11        | 23.58           | 63.1          | 1324.22                       | 2.84           | 2.05            |
|                 | 20rps-30ms | 10.56       | 18.03           | 35.3          | 1822.26                       | 3.59           | 2.66            |
|                 | 40rps-60ms | 10.95       | 41.97           | 61.6          | 3980.45                       | 6.97           | 5.00            |
|                 | 40rps-30ms | 24.63       | 33.34           | 35.6          | 4430.91                       | 7.73           | 5.50            |
| <b>Axial</b>    | 20rps-60ms | 6.79        | 23.95           | 72.0          | 1982.61                       | 5.39           | 2.65            |
|                 | 20rps-30ms | 7.10        | 16.45           | 31.0          | 2224.06                       | 7.55           | 3.64            |
|                 | 40rps-60ms | 13.88       | 43.65           | 62.0          | 3355.58                       | 10.07          | 4.82            |
|                 | 40rps-30ms | 30.89       | 38.24           | 29.1          | 4323.94                       | 14.77          | 6.89            |

Table C-5: Summary of peak head kinematics and brain deformation for specimen 903.

| Specimen 903    | Test       | Max LAC (g) | Max ARS (rad/s) | Duration (ms) | Max AAC (rad/s <sup>2</sup> ) | Max Pk-Pk (mm) | Mean Pk-Pk (mm) |
|-----------------|------------|-------------|-----------------|---------------|-------------------------------|----------------|-----------------|
| <b>Sagittal</b> | 20rps-60ms | 3.93        | 24.29           | 60.4          | 1484.73                       | 3.50           | 1.69            |
|                 | 20rps-30ms | 5.95        | 12.37           | 34.7          | 1099.36                       | 3.12           | 1.54            |
|                 | 40rps-60ms | 7.87        | 44.89           | 55.7          | 3464.63                       | 8.17           | 3.77            |
|                 | 40rps-30ms | 14.96       | 40.54           | 35.0          | 5740.37                       | 12.95          | 6.28            |
| <b>Coronal</b>  | 20rps-60ms | 5.25        | 26.33           | 64.0          | 1556.98                       | 4.15           | 2.53            |
|                 | 20rps-30ms | 9.49        | 15.29           | 41.9          | 1266.71                       | 4.34           | 2.48            |
|                 | 40rps-60ms | 12.03       | 45.31           | 60.8          | 4458.26                       | 9.41           | 5.59            |
|                 | 40rps-30ms | 21.51       | 33.05           | 36.3          | 4215.42                       | 10.68          | 6.26            |
| <b>Axial</b>    | 20rps-60ms | 6.02        | 22.93           | 74.0          | 1774.65                       | 7.49           | 3.74            |
|                 | 20rps-30ms | 7.87        | 18.51           | 31.4          | 2351.43                       | 10.86          | 5.08            |
|                 | 40rps-60ms | 10.77       | 43.97           | 64.4          | 3365.98                       | 15.38          | 7.18            |
|                 | 40rps-30ms | 26.67       | 37.61           | 29.7          | 4460.66                       | 19.68          | 9.14            |

Table C-6: Summary of peak head kinematics and brain deformation for specimen 904.

| <b>Specimen<br/>904</b> | <b>Test</b> | <b>Max<br/>LAC (g)</b> | <b>Max ARS<br/>(rad/s)</b> | <b>Duration<br/>(ms)</b> | <b>Max AAC<br/>(rad/s<sup>2</sup>)</b> | <b>Max<br/>Pk-Pk<br/>(mm)</b> | <b>Mean<br/>Pk-Pk<br/>(mm)</b> |
|-------------------------|-------------|------------------------|----------------------------|--------------------------|--|-------------------------------|--------------------------------|
| <b>Sagittal</b>         | 20rps-60ms  | 3.44                   | 24.75                      | 62.5                     | 1253.24                                | 3.18                          | 1.65                           |
|                         | 20rps-30ms  | 9.33                   | 16.15                      | 34.2                     | 1458.64                                | 3.81                          | 2.25                           |
|                         | 40rps-60ms  | 5.76                   | 45.83                      | 60.9                     | 3517.51                                | 6.86                          | 4.11                           |
|                         | 40rps-30ms  | 12.60                  | 41.59                      | 32.8                     | 4711.59                                | 11.52                         | 6.41                           |
| <b>Coronal</b>          | 20rps-60ms  | 2.46                   | 24.09                      | 62.7                     | 1271.00                                | 4.85                          | 2.96                           |
|                         | 20rps-30ms  | 9.16                   | 18.70                      | 34.4                     | 1702.66                                | 6.79                          | 4.41                           |
|                         | 40rps-60ms  | 7.84                   | 43.93                      | 62.3                     | 3193.39                                | 8.59                          | 6.02                           |
|                         | 40rps-30ms  | 13.40                  | 32.79                      | 36.9                     | 3805.60                                | 11.40                         | 7.24                           |
| <b>Axial</b>            | 20rps-60ms  | 3.48                   | 22.14                      | 62.9                     | 1689.06                                | 6.57                          | 3.22                           |
|                         | 20rps-30ms  | 5.12                   | 17.28                      | 32.7                     | 2048.48                                | 9.66                          | 4.19                           |
|                         | 40rps-60ms  | 8.87                   | 45.39                      | 63.8                     | 3444.38                                | 13.33                         | 6.12                           |
|                         | 40rps-30ms  | 17.02                  | 37.40                      | 29.0                     | 4455.03                                | 17.62                         | 8.01                           |

## **APPENDIX D: BRAIN DEFORMATION PLOTS**

This appendix provides depictions of the trilaterated trajectories of all crystals for each specimen. The plots are shown in the plane of rotation for each rotation direction, and all severities are included for each specimen.

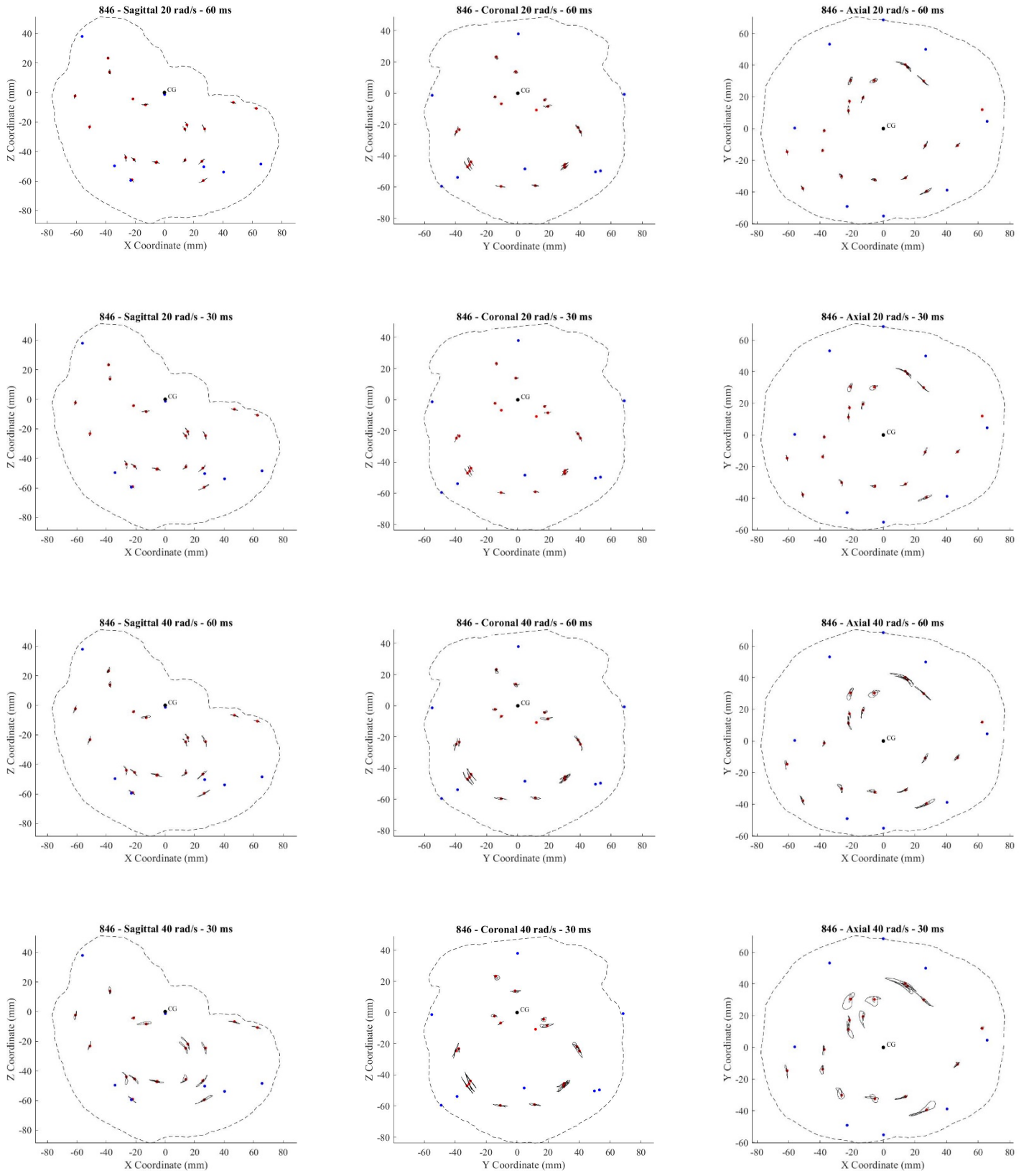


Figure D-1: Sonomicrometry trajectory plots for specimen 846.

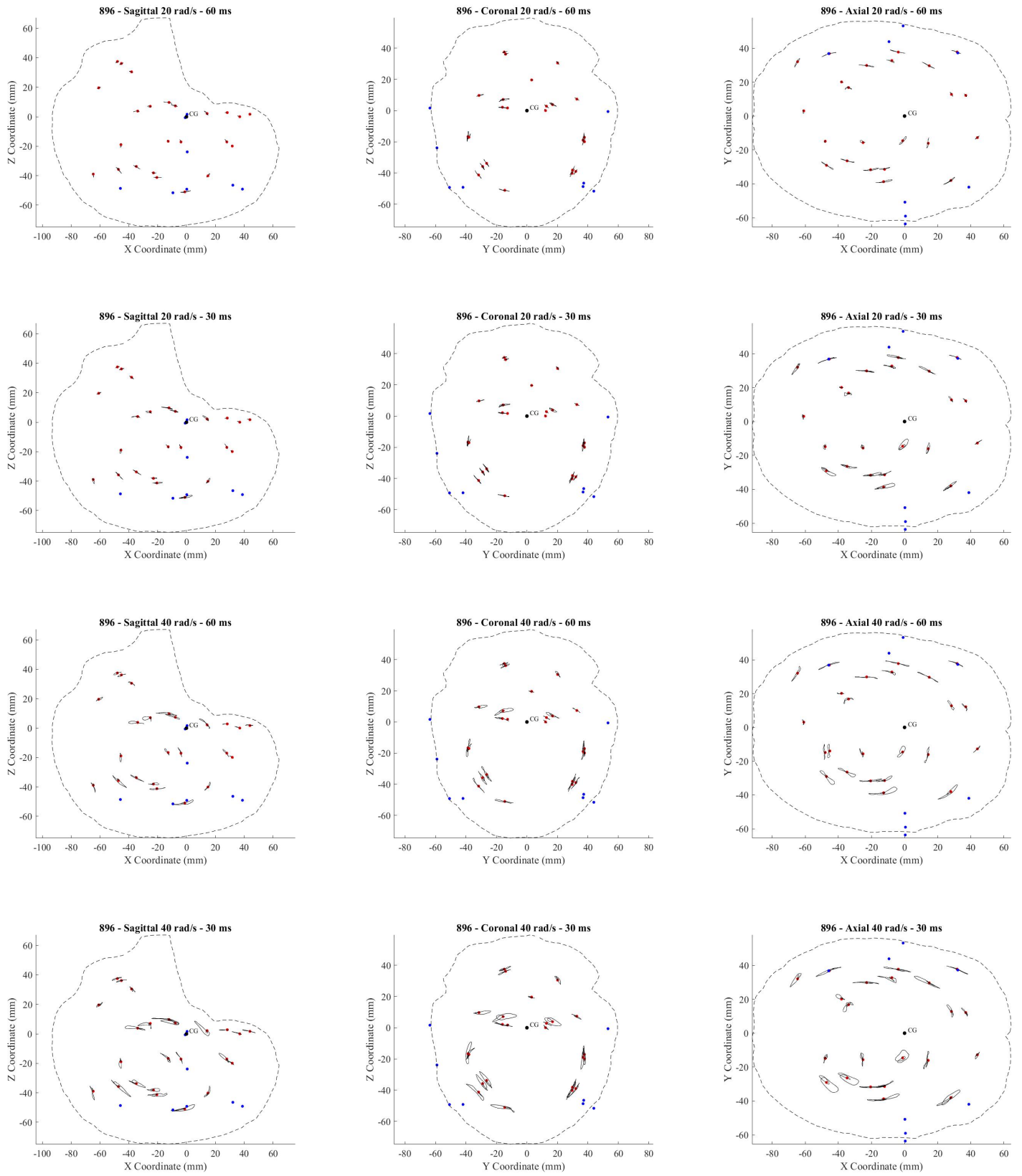


Figure D-2: Sonomicrometry trajectory plots for specimen 896.

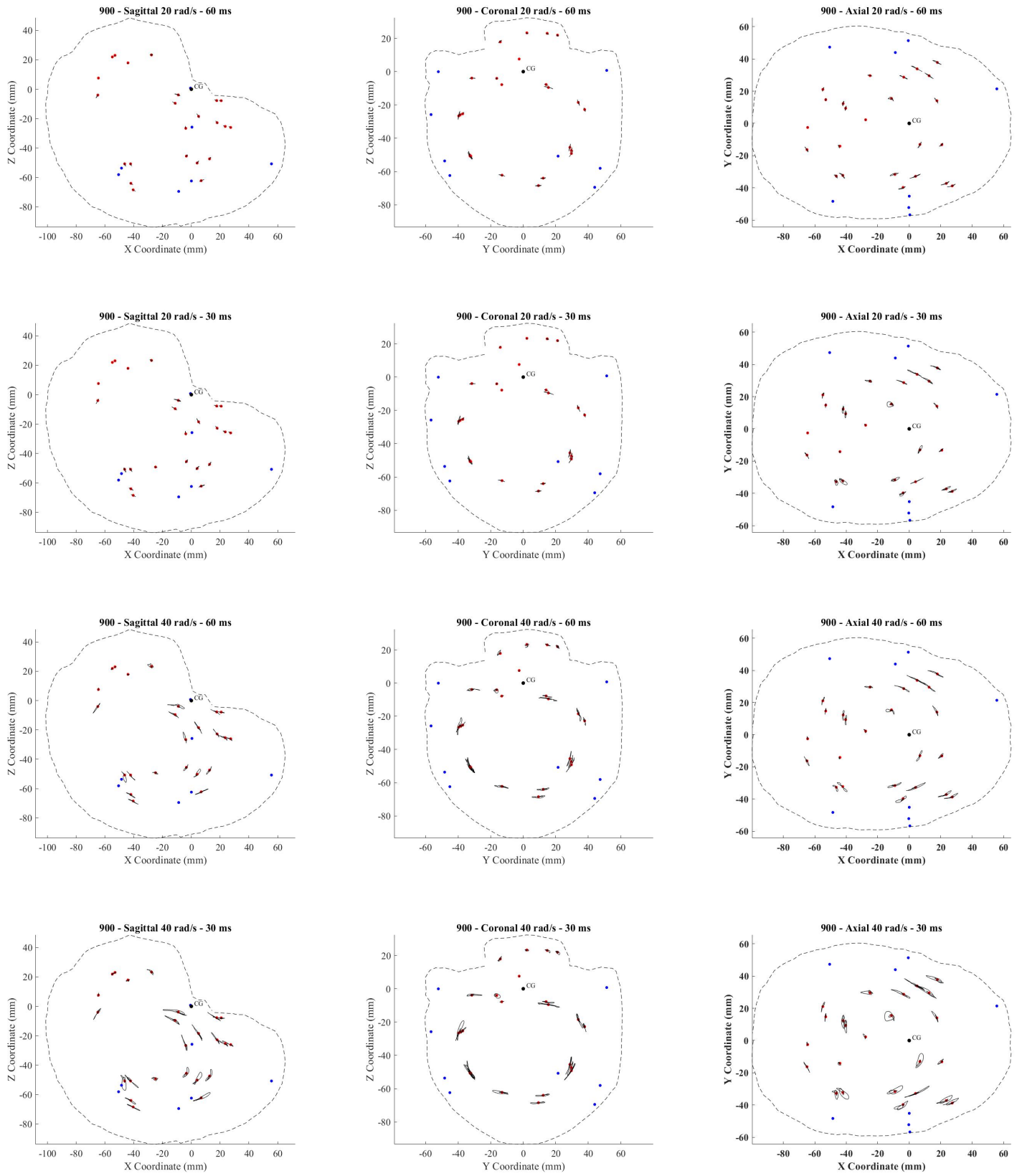


Figure D-3: Sonomicrometry trajectory plots for specimen 900.

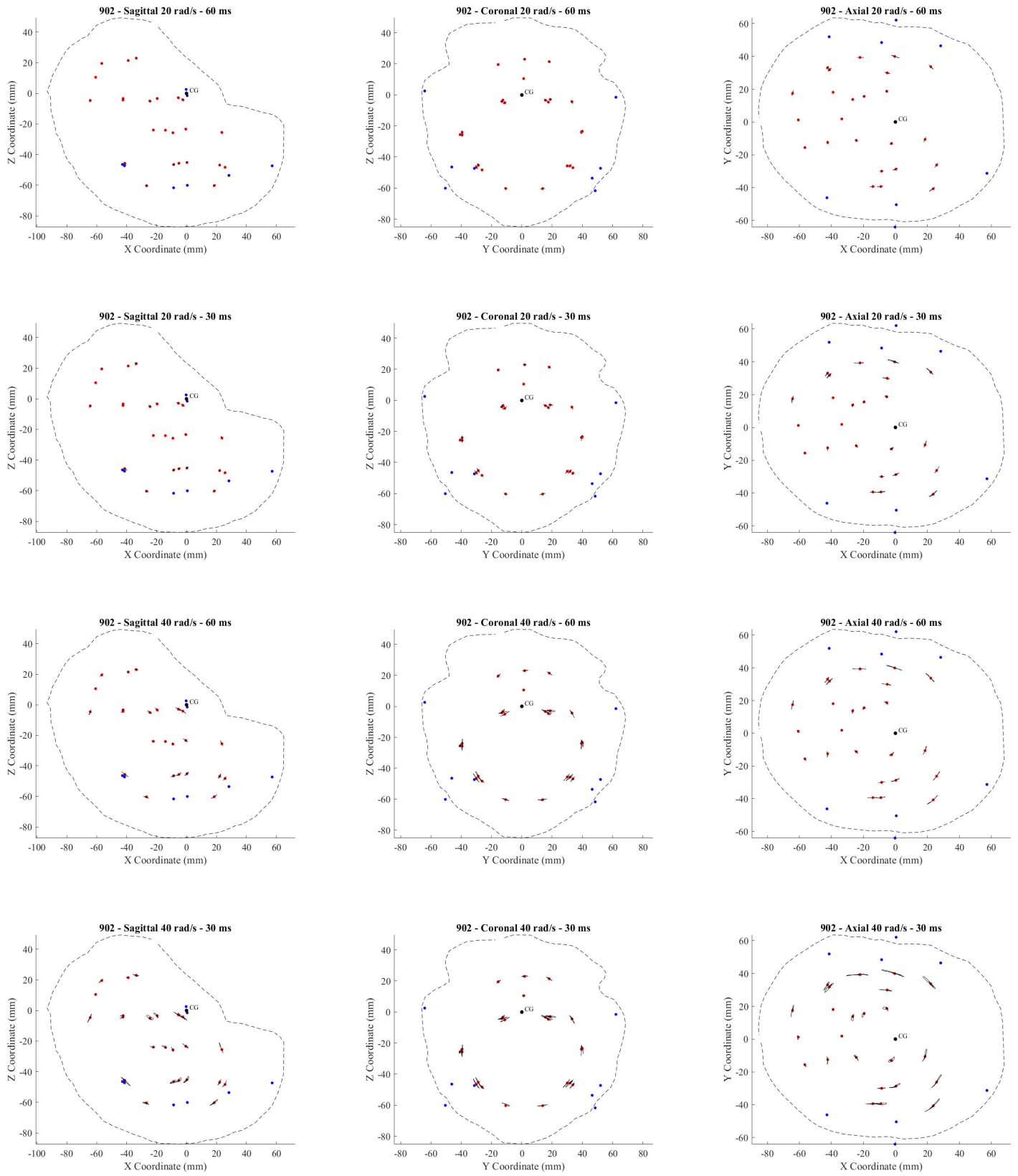


Figure D-4: Sonomicrometry trajectory plots for specimen 902.

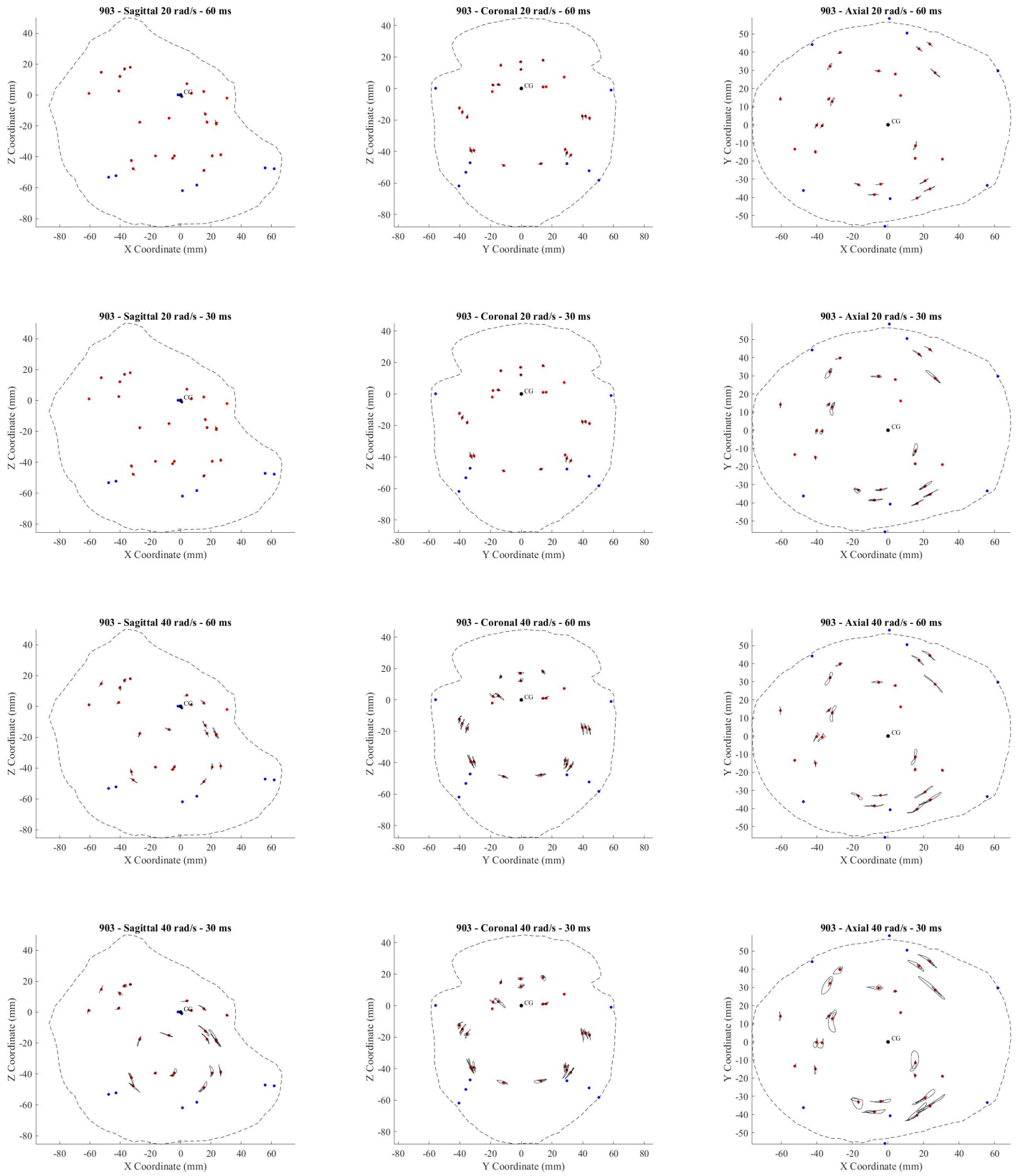


Figure D-5: Sonomicrometry trajectory plots for specimen 903.

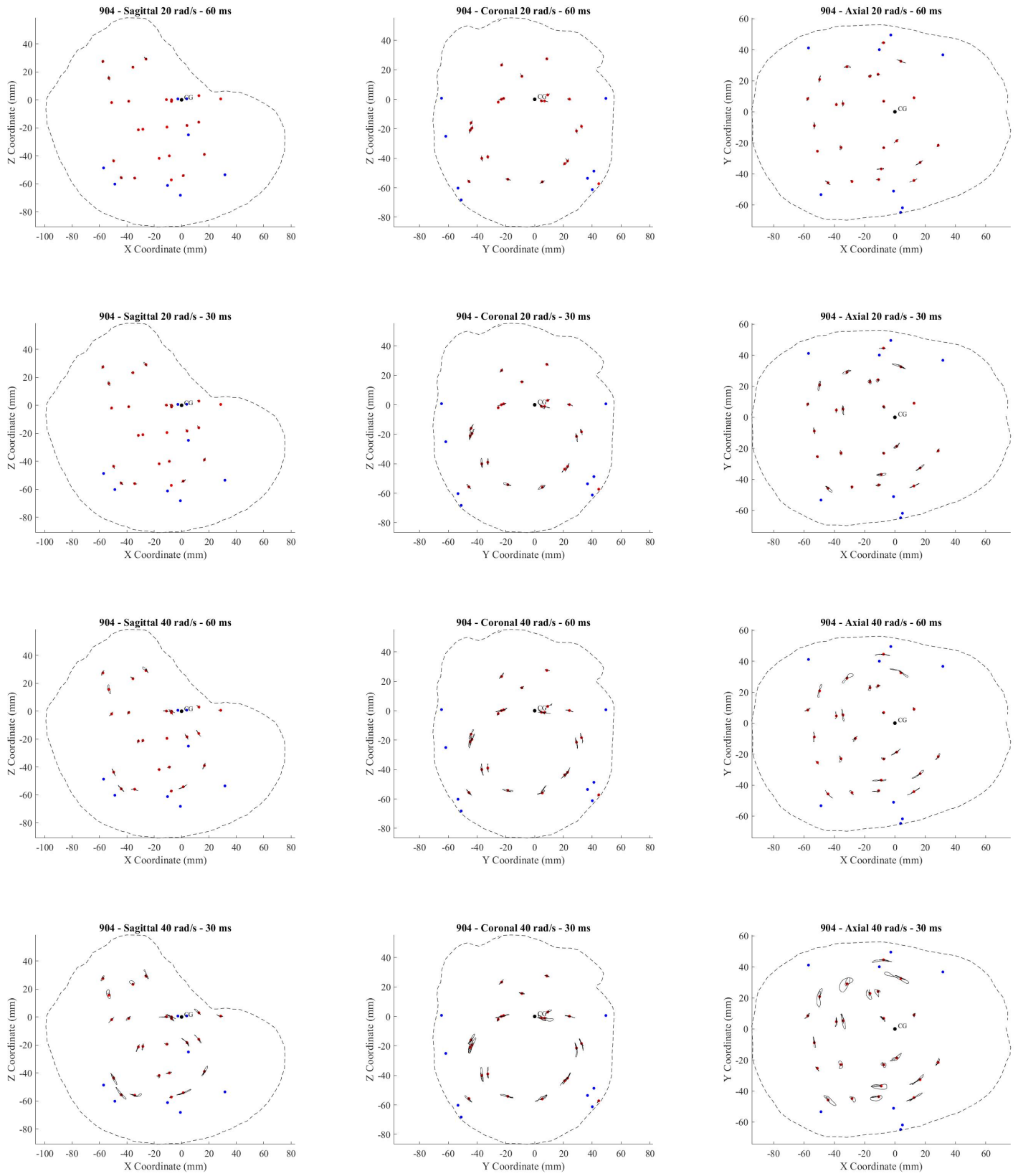
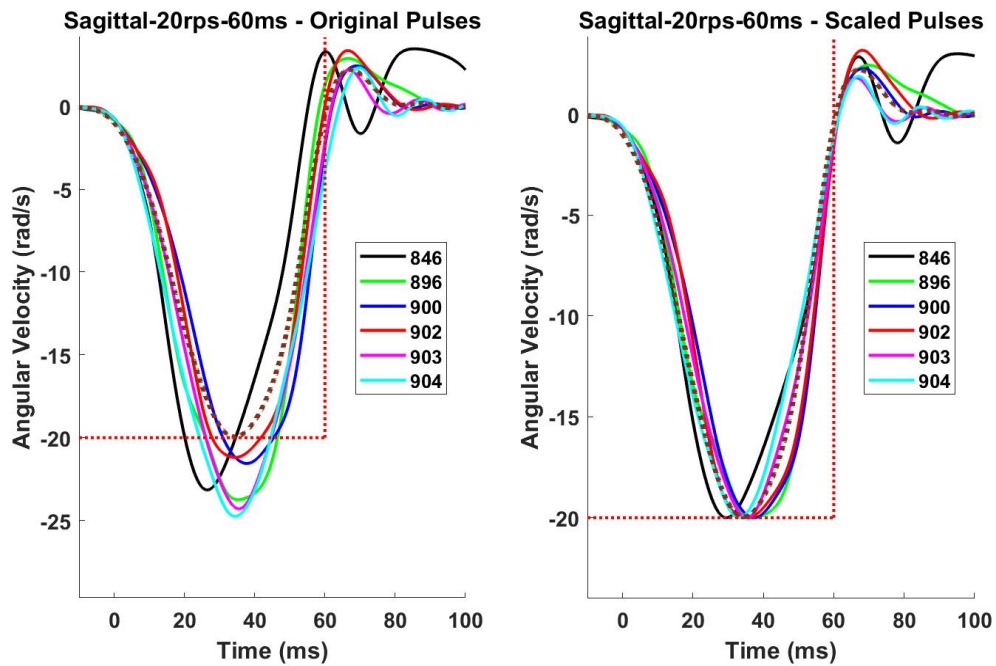
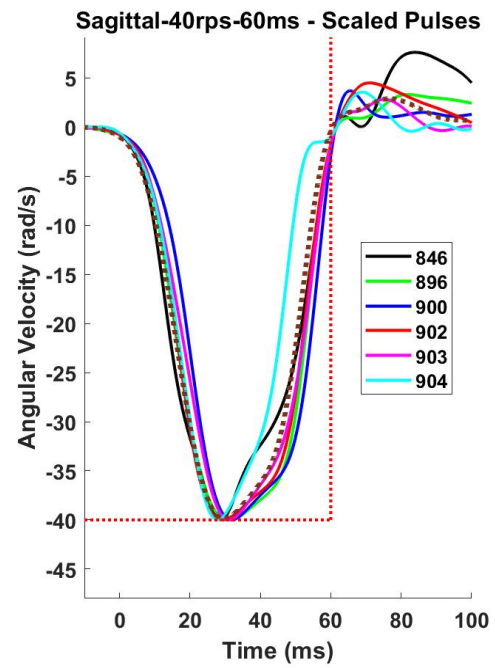
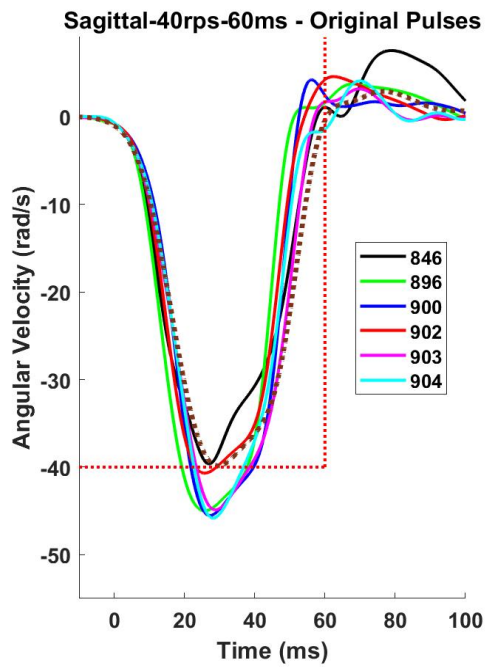
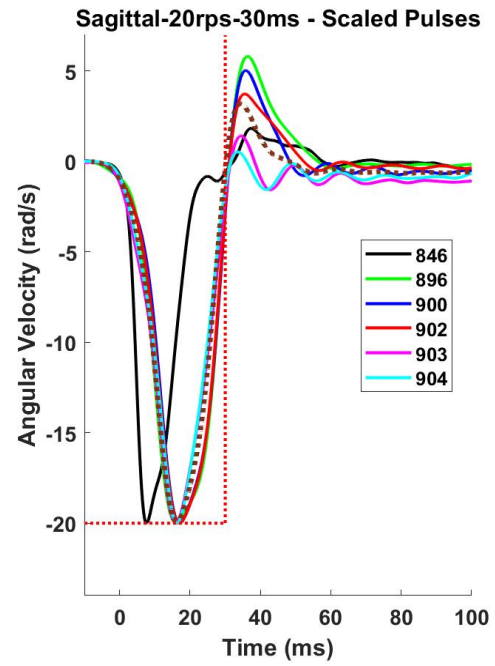
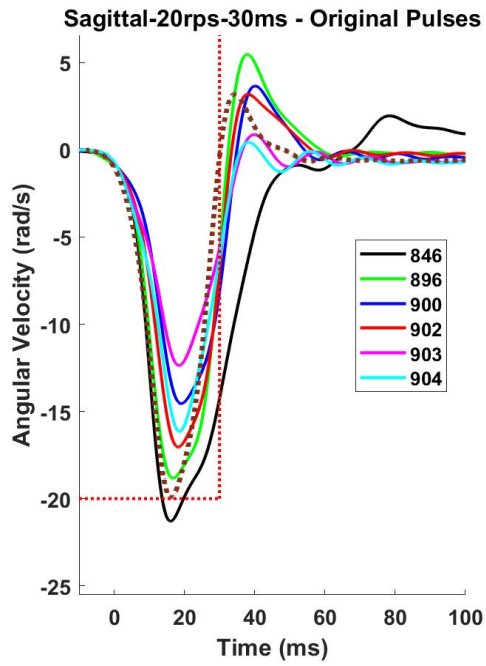


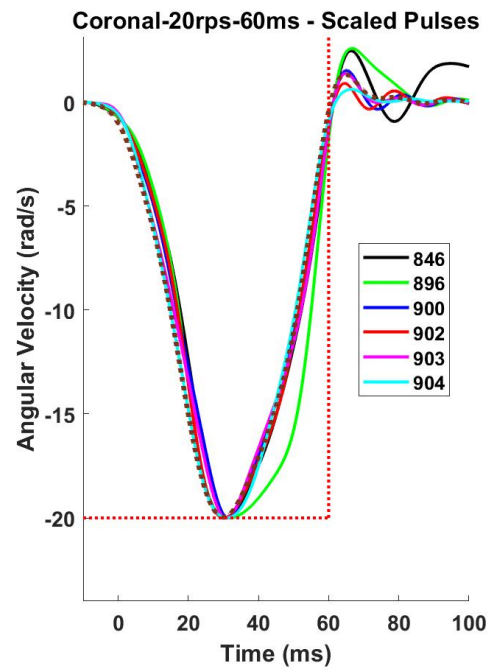
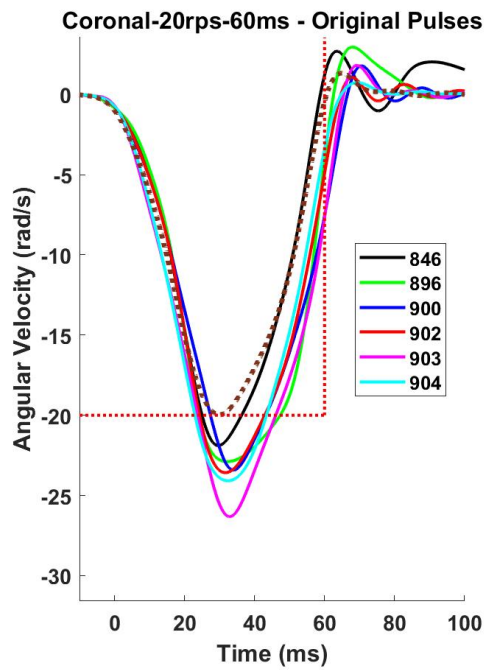
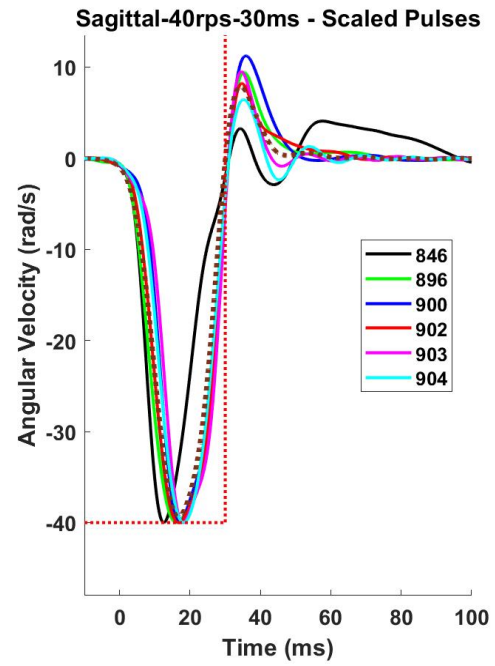
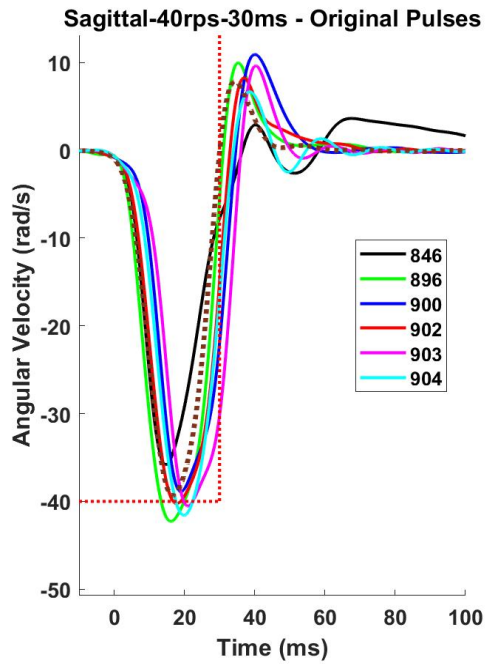
Figure D-6: Sonomicrometry trajectory plots for specimen 904.

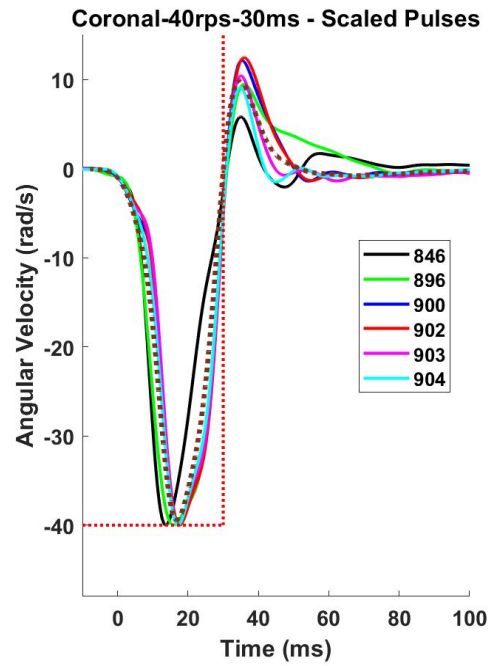
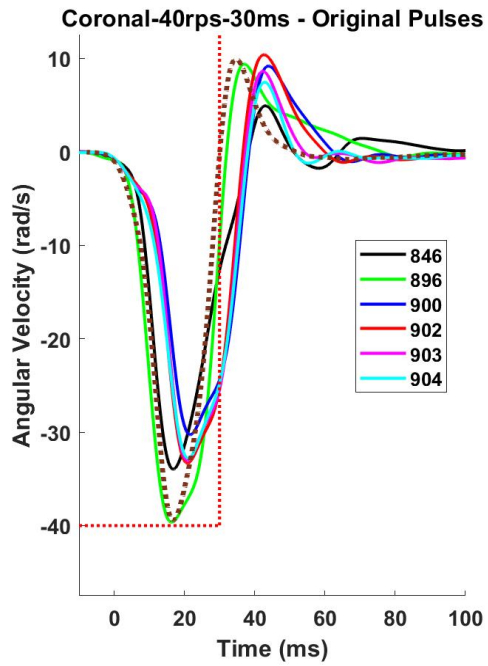
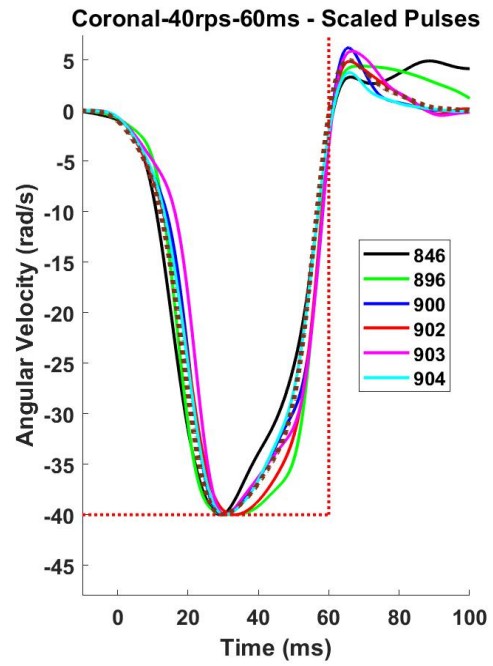
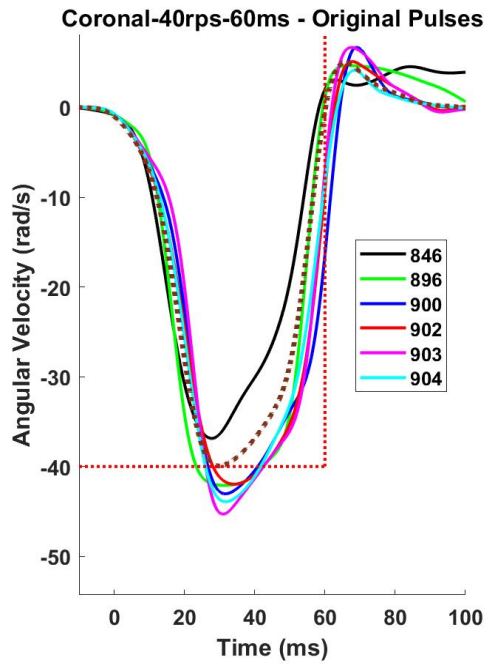
## APPENDIX E: CORRIDOR SCALED KINEMATICS

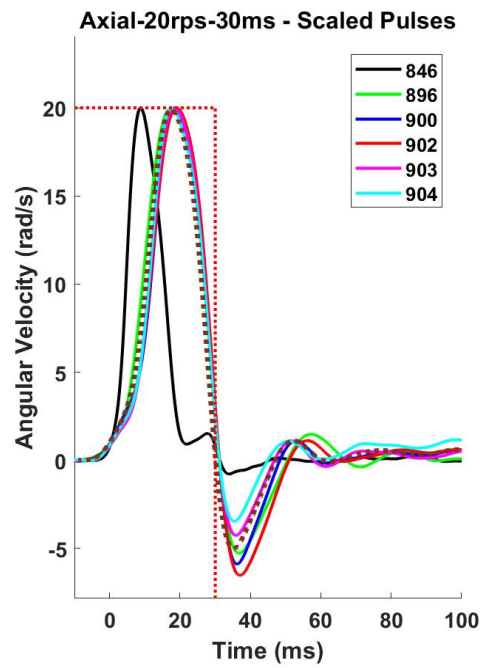
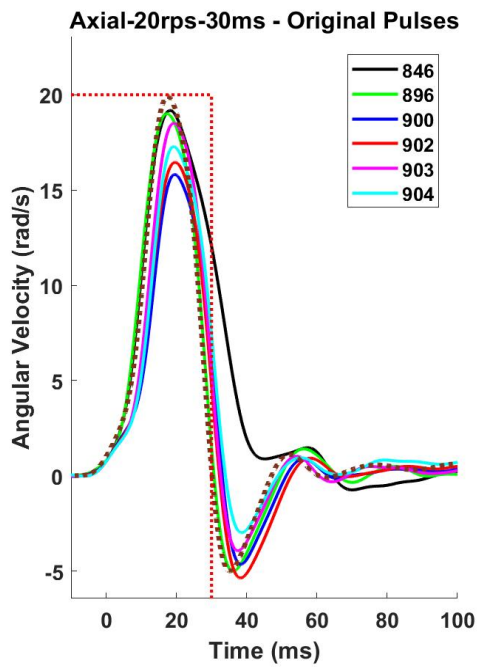
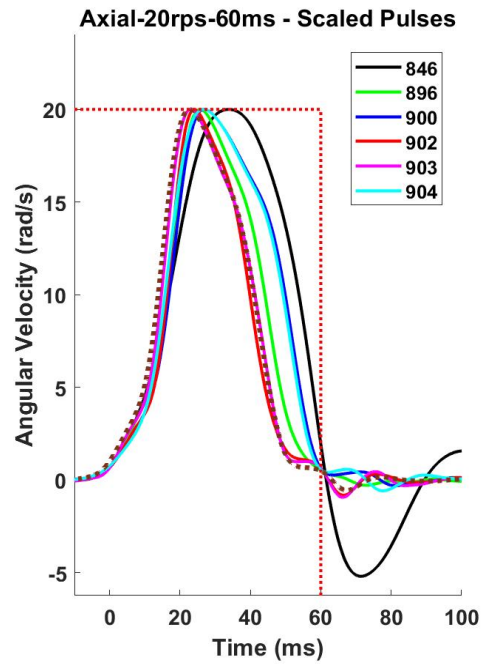
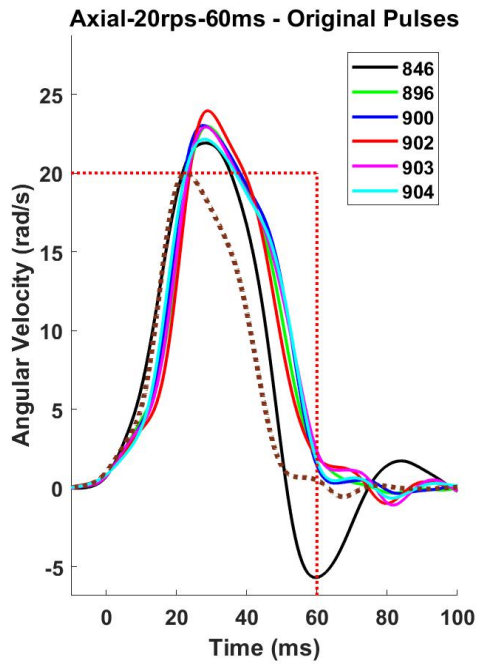
This appendix provides a depiction of the scaled kinematics used in the data corridor aggregation procedures (Chapter 6). The common scaled kinematics were calculated by scaling the kinematics of each specimen to match the desired angular velocity (20 rad/s or 40 rad/s) and pulse duration (30 ms or 60 ms). The scaled kinematics of the five specimens, excluding the pilot specimen (846), were averaged to acquire the corridor scaled kinematics, presented below.











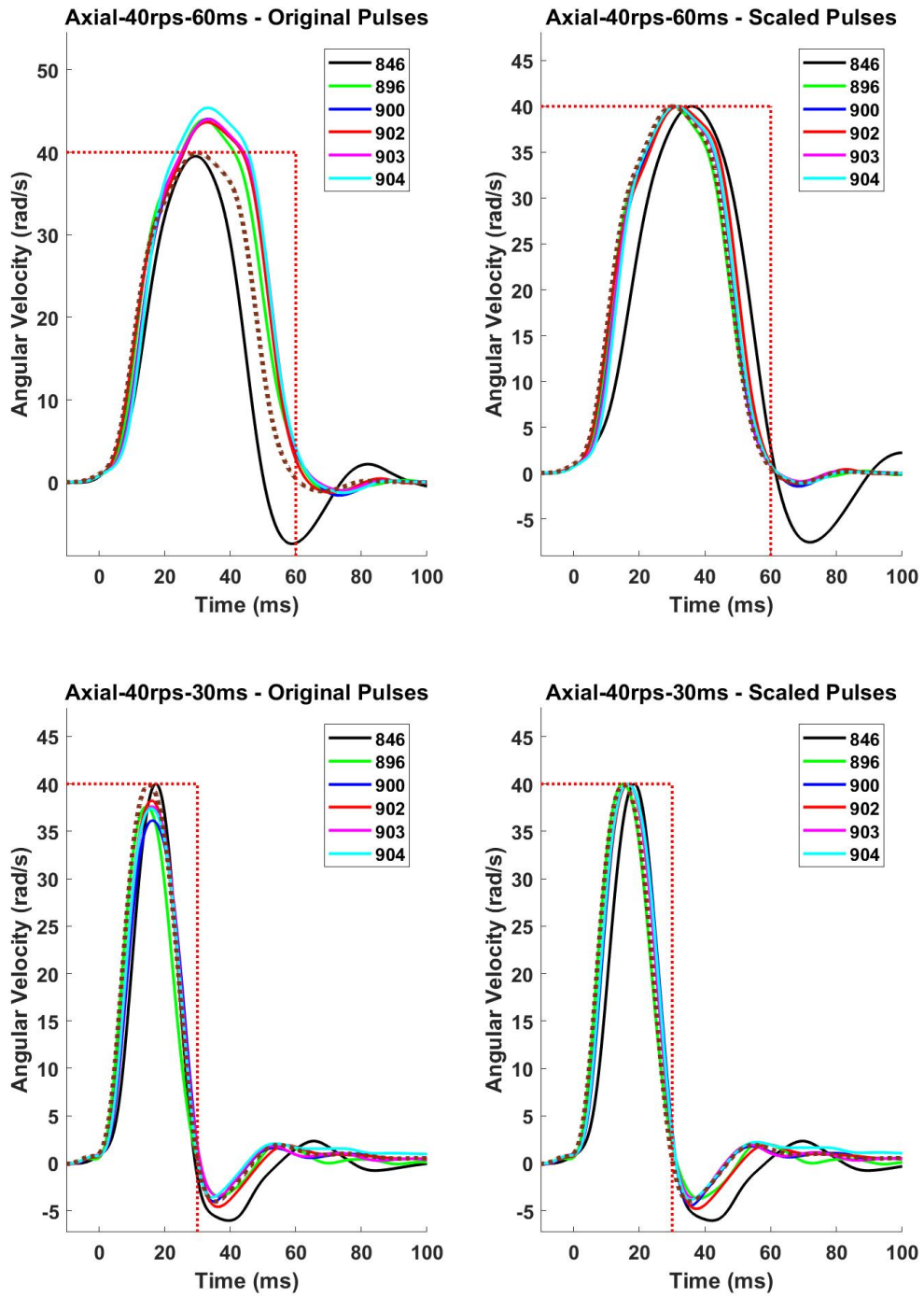


Figure E-1: Original and scaled angular velocity traces each test severity. The maroon dashed angular velocity trace indicates the common scaled corridor kinematics. The dotted red lines indicate the target peak angular velocity and pulse duration.

## APPENDIX F: FE EVALUATION SCORES

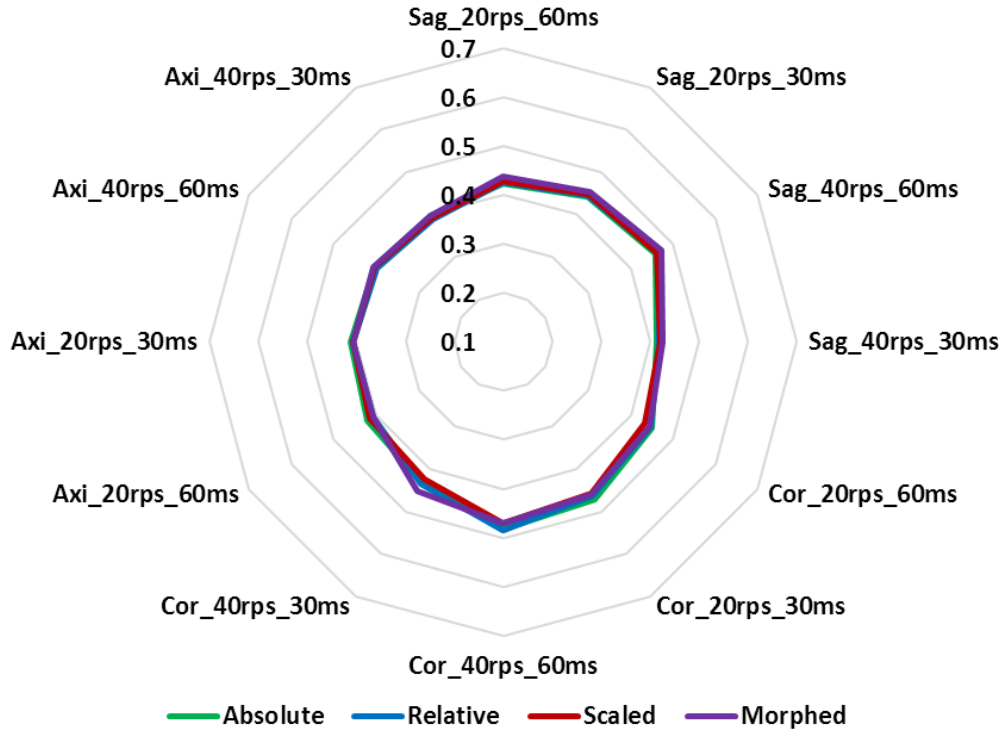
This appendix provides the FE brain model evaluation results for every specimen (Chapter 7). The following table provides the average and standard deviation of the weighted CORA score for all corresponding nodes to the sonomicrometry experiments.

*Table F-1: Average weighted CORA values for the GHBMC and SIMon models.*

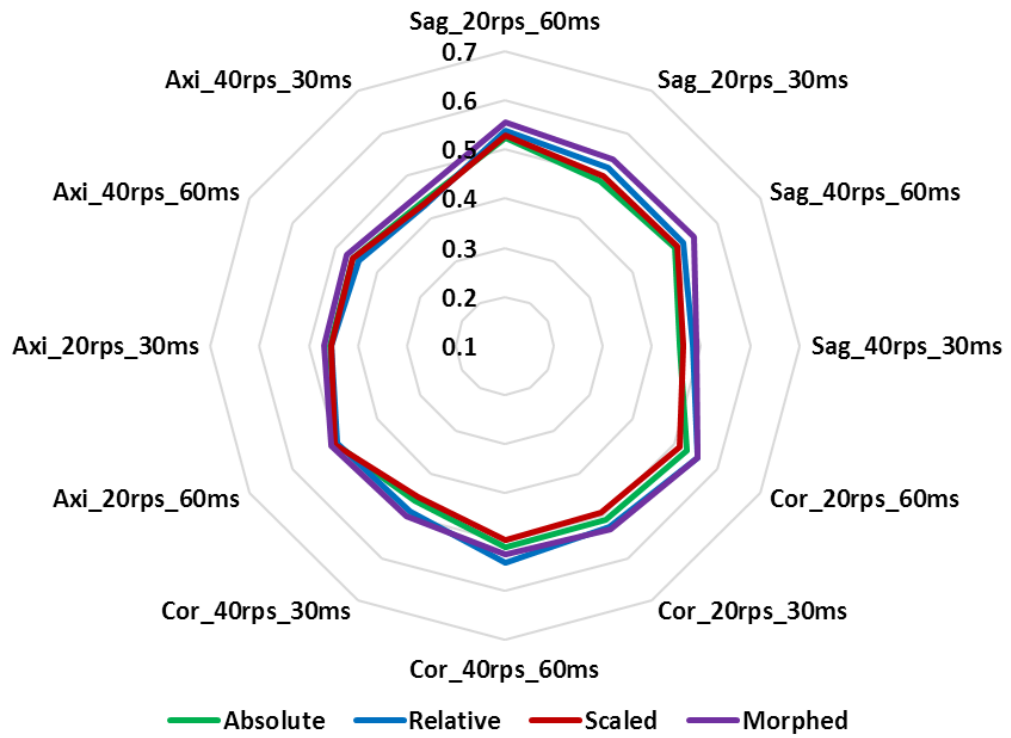
|              |          | 846           | 896           | 900           | 902           | 903           | 904           |
|--------------|----------|---------------|---------------|---------------|---------------|---------------|---------------|
| <b>GHBMC</b> | Absolute | 0.434 ± 0.027 | 0.486 ± 0.031 | 0.554 ± 0.027 | 0.489 ± 0.049 | 0.498 ± 0.039 | 0.505 ± 0.050 |
|              | Relative | 0.432 ± 0.029 | 0.499 ± 0.041 | 0.557 ± 0.030 | 0.497 ± 0.050 | 0.511 ± 0.043 | 0.505 ± 0.049 |
|              | Scaled   | 0.430 ± 0.025 | 0.483 ± 0.029 | 0.555 ± 0.028 | 0.503 ± 0.052 | 0.502 ± 0.029 | 0.506 ± 0.053 |
|              | Morphed  | 0.436 ± 0.027 | 0.512 ± 0.035 | 0.561 ± 0.048 | 0.517 ± 0.063 | 0.529 ± 0.045 | 0.500 ± 0.048 |
| <b>SIMon</b> | Absolute | 0.389 ± 0.029 | 0.407 ± 0.041 | 0.490 ± 0.024 | 0.472 ± 0.053 | 0.460 ± 0.031 | 0.425 ± 0.015 |
|              | Relative | 0.372 ± 0.041 | 0.404 ± 0.034 | 0.481 ± 0.017 | 0.471 ± 0.054 | 0.433 ± 0.041 | 0.417 ± 0.017 |
|              | Scaled   | 0.390 ± 0.026 | 0.405 ± 0.041 | 0.492 ± 0.031 | 0.467 ± 0.051 | 0.457 ± 0.030 | 0.419 ± 0.025 |
|              | Morphed  | 0.344 ± 0.034 | 0.349 ± 0.037 | 0.437 ± 0.016 | 0.427 ± 0.029 | 0.411 ± 0.031 | 0.366 ± 0.024 |

The following plots depict the average weighted CORA scores for each comparison method for each specimen for the GHBMC (Figure F-1) and SIMon (Figure F-2) models.

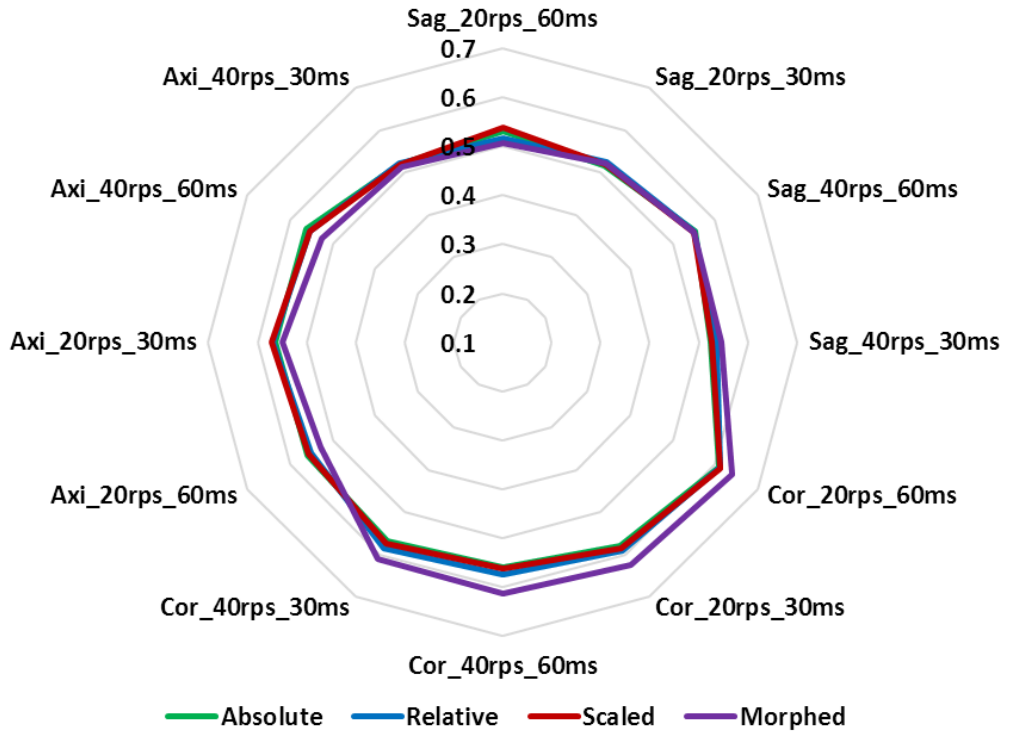
### Specimen 846 - GHBMC



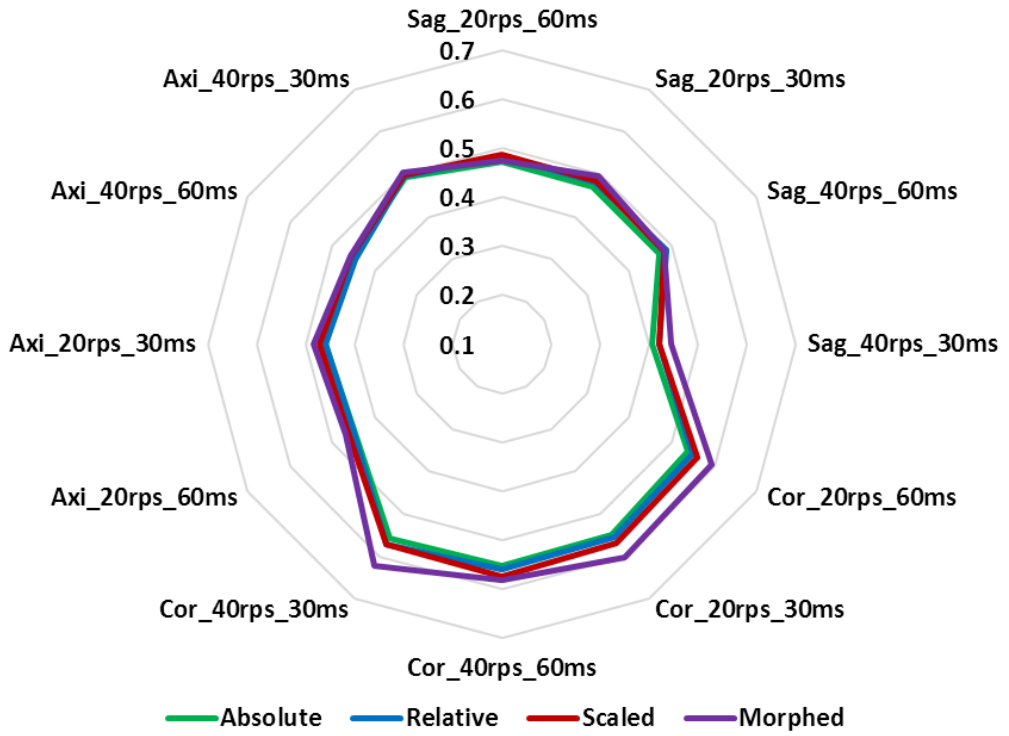
### Specimen 896 - GHBMC



### Specimen 900 - GHBMC



### Specimen 902 - GHBMC



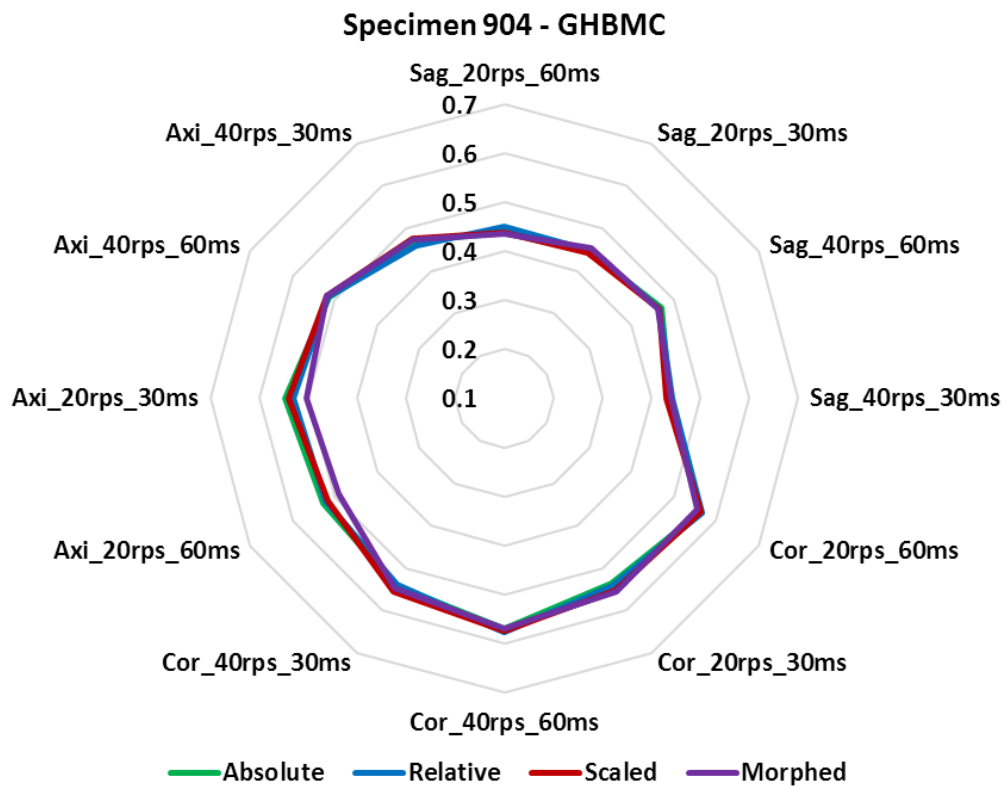
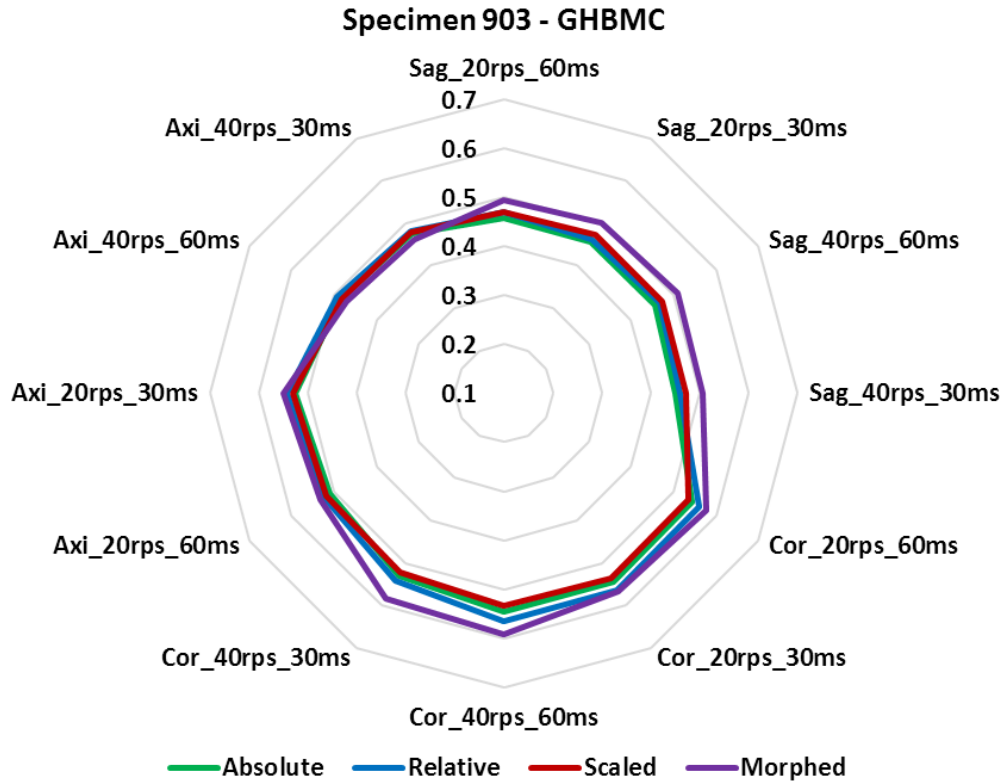
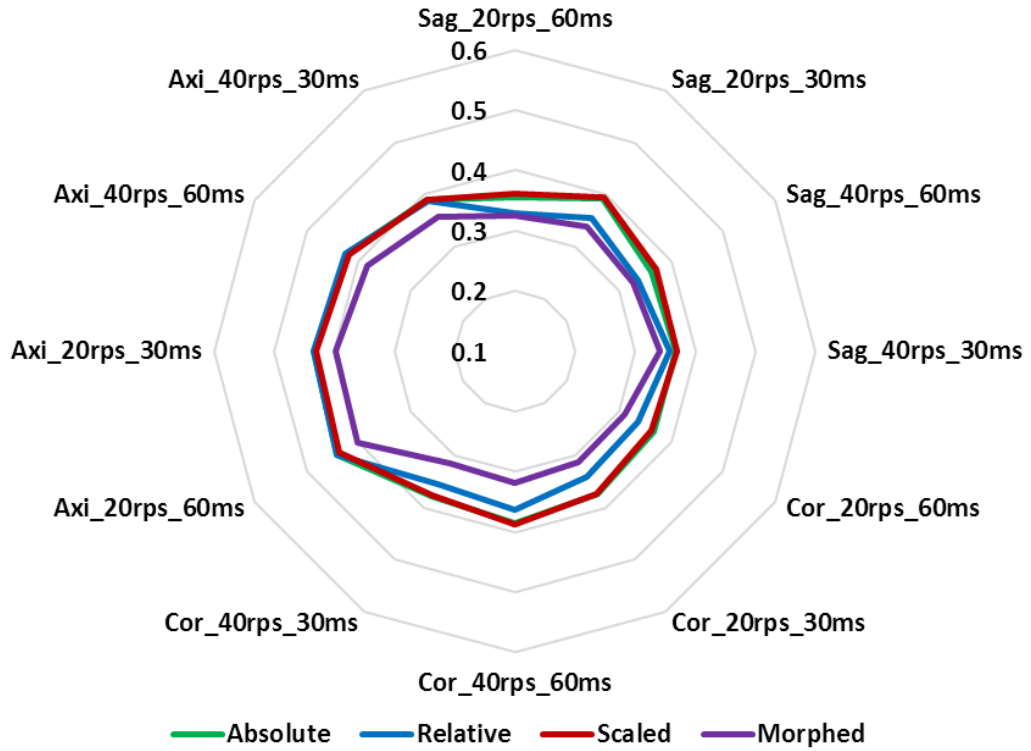
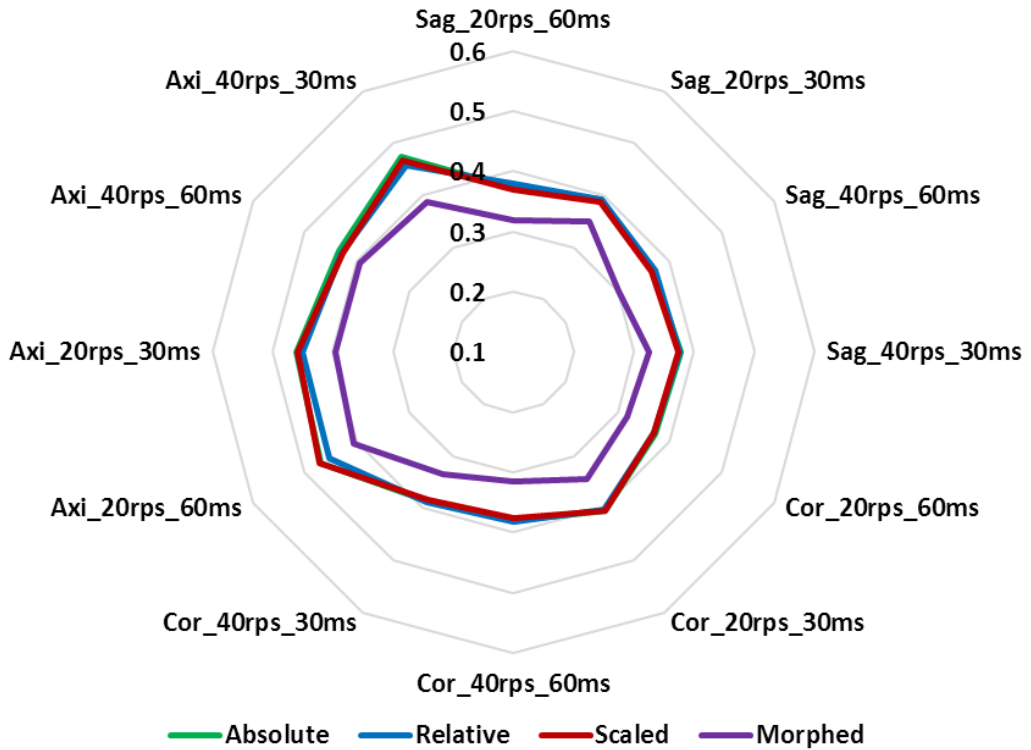


Figure F-1: The weighted CORA for all rotational loading conditions in the sagittal (sag), coronal (cor), and axial (axi) directions for all specimens for GHBMC.

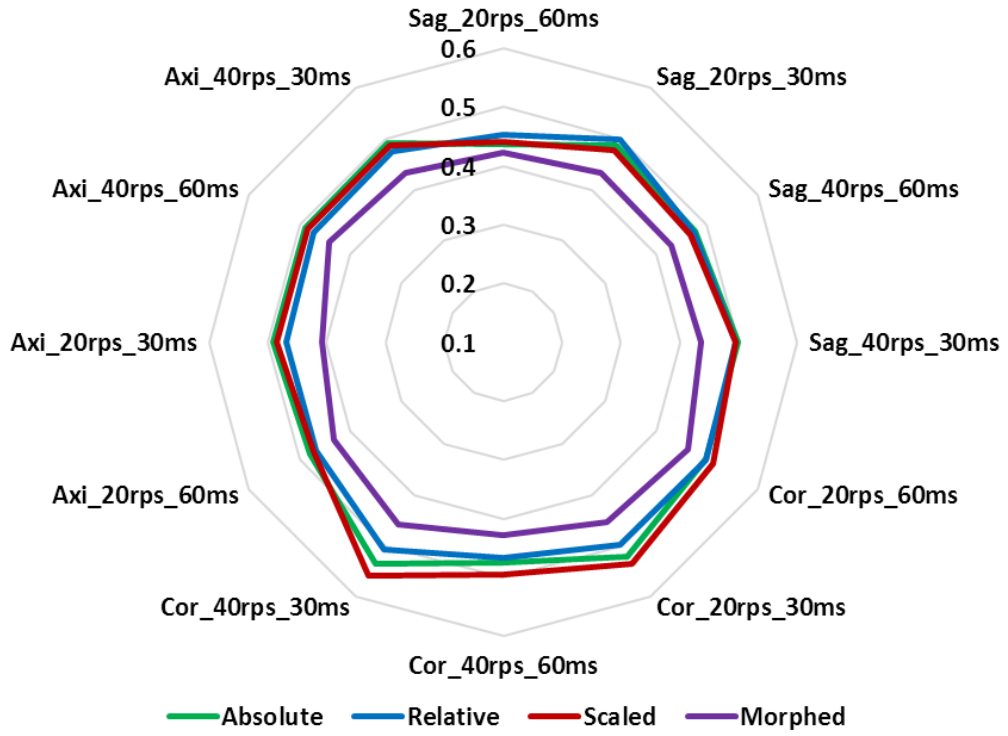
### Specimen 846 - SIMon



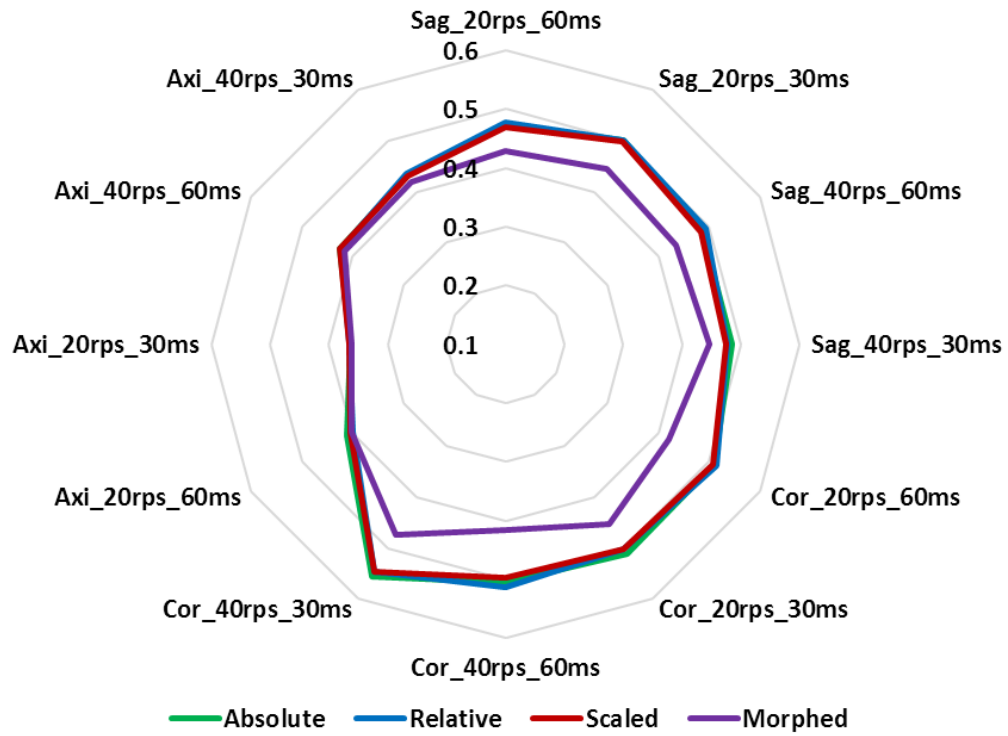
### Specimen 896 - SIMon



### Specimen 900 - SIMon



### Specimen 902 - SIMon



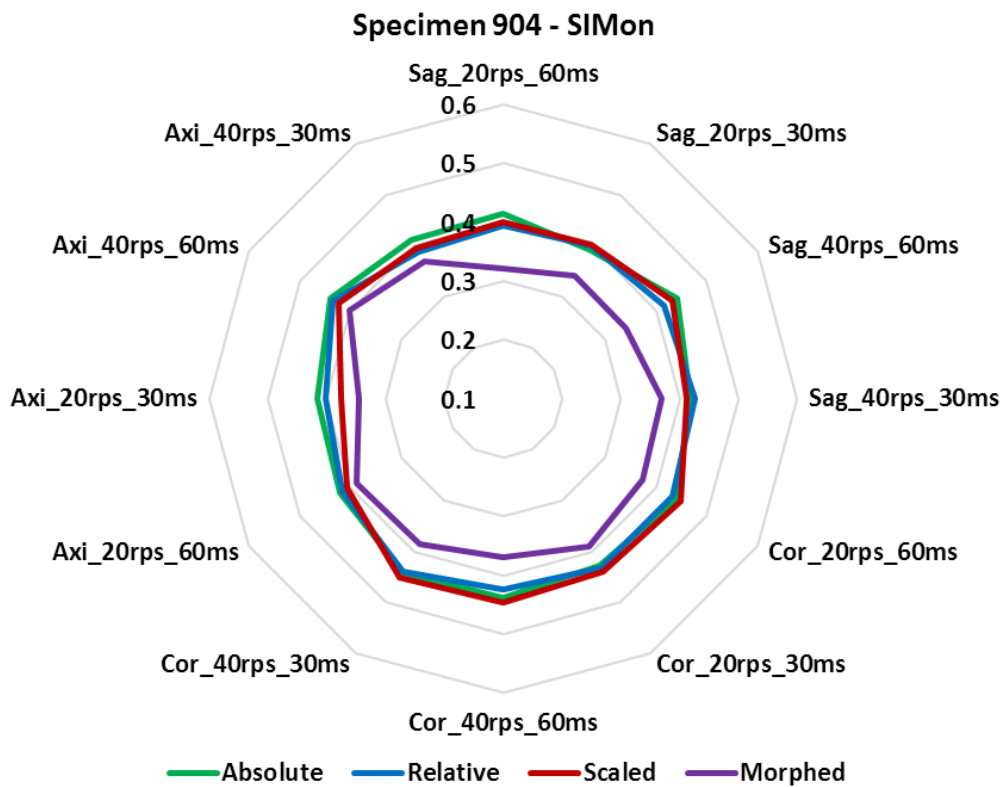
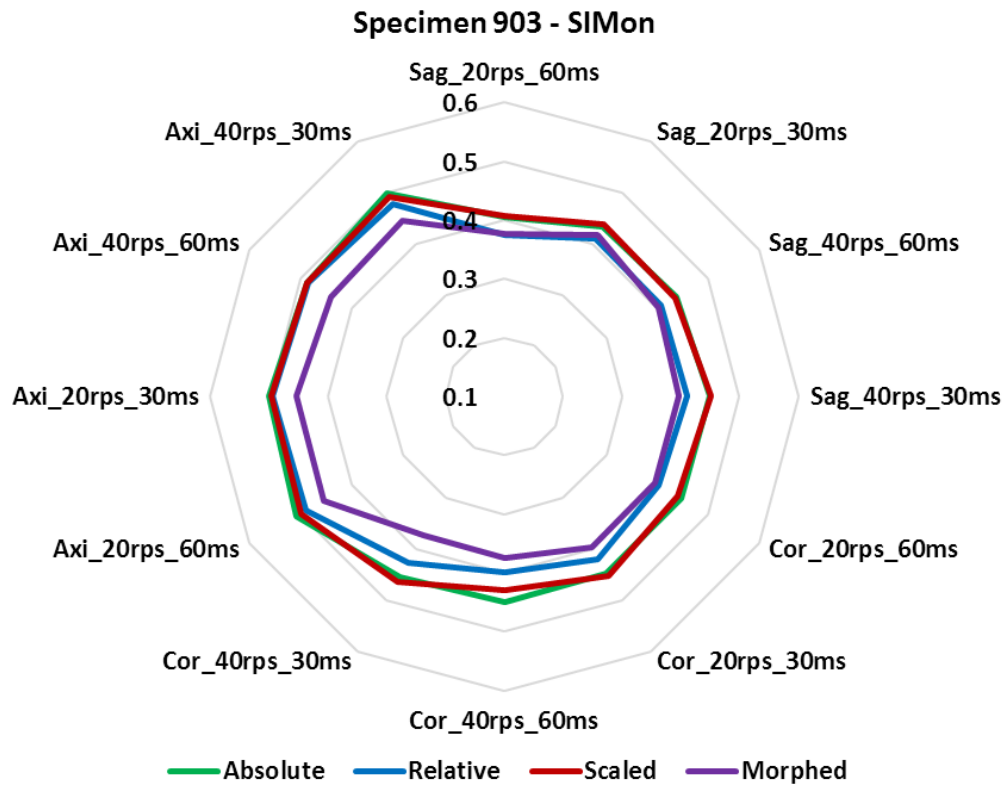
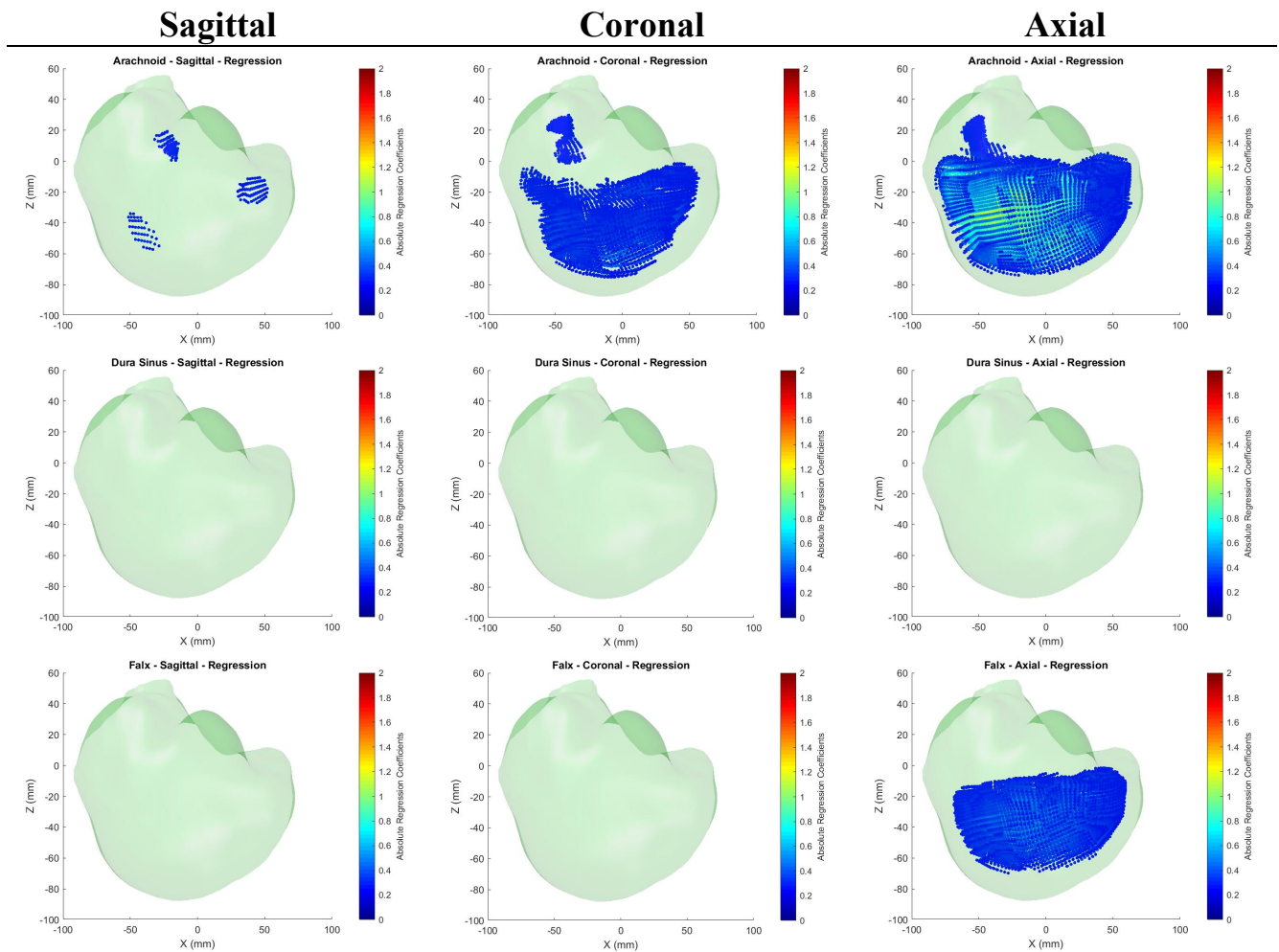
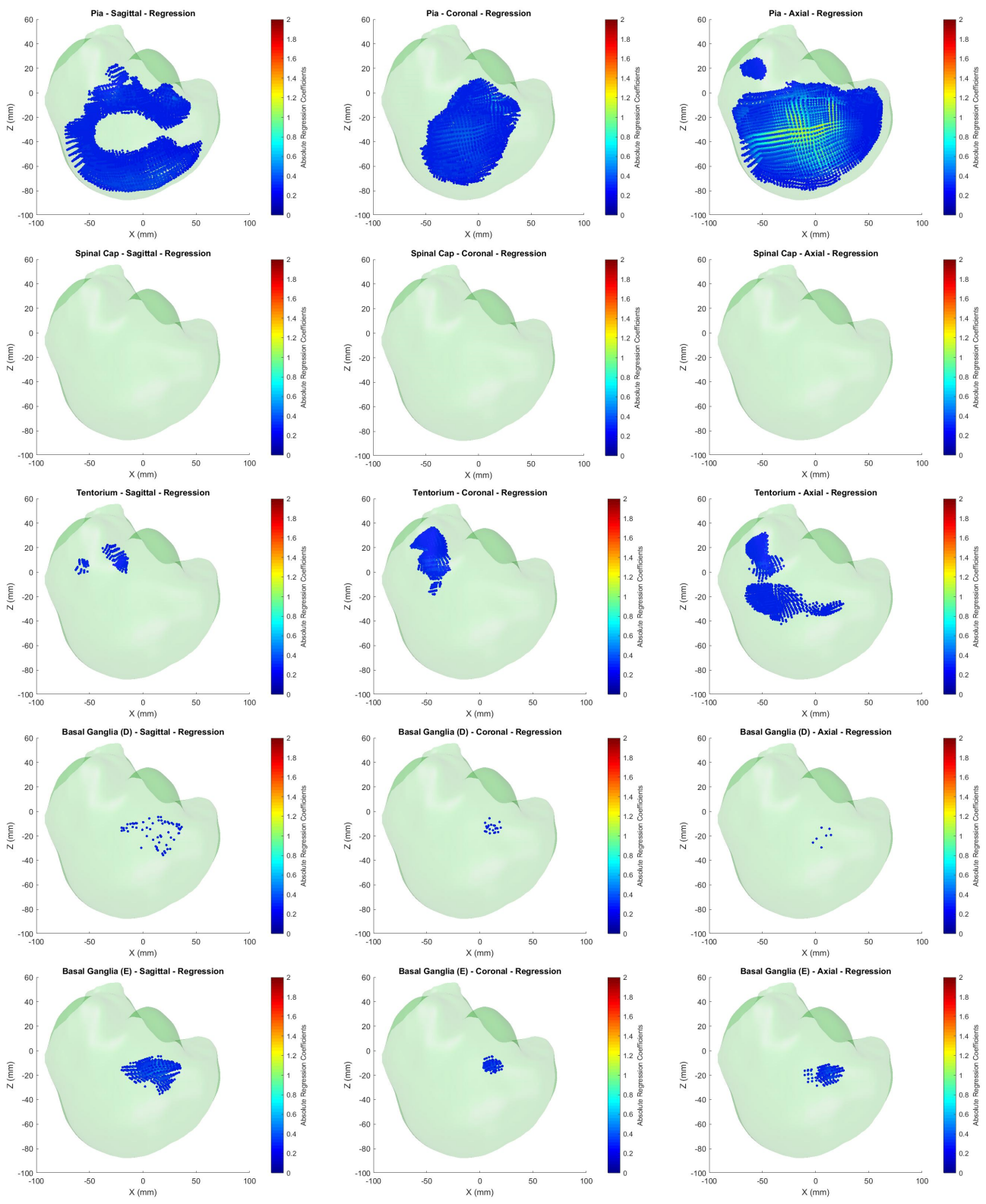


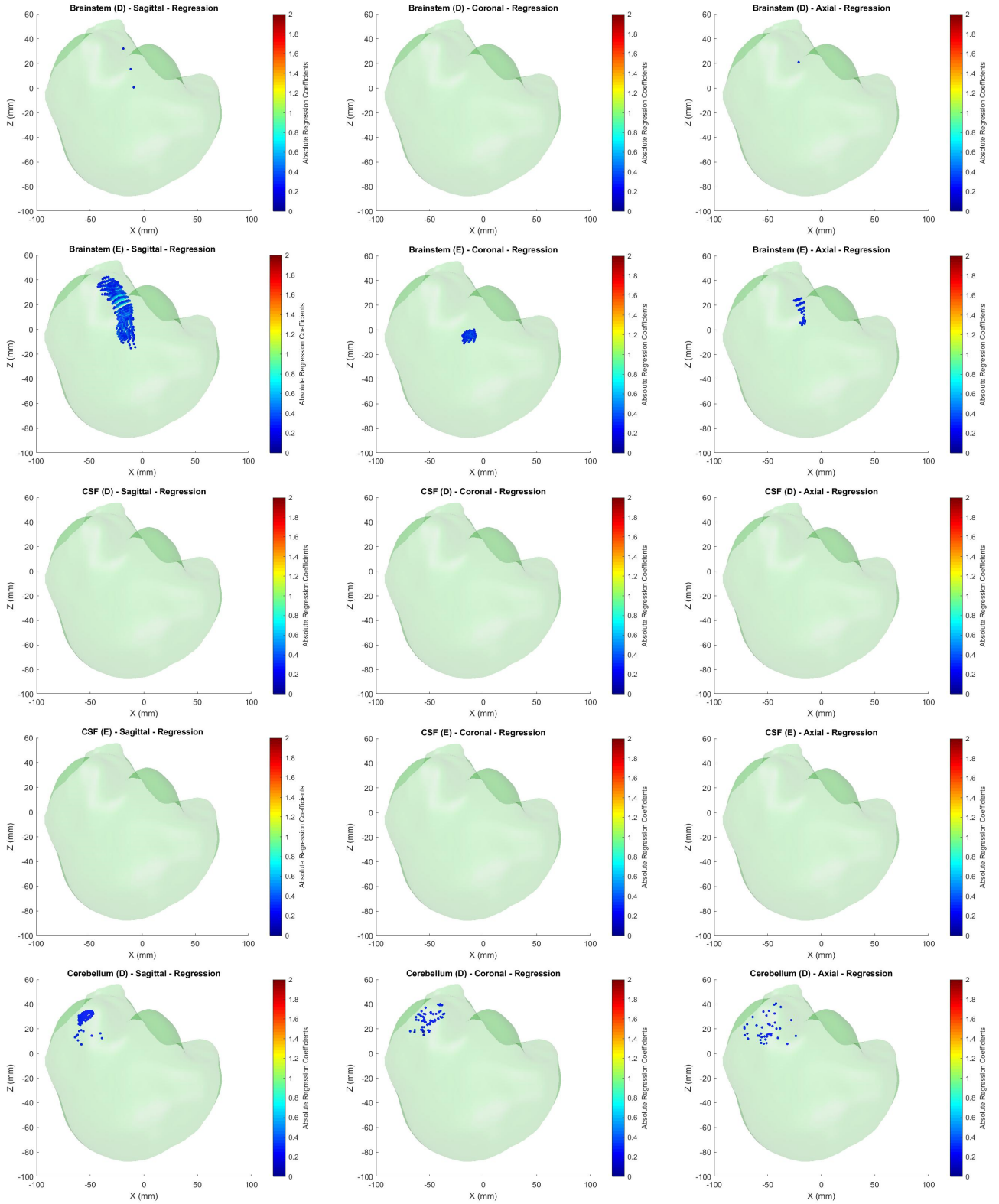
Figure F-2: The weighted CORA for all rotational loading conditions in the sagittal (sag), coronal (cor), and axial (axi) directions for all specimens for SIMon.

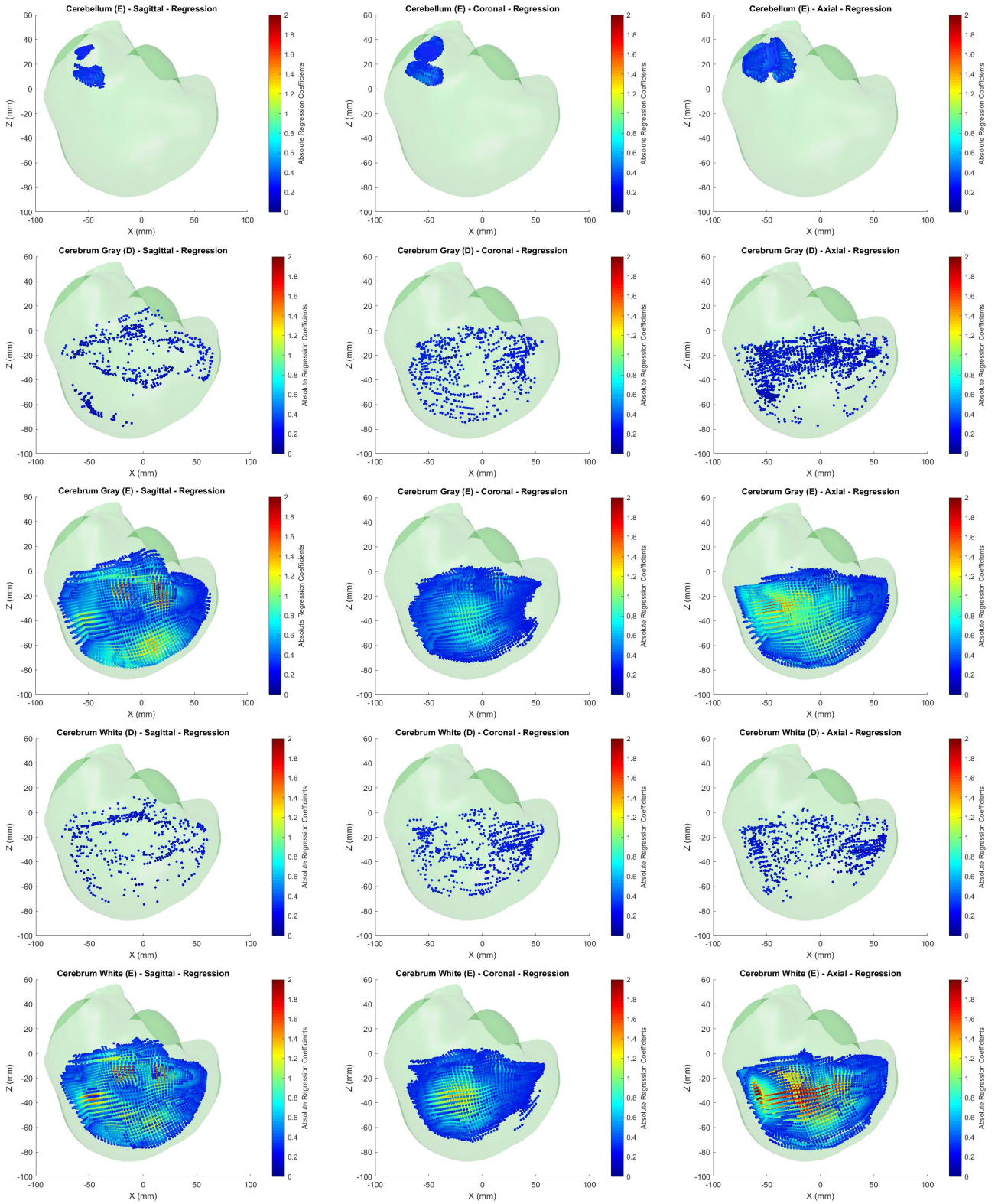
# APPENDIX G: FE SENSITIVITY RESULTS

This appendix provides the model material sensitivity results for the GHBMC (Figure G-1) and SIMon (Figure G-2) FE brain models (Chapter 8). The following plots depict the absolute value of the regression coefficients for every node in the models for the three rotation directions. The viscoelastic materials have two plots, for the complex modulus ( $E$ ) and damping ( $D$ ). The depicted nodes must have a regression coefficient greater than 0.1 and a p-value less than 0.05. For materials that depict no highlighted nodes, brain deformation was not sensitive to the change in the material parameter for the given thresholds.









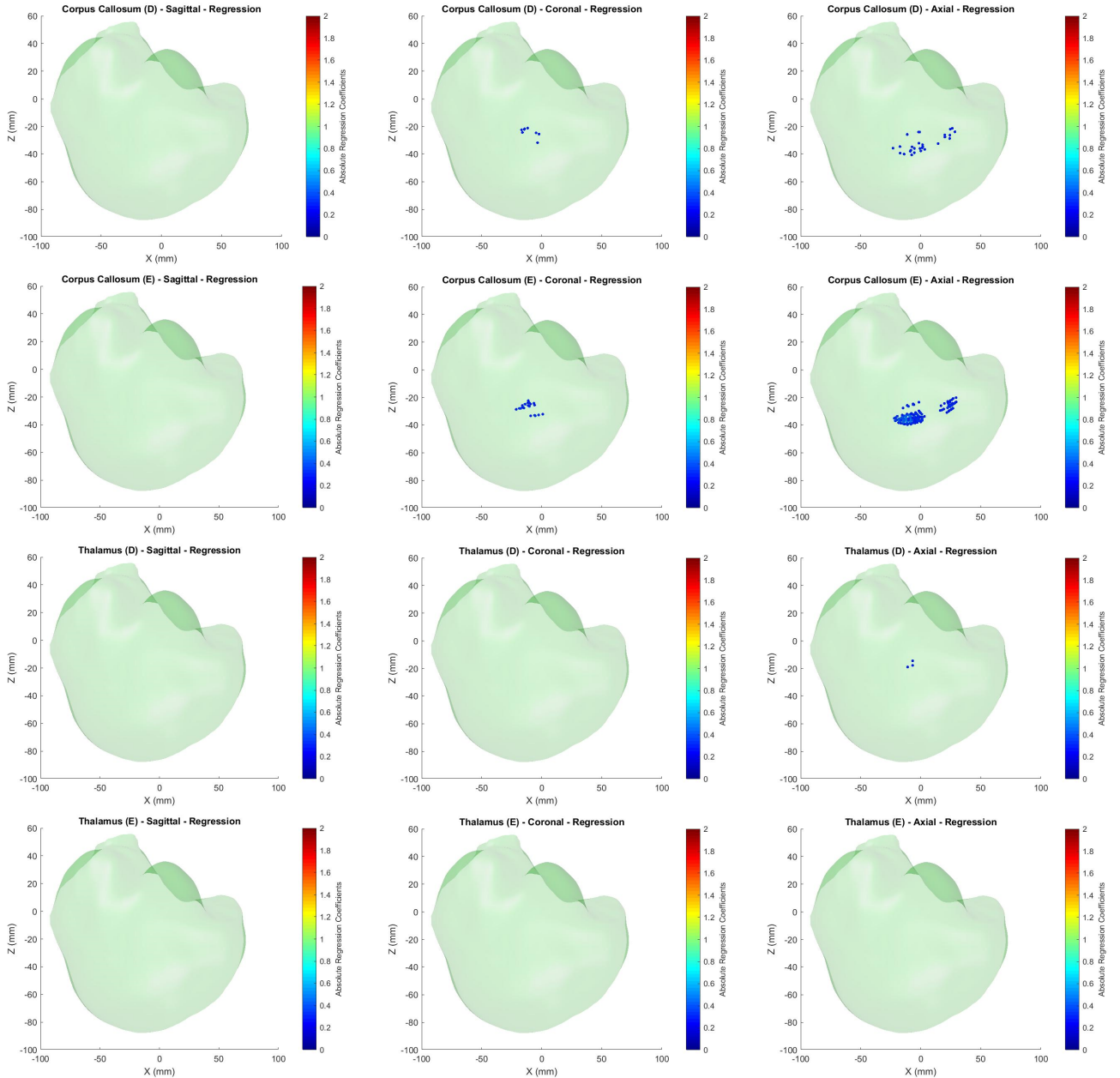
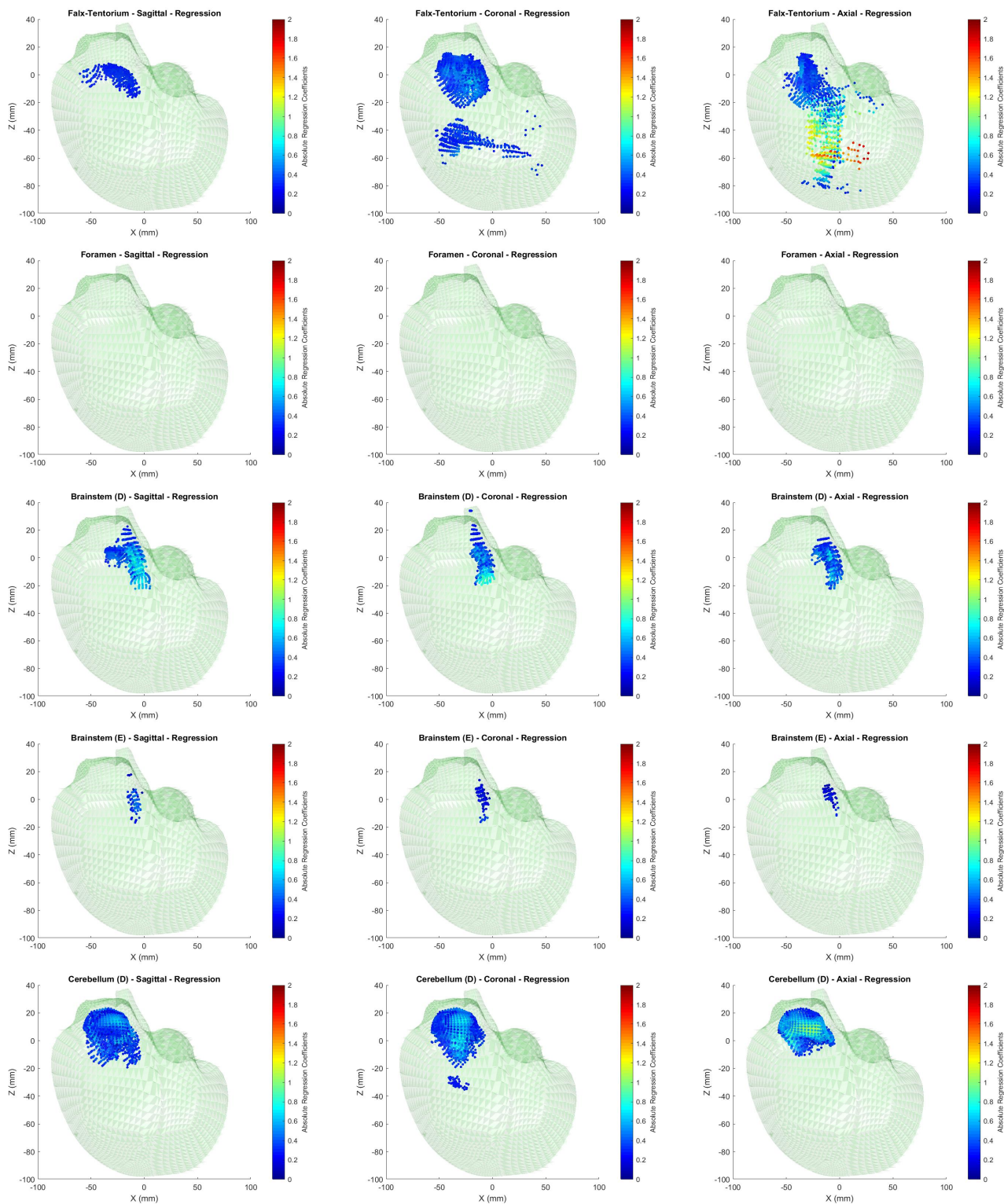


*Figure G-1: GHMC material sensitivity regression for the sagittal, coronal, and axial rotations for all materials.*

## Sagittal

## Coronal

## Axial



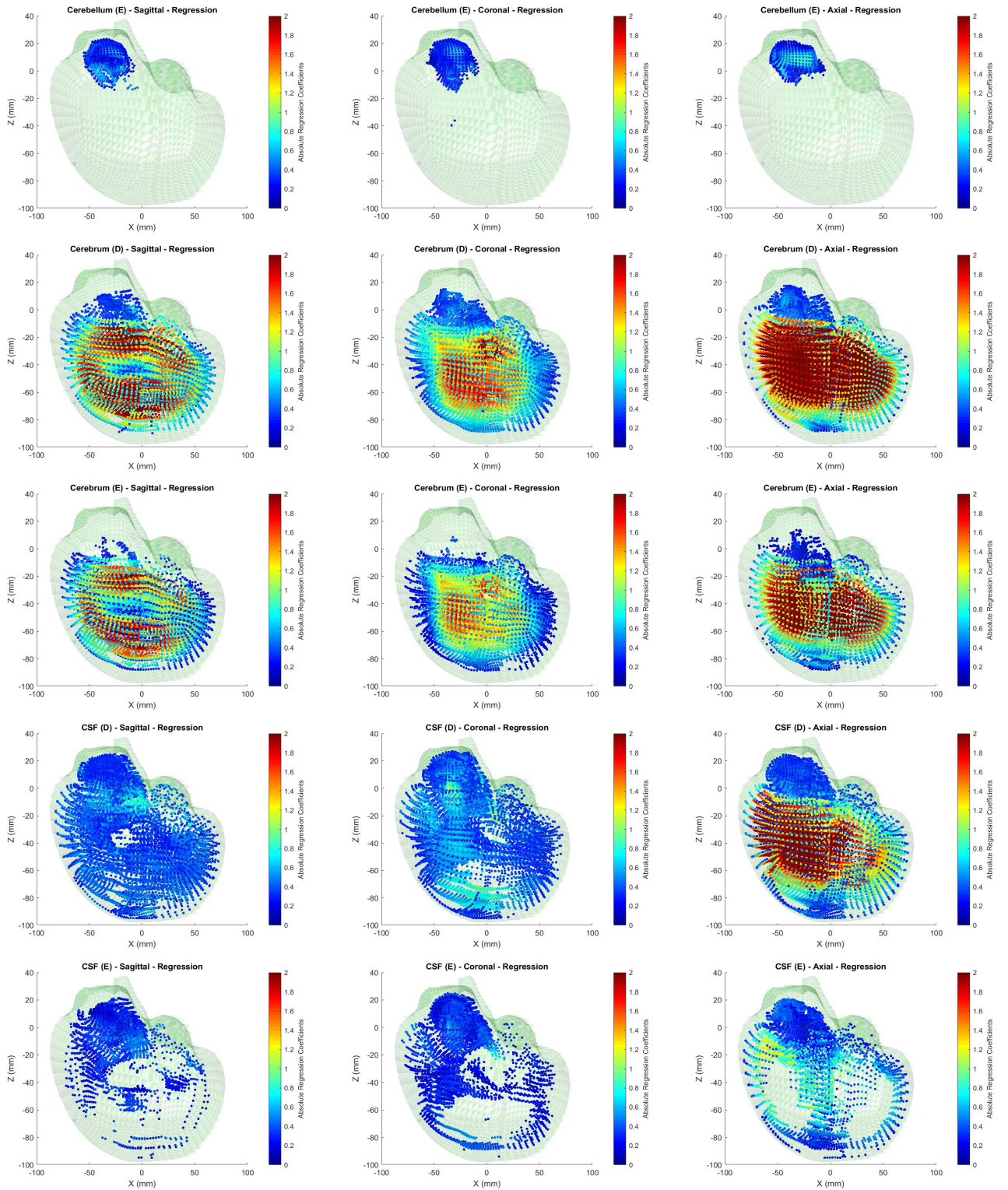


Figure G-2: SIMon material sensitivity regression for the sagittal, coronal, and axial rotations for all materials.

## REFERENCES

- Alshareef, A. (2019). Quantifying 3D Brain Deformation using Sonomicrometry During Dynamic Head Rotational Loading (Bethesda, Maryland, USA).
- Alshareef, A., Giudice, J.S., Forman, J., Salzar, R.S., and Panzer, M.B. (2018). A novel method for quantifying human in situ whole brain deformation under rotational loading using sonomicrometry. *J. Neurotrauma* 35, 780–789.
- Alshareef, A.A., Gabler, L.F., Stone, J.R., and Panzer, M.B. (2015). Changes in the Mechanical Response of Brain Tissue Following Primary Blast Injury. In 2015 Ohio State University Injury Biomechanics Symposium, p.
- Arbogast, K.B., and Margulies, S.S. (1998). Material characterization of the brainstem from oscillatory shear tests. *J. Biomech.* 31, 801–807.
- Ash, J.H., Lessley, D.J., Forman, J.L., Zhang, Q., Shaw, C.G., and Crandall, J.R. (2012). Whole-body kinematics: response corridors for restrained PMHS in frontal impacts. In Proceedings of IRCOBI Conference, pp. 142–154.
- Augustyniak, R.A., Collins, H.L., Ansoorge, E.J., Rossi, N.F., and O’Leary, D.S. (2001). Severe exercise alters the strength and mechanisms of the muscle metaboreflex. *Am. J. Physiol.-Heart Circ. Physiol.* 280, H1645–H1652.
- Avants, B.B., Tustison, N.J., Song, G., Cook, P.A., Klein, A., and Gee, J.C. (2011). A reproducible evaluation of ANTs similarity metric performance in brain image registration. *Neuroimage* 54, 2033–2044.
- Babak, O., and Deutsch, C.V. (2009). Statistical approach to inverse distance interpolation. *Stoch. Environ. Res. Risk Assess.* 23, 543–553.
- Bader, T., Wiedemann, A., Roberts, K., and Hanebeck, U.D. (2007). Model-based motion estimation of elastic surfaces for minimally invasive cardiac surgery. In Robotics and Automation, 2007 IEEE International Conference On, (IEEE), pp. 2261–2266.
- Bajaj, R., Ranaweera, S.L., and Agrawal, D.P. (2002). GPS: location-tracking technology. *Computer* 92–94.
- Bashkatov, A.N., Genina, E.A., Sinichkin, Y.P., Kochubey, V.I., Lakodina, N.A., and Tuchin, V.V. (2003). Glucose and mannitol diffusion in human dura mater. *Biophys. J.* 85, 3310–3318.
- Bayly, P.V., Cohen, T.S., Leister, E.P., Ajo, D., Leuthardt, E.C., and Genin, G.M. (2005). Deformation of the human brain induced by mild acceleration. *J. Neurotrauma* 22, 845–856.

- Bebek, O., and Cavusoglu, M.C. (2007). Intelligent control algorithms for robotic-assisted beating heart surgery. *IEEE Trans. Robot.* *23*, 468–480.
- Besl, P.J., and McKay, N.D. (1992). Method for registration of 3-D shapes. In *Sensor Fusion IV: Control Paradigms and Data Structures*, (International Society for Optics and Photonics), pp. 586–607.
- Bookstein, F.L. (1989). Principal warps: Thin-plate splines and the decomposition of deformations. *IEEE Trans. Pattern Anal. Mach. Intell.* *11*, 567–585.
- Borenstein, J., Everett, H.R., Feng, L., and Wehe, D. (1997). Mobile robot positioning: Sensors and techniques. *J. Robot. Syst.* *14*, 231–249.
- Brown Jr, P.M., Kim, V.B., Boyer, B.J., Lust, R.M., Chitwood Jr, W.R., and Elbeery, J.R. (1999). Regional left ventricular systolic function in humans during off-pump coronary bypass surgery. *Circulation* *100*, II–125.
- Bryan, R., Mohan, P.S., Hopkins, A., Galloway, F., Taylor, M., and Nair, P.B. (2010). Statistical modelling of the whole human femur incorporating geometric and material properties. *Med. Eng. Phys.* *32*, 57–65.
- Budday, S., Sommer, G., Paulsen, F., Holzapfel, G.A., Steinmann, P., and Kuhl, E. (2018). Region-and loading-specific finite viscoelasticity of human brain tissue. *PAMM* *18*, e201800169.
- Carey, J. (1990). *Brain Facts: A Primer on the Brain and Nervous System*.
- Carroll, A.M. (2004). Muscle activation and strain during suction feeding in the largemouth bass *Micropterus salmoides*. *J. Exp. Biol.* *207*, 983–991.
- Coronado, V.G., McGuire, L.C., Sarmiento, K., Bell, J., Lionbarger, M.R., Jones, C.D., Geller, A.I., Khoury, N., and Xu, L. (2012). Trends in traumatic brain injury in the US and the public health response: 1995–2009. *J. Safety Res.* *43*, 299–307.
- Crandall, J. (2015). *Brain Injury* (Munich, Germany).
- Crassidis, J.L. (2006). Sigma-point Kalman filtering for integrated GPS and inertial navigation. *IEEE Trans. Aerosp. Electron. Syst.* *42*, 750–756.
- Deck, C., and Willinger, R. (2009). The current state of the human head finite element modelling. *Int. J. Veh. Saf.* *4*, 85–112.
- Dione, D., Shi, P., Smith, W., DeMan, P., Soares, J., Duncan, J., and Sinusas, A. (1997). Three-dimensional regional left ventricular deformation from digital sonomicrometry. In *Engineering in Medicine and Biology Society, 1997. Proceedings of the 19th Annual International Conference of the IEEE, (IEEE)*, pp. 848–851.

- Dixit, P., and Liu, G.R. (2017). A Review on Recent Development of Finite Element Models for Head Injury Simulations. *Arch. Comput. Methods Eng.* 24, 979–1031.
- Duma, S.M., Manoogian, S.J., Bussone, W.R., Broinson, P.G., Goforth, M.W., Donnenwerth, J.J., Greenwald, R.M., Chu, J.J., and Crisco, J.J. (2005). Analysis of real-time head accelerations in collegiate football players. *Clin. J. Sport Med.* 15, 3–8.
- Elkin, B.S., Gabler, L.F., Panzer, M.B., and Siegmund, G.P. (2018). Brain tissue strains vary with head impact location: a possible explanation for increased concussion risk in struck versus striking football players. *Clin. Biomech.*
- Fallenstein, G.T., Hulce, V.D., and Melvin, J.W. (1969). Dynamic mechanical properties of human brain tissue. *J. Biomech.* 2, 217–226.
- Fang, B.T. (1986). Trilateration and extension to global positioning system navigation. *J. Guid. Control Dyn.* 9, 715–717.
- Faul, M., Xu, L., Wald, M.M., and Coronado, V.G. (2010). Traumatic brain injury in the United States. *Atlanta GA Cent. Dis. Control Prev. Natl. Cent. Inj. Prev. Control.*
- Feng, Y., Abney, T.M., Okamoto, R.J., Pless, R.B., Genin, G.M., and Bayly, P.V. (2010). Relative brain displacement and deformation during constrained mild frontal head impact. *J. R. Soc. Interface* 7, 1677–1688.
- Finan, J.D., Elkin, B.S., Pearson, E.M., Kalbian, I.L., and Morrison, B. (2012). Viscoelastic properties of the rat brain in the sagittal plane: effects of anatomical structure and age. *Ann. Biomed. Eng.* 40, 70–78.
- Fomovsky, G.M., Rouillard, A.D., and Holmes, J.W. (2012). Regional mechanics determine collagen fiber structure in healing myocardial infarcts. *J. Mol. Cell. Cardiol.* 52, 1083–1090.
- Fountoulakis, M., Hardmeier, R., Höger, H., and Lubec, G. (2001). Postmortem changes in the level of brain proteins. *Exp. Neurol.* 167, 86–94.
- Gabler, L.F., Crandall, J.R., and Panzer, M.B. (2016a). Assessment of kinematic brain injury metrics for predicting strain responses in diverse automotive impact conditions. *Ann. Biomed. Eng.* 44, 3705–3718.
- Gabler, L.F., Crandall, J.R., and Panzer, M.B. (2016b). Investigating brain injury tolerance in the Sagittal Plane using a finite element model of the human head. *Int. J. Automot. Eng.* 7, 37–43.
- Gabler, L.F., Crandall, J.R., and Panzer, M.B. (2016c). Assessment of Kinematic Brain Injury Metrics for Predicting Strain Responses in Diverse Automotive Impact Conditions. *Ann. Biomed. Eng.* 44, 3705–3718.

- Gabler, L.F., Joodaki, H., Crandall, J.R., and Panzer, M.B. (2017). Development of a Single-Degree-of-Freedom Mechanical Model for Predicting Strain-based Brain Injury Responses. *J. Biomech. Eng.*
- Gabler, L.F., Crandall, J.R., and Panzer, M.B. (2018a). Development of a Metric for Predicting Brain Strain Responses Using Head Kinematics. *Ann. Biomed. Eng.* *46*, 972–985.
- Gabler, L.F., Crandall, J.R., and Panzer, M.B. (2018b). Development of a Second-Order System for Rapid Estimation of Maximum Brain Strain. *Ann. Biomed. Eng.* 1–11.
- Gadd, C.W. (1966). Use of a weighted-impulse criterion for estimating injury hazard (SAE Technical Paper).
- Ganpule, S., Daphalapurkar, N.P., Cetingul, M.P., and Ramesh, K.T. (2018). Effect of bulk modulus on deformation of the brain under rotational accelerations. *Shock Waves* *28*, 127–139.
- Garo, A., Hrapko, M., Van Dommelen, J.A.W., and Peters, G.W.M. (2007). Towards a reliable characterisation of the mechanical behaviour of brain tissue: the effects of post-mortem time and sample preparation. *Biorheology* *44*, 51–58.
- Gefen, A., Gefen, N., Zhu, Q., Raghupathi, R., and Margulies, S.S. (2003). Age-dependent changes in material properties of the brain and braincase of the rat. *J. Neurotrauma* *20*, 1163–1177.
- Gehre, C., Gades, H., and Wernicke, P. (2009). Objective rating of signals using test and simulation responses. In *21st International Technical Conference on the Enhanced Safety of Vehicles*, Stuttgart, Germany, p.
- Gennarelli, T.A. (1993). Mechanisms of brain injury. *J. Emerg. Med.* *11*, 5–11.
- Gennarelli, T.A. (2015). The centripetal theory of concussion (CTC) revisited after 40 years and a proposed new symptomcentric concept of the concussions. In *IRCOBI Conference Proceedings*, p.
- Gennarelli, T.A., Thibault, L.E., and Ommaya, A.K. (1972). Pathophysiologic responses to rotational and translational accelerations of the head (SAE Technical Paper).
- Gennarelli, T.A., Thibault, L.E., Adams, J.H., Graham, D.I., Thompson, C.J., and Marcincin, R.P. (1982). Diffuse axonal injury and traumatic coma in the primate. *Ann. Neurol.* *12*, 564–574.
- Gennarelli, T.A., Thibault, L.E., Tomei, G., Wisner, R., Graham, D., and Adams, J. (1987). Directional dependence of axonal brain injury due to centroidal and non-centroidal acceleration (SAE Technical Paper).

- Ghajari, M., Hellyer, P.J., and Sharp, D.J. (2017). Computational modelling of traumatic brain injury predicts the location of chronic traumatic encephalopathy pathology. *Brain* 140, 333–343.
- Giudice, J.S., Zeng, W., Wu, T., Alshareef, A., Shedd, D.F., and Panzer, M.B. (2018a). An Analytical Review of the Numerical Methods used for Finite Element Modeling of Traumatic Brain Injury. *Ann. Biomed. Eng.* 1–18.
- Giudice, J.S., Park, G., Kong, K., Bailey, A., Kent, R., and Panzer, M.B. (2018b). Development of open-source dummy and impactor models for the assessment of American football helmet finite element models. *Ann. Biomed. Eng.* 1–11.
- Giudice, J.S., Zeng, W., Wu, T., Alshareef, A., Shedd, D.F., and Panzer, M.B. (2018c). An Analytical Review of the Numerical Methods used for Finite Element Modeling of Traumatic Brain Injury. *Ann. Biomed. Eng.*
- Grewal, M.S. (2011). Kalman filtering. In *International Encyclopedia of Statistical Science*, (Springer), pp. 705–708.
- Guvenc, I., Gezici, S., Watanabe, F., and Inamura, H. (2008). Enhancements to Linear Least Squares Localization Through Reference Selection and ML Estimation. In *2008 IEEE Wireless Communications and Networking Conference*, (Las Vegas, Nevada, USA: IEEE), pp. 284–289.
- Hardy, W.N., Foster, C.D., King, A.I., and Tashman, S. (1997). Investigation of brain injury kinematics: introduction of a new technique. *ASME Appl. Mech. Div.-Publ.-AMD* 225, 241–254.
- Hardy, W.N., Foster, C.D., Mason, M.J., Yang, K.H., King, A.I., and Tashman, S. (2001). Investigation of Head Injury Mechanisms Using Neutral Density Technology and High-Speed Biplanar X-ray. *Stapp Car Crash J.* 45, 337–368.
- Hardy, W.N., Mason, M.J., Foster, C.D., Shah, C.S., Kopacz, J.M., Yang, K.H., King, A.I., Bishop, J., Bey, M., Anderst, W., et al. (2007). A study of the response of the human cadaver head to impact. *Stapp Car Crash J.* 51, 17.
- Harmon, K.G., Drezner, J.A., Gammons, M., Guskiewicz, K.M., Halstead, M., Herring, S.A., Kutcher, J.S., Pana, A., Putukian, M., and Roberts, W.O. (2013). American Medical Society for Sports Medicine position statement: concussion in sport. *Br J Sports Med* 47, 15–26.
- Helmick, K.M., Spells, C.A., Malik, S.Z., Davies, C.A., Marion, D.W., and Hinds, S.R. (2015). Traumatic brain injury in the US military: epidemiology and key clinical and research programs. *Brain Imaging Behav.* 9, 358–366.
- Hide, C., Moore, T., and Smith, M. (2004). Adaptive Kalman filtering algorithms for integrating GPS and low cost INS. In *Position Location and Navigation Symposium, 2004. PLANS 2004*, (IEEE), pp. 227–233.

- Hodgson, V.R. (1975). National Operating Committee on Standards for Athletic Equipment football helmet certification program. *Med. Sci. Sports* 7, 225–232.
- Holbourn, A.H.S. (1943). Mechanics of head injuries. *The Lancet* 242, 438–441.
- Holmes, J.W. (2004). Candidate mechanical stimuli for hypertrophy during volume overload. *J. Appl. Physiol.* 97, 1453–1460.
- Horgan, T.J., and Gilchrist, M.D. (2004). Influence of FE model variability in predicting brain motion and intracranial pressure changes in head impact simulations. *Int. J. Crashworthiness* 9, 401–418.
- Horiuchi, T., Tuna, E.E., Masamune, K., and Çavuşoğlu, M.C. (2012). Heart motion measurement with three dimensional sonomicrometry and acceleration sensing. In *Intelligent Robots and Systems (IROS), 2012 IEEE/RSJ International Conference On*, (IEEE), pp. 4143–4149.
- Hrapko, M., Van Dommelen, J.A., Peters, G.W., and Wismans, J.S. (2008). The influence of test conditions on characterization of the mechanical properties of brain tissue. *J. Biomech. Eng.* 130, 031003.
- Ji, S., Zhao, W., Ford, J.C., Beckwith, J.G., Bolander, R.P., Greenwald, R.M., Flashman, L.A., Paulsen, K.D., and McAllister, T.W. (2015). Group-wise evaluation and comparison of white matter fiber strain and maximum principal strain in sports-related concussion. *J. Neurotrauma* 32, 441–454.
- Jin, X., Lee, J.B., Leung, L.Y., Zhang, L., Yang, K.H., and King, A.I. (2006). Biomechanical Response of the Bovine Pia-Arachnoid Complex to Tensile Loading at Varying Strain Rates (SAE Technical Paper).
- Jin, X., Yang, K.H., and King, A.I. (2011). Mechanical properties of bovine pia–arachnoid complex in shear. *J. Biomech.* 44, 467–474.
- Jin, X., Zhu, F., Mao, H., Shen, M., and Yang, K.H. (2013). A comprehensive experimental study on material properties of human brain tissue. *J. Biomech.* 46, 2795–2801.
- Julier, S.J., and Uhlmann, J.K. (2004). Unscented filtering and nonlinear estimation. *Proc. IEEE* 92, 401–422.
- Kaya, M., Carvalho, W., Leonard, T., and Herzog, W. (2002). Estimation of cat medial gastrocnemius fascicle lengths during dynamic contractions. *J. Biomech.* 35, 893–902.
- Kim, T., Shin, J., Ye, X., Crandall, J., Knospe, C., and Funk, J. (2013). Evaluation of methods for the development of representative responses and corridors from biomechanical data using mechanical models. *Int. J. Crashworthiness* 18, 633–646.
- Kimpara, H., and Iwamoto, M. (2012). Mild traumatic brain injury predictors based on angular accelerations during impacts. *Ann. Biomed. Eng.* 40, 114–126.

- Kimpara, H., Nakahira, Y., Iwamoto, M., Rowson, S., and Duma, S. (2011). Head injury prediction methods based on 6 degree of freedom head acceleration measurements during impact. *Int. J. Automot. Eng.* 2, 13–19.
- Kleiven, S. (2007). Predictors for traumatic brain injuries evaluated through accident reconstructions. *Stapp Car Crash J.* 51, 81.
- Knutsen, A.K., Magrath, E., McEntee, J.E., Xing, F., Prince, J.L., Bayly, P.V., Butman, J.A., and Pham, D.L. (2014). Improved measurement of brain deformation during mild head acceleration using a novel tagged MRI sequence. *J. Biomech.* 47, 3475–3481.
- Kotanan, A., Hannikainen, M., Leppakoski, H., and Hamalainen, T.D. (2003). Experiments on local positioning with Bluetooth. In *Information Technology: Coding and Computing [Computers and Communications]*, 2003. Proceedings. ITCC 2003. International Conference On, (IEEE), pp. 297–303.
- Kremkau, F.W., Barnes, R.W., and McGraw, C.P. (1981). Ultrasonic attenuation and propagation speed in normal human brain. *J. Acoust. Soc. Am.* 70, 29–38.
- Laksari, K., Shafieian, M., and Darvish, K. (2012). Constitutive model for brain tissue under finite compression. *J. Biomech.* 45, 642–646.
- Langlois, J.A., Rutland-Brown, W., and Thomas, K.E. (2006). Traumatic brain injury in the United States; emergency department visits, hospitalizations, and deaths.
- Larsson, M., Heyde, B., Kremer, F., Brodin, L., Aake, and D’hooge, J. (2015). Ultrasound speckle tracking for radial, longitudinal and circumferential strain estimation of the carotid artery—an in vitro validation via sonomicrometry using clinical and high-frequency ultrasound. *Ultrasonics* 56, 399–408.
- Lessley, D., Crandall, J., Shaw, G., Kent, R., and Funk, J. (2004). A normalization technique for developing corridors from individual subject responses (SAE Technical Paper).
- Li, J., Yue, X., Chen, J., and Deng, F. (2017). A novel robust trilateration method applied to ultra-wide bandwidth location systems. *Sensors* 17, 795.
- Li, X., Cheng, G., and Lu, L. (2000). Comparison of spatial interpolation methods [J]. *Adv. Earth Sci.* 3.
- Li, Z., Hu, J., Reed, M.P., Rupp, J.D., Hoff, C.N., Zhang, J., and Cheng, B. (2011). Development, validation, and application of a parametric pediatric head finite element model for impact simulations. *Ann. Biomed. Eng.* 39, 2984–2997.
- Liszka, T. (1984). An interpolation method for an irregular net of nodes. *Int. J. Numer. Methods Eng.* 20, 1599–1612.

- Lukaszuk, S. (2004). A new concept of probability metric and its applications in approximation of scattered data sets. *Comput. Mech.* 33, 299–304.
- Madhukar, A., and Ostojca-Starzewski, M. (2019). Finite element methods in human head impact simulations: a review. *Ann. Biomed. Eng.* 1–23.
- Mallory, A.E. (2014). Measurement of Meningeal Motion Using B-Mode Ultrasound as a Step Toward Understanding the Mechanism of Subdural Hematoma. The Ohio State University.
- Mao, H., Zhang, L., Jiang, B., Genthikatti, V.V., Jin, X., Zhu, F., Makwana, R., Gill, A., Jandir, G., Singh, A., et al. (2013). Development of a finite element human head model partially validated with thirty five experimental cases. *J. Biomech. Eng.* 135, 111002.
- Margulies, S.S., Thibault, L.E., and Gennarelli, T.A. (1990). Physical model simulations of brain injury in the primate. *J. Biomech.* 23, 823–836.
- Matsumae, M., Kikinis, R., Mórocz, I.A., Lorenzo, A.V., Sándor, T., Albert, M.S., Black, P.M., and Jolesz, F.A. (1996). Age-related changes in intracranial compartment volumes in normal adults assessed by magnetic resonance imaging. *J. Neurosurg.* 84, 982–991.
- McCrea, M., Hammeke, T., Olsen, G., Leo, P., and Guskiewicz, K. (2004). Unreported concussion in high school football players: implications for prevention. *Clin. J. Sport Med.* 14, 13–17.
- McCrory, P.R., and Berkovic, S.F. (2001). Concussion The history of clinical and pathophysiological concepts and misconceptions. *Neurology* 57, 2283–2289.
- McCrory, E.J., Gerin, M.I., and Viding, E. (2017). Annual research review: childhood maltreatment, latent vulnerability and the shift to preventative psychiatry—the contribution of functional brain imaging. *J. Child Psychol. Psychiatry* 58, 338–357.
- Meaney, D.F., Morrison, B., and Bass, C.D. (2014). The mechanics of traumatic brain injury: a review of what we know and what we need to know for reducing its societal burden. *J. Biomech. Eng.* 136, 021008.
- Meoli, D., Mazhari, R., Dione, D., Omens, J., McCulloch, A., and Sinusas, A. (1998). Three-dimensional digital sonomicrometry: comparison with biplane radiography. In *Bioengineering Conference, 1998. Proceedings of the IEEE 24th Annual Northeast, (IEEE)*, pp. 64–67.
- Meyer, S.A., and Wolf, P.D. (1997). Application of sonomicrometry and multidimensional scaling to cardiac catheter tracking. *IEEE Trans. Biomed. Eng.* 44, 1061–1067.
- Miller, K., and Chinzei, K. (2002). Mechanical properties of brain tissue in tension. *J. Biomech.* 35, 483–490.

- Miller, L.E., Urban, J.E., and Stitzel, J.D. (2016). Development and validation of an atlas-based finite element brain model. *Biomech. Model. Mechanobiol.* 15, 1201–1214.
- Miller, L.E., Urban, J.E., and Stitzel, J.D. (2017). Validation performance comparison for finite element models of the human brain. *Comput. Methods Biomech. Biomed. Engin.* 20, 1273–1288.
- Murphy, W., and Hereman, W. (1995). Determination of a position in three dimensions using trilateration and approximate distances. *Dep. Math. Comput. Sci. Colo. Sch. Mines Gold. Colo. MCS-95* 7, 19.
- Nahum, A.M., Smith, R., and Ward, C.C. (1977). Intracranial pressure dynamics during head impact (SAE Technical Paper).
- Nalder, I.A., and Wein, R.W. (1998). Spatial interpolation of climatic normals: test of a new method in the Canadian boreal forest. *Agric. For. Meteorol.* 92, 211–225.
- Newman, J.A. (1986). A generalized acceleration model for brain injury threshold (GAMBIT). In *Proceedings of International IRCOBI Conference, 1986*, p.
- Newman, J.A., Shewchenko, N., and Welbourne, E. (2000). A proposed new biomechanical head injury assessment function—the maximum power index. *Stapp Car Crash J.* 44, 215–247.
- Nusholtz, G.S., Lux, P., Kaiker, P., and Janicki, M.A. (1984). Head impact response—Skull deformation and angular accelerations (SAE Technical Paper).
- Ommaya, A.K. (1984). *The head: kinematics and brain injury mechanisms* (Elsevier: Amsterdam).
- Ommaya, A.K., Grubb Jr, R.L., and Naumann, R.A. (1971). Coup and contre-coup injury: observations on the mechanics of visible brain injuries in the rhesus monkey. *J. Neurosurg.* 35, 503–516.
- Ono, K., Kikuchi, A., Nakamura, M., Kobayashi, H., and Nakamura, N. (1980). Human Head Tolerance to Sagittal Impact—Reliable Estimation Deduced from Experimental Head Injury Using Subhuman Primates and Human Cadaver Skulls. *SAE Trans.* 3837–3866.
- Panzer, M.B. (2012). *Numerical Simulation of Primary Blast Brain Injury*. PhD Thesis. Duke University.
- Panzer, M.B., Giudice, J.S., Caudillo, A., Mukherjee, S., Kong, K., Cronin, D.S., Barker, J., Gierczycka, D., Bustamante, M., and Bruneau, D. (2018). NUMERICAL CROWDSOURCING OF NFL FOOTBALL HELMETS. In *Journal of Neurotrauma*, (Mary Ann Liebert), pp. A148–A148.

- Park, G., Kim, T., Forman, J., Panzer, M.B., and Crandall, J.R. (2017). Prediction of the structural response of the femoral shaft under dynamic loading using subject-specific finite element models. *Comput. Methods Biomech. Biomed. Engin.* *20*, 1151–1166.
- Prange, M.T., and Margulies, S.S. (2002). Regional, directional, and age-dependent properties of the brain undergoing large deformation. *J. Biomech. Eng.* *124*, 244–252.
- Prevost, T.P., Balakrishnan, A., Suresh, S., and Socrate, S. (2011). Biomechanics of brain tissue. *Acta Biomater.* *7*, 83–95.
- Purves, D., Augustine, G.J., Fitzpatrick, D., Katz, L.C., LaMantia, A.-S., McNamara, J.O., and Williams, S.M. (2001). *Neuroglial Cells*. Neurosci. 2nd Ed.
- Purves, D., Augustine, G.J., Fitzpatrick, D., Hall, W.C., LaMantia, A.-S., and White, L.E. (2011). *Neuroscience* (Sinauer Associates is an imprint of Oxford University Press).
- Rahman, M.Z. (2012). Beyond trilateration: GPS positioning geometry and analytical accuracy. In *Global Navigation Satellite Systems: Signal, Theory and Applications*, (InTech), p.
- Ramo, N.L., Troyer, K.L., and Puttlitz, C.M. (2018). Viscoelasticity of spinal cord and meningeal tissues. *Acta Biomater.* *75*, 253–262.
- Reina, M.A., Casasola, O.D.L., Villanueva, M.C., López, A., Machés, F., and De Andrés, J.A. (2004). Ultrastructural findings in human spinal pia mater in relation to subarachnoid anesthesia. *Anesth. Analg.* *98*, 1479–1485.
- Reina, M.A., Prats-Galino, A., Sola, R.G., Puigdemívol-Sánchez, A., Arriazu, R.N., and De, J.A. (2010). Structure of the arachnoid layer of the human spinal meninges: a barrier that regulates dural sac permeability. *Rev. Esp. Anesthesiol. Reanim.* *57*, 486–492.
- Robbins, D.H., Schneider, L.W., Snyder, R.G., Pflug, M., and Haffner, M. (1983). Seated posture of vehicle occupants (SAE Technical Paper).
- Rohr, K., Stiehl, H.S., Sprengel, R., Buzug, T.M., Weese, J., and Kuhn, M.H. (2001). Landmark-based elastic registration using approximating thin-plate splines. *IEEE Trans. Med. Imaging* *20*, 526–534.
- Rowson, S., and Duma, S.M. (2013). Brain injury prediction: assessing the combined probability of concussion using linear and rotational head acceleration. *Ann. Biomed. Eng.* *41*, 873–882.
- Sabet, A.A., Christoforou, E., Zatlin, B., Genin, G.M., and Bayly, P.V. (2008). Deformation of the human brain induced by mild angular head acceleration. *J. Biomech.* *41*, 307–315.

- Sack, I., Beierbach, B., Wuerfel, J., Klatt, D., Hamhaber, U., Papazoglou, S., Martus, P., and Braun, J. (2009). The impact of aging and gender on brain viscoelasticity. *Neuroimage* 46, 652–657.
- SAE, S. (2007). J211-1 Instrumentation for Impact Test—Part 1—Electronic Instrumentation. SAE Int.
- Sanchez, E.J., Gabler, L.F., McGhee, J.S., Olszko, A.V., Chancey, V.C., Crandall, J., and Panzer, M.B. (2017). Evaluation of head and brain injury risk functions using sub-injurious human volunteer data. *J. Neurotrauma*.
- Santiago, L.A., Oh, B.C., Dash, P.K., Holcomb, J.B., and Wade, C.E. (2012). A clinical comparison of penetrating and blunt traumatic brain injuries. *Brain Inj.* 26, 107–125.
- Sarazan, R.D., and Schweitz, K.T. (2009). Standing on the shoulders of giants: Dean Franklin and his remarkable contributions to physiological measurements in animals. *Adv. Physiol. Educ.* 33, 144–156.
- Senesh, M., and Wolf, A. (2009). Motion estimation using point cluster method and Kalman filter. *J. Biomech. Eng.* 131, 051008.
- Shafieian, M., Darvish, K.K., and Stone, J.R. (2009). Changes to the viscoelastic properties of brain tissue after traumatic axonal injury. *J. Biomech.* 42, 2136–2142.
- Shakarami, M., Suratgar, A.A., and Talebi, H.A. (2018). Intraoperative Brain Shift Estimation Using Atlas of Brain Deformations and Constrained Kalman Filter. *IEEE Trans. Control Syst. Technol.* 1–10.
- Shepard, D. (1968). A two-dimensional interpolation function for irregularly-spaced data. In *Proceedings of the 1968 23rd ACM National Conference*, (ACM), pp. 517–524.
- Shuck, L.Z., and Advani, S.H. (1972). Rheological response of human brain tissue in shear. *J. Basic Eng.* 94, 905–911.
- Sipes, N.S., Shearn, J.T., and Butler, D.L. (2005). Evaluation of a Sonomicrometry Device for Measuring in vivo Dynamic Joint Kinematics: Applications to Functional Tissue Engineering. *J Biomech* 38, 2486–2490.
- Smith, D.H., and Meaney, D.F. (2000). Axonal damage in traumatic brain injury. *The Neuroscientist* 6, 483–495.
- Smith, D.H., Chen, X., Xu, B.-N., McIntosh, T.K., Gennarelli, T.A., and Meaney, D.E. (1997). Characterization of diffuse axonal pathology and selective hippocampal damage following inertial brain trauma in the pig. *J. Neuropathol. Exp. Neurol.* 56, 822–834.
- Stalnaker, R.L., Melvin, J.W., Nusholtz, G.S., Alem, N.M., and Benson, J.B. (1977). Head impact response (SAE Technical Paper).

Stonecash, R.M. (2005). Evaluation of a Sonomicrometry System for the Measurement of Joint Kinematics. University of Cincinnati.

Subhan, F., Hasbullah, H., and Ashraf, K. (2013). Kalman filter-based hybrid indoor position estimation technique in bluetooth networks. *Int. J. Navig. Obs.* 2013.

Sugawara, O., Atsuta, Y., Iwahara, T., Muramoto, T., Watakabe, M., and Takemitsu, Y. (1996). The effects of mechanical compression and hypoxia on nerve root and dorsal root ganglia: an analysis of ectopic firing using an in vitro model. *Spine* 21, 2089–2094.

Takahashi, Y., and Yanaoka, T. (2017). A Study of Injury Criteria for Brain Injuries in Traffic Accidents. In 25th International Technical Conference on the Enhanced Safety of Vehicles (ESV) National Highway Traffic Safety Administration, p.

Takhounts, E.G., Crandall, J.R., and Darvish, K. (2003). On the importance of nonlinearity of brain tissue under large deformations (SAE Technical Paper).

Takhounts, E.G., Ridella, S.A., Hasija, V., Tannous, R.E., Campbell, J.Q., Malone, D., Danelson, K., Stitzel, J., Rowson, S., and Duma, S. (2008a). Investigation of traumatic brain injuries using the next generation of simulated injury monitor (SIMon) finite element head model. *Stapp Car Crash J.* 52, 1.

Takhounts, E.G., Ridella, S.A., Hasija, V., Tannous, R.E., Campbell, J.Q., Malone, D., Danelson, K., Stitzel, J., Rowson, S., and Duma, S. (2008b). Investigation of traumatic brain injuries using the next generation of simulated injury monitor (SIMon) finite element head model. *Stapp Car Crash J.* 52, 1.

Takhounts, E.G., Craig, M.J., Moorhouse, K., McFadden, J., and Hasija, V. (2013a). Development of brain injury criteria (BrIC). *Stapp Car Crash J.* 57, 243.

Takhounts, E.G., Craig, M.J., Moorhouse, K., McFadden, J., and Hasija, V. (2013b). Development of brain injury criteria (BrIC). *Stapp Car Crash J.* 57, 243–266.

Tanielian, T., Haycox, L.H., Schell, T.L., Marshall, G.N., Burnam, M.A., Eibner, C., Karney, B.R., Meredith, L.S., Ringel, J.S., and Vaiana, M.E. (2008). Invisible wounds of war. Summary and recommendations for addressing psychological and cognitive injuries (RAND CORP SANTA MONICA CA).

Taylor, C.A., Bell, J.M., Breiding, M.J., and Xu, L. (2017). Traumatic Brain Injury–Related Emergency Department Visits, Hospitalizations, and Deaths — United States, 2007 and 2013. *MMWR Surveill. Summ.* 66, 1–16.

Thibault, K.L., and Margulies, S.S. (1998). Age-dependent material properties of the porcine cerebrum: effect on pediatric inertial head injury criteria. *J. Biomech.* 31, 1119–1126.

Thomas, F., and Ros, L. (2005). Revisiting trilateration for robot localization. *IEEE Trans. Robot.* 21, 93–101.

- Trosseille, X., Tarriere, C., Lavaste, F., Guillon, F., and Domont, A. (1992). Development of a FEM of the human head according to a specific test protocol (SAE Technical Paper).
- Van Trigt, P., Bauer, B.J., Olsen, C.O., Rankin, J.S., and Wechsler, A.S. (1981). An improved transducer for measurement of cardiac dimensions with sonomicrometry. *Am. J. Physiol.-Heart Circ. Physiol.* *240*, H664–H668.
- Versace, J. (1971). A review of the severity index (SAE Technical Paper).
- Viano, D., Aldman, B., Pape, K., Hoof, J. van, and Holst, H. von (1997). Brain kinematics in physical model tests with translational and rotational acceleration. *Int. J. Crashworthiness* *2*, 191–206.
- Wu, T., Alshareef, A., Giudice, J.S., and Panzer, M.B. (2019). Explicit Modeling of White Matter Axonal Fiber Tracts in a Finite Element Brain Model. *Ann. Biomed. Eng.* 1–15.
- Xu, J., He, J., Zhang, Y., Xu, F., and Cai, F. (2016). A distance-based maximum likelihood estimation method for sensor localization in wireless sensor networks. *Int. J. Distrib. Sens. Netw.* *12*, 2080536.
- Yanaoka, T., Dokko, Y., and Takahashi, Y. (2015). Investigation on an injury criterion related to traumatic brain injury primarily induced by head rotation (SAE Technical Paper).
- Yim, J., Park, C., Joo, J., and Jeong, S. (2008). Extended Kalman filter for wireless LAN based indoor positioning. *Decis. Support Syst.* *45*, 960–971.
- Yim, J., Jeong, S., Gwon, K., and Joo, J. (2010). Improvement of Kalman filters for WLAN based indoor tracking. *Expert Syst. Appl.* *37*, 426–433.
- Zhang, L., Yang, K.H., and King, A.I. (2004). A proposed injury threshold for mild traumatic brain injury. *Trans.-Am. Soc. Mech. Eng. J. Biomech. Eng.* *126*, 226–236.
- Zhou, Y. (2009). An efficient least-squares trilateration algorithm for mobile robot localization. In *Intelligent Robots and Systems, 2009. IROS 2009. IEEE/RSJ International Conference On*, (IEEE), pp. 3474–3479.
- (1995). SAE Recommended Practice, Instrumentation for Impact Tests, I: Electronic Instrumentation.
- (2011). NCI Dictionary of Cancer Terms.
- (2015). NHTSA New Car Assessment Program (NCAP).
- The Brain: Facts (Science Trek: Idaho Public Television).

